Improve the Flexibility of Power Distribution Network by Using Back-to-back Voltage Source Converter

By

Ruizhu Wu

A Thesis Submitted for the Degree of
Doctor of Philosophy

University of Warwick, School of Engineering
October 2018

Contents

List of Figures

List of Tables

Acknowledgement

I would like to present my sincerely thanks to all people and organisations who offered help and supports to me during my PhD study. Among them, there are some persons I would like to present my thankfulness individually.

First and foremost, I would like to present my most gratefully and sincerely thanks to my supervisor, Professor Li Ran, for all his help, encouragement, guidance and care during my whole PhD study in the University of Warwick. I have been extremely lucky to have a supervisor who cared so much about my work and life; who taught me a lot about academics and researches; and who spent so much time and effort to revise my papers.

I would also like to thank Dr. James Yu for offering me the opportunity to participate in the Offshore Low Frequency ac Power Transmission project. I am especially grateful for the scholarship and support from James.

I would like to thank the Technician Team in the school of Engineering for supporting my researches. I would like to thank Ian Griffith, Gavin Downs and especially Jonathan Meadows for helping build the test platform for the induction machine research and of course for other experiment setup. I would also like to thank Jose Ortiz Gonzalez for helping me on experiments with his rich experience.

I would like to thank my colleague Tianqu Hao for guiding me use dSpace for experiments. I would like to thank Han Qin, Erfan Bashar and Weihua Shao for the great time that we wrote papers together. I would also like to thank all my other friends and colleagues: Yuan Tang, Ji Hu, Fan Li, Tianxiang Dai, Xuan Guo, Roozbeh Bonyadi, Saeed, Ben, Guy for their support and the happy memories on dinners, drinks, jokes and football games!

Finally, and most importantly, I would like to thank my beloved family including my father, mother, father-in-law and mother-in-law for the love, support, understanding and encouragement they provided to me. I would like to present my love and sincerely thankfulness to my beloved wife, Kaijing Wang for her thoughtful support to my life and study and the sacrifice she made to accompany me walk through my PhD life.

Declaration

The work presented in this thesis is based on research carried out by the candidate in the School of Engineering, the University of Warwick, UK. No part of this thesis has been submitted for any other degree or qualifications at any other university. Part of the work presented in Chapter 2 has been published in C1 (list of publication is in Appendix III). Part of the work presented in Chapter 4 has been published in C2. C1 and C2 are based on collaborative researches and the contents presented in this thesis are contributed by the candidate. The work presented in Chapter 6 has been published in J1.

Ruizhu Wu

October 2018

Abstract

Employing increasing distributed generations (DGs) into existing distribution networks is an inevitable trend of the development of modern electric power systems because of the benefits including the environmentally friendly generation, higher efficiency and improved flexibility and reliability. However, high DG penetration level could pose various issues among which the voltage violation and fault level increase are the most concerned. According to the current situation of UK distribution networks, voltage violation is likely to be the first constraint to be met when DG penetration level is increased to certain level. Therefore, compensators are considered to be implemented to regulate the voltage. The reactive power compensators that widely used in transmission systems appear less effective in distribution networks thus active power compensation is desired. Soft-open points (SOPs) are power-electronic devices used replacing the normally-open points which can control active power transfer between two feeders and/or provide reactive power compensation. The back-to-back voltage source converter (B2B-VSC) is preferred as the SOP because of its capability of restricting fault current despite that it has higher power loss and associated capital cost. Two types of controller are developed for the B2B-VSC-based SOP: one is based on the PI control theory and the other is based on the concept of synchronverters. For the former type, the controller design is introduced comprehensively including system modelling and parameters selection. The precise selection of the damping ratio for nonstandard second-order system is derived, and a technique of resetting integrator in output voltage controller loop to achieve fast and smooth islanding transition is proposed. For the latter type, modifications are made to adapt the synchronverter idea to the application of an SOP. Simulations and experiments are carried out to validate the controller designs and both the controllers are verified to be able to provide sufficient performance on voltage regulation, fault current restriction and independent load supply in island mode. In general, the controller based on PI control theory has better performance in fault condition thanks to the current control loop, and the controller based on synchronverter owns better reliability because it does not require additional detections and signal switches inside the controller. At last, the use of an SOP in a dynamic load dominated network after the loss of mains is further investigated. Torque-speed characteristic is used to analyse the influence of the VSC's filter impedance on the stability margin of an induction motor. Though the filter impedance can significantly decrease the stability margin, the output impedance of the VSC can be mitigated by properly designing the output voltage controller. Simulation and experiment are carried out to validate the analyses and controller design. The results show that the VSC is capable of supplying an induction motor in island mode.

Abbreviation

AC	alternating current
DC	direct current
NGET	National Grid Electricity Transmission plc
DNOs	Distribution Network Operators
DG	distributed generation
CHP	combined heat and power
SOP	Soft-open point
NOP	normally-open point
VSC	voltage source converter
B2B	back-to-back
FL	fault level
V_{Lnom}	nominal line voltage
I_f	fault current
rms	root-mean-square
p.u.	per unit
OLTC	on-load tap changer
R_L	resistance of a power line
X_L	reactance of a power line
X_C	capacitor reactance
X_{re}	reactor reactance
FACTS	Flexible AC Transmission System
SVC	static VAR compensator
TCR	Thyristor-Controlled Reactor
TSR	Thyristor-Switched Reactor
TSC	Thyristor-Switched Capacitor
FC-TCR	Fixed Capacitor Thyristor-Controlled Reactor
TSC-TCR	Thyristor-Switched Capacitor-Thyristor-Controlled Reactor
TSSC	Thyristor-Switched Series Capacitor
TCSC	Thyristor-Controlled Series Capacitor
TCSR	Thyristor-Controlled Series Reactor
STATCOM	static synchronous compensator
GTO	Gate Turn-Off Thyristor
IGBT	Integrated Gate Bipolar Transistor
MTO	MOS Turn-off Thyristor
IGCT	Integrated Gate-commutated Thyristor
SSSC	static synchronous series compensator
V_{inj}	Injected voltage to the network by a compensator
UPFC	unified power flow controller
HVDC	High-voltage direct current
V_s	sending voltage
V_r	receiving voltage
φ	phase angle between current and voltage

R	general resistance
X	general reactance
P	active power
Q	reactive power
P_L	load demand power
P_{DG}	output power by DG
V_{ce}	voltage between collector and emitter
I_{c}	collector current
E_{total}	total energy loss of a device
e_{on}	device's turn-on loss
e_{off}	device's turn-off loss
e_{rec}	diode's reverse recovery loss
PR	proportion-resonant
PI	proportional-integral
R_f	filter resistance
L_f	filter inductance
C_f	filter capacitance
v_i	phase voltage before filter
v_o	output phase voltage
i_L	filter inductor current
i_o	output current
i_c	capacitor current
ω	angular velocity
v_{DC}	DC link voltage
X_{abc}	balanced three-phase quantities
X^*	reference value to a quantity
X_d	quantity at d axis
X_q	quantity at q axis
X_{dq}	$X_{dq}=X_d+jX_q$
X_α	quantity at α axis
X_β	quantity at β axis
$X_{\alpha\beta}$	$X_{\alpha\beta}=X_\alpha+jX_\beta$
$dq0$	direct-quadrature-zero
SRF	synchronous reference frame
K_c	amplitude-invariant Clark transformation matrix
K_p	Park transformation matrix
$T[\theta]$	$dq0$ transformation matrix
$T^{-1}[\theta]$	inverse $dq0$ transformation matrix
V_m	voltage amplitude
θ_0	angle of reference voltage
θ	angle of controlled voltage
PLL	phase-locked loop
$G_{PLL}(s)$	phase-locked loop controller
K_{P_PLL}	PLL controller proportional gain
K_{I_PLL}	PLL controller integral gain
ω_{PLL}	PLL natural frequency

ξ_{PLL}	PLL damping ratio
K_{P_C}	current controller proportional gain
K_{I_C}	current controller integral gain
T_d	total delay in VSC process
f_s	PWM sampling and converter switching frequency
T_s	PWM sampling time Ts=1/fs
$e^{-(s+j\omega)T_d}$	total delay in SRF
$e^{j\omega T_d}$	delay compensation term in SRF
$G_C(s)$	current controller gain
$H_C(s)$	current loop plant
$G_{CL}(s)$	current loop closed-loop transfer function
$\hat{L}_f$	estimations of the filter inductance
$\hat{R}_f$	estimations of the filter resistance
τ	current loop time constant
n	n=1/ τ
P_{DC}	power flowing into or out from the DC link
u	square of the DC link voltage
$U(s)$	square of the DC link voltage is *s* domain
C	DC link capacitance
$G_{DC}(s)$	DC link voltage controller gain
$H_{DC}(s)$	DC link voltage plant transfer function
K_{P_DC}	DC link voltage controller proportional gain
K_{I_DC}	DC link voltage controller integral gain
$N_{DCVL}(s)$	open-loop transfer function of DC link voltage loop
$G_{DCVL}(s)$	closed-loop transfer function of DC link voltage loop
$G'_{DCVL}(s)$	simplified closed-loop transfer function of DC link voltage loop
ω_{DC}	DC link voltage control loop natural frequency
ξ_{DC}	DC link voltage control loop damping ratio
ω_n	arbitrary natural frequency of a second-order system or nominal angular velocity
ξ	arbitrary damping ratio of a second-order system
ω_d	$\omega_d = \omega_n\sqrt{1-\xi^2}\ (0<\xi<1)$
$H_{step}(s)$	step response in *s* domain
$h_{step}(t)$	step response in time domain
t_p	time required to reach the first peak
h_{peak}	Peak value of the overshoot
M_p	Maximum overshoot
t_r	rising time of second-order systems
$H_V(s)$	transfer function of output voltage loop
$GV(s)$	output voltage controller gain
K_{P_V}	output voltage controller proportional gain
K_{I_V}	output voltage controller integral gain
$G'_{VL}(s)$	simplified closed-loop transfer function of output voltage loop
ω_V	output voltage control loop natural frequency
ξ_V	output voltage control loop damping ratio

t_{r_V}	rising time of output voltage control loop
$u1$	input 1 of the state-space matrices of output voltage control loop
$u2$	input 2 of the state-space matrices of output voltage control loop
$u3$	input 3 of the state-space matrices of output voltage control loop
$u4$	input 4 of the state-space matrices of output voltage control loop
$y1$	output 1 of the state-space matrices of output voltage control loop
$y2$	output 2 of the state-space matrices of output voltage control loop
X_1	quantities at or connected to *Feeder 1*
X_2	quantities at or connected to *Feeder 2*
PF	power factor
THD	total harmonic distortion
variac	variable transformer
R_s	stator resistance
L_s	stator inductance
M	mutual inductance between two stator phase windings across the air-gap and a round rotor
M_{ar}, M_{br}, M_{cr}	mutual inductances between each stator phase and the rotor excitation winding
ir	rotor excitation current
λ	flux linkages
v_{in}	induced voltage in a synchronous machine
e	voltage induced by rotor current
J	inertia of the rotor
T_m	mechanical torque
T_e	electromagnetic torque
K	control gain of Q-V loop
P_m	actually the electric power exchanged with the DC link
P_e	output electric power to the AC terminal
D_{P_t}	angular velocity damping factor
D_P	$D_P = \omega \cdot D_{P\_t}$
D_q	droop gain of Q-V loop
τ_1	time constant of P-ω loop
τ_2	time constant of Q-V loop
ω_g	grid angular velocity
K_p	proportional gain of PI controller in P-ω loop
K_i	integral gain of PI controller in P-ω loop
K_{DC}	control gain of DC link voltage controller
L_M	magnetizing inductance
X_M	magnetizing reactance
L_r	referred rotor inductance
X_r	referred rotor reactance
R_r	referred rotor resistance
X_s	stator reactance
s	slip
I_r	rotor current
n_{sync}	magnetic field speed

n_m	mechanical shaft speed
T	induced toque in an induction machine
P_{ag}	air-gap power
ω_{sync}	synchronous angular velocity
V_{th}	Thevenin equivalent voltage
Z_{th}	Thevenin equivalent impedance
R_{th}	Thevenin equivalent resistance
X_{th}	Thevenin equivalent reactance
X_{Lf}	filter reactance by the inductor
X_{Cf}	filter reactance by the capacitor
V_{fth}	Thevenin equivalent voltage for VSC filter
Z_{fth}	Thevenin equivalent impedance for VSC filter
R_{fth}	Thevenin equivalent resistance for VSC filter
X_{fth}	Thevenin equivalent reactance for VSC filter
ω_{LF}	cut-off frequency of the low pass filter
$G(s)$	current feedforward gain
DBC	direct bonded copper

1.Introduction

1.1 Conventional Electric Power System

Electric power systems have been formed by centralised power stations, transmission systems and distribution networks for over several decades. However, in early days of electricity, power stations were constructed in the adjacent of customers and relatively simple networks were built to connect them. Then, this scheme was replaced by the unified electricity grid due to the rapid increase of power demand. In Great Britain, the 'national grid' was first established in 1930. Those simple networks built in the early days were converted to distribution networks. Following by a rapid development period in the 1950s and 1960s, the National Supergrid system in the United Kingdom today was formed [1].

In today's electric systems the majority of electric power is generated in large power stations in three-phase form to achieve constant power generation and defined as the product of two quantities: AC current and AC voltage. Then the power is stepped up to high voltage level by transformers and then carried by the transmission systems from generating centres to load centres. Approximately 85% of the total generating capacity in the UK is connected to the national transmission system which is operated by National Grid Electricity Transmission plc (NGET). At downstream system are distribution networks, operated by Distribution Network Operators (DNOs), by which the power is stepped down to medium and low voltage levels and fed to customers such as residences, hospitals and industries. Figure 1.1 shows a brief figure for the conventional electric power system.

Large power stations converting energy from coal, gas, nuclear and hydroelectric power are located either close to primary sources or far away from populated areas. Therefore, conventional electric systems generally have bulk power transmitted for a long distant in transmission systems which causes considerable power loss and associated construction expenses.

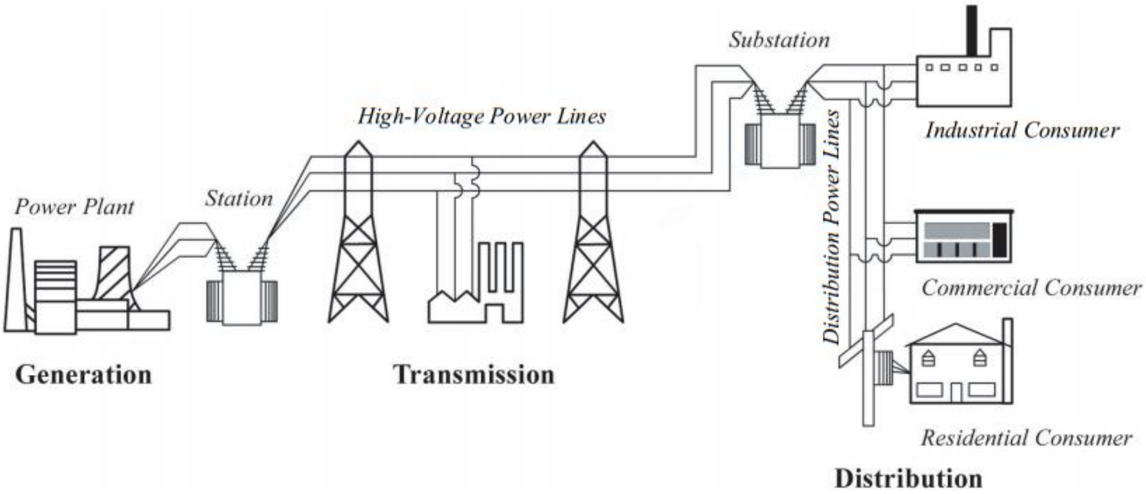

Figure 1.1 Electric power system [2].

With the rapidly increasing consumption of electricity, the reserves of fossil fuels will be greatly consumed in the near future. The exhaustion of oil and gas could happen in a century and the exhaustion of coal could happen in two or three centuries [3, 4]. Besides, although electricity has been providing great development and convenience to human beings, the generation of it causes pollutions to environment. Therefore, to seek cleaner and more sufficient electricity generation becomes an inevitable demand throughout the world.

1.2 Distributed Generation

Distributed generation (DG), also known as embedded generation or on-site generation or dispersed generation, can be described as the generation of electricity from decentralized and small-scale generators which are mostly placed at load centres. DG units are connected to distribution networks rather than the transmission network [5-11]. It is more flexible than centralized power generation and has very low power loss in transmission as they are located in the vicinity of customers [6, 12]. Compared to conventional power system, a highly distributed system could provide benefits such as:

- Environmentally friendly – DG sources such as wind and sunlight are totally harmless to environment and most of CHP plants use either natural gas or renewable gases which are also friendly to environment;

- Higher efficiency – lower power loss in transmission and CHP is a more efficient way of utilising primary fuels;
- Improved flexibility and reliability – modular and decentralised system might be able to operate individually to secure local demand and adapt more readily to technology changes;
- More competition in the market – a decentralised system encourages more participants thus increasing competition [1].

In the past, distributed generation refers to combustion generators which is not clean. In recent years, renewable resources particularly wind and solar energy have been greatly developed as the distributed generation. Under the megatrends of low carbon footprints, it is expected that the distributed generation of renewable resources will play an important role in the future electric power system. The following part of this section will summarise the statistics of main types of distributed generation in the UK in recent years to illustrate the development trend.

1.2.1 Combined Heat and Power

Combined heat and power (CHP) or cogeneration is the simultaneous generation of electricity and useful heat. CHP is not necessarily low-carbon but is definitely more efficient than generating electricity and heat separately. The overall efficiency of the energy conversion of a CHP plant can be over 80% which is approximately 1.6 times of the efficiency of a good combined cycle gas turbine station [13]. CHP was used in manufacturing industry in the early days and the first installation was probably in Glasgow in 1898. In 1980s, CHP-based district heating, which is to district the heat generated in power stations to local buildings, was greatly developed by the support from government in the UK [14]. In 1990s, the UK's first major modern heat-distribution grid was built in Sheffield, and small-scale CHPs were being developed [15].

Table 1-1 shows the development of CHP in the UK in the recent five years [16]. The number of CHP schemes has been increasing gradually over the past five years and 162 schemes were added during 2017. Installed electrical capacity reached 5835 MWe in 2017, an increase of 209 MWe (3.7%) compared to 2016. Electricity generation overall had an increasing trend and stood at 21648 GWh in 2017 which is 6.4% of the total electricity generated in the UK. The overall efficiencies are always over 70% thanks to the UK's CHP Quality Assurance programme which requires a Good Quality CHP scheme over 1 MWe must achieve 10% primary energy savings compared to separate generation of heat and power.

Table 1-1 Recent development of CHP in the UK

	Unit	2013	2014	2015	2016	2017
Number of schemes		2024	2017	2130	2224	2386
Electrical capacity	MWe*(1)*	5919	5888	5708	5625	5835
Heat capacity	MWth*(2)*	22161	22223	20091	19795	20191
Fuel input	GWh	88403	86184	82576	85123	90279
Electricity generation	GWh	19515	19690	19534	20405	21648
Heat generation	GWh	44342	41950	40234	40670	42238
Overall efficiency	Per cent	72.2	71.5	72.4	71.7	70.8

(1) MWe: Megawatt electric.   (2) MWth: Megawatt thermal.

In general, CHP plants can be divided into three levels depending on the size [17]:

- Micro CHP plants for domestic use generating both electricity and heat for the home;
- Medium CHP plants generating both electricity and heat for a whole building or community area;
- Large CHP plants generating heat for local use and electricity that fed into high voltage distribution network or even transmission network.

A statistic of CHP by capacity size in 2017 is shown in Table 1-1. Micro and Medium CHP plants are dominant in numbers (over 80%), but large CHP plants output the majority of electricity (72%). It is worth noting that, from the electricity generation point of view, some of the large CHP plants should not be counted as distributed generation because though the heat generated is used locally, the electricity generated is fed into transmission networks rather than distribution networks.

The majority of fuels used for CHP in the UK in 2017 was natural gas (68.7%), and renewable sources come at the second (16.5%) as shown in Figure 1.2. The proportion of the renewable fuel consumption increased from 13% in 2016 to 16.5% in 2017.

Table 1-2 CHP schemes by capacity size ranges in the UK in 2017

Electrical capacity size range	Number of schemes and share of total	Total electricity capacity (MWe) and share of total
<100kWe	605 (25%)	36 (0.6%)
100kWe ~ 1MWe	1291 (54%)	331 (5.7%)
1MWe ~ 2MWe	183 (7.7%)	259 (4.4%)
2MWe ~ 10MWe	240 (10%)	1027 (18%)
>10MWe	67 (2.8%)	4181 (72%)
Total	2386	5835

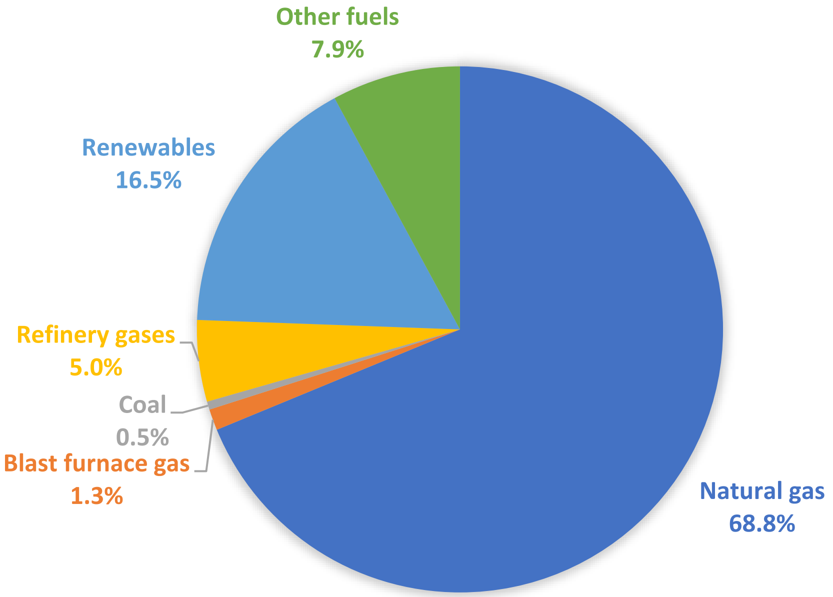

Figure 1.2 Types of fuel used for CHP in the UK in 2017.

1.2.2 Renewable Energies

Renewable energy is the energy from renewable resources which are naturally replenished on a human timescale such as wind, sunlight and tides. Renewable energies are not new to human society. In fact, human beings started to use traditional biomass to fuel fires about 790,000 years ago [18]. However, the electricity generation by renewable energies has only been developed and implemented in recent decades.

The development of electricity supply in the UK since 1980 is shown in Figure 1.3 [19]. Electricity supply is fully driven by demand. The demand for electricity has been dropping because of the improving energy efficiency and overall warmer weather in the UK. However, the proportion of renewables has been greatly increased, trebled in 2017 compared to 2010. On the contrary, the use of fossil fuels has seen a large reduction since 2010, 44% reduction from 2010 to 2017. These changes on electricity supply in the UK are due to a continuation of the shift in fuel mix away from coal [19].

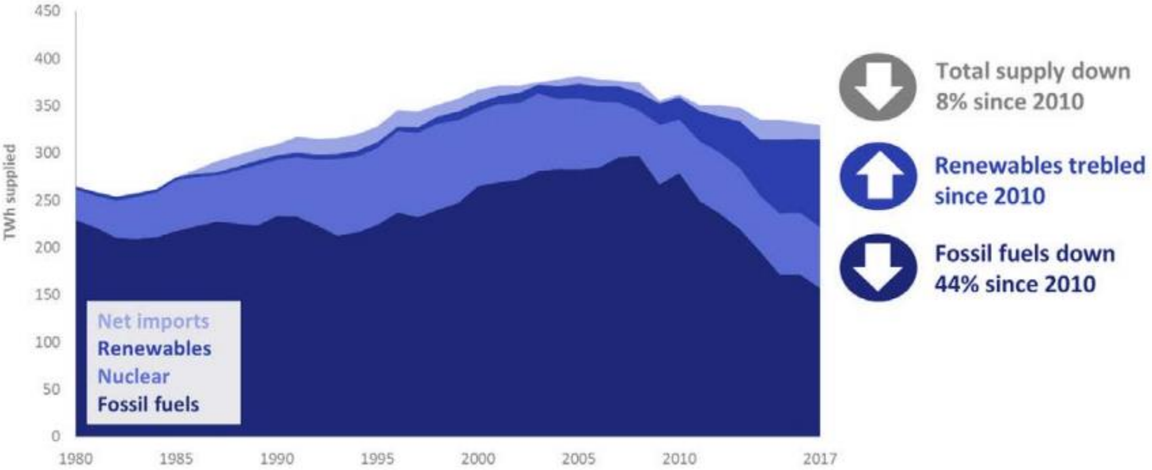

Figure 1.3 UK electricity supply since 1980 [19].

In terms of the share of electricity generation by renewable energies, wind occupied half of the electricity generation, 29% and 21% by onshore and offshore respectively in the UK in 2017 as shown in Figure 1.4. The proportion of the electricity generated by renewable sources to the total electricity generation is 29.3% (99.3 TWh) in the UK in 2017, was 24.5% (83.1-TWh) in 2016 [20]. A long-term trend of electricity generation by renewable sources is shown in Figure 1.5. From 2010, renewable energies have been greatly exploited where wind and solar share the major proportion of the increase of electricity generation.

It should be noted that not all the renewable sources are counted as DG, i.e. offshore windfarms are usually connected to transmission network. However, it still shows a promising trend of the increasing DG from renewable sources.

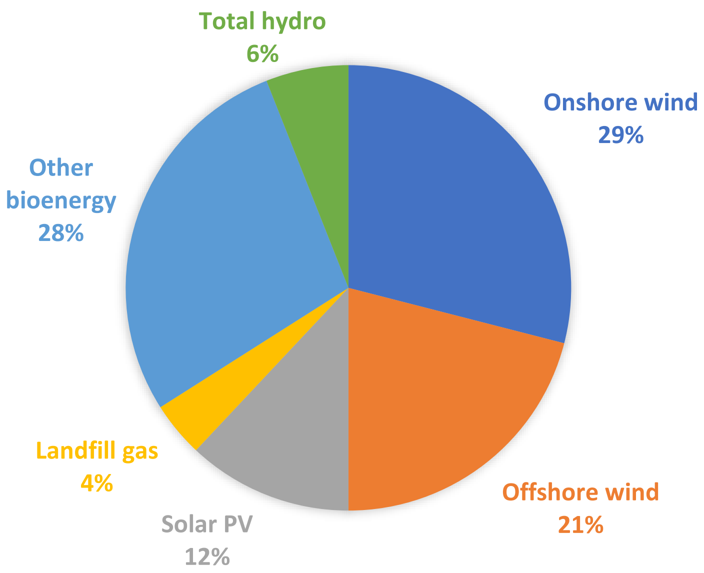

Figure 1.4. Electricity generation by fuel types in the UK in 2017.

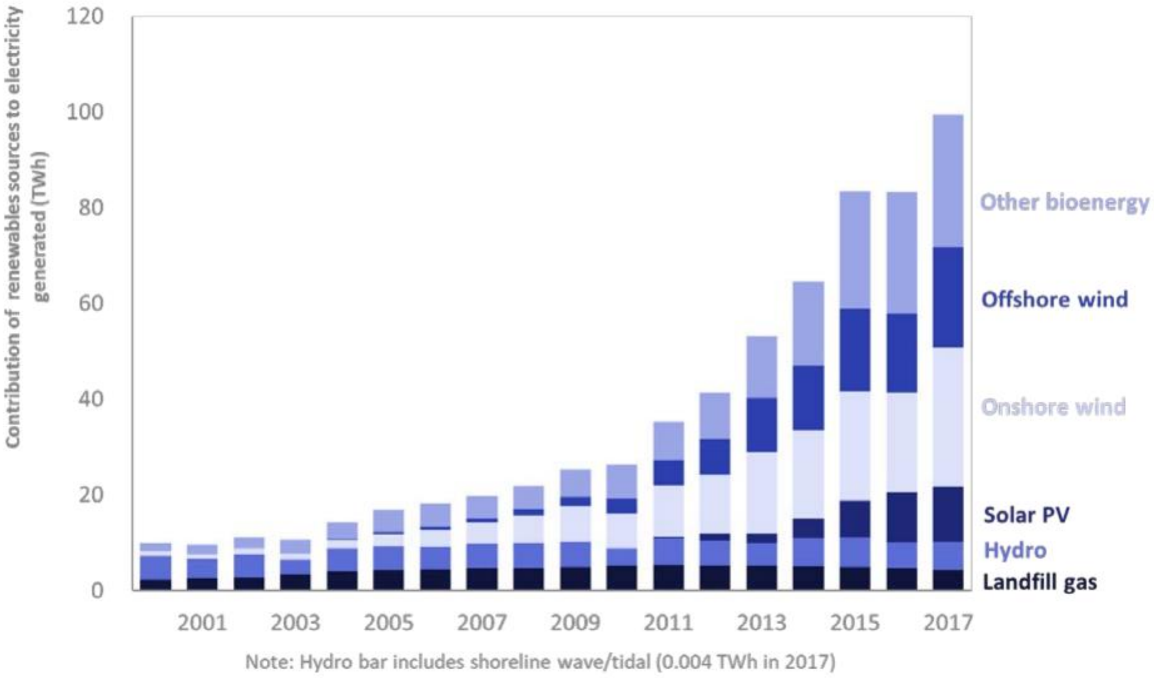

Figure 1.5 Electricity generation by main renewable sources in the UK [20].

1.3 Next Generation of Power Grid

The smart grid or known as the intelligent/micro grid is a promising trend of the future power grid. The smart grid combines a large amount of renewable energy resources that are distributed in the adjacent of customers. The smart grid in principle can run alone in islanded mode or have power exchange with the whole power grid depending on different scenarios. In comparison with the conventional power system, the main advantages of the smart grid include cleaner resources, higher power efficiency and reliability, faster response and can be thoroughly controlled [21-26]. However, in order to achieve that, sensors are required throughout the network and lacking large inertia could be a potential risk for the system's stability [27, 28]. More importantly, most of the renewable energy resources are inherently intermittent which could cause serious problems in extreme cases.

The smart grid system cannot be built in one day. There must be a gradual and sustained development for the electric power system to evolve to the next generation. To install increasing number of DG to the existing distribution networks is in the way of the system's evolution [29]. To address issues introduced by the integration of DGs will help us improve the network performance and have a better understanding of the future power system.

In this thesis, the issues introduced by increasing DGs are firstly analysed. Then, solutions by using power-electronic converters and associated control systems are proposed and studied.

1.4 Outline of the Thesis

In Chapter 1, the history of the electric power system is briefly introduced and a trend of increasing renewable DG in distribution networks in the UK is showed based on the historical statistics from government reports.

In Chapter 2, the issues in voltage regulation and fault level of distribution networks with high DG penetration level are investigated. Simulation results show that the voltage violation is likely to be the first constraint with the increase of DG. This demonstrates the motivation of this thesis which is to look for solutions for the voltage violation in distribution networks with high DG penetration level.

In Chapter 3, popular compensating technologies that normally used in transmission system are reviewed to seek solutions to the problem raised in Chapter 2.

In Chapter 4, the idea of a soft-open point (SOP) is introduced: using power-electronic based devices (reviewed in Chapter 3) to replace a normally-open point (refer to conventional circuit breaker) to gain advantages of meshed networks. Comparisons between the SSSC-based SOP as the most simple and economic option and the B2B-VSC-based SOP as the most versatile option are made by simulation. The B2B-VSC is preferred to be selected to be implemented to improve the network flexibility because of its capability of restricting fault current

In Chapter 5, the controller of a B2B-VSC based on proportional-integral (PI) theory is developed including detailed analyses on parameter design. The importance of resetting an integrator in the controller to achieve smooth transition from grid-connected mode to island mode is proposed. The controller is validated fully by simulation and partially by experiment.

In Chapter 6, a synchronverter-based controller for the B2B-VSC is developed which makes the converters behave like synchronous machines thus can automatically work in both grid-connected mode and island mode. It requires less detections and logic switches in controller compared to the controller built in Chapter 5, and offers better performance in islanding transition. The controller is validated fully by simulation and partially by experiment.

In Chapter 7, the use of an SOP in network dominated by dynamic load is investigated. The focus is on the influence of a fault and the loss of mains on a dynamic load, i.e. an induction motor. How the stability margin of an induction motor is affected by the filter impedance of a voltage source converter is analysed using the torque-speed characteristic. A controller reducing the VSC's output impedance is proposed and validated by simulation and experiment.

In Chapter 8, the conclusion is made, and further works are discussed.

2.Issues of Distribution Networks with High DG Penetration Level

2.1 DG Penetration Level

DG penetration level is the ratio of the total capacity of DG to the total capacity of load in a distribution network. Although DG has been widely researched and used in the world [30], the DG penetration level is still low because the integration of DG could pose problems regarding the voltage profile, the fault current and the operational stability [31-35]. Especially for DGs powered by wind and solar energies, the inherent intermittency and seasonal variations pose more challenges [36-38]. The power systems we have today are built on the basis that the power flow is unidirectional from the upstream (generating centres) to downstream (end users) via transmission and distribution networks. However, with the integration of DG the power flow in the grid will be affected and could be reversed to flow from downstream to upstream in some situations. The new pattern of power flow will pose great challenges to the existing power system. Furthermore, the inherent intermittency of the DG using wind and solar energies increases the difficulty to manage the system.

In electric power systems, losses of power and voltage are caused by the impedance of transmission lines and power lines/cables. Figure 2.1 shows a brief single-line diagram of a distribution network and its corresponding vector diagram of voltages and current. For a conventional distribution network, active and reactive power are transmitted from the substation in the upstream to load in the downstream via power lines/cables with electric impedance in all circumstances. As shown in Figure 2.1 (a), V_s and V_r are the phase voltages at sending and receiving ends, I is current flowing in the power line/cable, φ is the phase ang between I and V_r, R and X are the electric resistance and reactance of the power line/cable, P and Q are the active and, respectively, reactive power received at the load busbar. Then, the voltages can be described by the line impedance, active and reactive power which are usually specified in power systems.

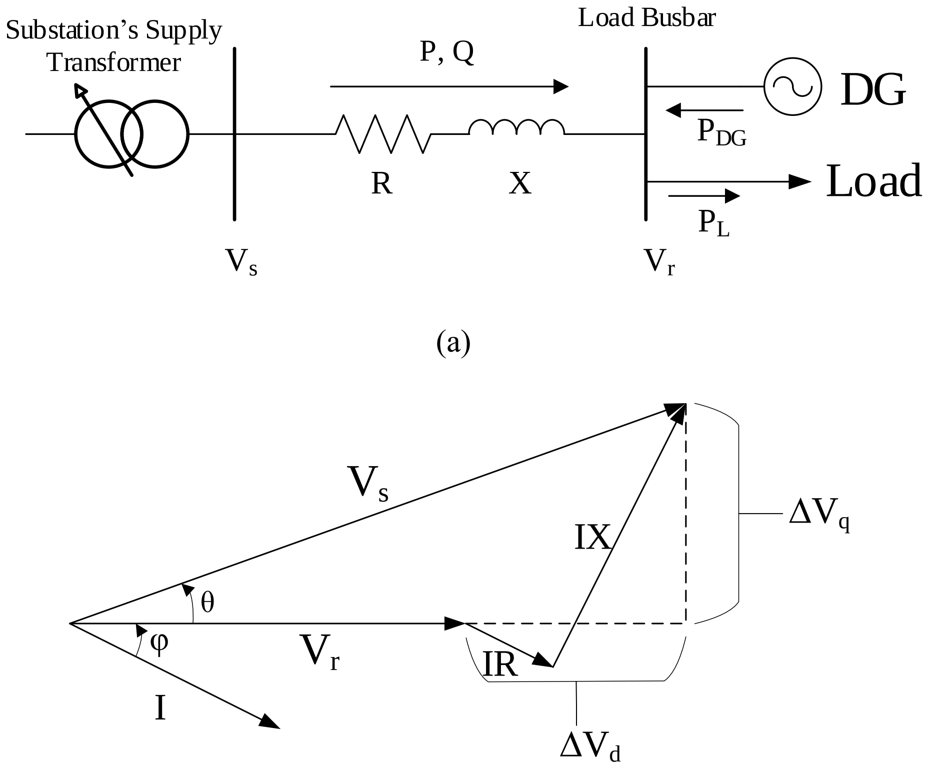

(a)

(b)

Figure 2.1 (a) Power flow in distribution network; (b) Corresponding phasor diagram.

The derivative is shown as

$$\begin{aligned} V_s^2 &= \left(V_r + \Delta V_d\right)^2 + \Delta V_q^2 \\ &= \left(V_r + RI\cos\varphi + XI\sin\varphi\right)^2 + \left(XI\cos\varphi - RI\sin\varphi\right)^2 \\ &= \left(V_r + \frac{PR}{V_r} + \frac{QX}{V_r}\right)^2 + \left(\frac{PX}{V_r} - \frac{QR}{V_r}\right)^2 \end{aligned} \tag{2.1}$$

where

$$\Delta V_d = \frac{PR + QX}{V_r} \text{ and } \Delta V_q = \frac{PX - QR}{V_r}. \tag{2.2}$$

If and normally,

$$V_r + \Delta V_d \gg \Delta V_q \tag{2.3}$$

then equation (2.1) can be rewritten as

$$V_s \doteq V_r + \frac{PR+QX}{V_r}. \tag{2.4}$$

Therefore, the arithmetic difference between the sending and receiving voltages, that is the voltage drop, can be approximately expressed as

$$\Delta V \doteq \frac{PR+QX}{V_r}. \tag{2.5}$$

Because of the low *X/R* ratio of cables and the generally high load power factor in distribution networks, it is reasonable to simplify equation (2.5) as

$$\Delta V \doteq \frac{PR}{V_r} \tag{2.6}$$

which indicates that the voltage drop is dominantly affected by the active power flow.

In a distribution network with DG, the active power passing the cable should be the active power consumed by the load minus the active power generated by DG which is represented by $P=P_L - P_{DG}$. This explains that the lower voltage drops and power loss on lines/cables can be achieved as DG shares the load demand. However, the power could flow reversely from downstream to upstream if the DG outputs excessive power to the load demand which could cause a voltage rise at load busbar.

It does not pose problems with low DG penetration level as the limited amount of reversed power flow can only result in slight voltage rise. But, with high DG penetration level, i.e. 100% penetration level - DG capacity equals load capacity, the voltage could rise beyond the permitted boundary which is called a voltage violation. Furthermore, high DG penetration level could also result in the fault current exceeding the making/breaking duties of circuit breakers as there are more sources contributing fault current. The following two sections investigate two major issues, fault level increase and voltage violation, in a distribution network with high DG penetration level by simulation using reasonable parameters.

2.2 Distribution Network Operating Regulations and Modelling

To investigate the influence of DG on the voltage profile and fault level in distribution networks, firstly a distribution network model needs to be built. In the UK, the supply transformers in substations step down the voltage from 132kV or 33kV to 11kV and feed the load demand which is typically about 10MVA ~ 20MVA (generally higher in urban area and lower in rural area) with an average power factor of about 0.97 in a radial distribution network. The loads are distributed along a feeder which has the length of about 5km ~ 10km (generally shorter in urban area and longer in rural area). The voltage must be within +6% ~ -6% of the nominal voltage which is set by DNOs in their operation [39]. The frequency must be within +1% ~ -1% of the nominal frequency which is 50Hz in the UK [40]. There are circuit breakers distributed in networks having the rating of typically 625MVA for make and 250MVA for break.

A distribution network is built based on the above information and is shown in Figure 2.2. At a 11kV distribution network, the loads are aggregated into 3 load groups each has the capacity of 5MVA with the power factor of 0.97 that evenly distributed at point a, b and c along the feeder of a total length of 9km. The cable's electric resistance and inductance per kilometre are 0.051Ω/km and 0.29mH/km, respectively.

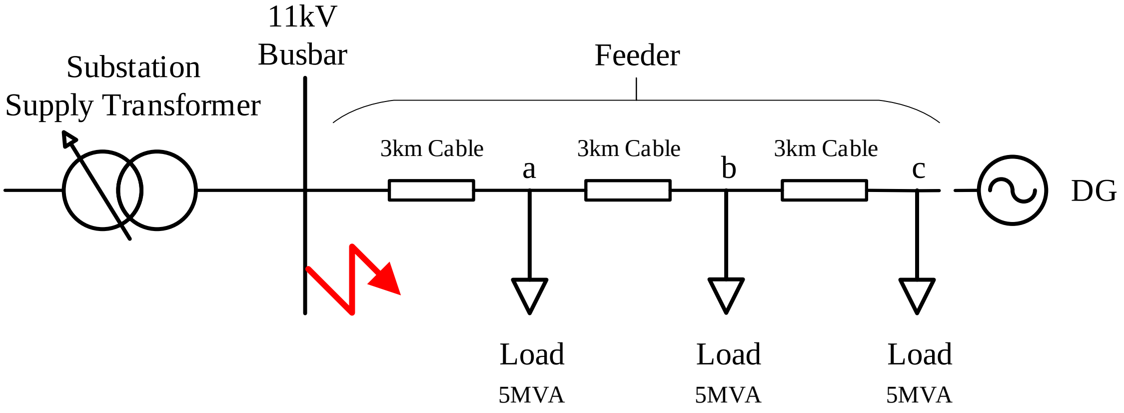

Figure 2.2 Studied 11kV distribution network

2.3 Fault Level Increase

The fault level is usually used, in the network design and operation, to represent the fault/short-circuit current in the unit of MVA. The three-phase fault level is defined as:

$$FL = \sqrt{3} \cdot V_{Lnom} \cdot I_f \tag{2.7}$$

where V_{Lnom} is the nominal line voltage and I_f is the fault current. A typical fault current in the AC electric system consists of an AC component and a decaying DC component due to the inductive part of the system. Two terms, 'make' and 'break', are used to express the first peak value, and respectively, the root-mean-square (rms) value of the AC component of the fault current. The making and breaking capacities of the circuit breaker in 11kV distribution networks in the UK are typically 625MVA and 250MVA. Currently in the UK the average fault level of a 11kV distribution network is at about 70% of the capacity of the circuit breaker.

Besides the substation and dynamic loads, DG units also contribute the fault current when a short-circuit fault occurs. Among all the types of DG, the units using synchronous machine, which is dominantly in CHP, contribute the highest fault current. From the study in [41], per MVA DG of synchronous machine type can be taken to contribute 4.5MVA fault level on average.

In this study, the influence of DG on the fault level at the primary busbar as shown by the red zigzag arrow in Figure 2.2, which is the highest fault level point, is investigated. The DG is considered to be centrally located at position *a*, *b*, or *c* which is from close to far away from the substation to have a better understanding of how the location affects the fault level contribution. The type of all DG units is selected as synchronous machine for the worst case.

The simulation result by Matlab/Simulink is shown in Figure 2.3. The per unit of breaking fault level (base is 250MVA) is shown with different penetration levels and locations of DG. In general, the higher DG penetration level contributes larger fault current and closer location results in higher fault level due to lower cable impedance. The largest fault level increase is observed at location a with 100% DG penetration level which makes the fault level to be 92.5% of the capacity of the circuit breaker. Considering the preservation of 5% safety margin in operation, it is very close to the upper limit which is 95%.

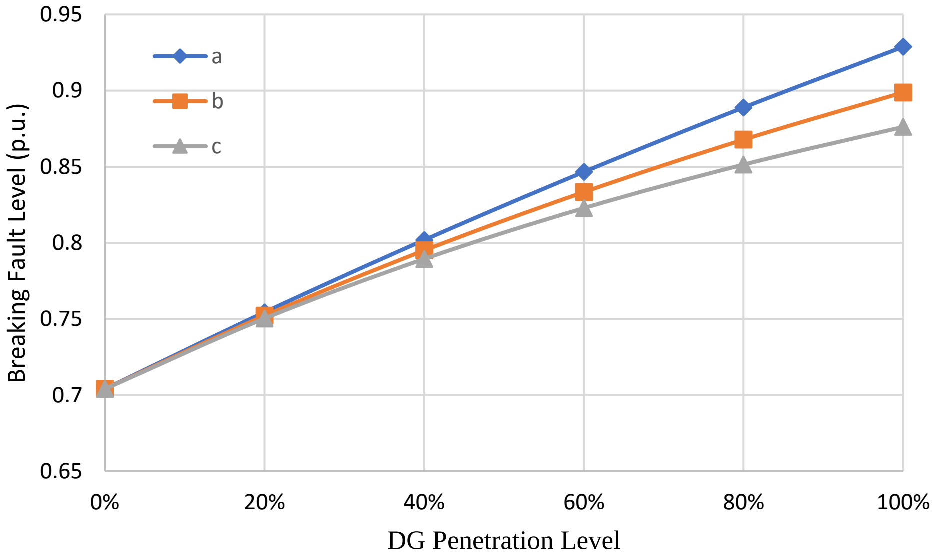

Figure 2.3 Breaking fault level increase with increasing DG Penetration level

2.4 Voltage Violation

The voltage violation means the voltage rises or drops outside the permitted range which is 0.94~1.06p.u. that adopted by UK DNOs in their operation. The majority of UK's distribution networks are built in meshed but operated in radial topology where a network is only supplied by one source from the distribution substation. The voltage at the end load busbar, location c in Figure 2.2, could drop considerably when the load demand is high as expressed by equation (2.6). Therefore, usually the output voltage at the substation is set higher than 1p.u. by positioning the on-load tap changer (OLTC) in the supply transformer to ensure the voltage at the end load busbar stays within the permitted range. A tap changer can have 16 taps for ±10% variation (each step providing 1.25% variation) from the nominal value. Tap changers are not operated dynamically because rapid changes can significantly reduce the lifetime. In this study, the voltage at the primary side is assumed at 0.9625p.u. (about 1.04p.u. at the secondary side) and the tap changer is remained at this position in all scenarios.

By integrating DG into the network, the voltage is expected to be increased because that less power from the substation experienced by the cable impedance. However, the voltage could rise beyond the upper limit when the network is lightly loaded. In an extreme case that the output of DG is at the maximum while the load demand is zero, voltage violation could occur. Figure 2.4 shows the simulation results of voltage rise in this extreme case with increasing DG penetration level at different locations. In general, higher DG penetration levels and farther locations result in higher voltage rises. The slowest voltage violation could happen when the DG penetration level increases to approximately 80% and the DG units are concentratedly placed at location *a*.

This is compliant with equation (2.6). In the extreme case, the load power P_L is zero. Thus, the power flowing through the feeder will be

$$P = P_L - P_{DG} = -P_{DG}\,. \tag{2.8}$$

Then, by neglecting the QX, equation (2.4) can be rewritten as

$$V_r \doteq V_s + \frac{P_{DG}R}{V_r}\,. \tag{2.9}$$

Therefore, for a certain DG penetration level - fixed P_{DG}, the farther location - larger R results in higher voltage rise; similarly, for a certain location - fixed R, the higher DG penetration level - larger P_{DG} results in higher voltage rise.

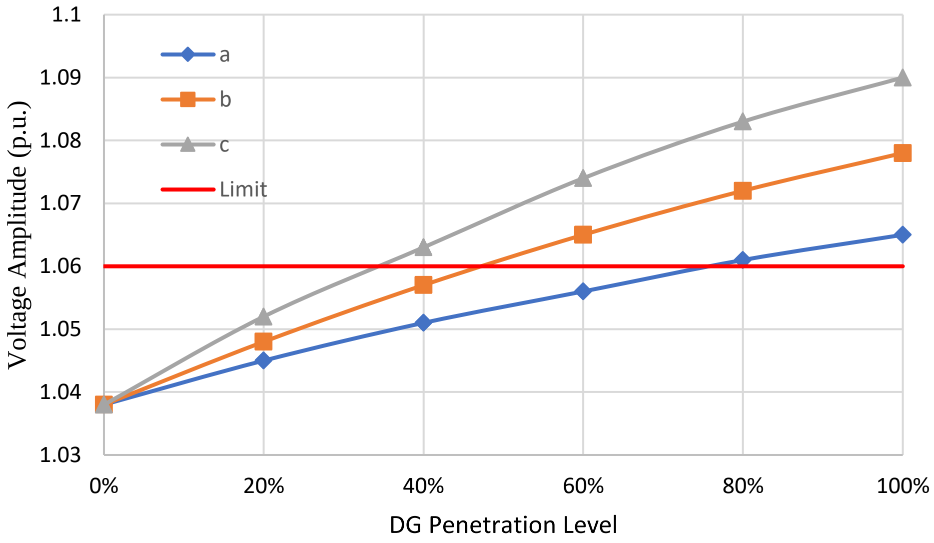

Figure 2.4 Voltage increase with increasing DG penetration level

2.5 Summary

In a distribution network, the voltage violation issue is likely to be met first when the DG penetration level increases. And UK DNOs in practice are inclined to allow very limited DG to be installed close to the primary busbar from the safety point of view. Therefore, the voltage violation would be a more common issue for building distribution networks with high DG penetration level. However, for networks already having high fault levels, the increase on the fault level should be treated prudently.

3.Review of Compensating Devices

3.1 Active and Reactive Power

Before discussing the compensating devices, it is important to introduce the concept of active and reactive power first. In electric system, active power is easy to understand as it is the power that does the real work. It is determined by the voltage amplitude, current amplitude and the angle between them. For defined voltage and current, the smaller angle corresponds to higher power factor which results in higher active power and relatively lower reactive power, and vice versa. Reactive power is also an essential part of the electric system and is generated when the current is not in phase with the voltage due to inductive or capacitive components. It produces alternating magnetic fields in asynchronous motors and electrical transformers. Around 65% and 25% of the reactive power is used to produce alternating magnetic fields in asynchronous motors and electrical transformers. For industrial case, the weight is around 70% and 20% [42].

For a long radial overhead line in a transmission system, the voltage drop is mainly affected by the reactive power experienced by the transmission lines because of the high *X/R* impedance ratio of the line. In fact, the resistance of transmission lines is usually negligible compared to the reactance [43]. Therefore, equation (2.5) can be written as

$$\Delta V \doteq \frac{QX}{V_r} \tag{3.1}$$

which indicates that the reactive power is the main factor of the voltage drop for a long radial overhead line in transmission systems.

The situation is slightly different for the power transmission between two sources. A typical two-machine power system is shown in Figure 3.1.

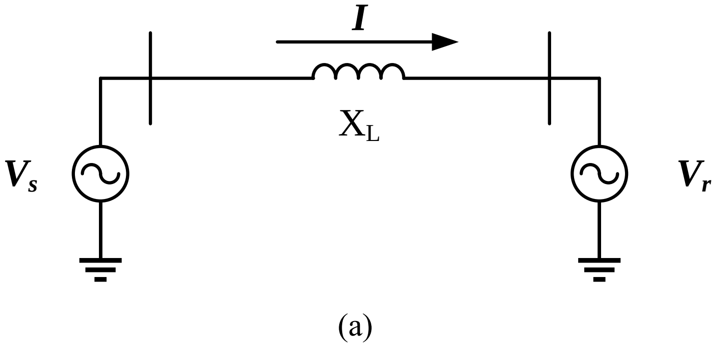

(a)

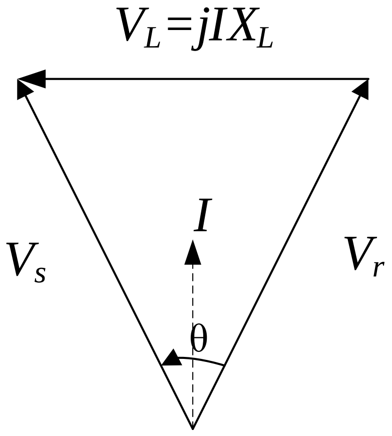

(b)

Figure 3.1 (a) Single-line diagram of two-machine power system; (b) Corresponding phasor diagram.

The reactance of the transmission line is X_L and the resistance is neglected. The sending voltage V_s is leading the receiving voltage V_r by the angle θ. Assuming that $V_s=V_r=V$, the angles between the current and the voltages V_s and V_r are $-\theta/2$ and $+\theta/2$, respectively. The current can be calculated by:

$$I = \frac{V_L}{X_L} = \frac{2V}{X_L}\sin\frac{\theta}{2}. \tag{3.2}$$

Then, the active power and reactive power at the receiving end can be given as:

$$P_r = \frac{V^2}{X_L}\sin\theta \tag{3.3}$$

and

$$Q_r = \frac{V^2}{X_L}\left(1-\cos\theta\right). \tag{3.4}$$

In the following sections of this chapter, technologies that have been developed to compensate the reactive power in transmission systems to achieve higher active power transmitted and better voltage profile will be introduced.

3.2 Conventional Compensators

In early years, reactive power compensation is carried out by large equipment such as capacitor banks, reactors or synchronous condensers.

3.2.1 Shunt and Series Capacitor

As the names imply, shunt and series capacitors are the capacitors connected in shunt and series with power lines, respectively. Parallel capacitors generate reactive power to increase the power factor thus increasing the active power capacity in transmission. Series capacitors create a negative reactance in power lines to reduce the active and reactive power consumption.

3.2.2 Reactor

Reactors in electric power system are usually used to consume excessive reactive power which functions as opposite to shunt capacitors. They are usually placed at the end of transmission lines or in substations to avoid overvoltage.

3.2.3 Synchronous Condenser

A synchronous condenser is a DC-excited synchronous motor which operates at no load condition. By controlling its excitation current, it can generate or absorb reactive power as required to improve the voltage profile and power factor. In under-excited condition, the synchronous condenser absorbs both active and reactive power from the network. And in over-excited condition, it draws active power but outputs reactive power to the network.

Compared to capacitor banks, synchronous condensers can be dynamically and continuously adjusted without steps and do not have switching transients. Besides, synchronous condensers are not affected by system harmonics or susceptible to resonances. However, the disadvantage of synchronous condensers is the relatively high power loss.

3.3 Basic Principles of Reactive Power Compensation

The reactive power compensation can be divided into shunt and series compensations from the aspect of connection type. There are also two types of system commonly used for analyses of compensation: the two-machine system and radial system. In two-machine systems, both the sending and receiving voltages are considered to be fixed which is usually used for transmission networks. In radial systems, only either the sending or receiving end voltage is considered to be fixed which is usually used for distribution networks or downstream sections of transmission networks. In this section, basic principles of shunt and series compensations are introduced including both capacitive and inductive types with the help of phasor diagrams.

3.3.1 Shunt Compensation

3.3.1.1 Shunt Compensation in Radial System

Figure 3.2 (a) shows a loss-less transmission line with the reactance X_L connecting the sending and receiving busbars. The receiving voltage V_r with zero phase angle is defined. The load current I is lagging V_r by the angle φ and the sending voltage V_s is leading V_r by the angle θ. Without compensation, the sending and receiving voltages along with the current are shown by the solid lines V_s, V_r and I, respectively in Figure 3.2 (b).

For shunt compensation, a capacitor with the reactance X_C is placed at the receiving busbar in shunt. The capacitor draws the current I_c which is leading V_r by 90 degree as shown in Figure 3.2 (b). As a result, the line current is reduced as shown by dotted arrow I_L which leads to lower power loss in the power line. The required sending voltage in order to maintain a certain receiving voltage is also reduced as shown by dotted arrow V_s'. Moreover, the phase angle between the sending voltage and current is also reduced. It explains that less reactive power is required from the sending end because of the reactive power compensation by the shunt capacitor. In summary, the shunt capacitor compensates required reactive power which results in lower power loss and smaller voltage drop on the power line.

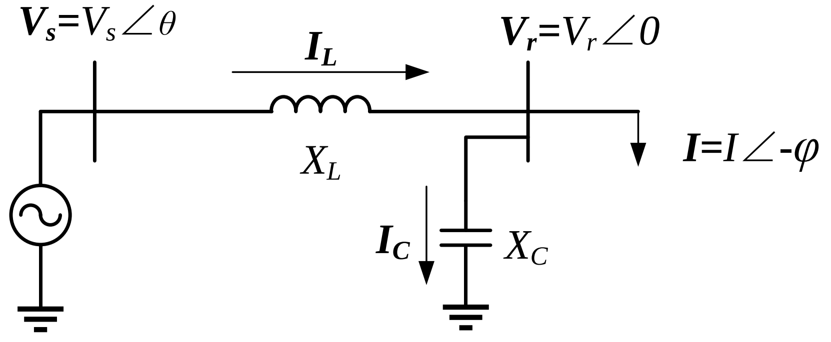

(a)

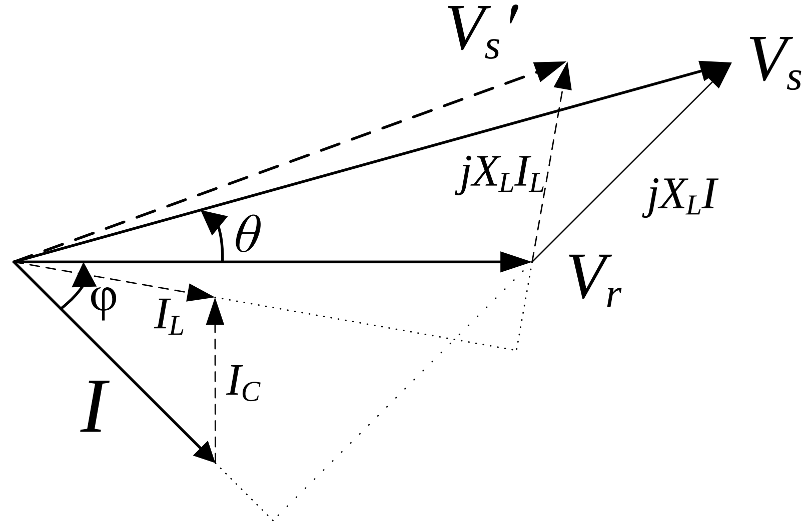

(b)

Figure 3.2 (a) Single-line diagram of shunt capacitor compensation for radial system; (b) corresponding phasor diagram.

When excessive reactive power appears in the network, i.e. due to highly capacitive load, shunt reactors can be implemented to absorb reactive power. Figure 3.3 (a) shows a network similar to Figure 3.2 (a) but with the current leading the voltage. For a defined receiving voltage V_r with zero phase angle, the current I is leading V_r by the phase angle φ and the sending voltage V_s is leading V_r by the phase angle θ. Without compensation, a significant increase on the receiving voltage V_r compared to the sending voltage V_s can be observed.

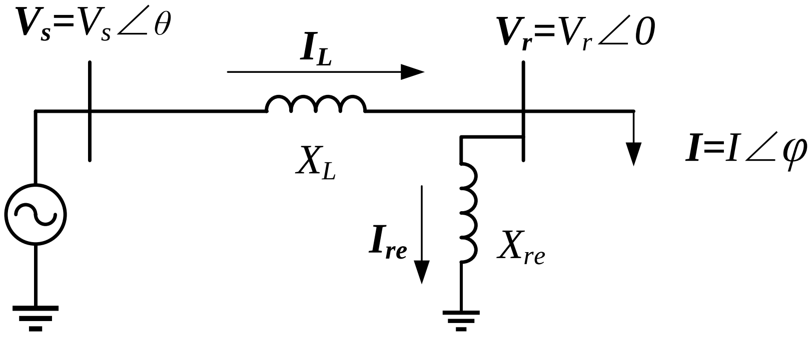

(a)

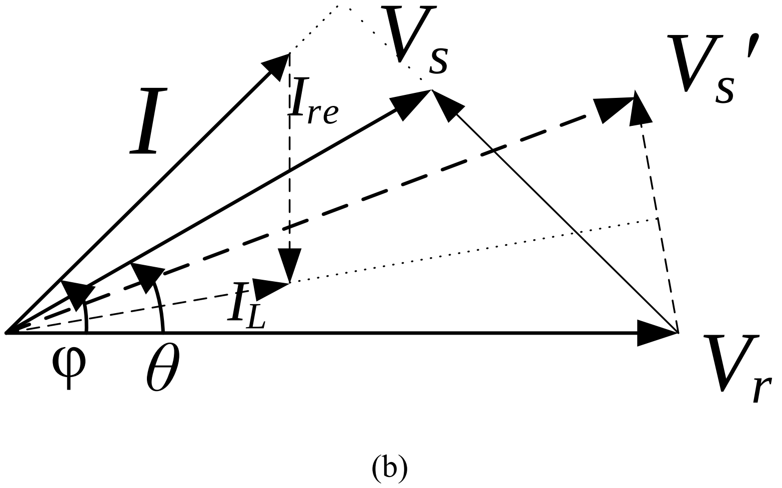

(b)

Figure 3.3 (a) Single-line diagram of shunt reactor compensation for radial system; (b) corresponding phasor diagram.

To avoid the voltage violation of upper limit, a reactor with the reactance X_{re} is placed at the receiving busbar in shunt to consume reactive power. The current passing the reactor I_{re}

is lagging the receiving voltage V_r by 90 degree as shown in Figure 3.3 (b). As a result, a smaller line current I_L which results in lower power loss in the power line is achieved. The sending voltage becomes V_s' which is now with a close amplitude to the receiving voltage V_r. And the line current I_L is now lagging the sending voltage V_s' which represents reactive power is drawn from the source. In summary, the shunt reactor consumes excessive reactive power to achieve lower power loss on the line and diminish voltage increase at the receiving end.

3.3.1.2 Shunt Compensation in Two-machine System

In terms of the power transmission between two busbars both having voltage sources, Figure 3.4 (a) shows an example of an ideal compensation by shunt capacitor banks to achieve higher transmittable active power. The capacitor bank is located right in the mid-point to divide the transmission line into two equal segments. From Figure 3.4 (b), assuming $V_s=V_r=V$, it is readily to obtain the real power transmitted becomes

$$P = 2\frac{V^2}{X_L}\sin\frac{\theta}{2} \tag{3.5}$$

which is doubled of the original active power in equation (3.3). Similarly, the reactive power generated by the compensator is now given as

$$Q_C = 4\frac{V^2}{X_L}\left(1-\cos\frac{\theta}{2}\right) \tag{3.6}$$

which shows a maximum reactive power required by the compensator is 4 times of original reactive power by equation (3.4). Briefly, a significant increase of transmittable active power can be achieved by shunt compensation at the expense of a large reactive power demand on the compensator.

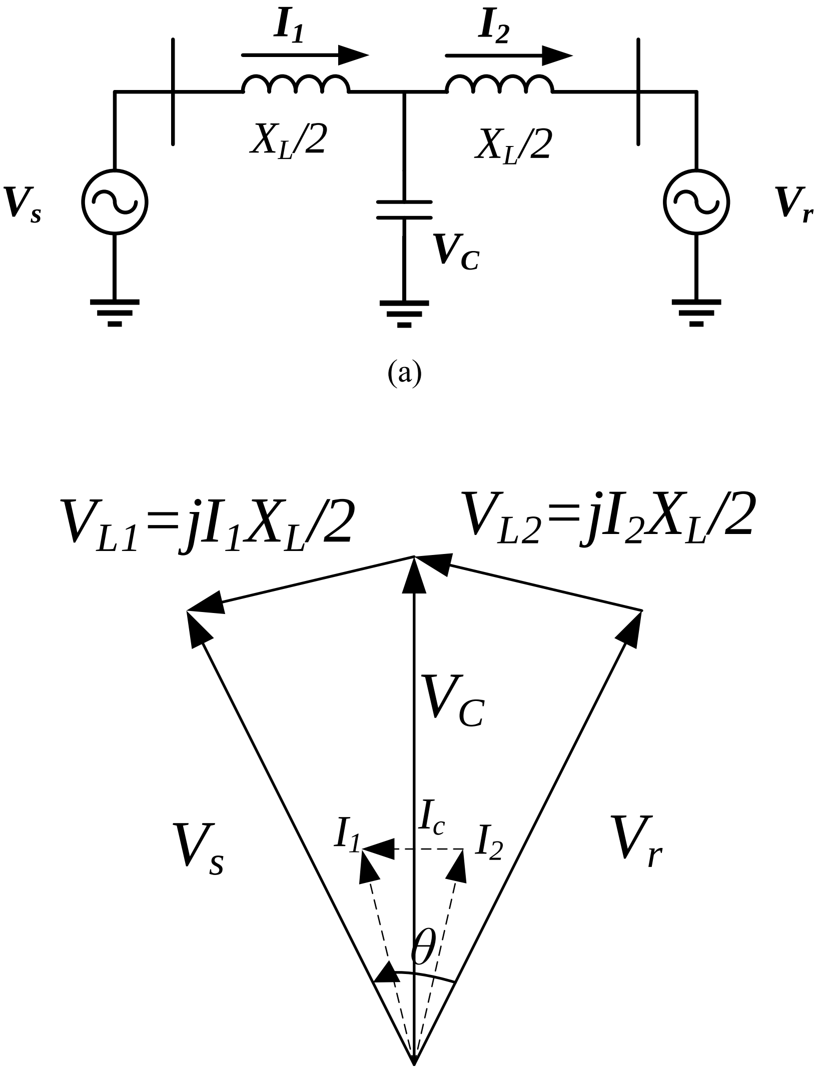

(a)

(b)

Figure 3.4 (a) Single-line diagram of ideal mid-point shunt compensation for two-machine system; (b) Corresponding phasor diagram.

3.3.2 Series Compensation

3.3.2.1 Series Compensation in Radial System

The same network setup is applied again, the receiving voltage V_r with zero phase angle is defined in a loss-less radial transmission line. The load current I is lagging V_r by angle φ

and the sending voltage V_s is leading V_r by the angle θ.

For series compensation, a capacitor is connected in series with the transmission line as shown in Figure 3.5 (a). The reactance of the capacitor neutralizes part of the inductive reactance of the power line. As a result, the total line reactance becomes X_L-X_C which leads to a reduced voltage across the line as $j(X_L\text{-}X_C)I$ as shown by the phasor diagram in Figure 3.5 (b). The sending voltage after compensation becomes V_s' which has a closer amplitude to the receiving voltage V_r than before. In summary, series capacitor neutralizes the inductive reactance to achieve lower voltage drop on the line.

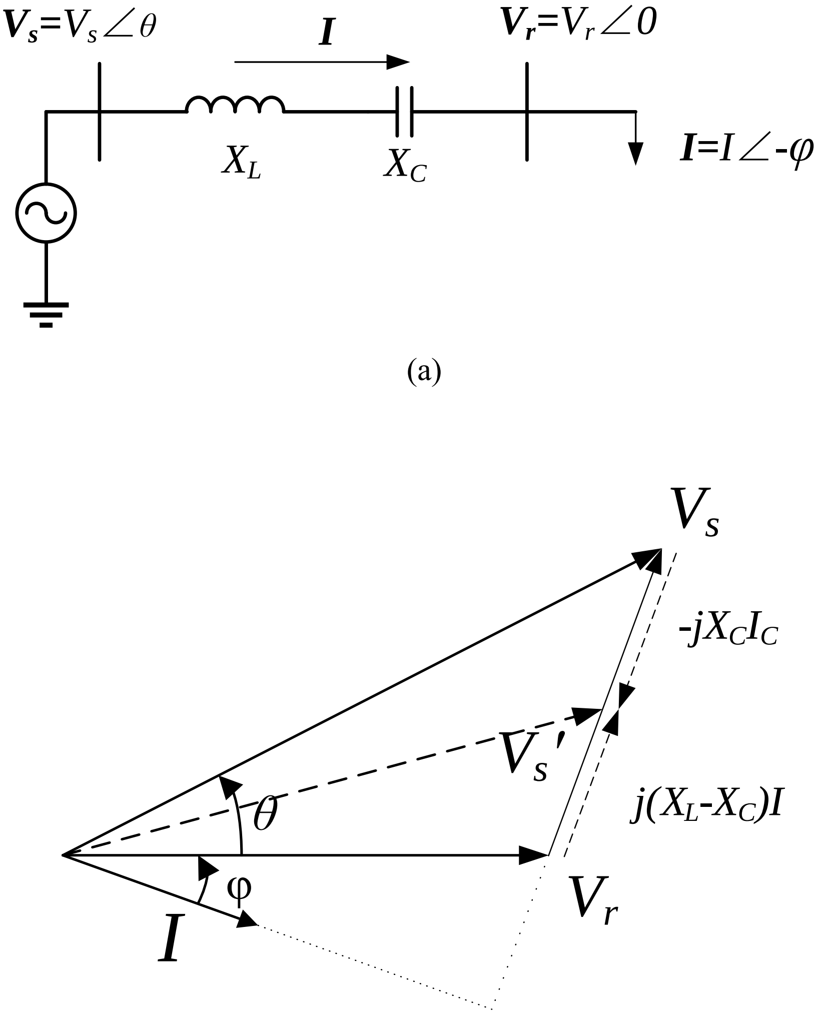

Figure 3.5 (a) Single-line diagram of series capacitor compensation for radial system; (b) corresponding phasor diagram.

In terms of there is excessive reactive power in the network, series reactors can be implemented. Figure 3.6 (a) shows a series reactor compensation in a radial network with leading current. For a defined receiving voltage V_r with zero phase angle, the current I is leading V_r by the phase angle φ and the sending voltage V_s is leading V_r by the phase angle θ.

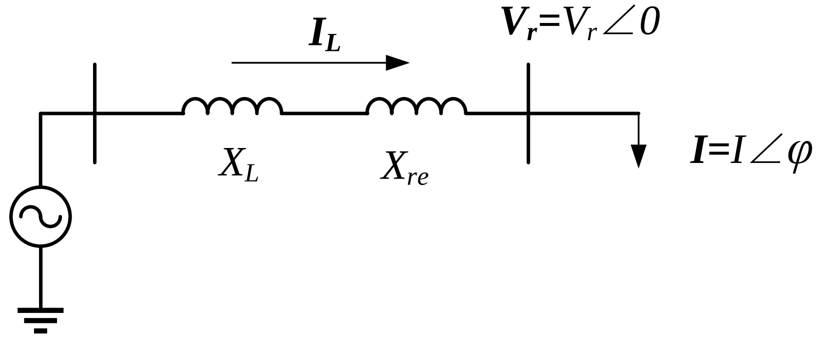

(a)

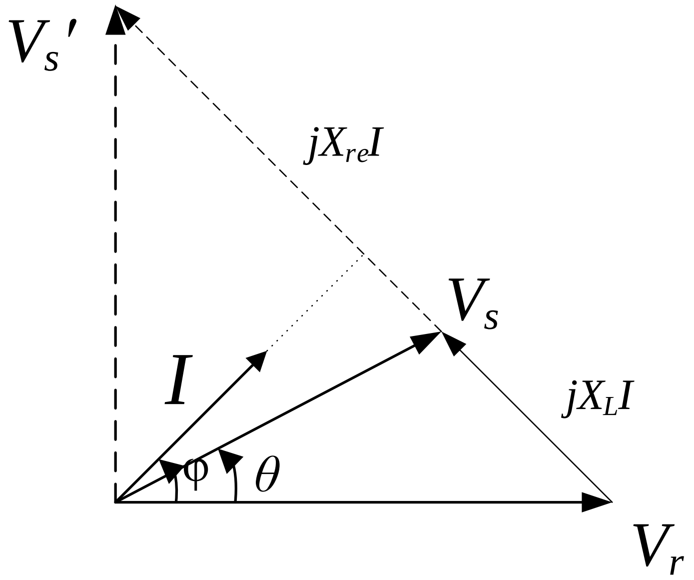

(b)

Figure 3.6 (a) Single-line diagram of series reactor compensation for radial system; (b) corresponding phasor diagram.

The series reactor insets an inductive reactance in series with the line. Hence, the voltage across the line becomes $j(X_L+X_{re})I$ as shown in Figure 3.6 (b). And the sending voltage becomes V_s' which is leading the current now. By this compensation, the amplitude difference between the sending and receiving voltages is reduced. Briefly, series reactor compensation reduces the voltage increase at the receiving end by increasing the line inductance.

3.3.2.2 Series Compensation in Two-machine System

In terms of series compensation in systems with two sources, Figure 3.7 (a) shows a basic idea of the series compensation using a capacitor. The capacitor with the reactance of X_C is connected in series with the transmission line. Assuming $V_s=V_r=V$, from Fig. 3.7 (b), the current can be calculated as

$$I=\frac{2V}{X_L-X_C}\sin\frac{\theta}{2} \tag{3.7}$$

which is clearly larger than the original current shown by equation (3.2). Then, accordingly the transmittable active power is given as

$$P=\frac{V^2}{X_L-X_C}\sin\theta \tag{3.8}$$

where the transmittable power P increases rapidly when the compensating capacity X_C increases. The required reactive power compensation is given as

$$Q_C=I^2X_C=2V^2\frac{X_C}{X_L-X_C}\left(1-\cos\theta\right) \tag{3.9}$$

which shows the reactive power demand on the compensator increases more sharply than P with the increase of X_C. In summary, the transmittable active power can be significantly increased by series capacitive compensation at the expense of rapidly increased reactive power demand.

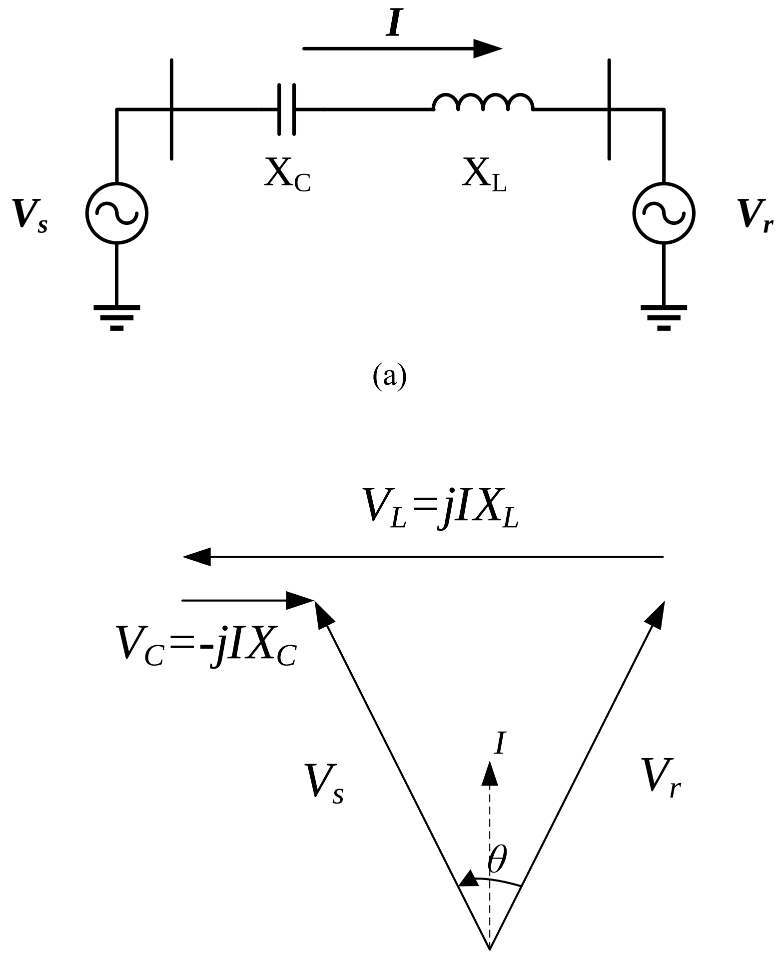

(a)

(b)

Figure 3.7 (a) Single-line diagram of series capacitive compensation; (b) corresponding phasor diagram.

3.4 FACTS Compensators

In 1988, the concept of Flexible AC Transmission System - FACTS was first proposed by Narain G. Hingorani for optimizing the power transmission system [44-46] . By IEEE, FACTS is defined as: Alternating current transmission systems incorporating power-electronic-based and other static controllers to enhance controllability and increase power transfer capability [47].

In the earliest stage, FACTS members were only the thyristor-controlled devices which usually a combination of inductive or capacitive components and thyristor-based switches. Different from conventional compensators such as reactors and synchronous condensers, these FACTS members are more ‘static’ as they do not include a rotating part. More recently, thanks to the development of self-commutated devices, compensators based on the voltage source converter (VSC) become available to compensate the network by injecting a controlled voltage. Compared to thyristor-based FACTS compensators, VSC-based ones generally possess superior performance characteristics [48].

3.4.1 Thyristor-based Compensator

Thyristor-based compensators are the first members of the FACTS. A thyristor-based compensator consists of thyristor-based switches along with inductive and capacitive components to provide variable compensations to the network. The fundamental mechanisms are as the same as the conventional compensators, but the values are adjustable.

3.4.1.1 Shunt-connected Type

Shunt-connected thyristor-based compensators, also known as static VAR compensators (SVC), are connected in parallel to the network. The purpose of these devices is to adjust capacitive or inductive current to control specific parameters of the network. The main types of SVC are shown in Figure 3.8 as

- Thyristor-Controlled Reactor (TCR): consisting of a reactor and a thyristor-based switch which allows the effective reactance to be changed continuously by firing angle control of the thyristors;
- Thyristor-Switched Capacitor (TSC): consisting of several parallel capacitor banks and thyristor-based switches which provides required reactive power by switching on required number of units; but no firing angle control means no continuous reactive power adjustment;
- Fixed Capacitor Thyristor-Controlled Reactor (FC-TCR): a common application which combines a fixed capacitor bank and a TCR that can be continuously controlled to generate or absorb reactive power;

- Thyristor-Switched Capacitor-Thyristor-Controlled Reactor (TSC-TCR): consisting of one TCR and several TSC branches which allows accurate control of reactive power compensation by using TCR to cancel the excessive reactive power from TSC.

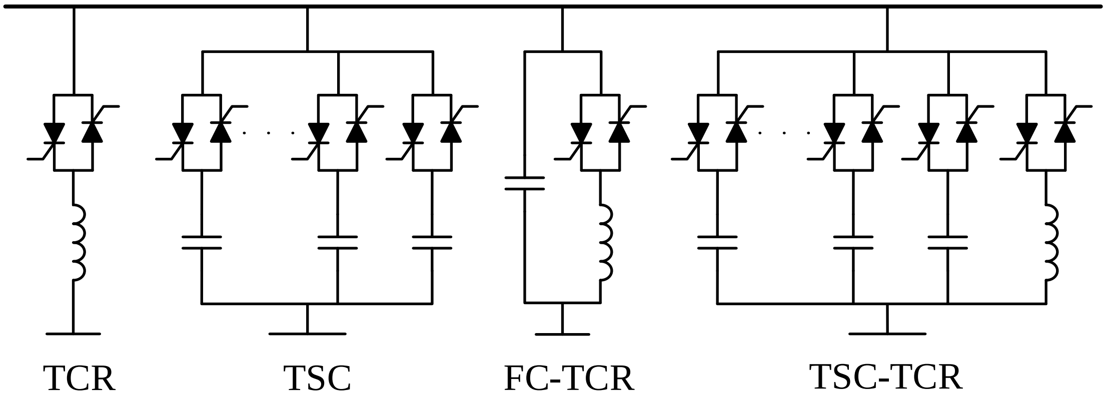

Figure 3.8 Single-line diagram of shunt compensators: TCR, TSC, FC-TCR and TSC-TCR.

3.4.1.2 Series-connected Type

Figure 3.9 shows three main types of series-connected thyristor-based compensators as

- Thyristor-Switched Series Capacitor (TSSC): consisting of a capacitor and thyristor-based switch in parallel which can only provide a discrete reactance;
- Thyristor-Controlled Series Capacitor (TCSC): consisting of a capacitor and a TCR in parallel which injects a variable capacitive reactance into the transmission line;
- Thyristor-Controlled Series Reactor (TCSR): consisting of a reactor and a TCR in parallel which provides continuously adjustable inductive reactance.

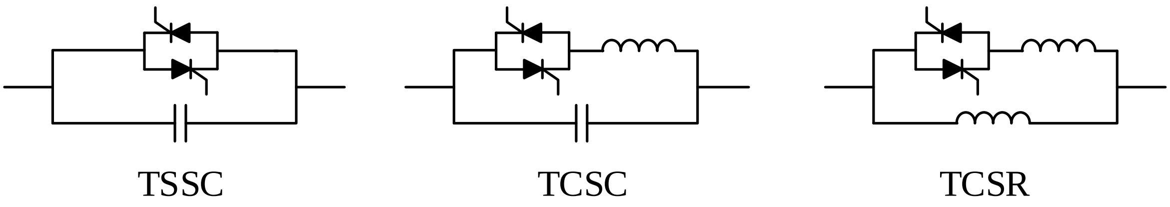

Figure 3.9 Single-line diagram of series compensators: TSSC, TCSC, TCSR

3.4.2 Static Synchronous Compensator

Thanks to the development of the self-commuted devices, new generation of FACTS with better performance characteristics becomes available. The static synchronous compensator (STATCOM) is the first compensator based on voltage source converter (VSC) in FACTS to be conceived. It is shunt-connected, usually with a transformer, to the network and dynamically controlled to output required inductive or capacitive current. The VSC is the fundament component of the STATCOM which is able to convert DC energy to AC and control the frequency, amplitude and phase. Different from thyristor devices which only has turn-on control (turn-off depends on current coming to zero), a VSC consists of devices that possess turn-on and turn-off capability such as Gate Turn-Off Thyristor (GTO), Integrated Gate Bipolar Transistor (IGBT), MOS Turn-off Thyristor (MTO), and Integrated Gate-commutated Thyristor (IGCT) and so forth. These devices have higher power losses but advantages on overall system cost and performance. A VSC is the self-commutating converter in which the DC voltage always has one polarity, and the reversal of power is by reversing the DC current polarity [49]. Among all kinds of topologies, the simplest three-phase VSC is a 6-arm, 2-level converter which is shown in Figure 3.10. It consists of 6 devices (IGBT/diode is taken as an example here) and is connected to a capacitive device at the DC terminal while to the AC terminal usually via a filter.

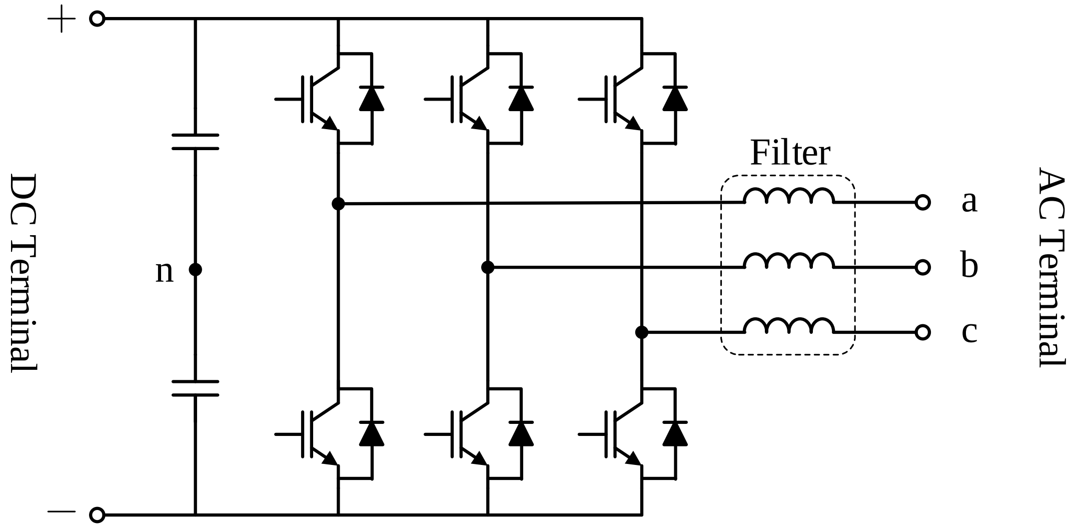

Figure 3.10 Three-phase 6-pulse, 2-level converter

The first STATCOM was commissioned at the Sullivan substation of the Tennessee Valley Authority in the United States in 1995 [48]. A single-line diagram for a STATCOM is shown in Figure 3.11 (a).

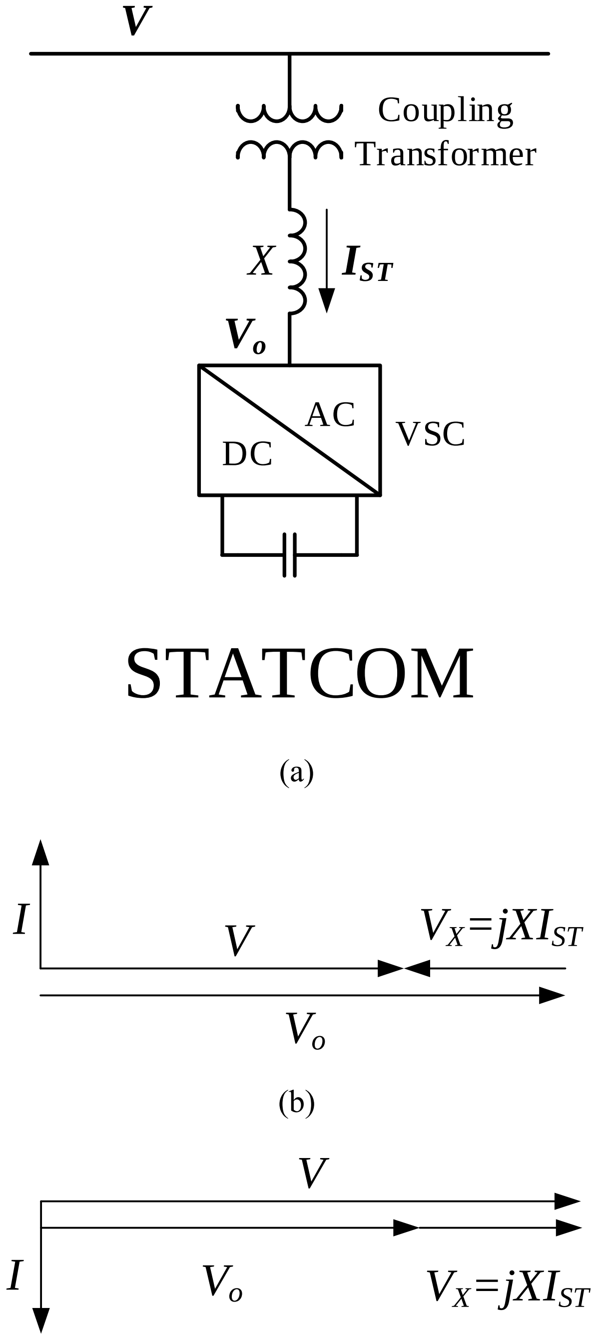

(a)

(b)

(c)

Figure 3.11 (a) Single-line diagram of a STATCOM; (b) corresponding phasor diagram in capacitive compensation mode; (c) corresponding phase diagram in inductive compensation mode.

The STATCOM is connected to the network in parallel via a coupling transformer at the AC terminal and connected to a capacitive DC device at the other terminal. In operation, a STATCOM generates a controlled voltage at the network frequency and in phase with the network voltage, that is synchronous with the network.

Assuming a loss-less coupling transformer with 1:1 turn ratio is used to connect the STATCOM to the power line in shunt. The total reactance of the transformer and filter is represented by X. When the STATCOM generates a voltage V_o in phase with the network voltage V, the phasor diagrams are shown in Figure 3.11 (b) and (c): if the amplitude of V_o is large than that of V, the STATCOM outputs current lagging by 90 degree, thus injecting reactive power to the network like a shunt capacitor; on the contrary, if the amplitude of V_o is less than that of V, the STATCOM outputs a current leading the voltage by 90 degree, thus drawing reactive power from the network like a shunt reactor. The basic principle of shunt compensation is previously introduced Section 3.3.1. In addition, the reactive power compensation by a STATCOM can be dynamically controlled by adjusting V_o.

STATCOM is highly effective on maintain the end voltage of a radial power line by manipulating the reactive power. It also has potential to have real power exchange with the network by installing DC storage devices at its DC terminal.

3.4.3 Static Synchronous Series Compensator

A static synchronous series compensator (SSSC) are VSC-based compensators that are connected in series with transmission line via a coupling transformer as shown in Figure 3.12 (a). The letter X denotes the total reactance of the coupling transformer and filter. Assuming the turn ratio of the coupling transformer is 1:1, the output current of the SSSC should be as the same as the current flowing on the line, that is $I_{SS}=I_L$. If the voltage across X is neglected, then the voltage injected into the line is the output voltage of the SSSC, that is $V_{inj}=V_o$. By controlling the output voltage V_o to be leading or lagging the current by 90 degree, the SSSC behaves like a series capacitor or reactor. The basic principle of series compensation is previously introduced in Section 3.3.2. In addition, the amplitude of the injected voltage V_{inj} can be continues changed by controlling the amplitude of V_o. The SSSC is effective to manipulate actual power transmitted at a given voltage where the shunt compensation is not effective.

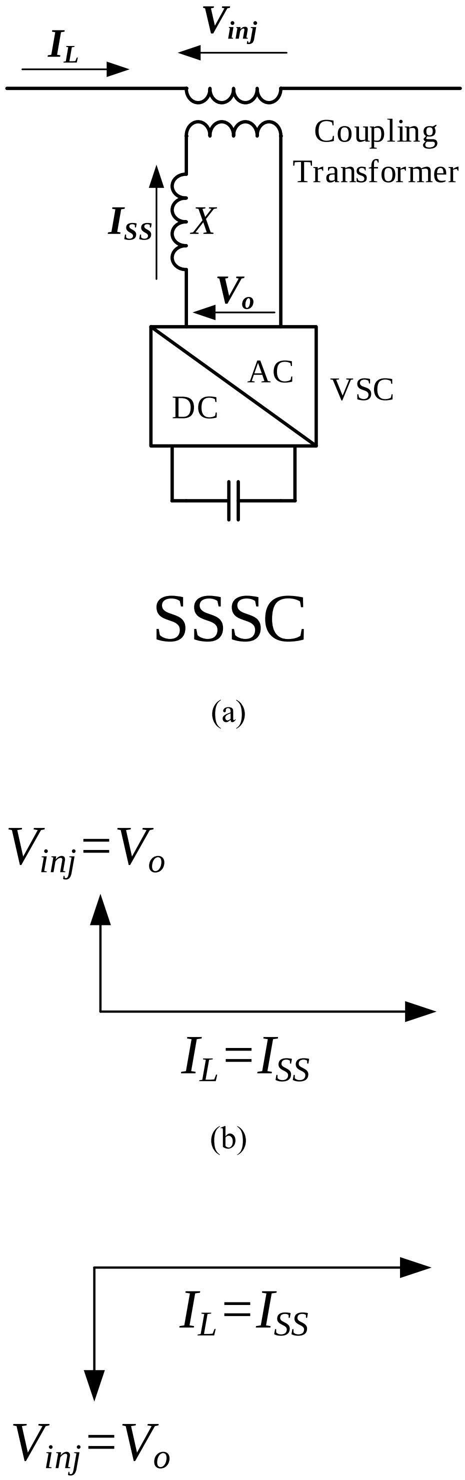

(a)

(b)

(c)

Figure 3.12 (a) Single-line diagram of a SSSC; (b) corresponding phasor diagram in capacitive compensation mode; (c) corresponding phasor diagram in inductive compensation mode.

3.4.4 Unified Power Flow Controller

A unified power flow controller (UPFC) is a combination of SSSC and STATCOM. As Figure 3.13 (a) shows, a UPFC consists of a STATOM and an SSSC connecting back-to-back by a DC link. The main function of UPFC is carried out by the SSSC part which can inject a series voltage into the network with totally controllable amplitude and phase angle. The STATCOM part of the UPFC is controlled to maintain the DC link voltage which means it can support active power required by the SSSC part. In addition, it can control the reactive power exchange with network independently of the active power required. Then, by the active power supported by the STATCOM part, the output voltage at the SSSC's terminal is no longer subjected to be in quadrature with the line current but can be any angle with the current. As shown in Figure 3.13 (b), for a defined V_2, V_1 can be manipulated by controlling the UPFC's injecting voltage V_{inj}. The end point of the compensating voltage V_{inj} can be at any point within the circle whose radius corresponds to the rating of the UPFC. The UPFC, as described by the adjective “unified” in its name, can accomplish a variety of functions that cover all the parameters affecting power flow in the transmission line.

From the above content it can be seen that the UPFC is the most versatile one among the members in FACTS. With the capability of active and reactive power control, it can accomplish various quests. Different allocations also determine the different salient points of the UPFC.

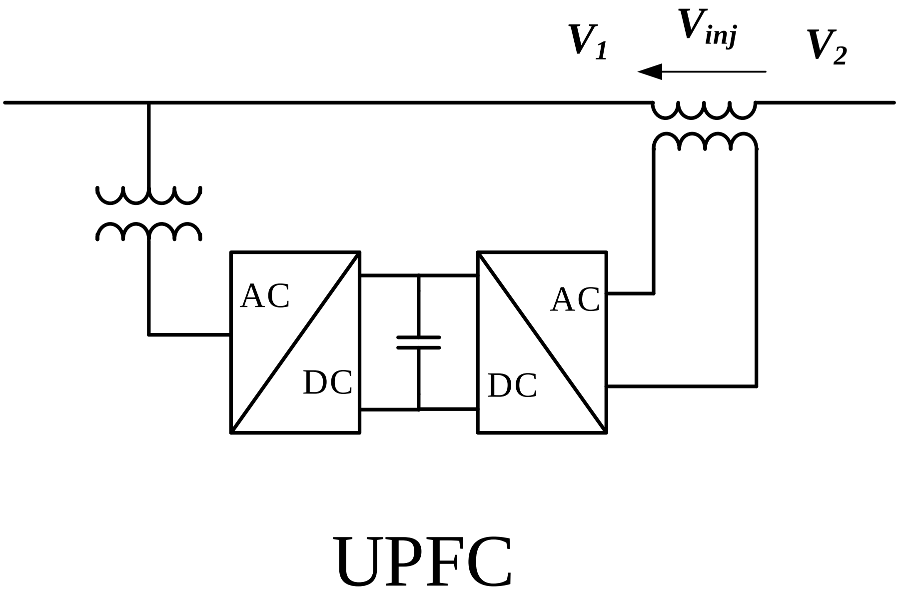

(a)

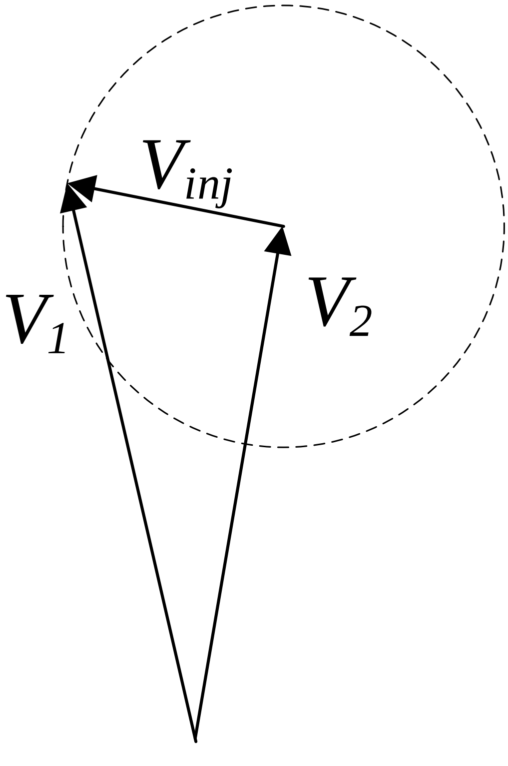

(b)

Figure 3.13 (a) Single-line diagram of a unified power flow controller; (b) phasor diagram of voltage compensation capability

3.5 Back-to-back Voltage Source Converter

A back-to-back voltage source converter (B2B-VSC) refers to an equipment that consists of two voltage source converters connecting back-to-back via a capacitive DC link and is connected in series with the network usually with isolation transformers as shown in Figure 3.14. This topology is very similar to the well-known VSC-HVDC system which is used for interconnect two AC networks that are separated by very long distances [48, 50]. The advantages of this topology include the independent active/reactive power control and the segmentation of network which means the connected two segments can be asynchronous even at different frequencies and fault can be isolated from one to the other.

The main difference between B2B-VSC and UPFC is that the B2B-VSC is connected in series with the power line and thus can restrict and even block the fault current. However, the power in the network must fully flow through the B2B-VSC which could cause higher power losses and bring higher risks in case of the device breaks down.

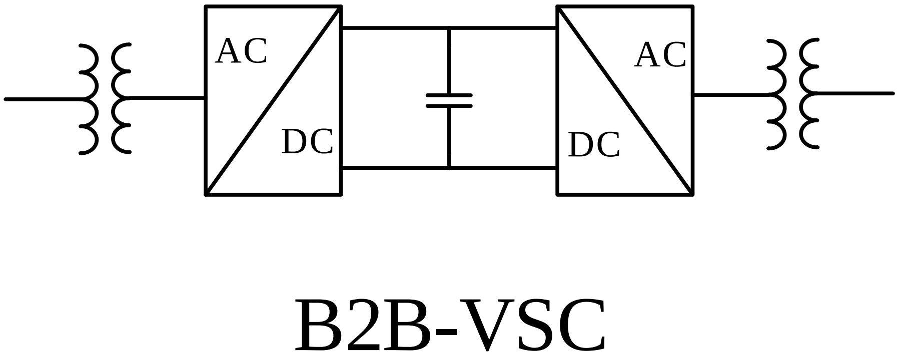

Figure 3.14 Back-to-back voltage source converter

3.6 Research on Using Power Electronics in Distribution Networks

Most of the distributed generation resources (DERs) cannot be connected to the power grid directly. Power-electronic converters are widely used as the interface for the access. Instead of reviewing the utilisation of power electronics in distribution networks for connecting DERs, which can be found in many papers [51-55], the utilisation of power electronics for improving distribution networks and addressing issues with DG will be reviewed.

In the Flexible Urban Networks – Low Voltage (FUN-LV) project led by UK Power Networks, field trials of three methods at 36 sites in LV distribution networks in London and Brighton in the UK have been carried out. The proposed three FUN-LV methods are all based on power electronics and they are the power-electronic-assisted circuit breakers and link box switches, the 2-port soft open points (SOPs) and the 3-port SOPs. These methods are used to reconfigure the network topology – change them from radial to meshed. The results have successfully demonstrated the benefits of the use of power electronics in distribution networks: mainly equalising the demand amongst the connected sites, making use of latent network capacity that can be provided for additional connections without increasing the transformer capacity; additionally improving the network voltage profile and reducing the voltage and current unbalance level. [56]

A Fully Flexible Power Transmission & Distribution System (FPTDS) for the next generation power grid has been proposed by researchers. Based on the Cyber Physical Systems (CPS), a Power-CPS interconnect reference model is developed, and the focus is on designing a fully flexible next generation equipment for Fully Flexible Power Distribution System (FPDS) including system structure, equipment architecture and core module. This paper provides a guide for building the next generation smart distribution grid. [57, 58]

A study has been carried out to investigate the voltage concern in relation to EV penetration in distribution networks. A solution by using STATCOM to compensate reactive power was proposed. Simulation results show that with 90% EV penetration, the voltage regulation of each phase in unbalance network is achievable. [59]

Greater Sudbury Hydro (GSH) has trialled a new power-electronic low voltage control device, the low voltage inline power regulator (LV-IPR) in distribution networks to tackle high voltage and other power quality problems introduced by DG. The proposed device is based on UPFC and controls voltage by injection series voltage to the line. It can also provide reactive and harmonic compensation. In the field trial, the device effectively regulates the voltage at sites and generally improve the power quality in the network.[60]

A flexible power distribution unit based on the power-electronic transformer (PET) has been proposed. It has not only the capability of transformation and isolation but also can control the power quality. The novel system design and control strategies were presented. A prototype has been developed and tested by experiment to prove the design is feasible. [61]

Another study has been carried out on multiport PETs. The increasing of the DG penetration level and energy storage systems provides not only the potential to form a micro grid but also possible alternative distribution manners such as DC distribution networks or AC/DC hybrid distribution networks. A flexible substation with high/low voltage AC and DC ports as an interface of AC/DC hybrid distribution network has been proposed. The structure, working principle and control strategy are designed and analysed. Besides the basic functionalities of a conventional transformer, the flexible substation can also control the power flow between the grid side and the load side. [62]

A comprehensive power flow control scheme has been designed based on a globalised multiport transmission model of the PET and droop control, which enables autonomous operation by coordinating power exchange among ports. A novel droop control method is presented to coordinate power flowing through each port. [63]

In conclusion, some research has been done on using PE compensators in the existing distribution networks to address voltage power quality issues from the increasing DG penetration level. A few field trials have been conducted to validate the methods. On the other hands, some research has been carried out focusing on the use of PET to improve the flexibility and performance of distribution networks. But there is no field trial has been conducted.

3.7 Summary

In this chapter, various compensators for electric power system have been reviewed. The conventional compensators are firstly introduced including their working principles with the help of phasor diagrams. Then, FACTS compensators with variable compensating values are introduced. The thyristor-based compensators as the early members of FACTS have the same working principles as conventional compensators, but the compensating value is variable. The compensators based on power-electronic converters are more recent members of FACTS. SSSCs and STATCOMs generate controlled voltage in quadrature with current to provide reactive power compensations. The compensating value is continuously adjustable and active power compensation can be implemented with energy storage units installed at the DC terminal. An UPFC is a versatile compensator which combines an SSSC and STATCOM that can manipulate all network parameters.

Unlike a thyristor-based compensator will require reverse bias or load current falling to zero to turn off, a power-electronic device can be switched off directly via the gate and thus providing higher flexibility and introducing much lower harmonics. Because of the stringent regulations on harmonics in the electric power grid and the requirement of flexibility for the next generation power grid, the power-electronic compensators tend to be greatly used in the future power networks. In terms of power conversion, thyristor-based devices such as line-commutated converters (LCCs) are used for point to point power transmission (HVDC) where high power rating is required. And power-electronic devices such as VSCs are widely used in applications such as photovoltaic panels and wind farms.

Some research and works that have already been done on the use of power electronics in distribution networks are reviewed in the last section. However, because FACTS devices are either connected in parallel or in series using a coupling transformers with the line, they lack the capability of restricting fault current on the line.. Therefore, a B2B-VSC was introduced at last which potentially can restrict fault current but has higher capital cost and power loss as a fully-rated compensator. In the next chapter, the utilisation of compensators in distribution networks will be discussed.

4.Compensating Distribution Networks by Meshing the Network

As previously discussed in Chapter 2, voltage violation could be the first constraint for increasing the DG penetration level of a distribution network. Besides, the inherent intermittency of wind and solar energy could increase the unpredictability of distribution networks thus affecting networks' stability. Furthermore, the integration of electric vehicle (EV) chargers in response to the accelerating development of EVs will certainly affect the peak demand for electricity in distribution networks [64]. Therefore, voltage and power management with fast response will be required to tackle the challenges.

Chapter 3 introduces well-known compensators for transmission networks along with their basic principles. In early days, plenty of articles and information on the utilisation of compensators for managing transmission networks' parameters were published [65-69]. Although the circumstances in distribution networks are different from that in transmission networks, the existing knowledges on the compensation technologies can be referred and used for the applications in distribution networks. Due to the unpredictability of a distribution network with high DG penetration level, power-electronic based compensators appear to be the better choices than conventional compensators because of their fast, continuous and independent active and/or reactive power control capabilities. A lot of researches have been done on using FACTS devices to improve distribution network parameters [70-76]. However, the limitation will be analysed in the following.

As introduced by equation (2.2) in Chapter 2, the voltage drop on the transmission line is given as

$$\Delta V \doteq \frac{PR+QX}{V_r} \ . \tag{4.1}$$

In transmission networks, it is reasonable to neglect *R* because of the high *X/R* ratio of the transmission overhead line. For an overhead line with an *X/R* ratio of ten, the error by neglecting *R* is 0.49%; and even for a low *X/R* ratio of 2.5, the error is 7.7% [43]. Therefore, equation (4.1) is usually simplified as

$$\Delta V \doteq \frac{QX}{V_r} \tag{4.2}$$

which indicates that reactive power dominantly affects the voltage drop. For this reason, reactive power compensation is important and effective in transmission networks. However, this practice does not apply in distribution networks.

In distribution networks, firstly the *X/R* ratio of the power lines/cables could be less than two and even close to one; secondly the load power factor is generally very high, i.e. about 0.97. These two factors result in that *PR* is usually larger than *QX*, and in some cases *QX* can be neglected. Therefore, for distribution networks, the equation (4.1) can usually be simplified as

$$\Delta V \doteq \frac{PR}{V_r} \ . \tag{4.3}$$

It means that sole reactive power compensation is less effective in distribution networks, and thus active power compensation is required. The most intuitive way is to use compensators with active power exchange capability such as STATCOMs and SSSCs having an energy storage device connected to their DC terminals. However, small-scale energy storages have a very low price-performance ratio.

4.1 Soft-open Points

It is well-known that meshed networks have better resilience to disturbances, and radial networks have much lower fault level and simpler protection scheme. In the UK, distribution networks are usually built as meshed but operated as radial due to the concern of system safety. That is to say there are power lines or cables connecting two adjacent distribution networks, but the circuit breakers are normally open. An example of this structure is shown in Figure 4.1. Two 132/11kV stepdown transformers at the same or different substations supply two adjacent distribution networks through the feeders. There are two power lines connecting the primary busbars and the endpoints of the feeders with the circuit breakers normally open. These normally-open circuit breakers are known as normally-open points (NOPs).

In recent years, the concept of soft-open points (SOPs) has been proposed which refers to a power-electronic based equipment, such as the SSSC, UPFC and B2B-VSC, that installed at a NOP [77]. The objective of SOPs is to increase the flexibility of distribution networks by looping or meshing distribution networks and controlling the active power flow. As previously analysed, the active power flow is the dominant coefficient of the voltage drop in distribution networks. Therefore, installing SOPs theoretically can be an effective method to regulate voltage profiles in distribution networks with high DG penetration level. A research to investigate the benefits and superiority of using SOPs to balance feeder load in medium voltage distribution networks has been carried out including a power injection model for steady state analysis [78]. An algorithm to appraise the increase of hosting capacity by looping two networks with a SOP via a stress majorization technique has been proposed [79]. Another algorithm for SOPs to solve thermal and voltage constraints in low voltage distribution networks has been proposed and validated by field trial results [80]. A coordinated voltage and VAR control method based on the SOP for active distribution networks has been presented to minimize the operation costs and improve the voltage profile [81]. A research has been done to investigate the effect of an SOP to the feeder automation, and simulation results has shown that the SOP can work properly without interrupting the existing feeder automation scheme [82]. A robust optimization model of SOPs for active distribution networks has been developed and solved to deal with the uncertainties of load and DGs [83]. A supply restoration model for distribution networks with SOPs has been built and solved by the primal-dual interior-point algorithm to find the optimal solution rapidly and accurately [84].

In regard to the place of installing an SOP, it is usually preferred to be at or close the endpoints of feeders rather than the primary busbars because the connection at the primary busbars is of little help to regulate voltage at feeder ends and creates the largest fault level increase. Using the network model shown in Figure 4.1 as the example to demonstrate how an SOP installed at the feeder endpoints could work: if *Feeder 1* is heavily loaded causing the voltage at the end of Feeder 1 drops below the lower limit, the SOP can be controlled to draw power from *Feeder 2* to feed *Feeder 1* thus mitigating the voltage drop on *Feeder 1*; on the other hand, if the DG output at *Feeder 1* is at the maximum while the load is at the minimum which results in a reverse power flow causing the voltage at the end of *Feeder 1* rises above the upper limit, the SOP can be controlled to extract the excessive power and transfer it to *Feeder 2* thus mitigating the voltage increase. Researches have been done to investigate how different types of compensation affect the achievable DG penetration level. Results show that higher DG penetration levels can be achieved by using SOPs (SSSCs, UPFCs or B2B-VSCs) to connect adjacent networks than using shunt compensation (SVCs or STATCOMs) independently in one distribution network [77]. This accords with the previous analysis that active power compensation is more effective in distribution networks.

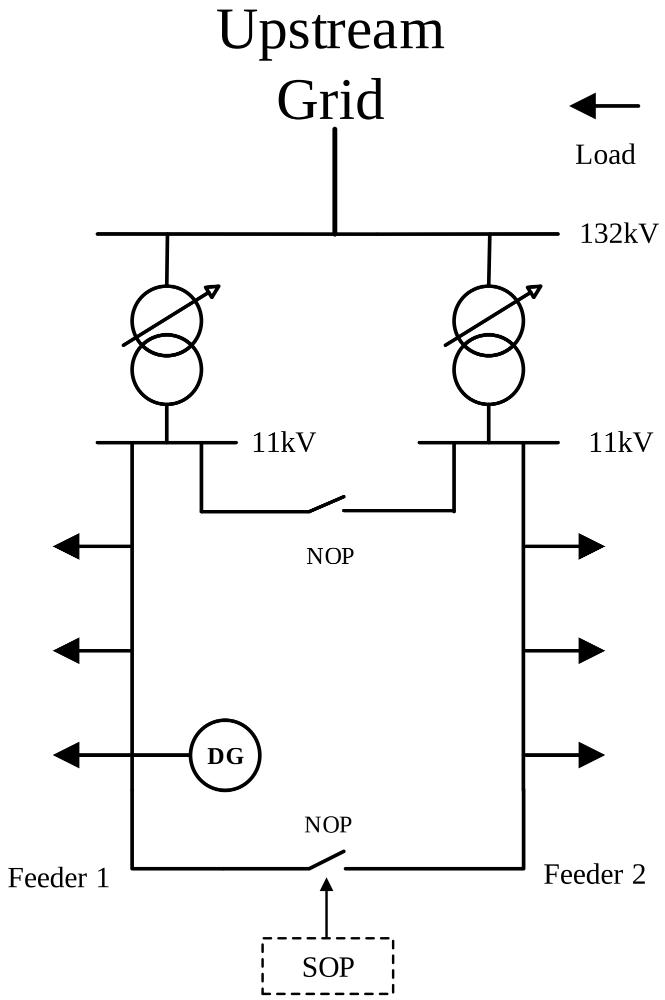

Figure 4.1 A brief single-line diagram of two adjacent distribution networks built in meshed but operated in radial.

A research has been carried out on the performance comparison of using SSSCs, UPFCs and B2B-VSCs as SOPs to increase allowable DG penetration levels. Results show that, for the same power rating, B2B-VSCs offer the best performance at high rating while UPFCs and SSSCs offer better performance at low rating, i.e. 1MVA [64]. The reason of UPFCs and SSSCs are effective at low power rating is that they are partially-rated compensators which can modify the power flow larger than their ratings.

Another research has been carried out to investigate the reduction of the total power loss by using a B2B-VSC as the SOP to balance the power flow in a distribution network. The power losses in the SOP device, associated filters and coupling transformer have all been considered. Simulation results show that the minimum total power loss can be achieved in most cases by implementing the SOP which evenly distributes the load to the two connected feeders. However, due to the power loss introduced by the SOP itself, in some cases, the use of the SOP might increase the total power loss [85].

The power dissipation is an important factor for evaluating the feasibility of SOPs. It is necessary to get knowledges on the power losses of different types of SOPs. In the following section, the SSSC will be used as the representative for partially-rated compensators to be compared with the B2B-VSC as the fully-rated compensator.

4.2 Comparison Between SSSC and B2B-VSC

The distribution networks studied in this section are shown in Figure 4.2. Two supply transformers each supplies a distribution network along a feeder. *Feeder 1* with the total length of 12km supplies 3 aggregated load groups with the capacities of 3MVA, 5MVA and 7MVA. *Feeder 2* with the total length of 6km supplies 3 aggregated load groups with the same capacity of 3MVA. The power factors of all the loads are assumed to be 0.98 in all circumstances. The resistance and inductance of the cable are 0.06Ω/km and 0.134mH/km, respectively. The SOP is installed in the middle of a 1km cable connecting the endpoints of *Feeder 1* and *Feeder 2*. An extreme scenario is selected to investigate the compensation performance of the SSSC and B2B-VSC: *Feeder 1* with the maximum load of 17MVA while *Feeder 2* with 1MVA load. It is expected to see a significant voltage drop at the endpoint of *Feeder 1* due to the high loading level.

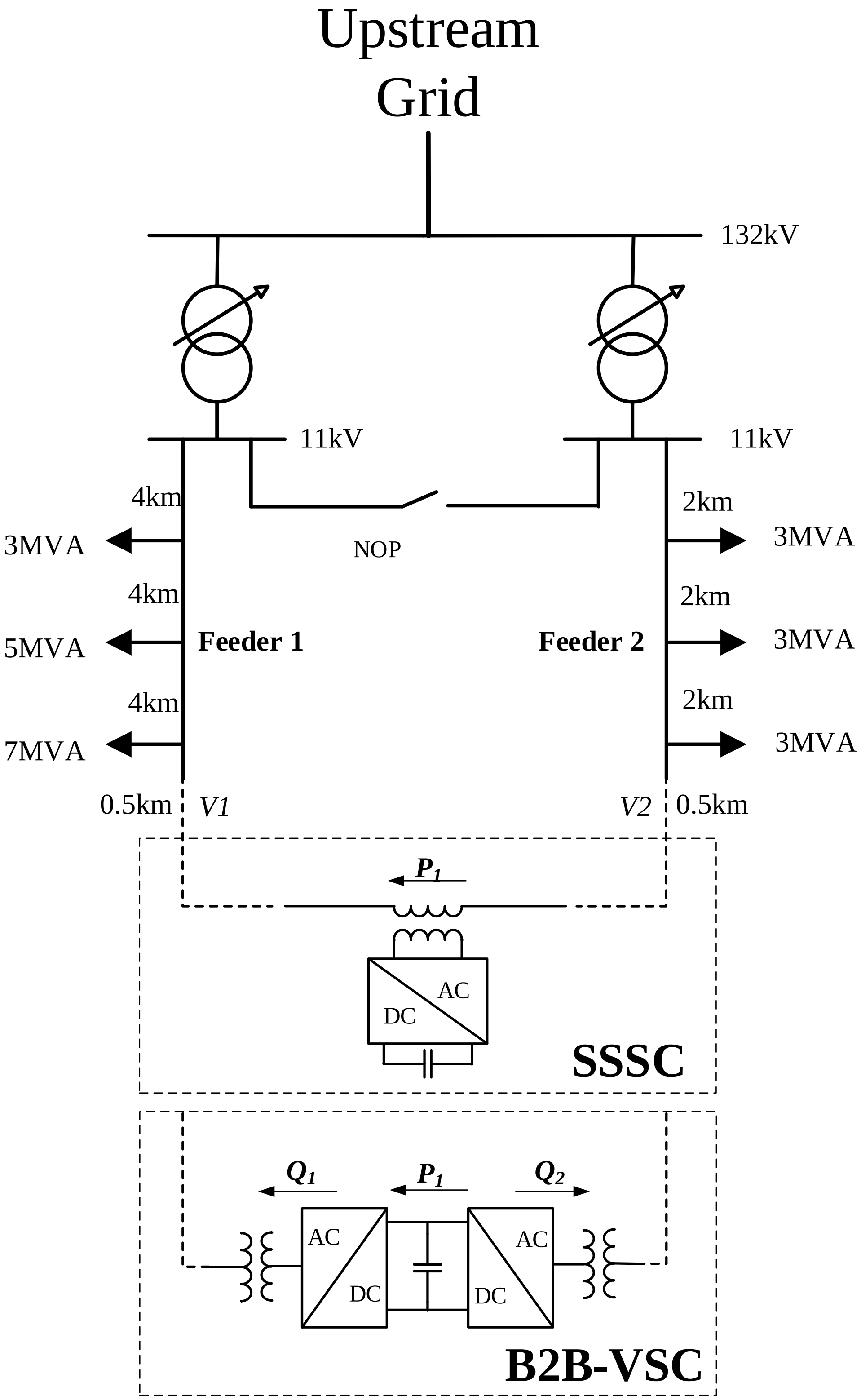

Figure 4.2 Single-line diagram of the studied network and SOP connections

Whether sole reactive power compensation would be enough is firstly analysed and simulated. As previously introduced, equation (4.1) can be used to estimate the voltage drop. In this specified case, for the voltage at the endpoint of *Feeder 1* (*V1*), assuming the load is at the maximum which is 7MVA, the coefficients *PR* and *QX* can be obtained as

$$\begin{aligned}
&PR = \left(7e6 \times 0.98\right) \times \left(0.06 \times 12\right) = 4.9e6 \\
&QX = \sqrt{\left(7e6\right)^2 - \left(7e6 \times 0.98\right)^2} \times \left(0.134e - 3 \times 100 \times \pi\right) = 0.5e6 \\
&\therefore QX \,/\, PR \approx 0.1
\end{aligned} \tag{4.4}$$

where the value of *QX* is only around one tenth of *PR*. This indicates that the dominant factor of the voltage drop on the cable is the active power which leads to the reactive power compensation to be less effective. Then, a simulation on the sole reactive power compensation by a STATCOM is carried out. This is done by setting the active power reference of the B2B-VSC to be zero so that the converters work just like STATCOMs. As shown in Figure 4.3, the simulation starts in the aforementioned extreme scenario and then the STATCOM is activated at *t=0.6s*. For the voltage at the endpoint of *Feeder 1* that is shown in Figure 4.3 (a): before compensation, the voltage *V1* is at 0.906p.u. in the beginning which is below the lower limit (0.94p.u. in the practical operation of DNOs); and after 100% reactive power compensation, the voltage rises to 0.934p.u. which is still lower than the limit. The power coming out from the supply transformer during this period is also measured and shown in Figure 4.3 (b): the reactive power of 3.5MVar is supplied by the substation before the compensation, and it drops to zero after the compensation because the STATCOM is controlled to compensate all the reactive power required. The simulation result shows that, for this extreme scenario in this distribution network, sole reactive power compensation is not sufficient to maintain the voltage at the feeder endpoint within the permitted range.

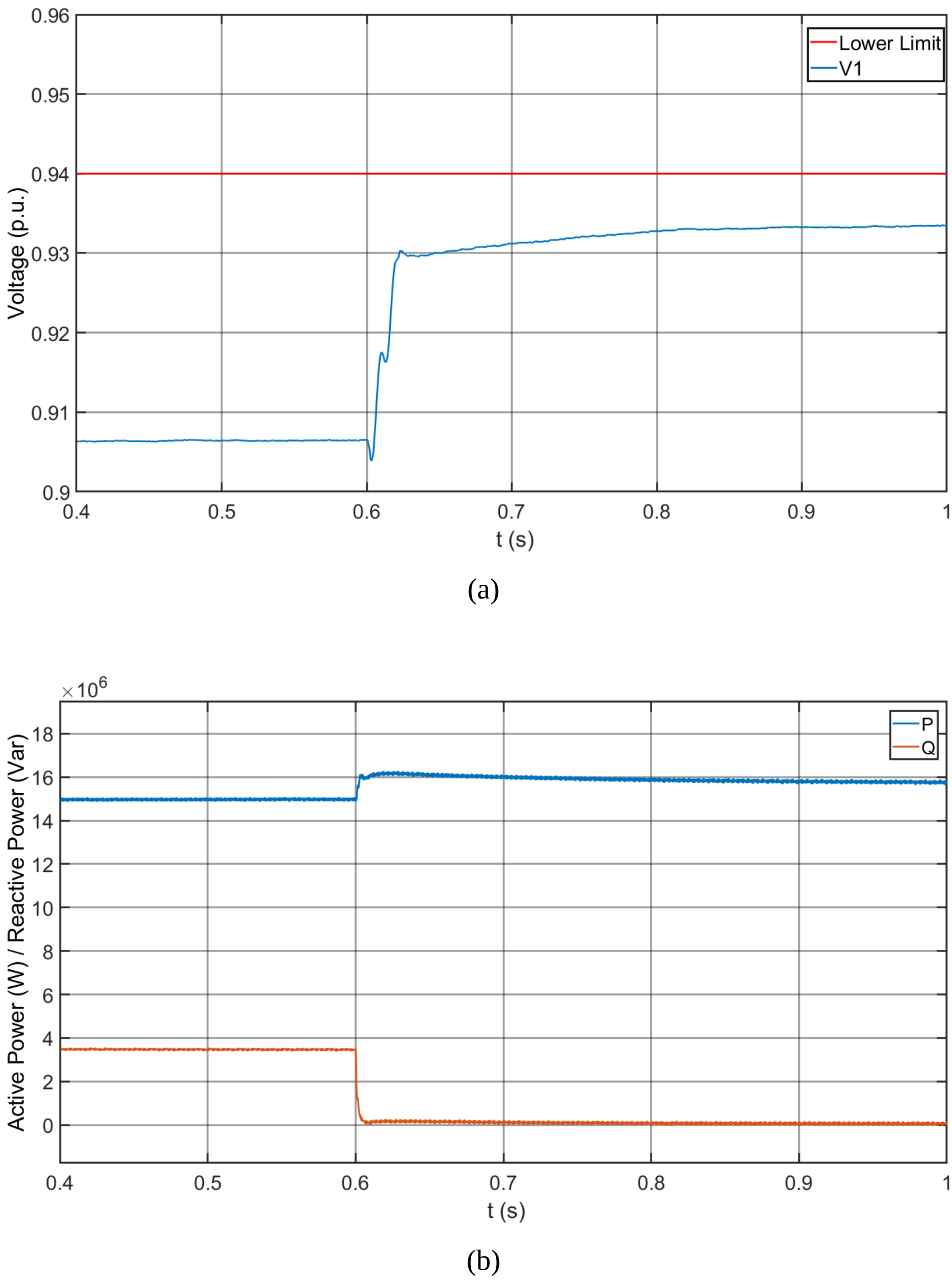

Figure 4.3 Reactive power compensation by STATCOM: (a) Phase-to-ground voltage in per unit before and after compensation; (b) Power coming out from the supply transformer to Feeder 1.

In the following, the compensation performances of SSSC and B2B-VSC types of SOP are investigated. The SOP is desired to transfer active power from the lightly-loaded feeder to the heavily-loaded feeder in order to compensate active power. The SSSC injects a voltage in quadrature with the line current to control the active power flow but the reactive power is not controlled. The B2B-VSC generates required voltages at its AC terminals to control the active power flow as well as the reactive power. The changes of the voltages at both feeder endpoints before and after compensation are all shown in Figure 4.4 (a). It can be seen that after the compensation from $t=0.6s$, voltages at the endpoint of Feeder 1 $V1$ rise to 0.977p.u. for B2B-VSC and 0.960p.u. for SSSC thanks to the effective active power compensation. The voltage at the endpoint of *Feeder 2* (*V2*) drops because increased power is now flowing in *Feeder 2*. The voltages at both feeder endpoints are higher with B2B-VSC than with SSSC because of the additional reactive power compensation by the B2B-VSC. The power coming out from supply transformers to *Feeder 1* and *Feeder 2* with B2B-VSC and SSSC types of SOP are shown in Figure 4.4 (b) and (c), respectively. The active power supplied to *Feeder 1* and *Feeder 2* are equalized after the compensation in both B2B-VSC and SSSC cases which demonstrates that the SOP is operated as desired to balance the load in the looped network. The reactive power becomes to zero with the B2B-VSC after compensation as the B2B-VSC compensates all the reactive power required. The reactive power in SSSC case is not controlled and it flows obeying Kirchhoff law.

From the simulation, it can be concluded that the SOP is more effective than STATCOM thanks to its capability of active power compensation. Furthermore, the B2B-VSC-based SOP has better performance than the SSSC-based SOP due to its independent reactive power compensation.

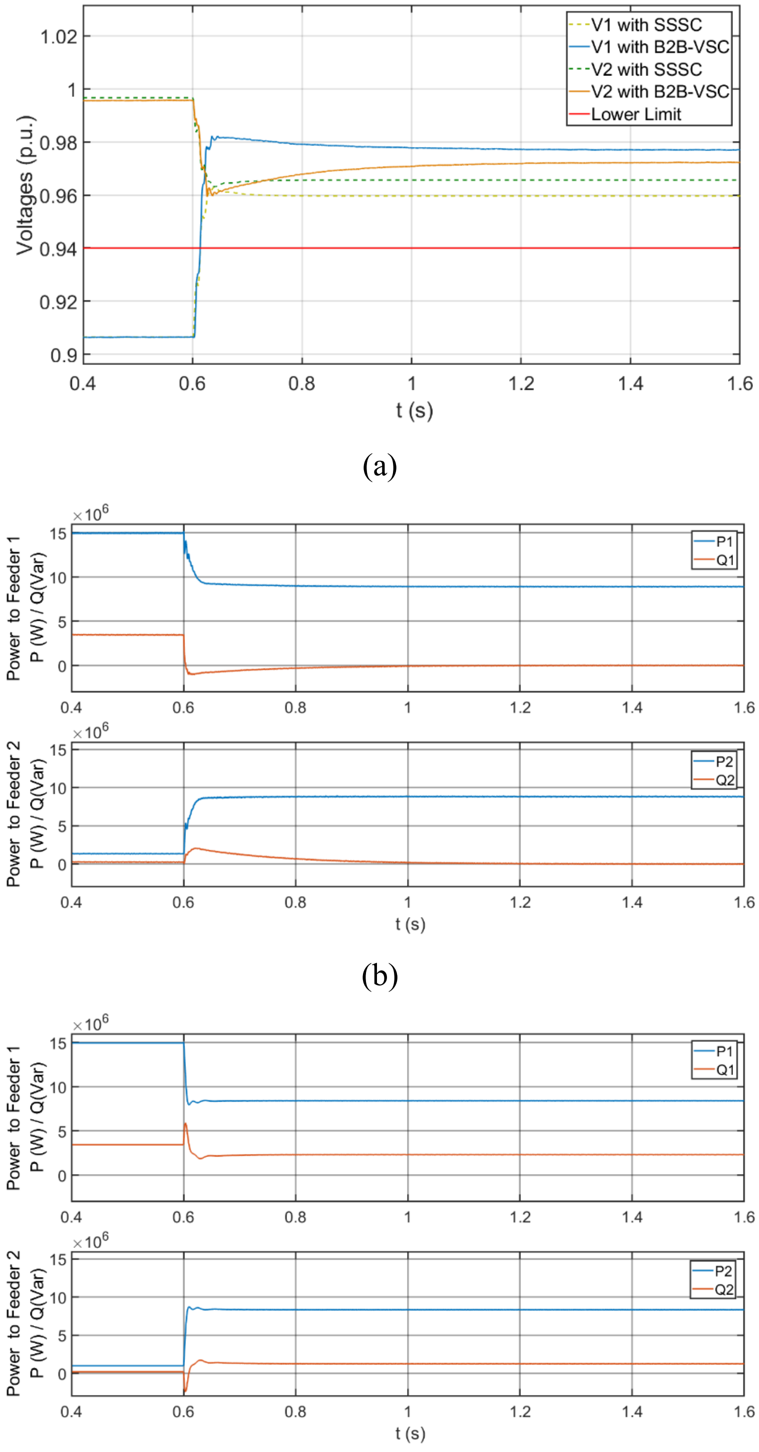

Figure 4.4 Active and reactive power compensation by SSSC and B2B-VSC: (a) The voltages at feeder endpoints before and after compensation shown in per unit; (b) Power fed to *Feeder 1* and *Feeder 2* with B2B-VSC; (c) Power fed to *Feeder 1* and *Feeder 2* with SSSC.

In terms of evaluating power losses, a power module and required numbers must be firstly defined. In the aforementioned extreme scenario, the active power of 8MW is required to be transfer from *Feeder 2* to *Feeder 1* to fully balance the load. Therefore, the power rating of the converter and associated devices are chosen to be 8MVA. In this study, the 'ABB HiPak IGBT Module 5SNE 0800M170100' with the rating of V_{ce}=1700V and I_c=800A' is selected for building the converters. Associated characteristics figures used for power loss calculation are listed in the Appendix II. For implementing the B2B-VSC, two three-phase 8MVA, 11/0.69kV coupling transformers are used. With the transformer to step down the voltage level, three-phase 2-level converters with 1100V DC link could be enough. However, the current with the peak value of 9500A is required to transmit 8MW power which results in that 24 modules for one arm are needed if leaving 100% current margin. Therefore, as there are two converters in one B2B-VSC, a total of 288 modules are required. For the SSSC, as a partially-rated compensator, the current flowing through it at the maximum operating point is less than 600A (peak) and the voltage is less than 300V (phase-to-neutral peak). Therefore, considering a 2000V coupling transformer with 1:1 turn ratio, a three-phase 2-level converter with two modules in each arm is more than sufficient.

The total power loss of a module should include the conduction losses of IGBT and diode, the switching losses of IGBT including turn-on and turn-off losses, and the reverse recovery loss of the diode. All the losses are functions of the current flowing through the device. The following equation can be used to describe the loss calculation

$$E_{total} = \int_0^T \left(v_{ce} \cdot i_c + v_f \cdot i_f \right) dt + \sum e_{on} + \sum e_{off} + \sum e_{rec} \tag{4.4}$$

where the total energy loss E_{total} during a period of T is the sum of the conduction losses and switching losses. The i_c and i_f are the currents flowing through the device and diode; v_{ce} and v_f are the voltages across the device and diode; e_{on}, e_{off} and e_{rec} are the device's turn-on, turn-off loss and diode's reverse recovery loss, respectively. The currents i_c and i_f are measured by a current meter, and v_{ce}, v_f, e_{on}, e_{off} and e_{rec} are obtained via look-up tables that are built from the module's datasheet listed in Appendix II. The flowchart in Figure 4.5 shows how the calculation is carried out in Matlab/Simulink. The current flowing through the device is measured and firstly passing through a logic part which divides the components flowing through the IGBT and diode, i_c and i_f, respectively. For the conduction losses, v_{ce} and v_f can be obtained directly by the look-up tables and the power loss is obtained as $v_{ce} \cdot i_c$ and $v_f \cdot i_f$ in the unit of watt. For the switching losses, the edge detections are used to detect the rising and falling edge of the gate signal in order to extract the current at correct moments. Then, the energy losses in Joule due to the switching are obtained by the look-up tables. Finally, the total energy loss can be obtained as the algebraic sum of the switching energy losses and the integration of the conduction power losses.

The power losses on filters and transformers are assumed to be 0.65% and 0.5% approximately.

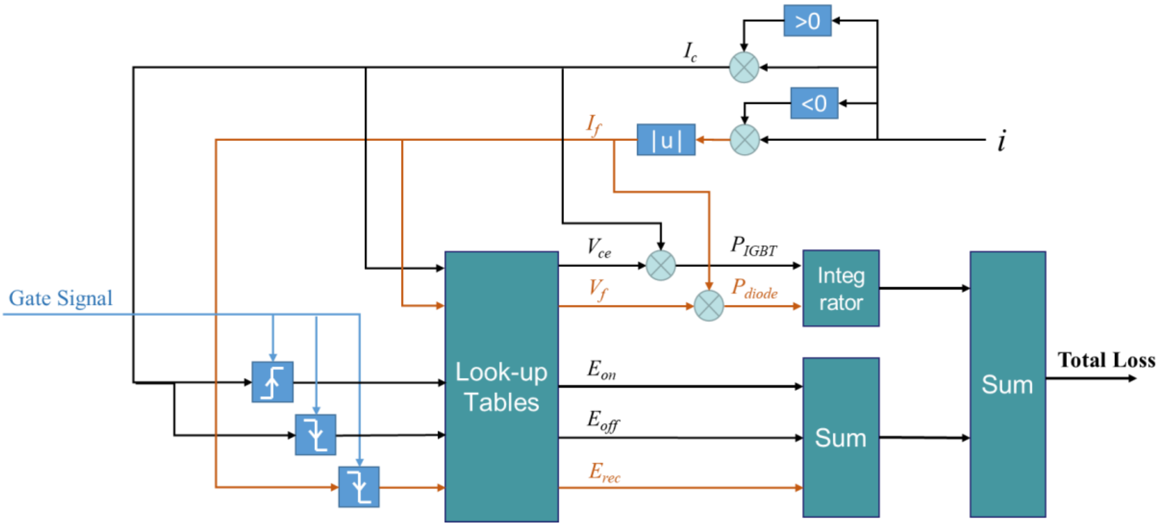

Figure 4.5 Flow chart of power loss calculation

The simulation results are shown in Figure 4.6 which is published in a conference paper [86]. The simulation time step is 1μs and the gate to emitter voltage V_{GE} is assumed to be 15V. When transferring 8MW active power at the switching frequency of 2550Hz, the total loss in the B2B-VSC is 360kW where the efficiency is 95.50%; the total loss in the SSSC is 10.5kW where the efficiency is 99.87%. The efficiency decreases with the operating point goes down. When transferring 1MW active power, the total loss of the B2B-VSC is 82kW where the efficiency is only 91.8%; the total loss of the SSSC is 3kW where the efficiency is 99.7%. In general, the SSSC has much lower power loss than the B2B-VSC (20 to 40 times) which presents an advantage of partially-rated compensator.

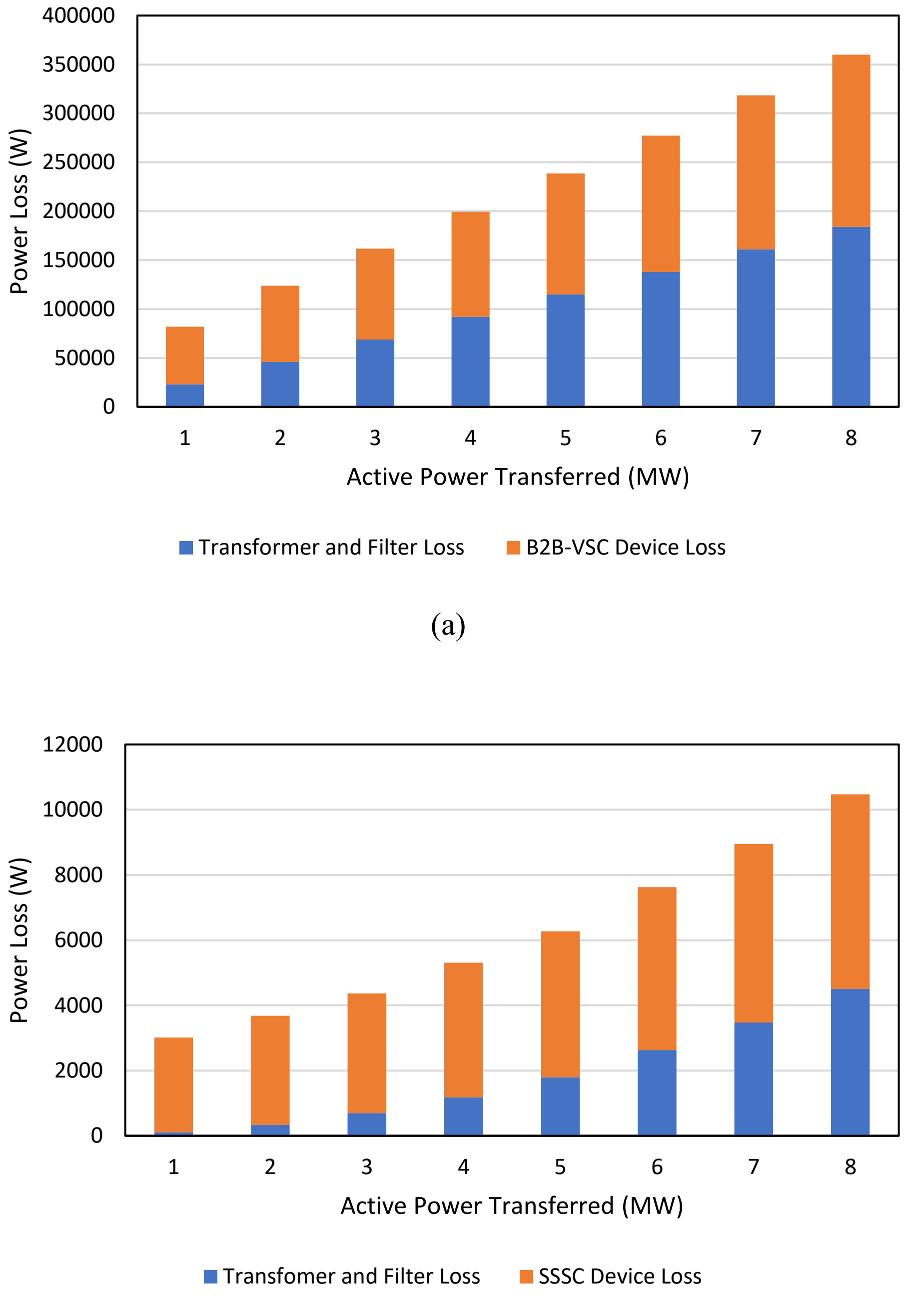

(a)

(b)

Figure 4.6 (a) Power loss of the B2B-VSC; (b) Power loss of the SSSC.

4.3 Summary

As the analysis and simulation results show, sole reactive power compensation is unlikely to be sufficient for distribution networks with high DG penetration level. The active power compensation by using SOP to mesh networks could be a solution to the voltage violation. The B2B-VSC type SOP has better voltage compensation performance because it can offer independent reactive power compensation along with the active power compensation. But, the B2B-VSC is a fully-rated compensator which results in much higher power loss and capital cost compared to the SSSC.

However, SSSC cannot block the fault current flowing between the two networks which means there will be a significant fault level increase in the network meshed by a SSSC-based SOP. Besides, at the fault instant, the voltage across the SSSC will be the full voltage (11kV) which is much higher than the rating of the SSSC. Therefore, additional protection must be implemented. A research about using thyristor crowbars to protect the SSSC-based SOP has been done by simulation [86]. On the other hand, the B2B-VSC-based SOP is a series-connected and fully-rated compensator which is capable of blocking the fault current thus isolating the fault from the other network. It can also be used to connect networks with different frequencies.

From the functionality point of view, the B2B-VSC is the most versatile one among all types of SOPs. It has a great potential to be an option to address issues from the high DG penetration level in distribution networks. In the following chapter, a research on the details of the controller design of a B2B-VSC-based SOP is carried out.

5.Controller Design of a B2B-VSC Based on Proportional-Integral Theory

In this chapter, a step by step controller design for a B2B-VSC-based SOP is introduced. And the details on how to choose control gains are also studied. To use a B2B-VSC as the most versatile SOP in a distribution network, its controller must satisfy the following three functionalities:

- independent active and reactive power control,
- fault current restriction,
- stand-alone load supply in island mode.

5.1 Controller Design

5.1.1 Overall Structure of the Control System

The overall structure of the control system for the B2B-VSC is shown in Figure 5.1. Only half of the B2B-VSC is shown because the controller is symmetric in spite of the outer loop is activated depending on different applications. An LC filter is used to filter out the harmonics introduced by the switching of the VSC. Three sensors for the output voltage, output current and filter inductor current (respectively the v_{oabc}, i_{oabc}, and i_{Labc} shown in Figure 5.1) are required for the control system. R_f, L_f, and C_f are the filter's resistance, inductance, and capacitance respectively.

There are two modes of the developed controller in response to the requirement which are grid-connected mode and island mode. In either mode, a current control loop is reserved as the inner loop in consideration of restricting overcurrent. In grid-connected mode, the B2B-VSC should be controlled to transfer desired active power from one feeder to the other in order to balance the load thus mitigating voltage variations due to DG and load changes. Reactive power compensation is optional which can further optimize the voltage profile. In one of the VSC, the selection switch *S* should be at *position 2* where the current reference is from the DC voltage controller. This VSC is made to maintain the DC link voltage. The selection switch *S* in the other VSC should be at *position 0* to control the active and reactive power flow.

In island mode, i.e. a loss of mains occurs and the VSC becomes the only power supply, the selection switch *S* in the VSC connected to the islanded network should be at *postion1* to link the output voltage controller. Furthermore, due to the absent of voltage reference, the angular velocity must be defined internally, i.e. the selection switch S_{PLL} at the islanding side should be switched to position 1. This VSC extracts power from the DC link and supplies three-phase voltages at rated amplitude and frequency to the load. The other VSC should transmit required power to the DC link to maintain the DC link voltage, i.e. selection switch *S* should be at *position 2*.

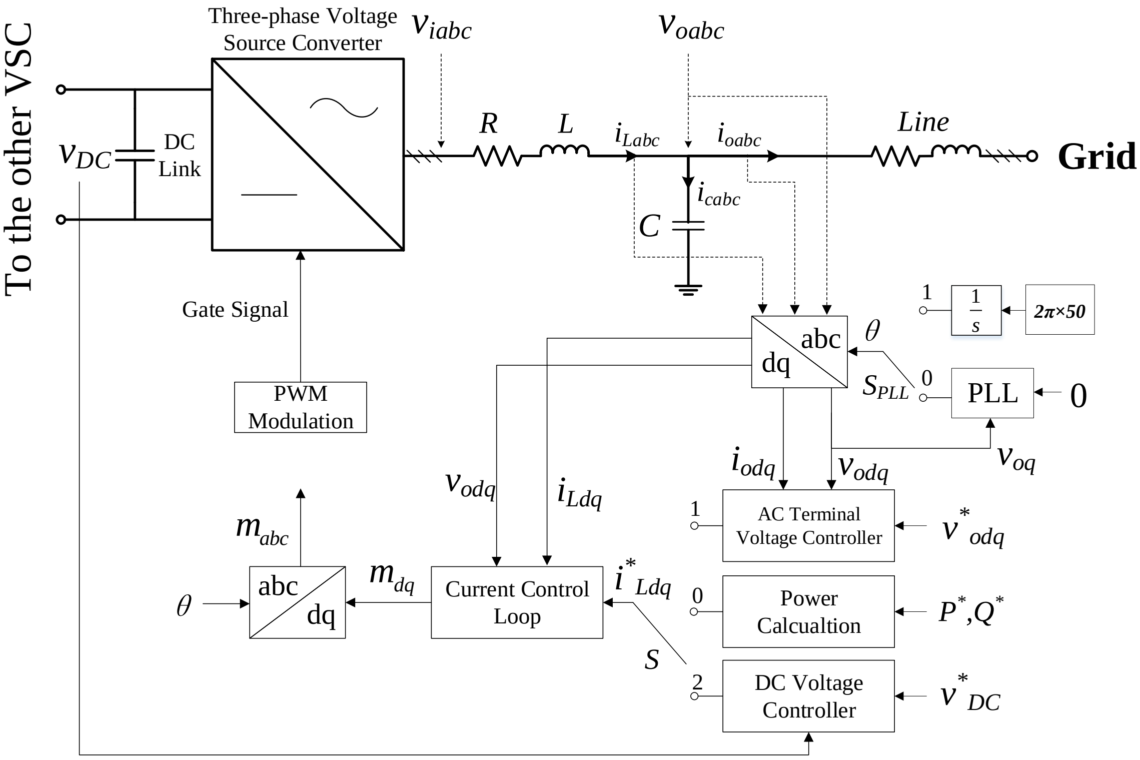

Figure 5.1 Controller diagram for the B2B-VSC.

5.1.2 Direct-quadrature-zero Transformation and Phase-locked Loop

In the controller design of a VSC, proportion-resonant (PR) and proportional-integral (PI) controls are the mostly used methods, and both in general can achieve excellent performance by carefully tuning the control gains. PR control has slightly better performance in rejecting the disturbance of grid voltage and the state variables in PI control has clearer meanings in response to active and reactive power [87-90]. In this chapter, PI control is adopted for the controller design of the B2B-VSC.

PR control can be directly used on vectors, but PI control can be only used on scalars. As AC voltage and current are vectors in stationary frame, therefore the direct-quadrature-zero (*dq0*) transformation needs to be applied to transfer the AC quantities from stationary frame to synchronous reference frame (SRF) where these AC quantities appear as scalars. The *dq0* transformation consists of Clarke and Park transformation that the former converts the AC quantities from *abc* stationary reference frame to *αβz* reference frame and the latter converts the quantities from *αβz* reference frame to *dq0* reference frame. The *dq0* reference frame is usually made to rotate at the grid angular velocity and for this reason it is also known as synchronous reference frame (SRF). In electric power system, the balanced three-phase voltages can be seen as the projections of a rotating vector v on stationery axes *a, b* and *c*. The amplitude-invariant Clark transformation matrix is given as equation (5.1) to project the three-phase voltages to *αβz* reference frame.

$$K_C = \frac{2}{3}\begin{bmatrix} 1 & -\frac{1}{2} & -\frac{1}{2} \\ 0 & \frac{\sqrt{3}}{2} & -\frac{\sqrt{3}}{2} \\ \frac{1}{\sqrt{2}} & \frac{1}{\sqrt{2}} & \frac{1}{\sqrt{2}} \end{bmatrix} \tag{5.1}$$

The projection on z axis is zero when the three-phase voltages are balanced. Then the Park transformation matrix is given as equation (5.2) to project the vector to *dq0* reference frame.

$$K_P = \begin{bmatrix} \cos\theta & \sin\theta & 0 \\ \sin\theta & -\cos\theta & 0 \\ 0 & 0 & 1 \end{bmatrix} \tag{5.2}$$

Then the *dq0* transformation matrix is made of the Clark and Park transformation matrices together as:

$$T\left[\theta\right]=K_P\cdot K_C=\frac{2}{3}\begin{bmatrix}\cos(\theta) & \cos(\theta-\frac{2\pi}{3}) & \cos(\theta+\frac{2\pi}{3})\\ \sin(\theta) & \sin(\theta-\frac{2\pi}{3}) & \sin(\theta+\frac{2\pi}{3})\\ \frac{1}{\sqrt{2}} & \frac{1}{\sqrt{2}} & \frac{1}{\sqrt{2}}\end{bmatrix} \tag{5.3}$$

where θ is the instantaneous angle of an arbitrary angular velocity. And the inverse transformation matrix is given as:

$$T^{-1}\left[\theta\right]=\begin{bmatrix}\cos(\theta) & \sin(\theta) & \frac{1}{\sqrt{2}}\\ \cos(\theta-\frac{2\pi}{3}) & \sin(\theta-\frac{2\pi}{3}) & \frac{1}{\sqrt{2}}\\ \cos(\theta+\frac{2\pi}{3}) & \sin(\theta+\frac{2\pi}{3}) & \frac{1}{\sqrt{2}}\end{bmatrix}. \tag{5.4}$$

The three-phase active and reactive power calculations in *dq0* reference frame when using amplitude-invariant transformation are given as:

$$\begin{aligned}P&=\frac{3}{2}\left(v_d i_d+v_q i_q\right)\\ Q&=\frac{3}{2}\left(v_d i_q-v_q i_d\right)\end{aligned}. \tag{5.5}$$

It should be noted that the matrices could be slightly different depending on how the frames are aligned and which axis is leading. The frame layouts used in this thesis are shown in Figure 5.2.

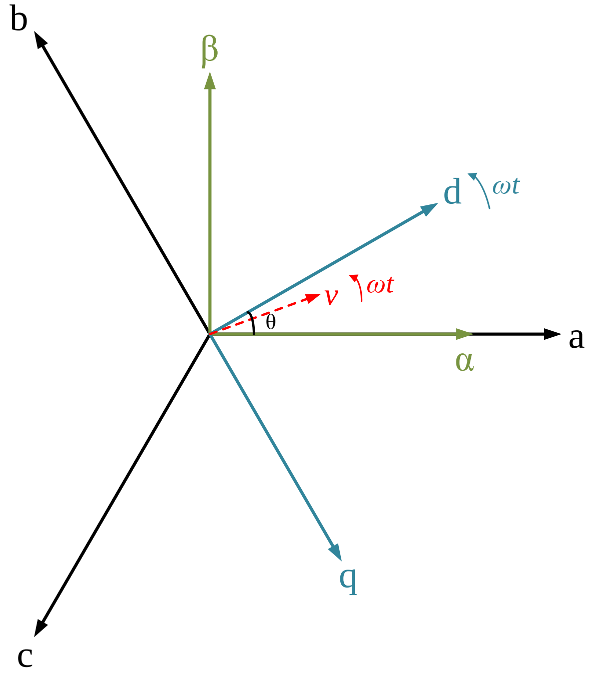

Figure 5.2 Reference frame layouts used in this thesis

In this thesis, the SRF is designed as the *d* axis in alignment with the vector. The projection of the vector on *q* axis is given as

$$v_q = V_m \sin(\theta - \theta_0) \tag{5.6}$$

where V_m and θ_0 are the amplitude and angle of the vector *v*, θ is the angle of the *dq0* reference frame. By making $v_q=0$, the *d* axis will be aligned with the vector thus the *dq0* reference frame can be successfully synchronized to the grid voltage. For a small value of θ-θ_0, equation (5.6) can be linearized as

$$v_q = V_m(\theta - \theta_0) \ . \tag{5.7}$$

A closed loop controller is built as shown in Figure 5.3 (a) to lock v_q to zero. The saturation block is optional for limiting the frequency output under some conditions. By implementing equation (5.7) to Figure 5.3 (a), the closed-loop block diagram can be equivalently re-drawn as Figure 5.3 (b) where the closed-loop transfer function can be readily obtained as:

$$\frac{\theta_0(s)}{\theta(s)} = \frac{V_m \cdot G_{PLL}(s)}{s + V_m \cdot G_{PLL}(s)}. \tag{5.8}$$

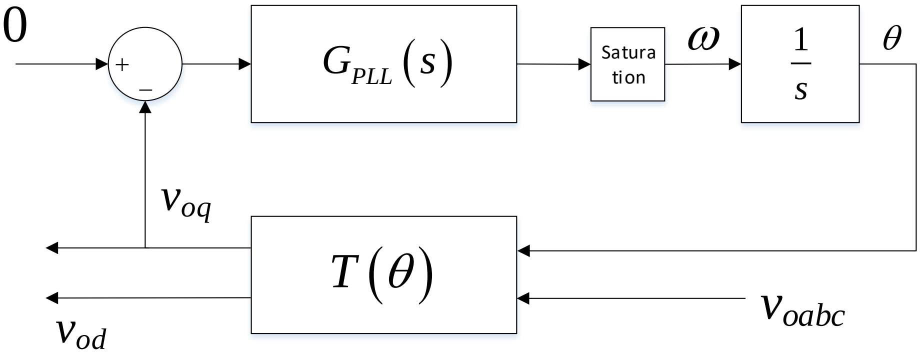

(a)

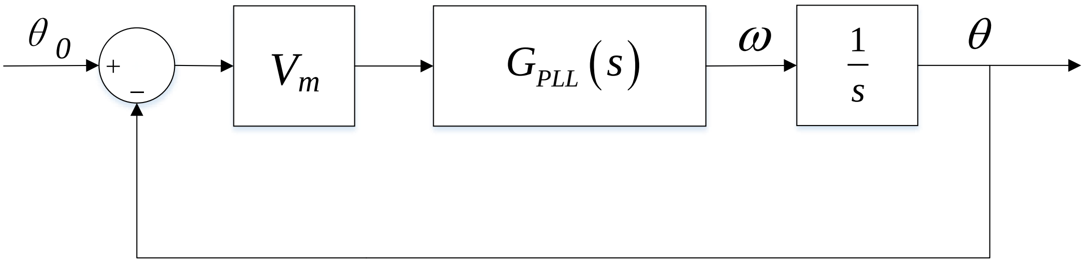

(b)

Figure 5.3 (a) Phase-locked loop; (b) Equivalent diagram for the Phase-locked loop.

When a standard PI controller as the following

$$G_{PLL}(s) = K_{P\_PLL} + \frac{K_{I\_PLL}}{s} \tag{5.9}$$

is used, the closed-loop transfer function is obtained by substituting it into (5.8):

$$\frac{\theta_0(s)}{\theta(s)}=\frac{V_m(K_{P\_PLL}+\frac{K_{I\_PLL}}{s})}{s+V_m(K_{P\_PLL}+\frac{K_{I\_PLL}}{s})}=\frac{V_mK_{P\_PLL}s+V_mK_{I\_PLL}}{s^2+V_mK_{P\_PLL}s+V_mK_{I\_PLL}}. \tag{5.10}$$

The closed-loop transfer function (5.10) is obviously a second-order system which can be rewritten as

$$\frac{\theta_0(s)}{\theta(s)}=\frac{2\xi_{PLL}\omega_{PLL}s+\omega_{PLL}^2}{s^2+2\xi_{PLL}\omega_{PLL}s+\omega_{PLL}^2} \tag{5.11}$$

where

$$\omega_{PLL}=\sqrt{V_m\cdot K_{I\_PLL}}\text{ and }\xi_{PLL}=\frac{K_{P\_PLL}}{2}\sqrt{\frac{V_m}{K_{I\_PLL}}} \tag{5.12}$$

are the natural frequency and damping ratio, respectively. Then, the knowledge of second-order system can be easily applied to choose the gains. When the values of ω_{PLL} and ξ_{PLL} are determined, the proportional and integral gains can be easily obtained by

$$K_{P\_PLL}=\frac{2\xi_{PLL}\omega_{PLL}}{V_m}\text{ and }K_{I\_PLL}=\frac{\omega_{PLL}^2}{V_m}. \tag{5.13}$$

5.1.3 Current Controller

The current controller is used for the control of the current flowing through the filter inductor i_L. The applications of power-electronic devices in power systems are limited due to the relatively low reliability compared to conventional devices and an overcurrent can easily damage power-electronic devices. Therefore, a current control loop is always recommended to be reserved because it can directly control the current flowing through the device.

To build the controller, the physical relation between the inductor current and other quantities must be found first. It is straightforward to find out that the inductor current is related to the voltage across the inductor. The small signal model is given as

$$\vec{v}_{iabc} - \vec{v}_{oabc} = R_f \cdot \vec{i}_{Labc} + L_f \cdot \frac{d\vec{i}_{Labc}}{dt} \tag{5.14}$$

where v_i, v_o are phase voltages before and after the filter, i_L is the current flowing through filter inductor, R_f and L_f are the resistance and inductance of the filter that are all shown in Figure 5.1. The subscript *abc* denotes the balanced three-phase vectors, i.e.

$$\vec{x}_{abc} = \begin{bmatrix} \vec{x}_a & \vec{x}_b & \vec{x}_c \end{bmatrix}^T . \tag{5.15}$$

For applying PI control to the current, the vectors must be transferred to scalars first. Therefore, the *dq0* transformation is substituted into (5.14):

$$\begin{aligned} T^{-1}[\theta]\cdot v_{idq} - T^{-1}[\theta]\cdot v_{odq} &= R\cdot T^{-1}[\theta]\cdot i_{Ldq} + L\cdot\frac{dT^{-1}[\theta]\cdot i_{Ldq}}{dt} \\ &= R\cdot T^{-1}[\theta]\cdot i_{Ldq} + L\cdot T^{-1}[\theta]\cdot\frac{di_{Ldq}}{dt} + L\cdot\frac{dT^{-1}[\theta]}{dt}\cdot i_{Ldq} \\ &= R\cdot T^{-1}[\theta]\cdot i_{Ldq} + L\cdot T^{-1}[\theta]\cdot\frac{di_{Ldq}}{dt} + L\cdot T^{-1}[\theta]\cdot\begin{bmatrix} 0 & \omega \\ -\omega & 0 \end{bmatrix}\cdot i_{Ldq} \end{aligned} \tag{5.16}$$

$$\Rightarrow v_{idq} - v_{odq} = R\cdot i_{Ldq} + L\cdot\frac{di_{Ldq}}{dt} + L\cdot\begin{bmatrix} 0 & \omega \\ -\omega & 0 \end{bmatrix}\cdot i_{Ldq} \tag{5.17}$$

where $T^{-1}[\theta]$ is the reverse *dq0* transformation given by equation (5.4) and ω is the grid angular velocity. The subscript *dq* denotes the components at *d* and *q* axis, i.e.

$$x_{dq} = \begin{bmatrix} x_d & x_q \end{bmatrix}^T . \tag{5.18}$$

Note that the three-phase voltages and currents are assumed to be balanced thus the component at *0* axis is neglected. Then, the plant transfer matrix of the current control loop can be obtained by applying Laplace transformation on (5.17):

$$\begin{bmatrix} V_{id}(s) \\ V_{iq}(s) \end{bmatrix} - \begin{bmatrix} V_{od}(s) \\ V_{oq}(s) \end{bmatrix} = \begin{bmatrix} R+sL & \omega L \\ -\omega L & R+sL \end{bmatrix} \cdot \begin{bmatrix} I_{Ld}(s) \\ I_{Lq}(s) \end{bmatrix} \tag{5.19}$$

As the *d* axis of SRF is aligned with the grid voltage, the component of current on *d* axis determines the real power and the component on *q* axis determines reactive power. Therefore, it is natural to write a quantity in SRF as a complex number, i.e. $x_{dq}=x_d+jx_q$. Then, equation (5.19) can be written as

$$V_{idq}(s) - V_{odq}(s) = \left(Ls + R - j\omega L\right) \cdot I_{Ldq}(s) \tag{5.20}$$

where a coupling component $-j\omega L$ is obviously observed. To achieve a sound performance, a controller with decoupling is built as shown in Figure 5.4. A positive $j\omega L$ is added to the controller to cancel the coupling component $-j\omega L$ in the plant. A feedforward compensation of v_{odq} is also added to achieve faster response. The PI controller with the proportion gain of K_{P_C} and integral gain of K_{I_C} are applied.

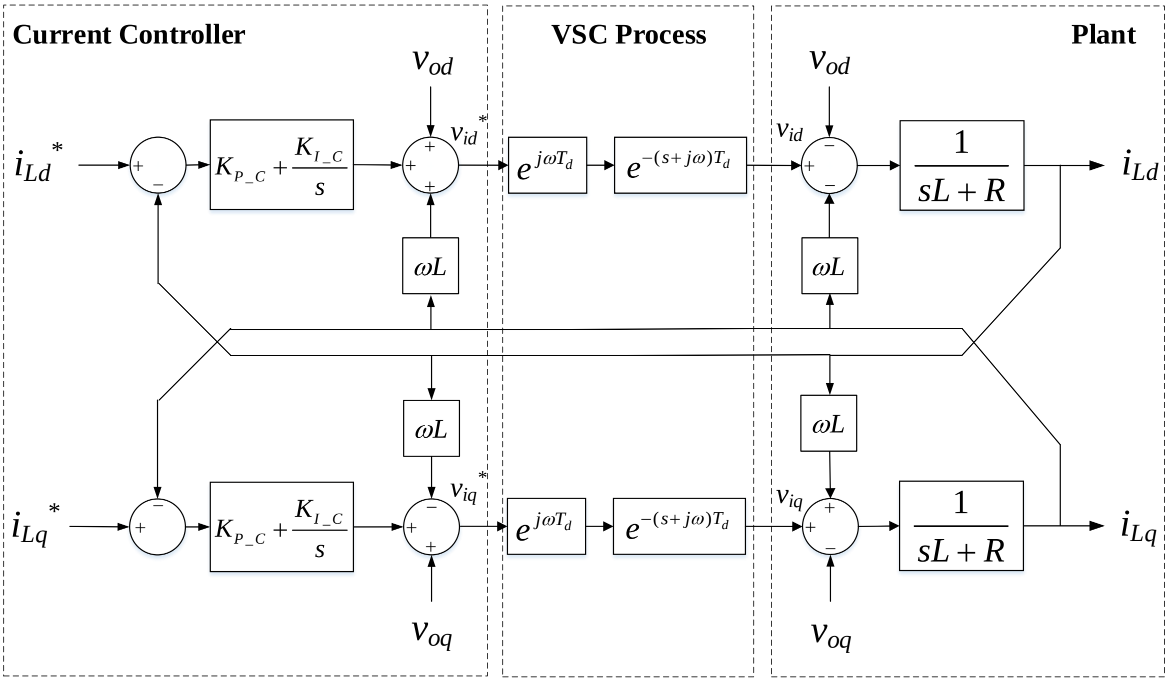

Figure 5.4 Full block diagram of the current control loop.

It should be noted that there are inevitable delays in the VSC process, i.e. digital control and modulation processes which may affect the performance of the system. The total delay T_d consists of the signal processing delay which is usually T_s or $0.5T_s$, and a Pulse-width Modulation (PWM) process delay which is typically $0.5T_s$. Note that $T_s = 1/f_s$ where f_s is the PWM sampling frequency. The delay is usually considered only when the switching frequency is less than 10 times of the output frequency [91]. In SRF, the delay can be expressed as $e^{-(s+j\omega)T_d}$, and a phase angle compensation $e^{j\omega T_d}$ is usually applied to mitigate the effect of delay [92]. For 2-level converters used in power system, the switching frequency of 2550Hz which is 51 times of the grid frequency in the UK could be a proper option considering the tradeoff between total harmonic distortion (THD) and power dissipation in switching. Thus, it is reasonable to neglect the effect of delay to the system when designing the controller. In the following parts of this thesis, the effect of delay is neglected after compensation, i.e.

$$e^{j\omega T_d} \cdot e^{-(s+j\omega)T_d} = e^{-sT_d} \approx 1. \tag{5.21}$$

Then, by defining the controller gain $G_C(s)$ and plant $H_C(s)$ as

$$G_C(s) = K_{P\_C} + \frac{K_{I\_C}}{s} \text{ and } H_C(s) = \frac{1}{L_f s + R_f}, \tag{5.22}$$

the closed-loop transfer function of the current control loop $G_{CL}(s)$ can be obtained:

$$G_{CL}(s) = \frac{G_C(s) \cdot H_C(s)}{1 + G_C(s) \cdot H_C(s)}. \tag{5.23}$$

Then, Internal Model Control (IMC) method can be used for simplifying the parameter design by estimating the system plant[93]:

$$K_{P\_C} = n \cdot L_f \text{ and } \frac{K_{I\_C}}{s} = n \cdot R_f. \tag{5.24}$$

where $\hat{L}_f$ and $\hat{R}_f$ are the estimations of the filter inductance L_f and resistance R_f, respectively. Researches have been done on how inaccurate estimations of L_f and R_f could affect the system [92]. In this thesis, good estimations are assumed. Therefore, the closed-loop transfer function (5.23) can be simplified as a standard first-order system:

$$G_{CL}(s) = \frac{1}{\tau s + 1} \tag{5.25}$$

where the time constant $\tau = 1/n$. The additional advantage of this design is that no matter how the time constant changes, the first-order system will have no overshoot which means no overcurrent to the device should appear.

5.1.4 DC Link Voltage Controller

The DC link is a capacitive device which should operate as a voltage source to the inverter. The energy stored in the DC link is determined by its capacitance and voltage as:

$$E = \frac{1}{2} C \cdot V^2 \tag{5.26}$$

where E, C and V are the energy, capacitance and voltage of the DC link, respectively. By making u=V^2 and then differentiating (5.26), the following equation can be derived:

$$P_{DC} = \frac{1}{2} C_f \frac{du}{dt} \tag{5.27}$$

where P_{DC} is the power flowing into or out from the DC link. Thus, the plant transfer function is obtained as

$$H_{DC}(s) = \frac{U(s)}{P_{DC}(s)} = \frac{2}{Cs} \ . \tag{5.28}$$

Now, design a PI controller for the DC voltage loop as:

$$G_{DC}(s) = K_{P\_DC} + \frac{K_{I\_DC}}{s} \, . \tag{5.29}$$

As aforementioned, a current control loop is recommended to be always applied. Therefore, the DC voltage loop is designed as an outer loop to provide reference value for the current control loop. It is not difficult to find out the relation between the power fed in to the DC link and the current on the filter inductor. Because of the law of conservation of energy, the power coming from the AC network to the converter should equal the power fed into the DC link. Although there is inevitable power loss, the integral gain will eliminate the error. And as introduced in Section 5.1.2, the voltage at q axis v_q is locked to zero by the PLL. Thus, for the amplitude-invariant *dq0* transformation used in this thesis, the voltage at d axis v_d should be equal to the amplitude of the grid voltage V_m. Thus, the power calculation equation (5.5) can be simplified as:

$$P = \frac{3}{2} v_d i_d \ . \tag{5.30}$$

Therefore, the reference current at *d* axis can be easily obtained by an algebraic operation. The full DC voltage control loop is given in Figure 5.5. The saturation block is used to limit the current reference in case of overcurrent damaging devices.

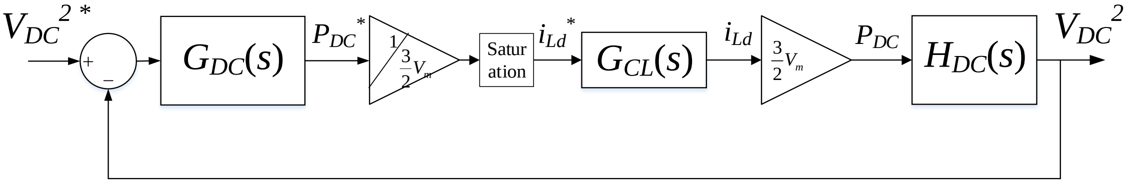

Figure 5.5 block diagram of DC link voltage loop

Then, the open-loop and closed-loop transfer function of DC link voltage loop are, respectively, obtained as

$$N_{DCVL}(s) = G_{DC}(s)G_{CL}(s)H_{DC}(s) , \tag{5.31}$$

and

$$G_{DCVL}(s) = \frac{G_{DC}(s)G_{CL}(s)H_{DC}(s)}{1 + G_{DC}(s)G_{CL}(s)H_{DC}(s)} \ . \tag{5.32}$$

Usually, inner loop can be neglected if it is much faster than the outer loop. Now the inner current control loop is firstly ignored, i.e. $G_{CL}(s)$=1, for the ease of tuning controller gains. To be rigorous, the effect of inner loop will be analysed afterwards. By substituting $G_{CL}(s)$=1 to (5.32), the simplified transfer function of DC link voltage loop will be

$$G'_{DCVL}(s)=\frac{G_{DC}(s)H_{DC}(s)}{1+G_{DC}(s)H_{DC}(s)}=\frac{\frac{2K_{P\_DC}}{C}s+\frac{2K_{I\_DC}}{C}}{s^2+\frac{2K_{P\_DC}}{C}s+\frac{2K_{I\_DC}}{C}}. \tag{5.33}$$

Then, rewrite it as

$$G'_{DCVL}(s)=\frac{2\xi_{DC}\omega_{DC}s+\omega_{DC}^2}{s^2+2\xi_{DC}\omega_{DC}s+\omega_{DC}^2} \tag{5.34}$$

where

$$K_{P\_DC}=C\xi_{DC}\omega_{DC} \text{ and } K_{I\_DC}=\frac{1}{2}C\omega_{DC}^2. \tag{5.35}$$

Similar to the PLL controller, second-order system knowledges can be used for designing gains at this step. But, it is worth mentioning that this is not the standard form of a second-order system as the standard second-order system only has one term ω_n^2 on the numerator. The damping ratio $\xi=0.707$ is usually adopted for standard second-order system to achieve sound performance because it results in no resonance at pole frequency and only about 4% overshoot in step response in time domain. However, the ξ of 0.707 actually results in about 20% overshoot for the second-order system in the form of (5.34). It is risky to have large overshoots when the controlled quantities are applied to power-electronic devices. Therefore, it is necessary to find out how to set the value of damping ratio in the specified system in this thesis.

Firstly, for a given second-order system taken the form of (5.34), its step response will be

$$H_{step}(s)=\frac{1}{s}\cdot\frac{2\xi\omega_n s+\omega_n{}^2}{s^2+2\xi\omega_n s+\omega_n{}^2}=\frac{1}{s}-\frac{s+\xi\omega_n}{(s+\xi\omega_n)^2+\omega_d^2}+\frac{\xi\omega_n}{(s+\xi\omega_n)^2+\omega_d^2} \tag{5.36}$$

where $\omega_d = \omega_n\sqrt{1-\xi^2}$ $(0 < \xi < 1)$. By applying Laplace inverse transformation to (5.36), the step response in time domain can be obtained as:

$$h_{step}\left(t\right)=1-\frac{e^{-\xi\omega t}}{\sqrt{1-\xi^2}}\sin\left(\theta-\omega_d t\right) \tag{5.37}$$

where $\theta = \tan^{-1}(\frac{\sqrt{1-\xi^2}}{\xi})$. By making $\frac{dh_{step}(t)}{dt} = 0$, t_p which is the time required by the output to reach its first peak can be derived as:

$$t_p = \frac{2\arccos\left(\xi\right)}{\omega_n\sqrt{1-\xi^2}} \ . \tag{5.38}$$

Then, by substituting (5.38) back into (5.37), the peak value of the overshoot can be obtained:

$$h_{peak} = h_{step}\left(t_p\right) = 1+e^{-\xi\frac{2\arccos(\xi)}{\sqrt{1-\xi^2}}} \ . \tag{5.39}$$

Defining the maximum overshoot of the step response as:

$$M_p = \frac{h_{step}\left(t_p\right)-h_{step}\left(\infty\right)}{h_{step}\left(\infty\right)}\times 100\% \ . \tag{5.40}$$

Results of the maximum overshoots of this second-order system with different damping ratios are shown in Table 5-1. For achieving a relatively smoother response, ξ=0.707 with the maximum overshoot below 15% is preferred in this thesis.

Once a damping ratio has been confirmed, the natural frequency ω_n can be easily determined for a desired response speed by:

$$t_r \approx \frac{1}{\xi\omega_n} \tag{5.41}$$

where t_r is the rising time of second-order systems. In the following, the bode diagrams along with step responses of the DC link voltage loop are plotted for different values of t_r at the fixed damping ratio ξ=0.93. The parameters are shown in Table 5-2.

Table 5-1 The maximum overshoots at different damping ratios

Damping ratio ξ	Maximum overshoot M_p
0.5	29.84 %
0.6	24.88 %
0.707	20.79 %
0.8	17.98 %
0.93	14.89 %
0.99	13.72 %

Table 5-2 Used parameters

Parameters	Description	Values
K_{P_C}	Current controller proportional gain	0.25
K_{I_C}	Current controller integral gain	1.571
τ	Current control loop time constant	0.2ms
C	DC link capacitance	10mF
ξ_{DC}	Damping ratio of DC link voltage controller	0.93

The bode diagrams of the open-loop transfer function $N_{DCVL}(s)$ when t_r at different values are potted in Figure 5.6 (a). The phase margins are 13.5°, 41.2°, 52.2° and 62.6° corresponding to t_r of 0.2ms, 0.6ms, 1ms and 2ms, respectively. To preserve a sufficient phase margin over 45°, rising time t_r over 1ms (5 times of the inner loop time constant) is recommended. The step responses of the closed-loop transfer function $G_{DCVL}(s)$ when t_r equals 0.2ms, 0.6ms, 1ms and 2ms are then plotted in Figure 5.6 (b). In general, when the rising time of the DC link voltage loop is close to the inner loop time constant, severer oscillations in the step response are observed as well as larger overshoots. It indicates that the influence of the inner loop to the whole system is inversely proportional to the difference between the speed of outer and inner loops. When t_r=2ms, the maximum over shoot is approximately 18% which is close to the theoretical value about 15%. In addition, the step response of the ideal closed-loop transfer function, i.e. regarding $G_{CL}(s)$=1, is also shown in Figure 5.6 (b) by the green line marked by triangles. It can be concluded that when the outer loop is at least 10 times slower than the inner loop, the error by neglecting the inner loop will be very small thus could be ignored.

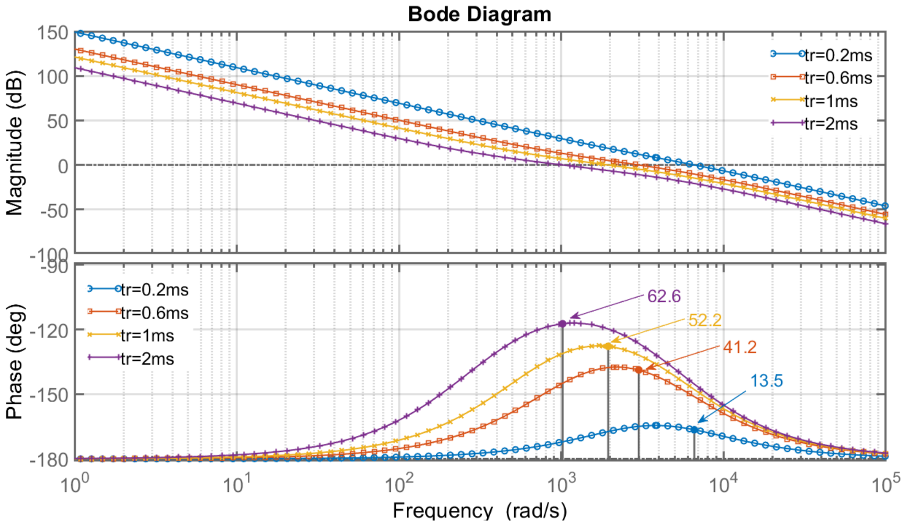

(a)

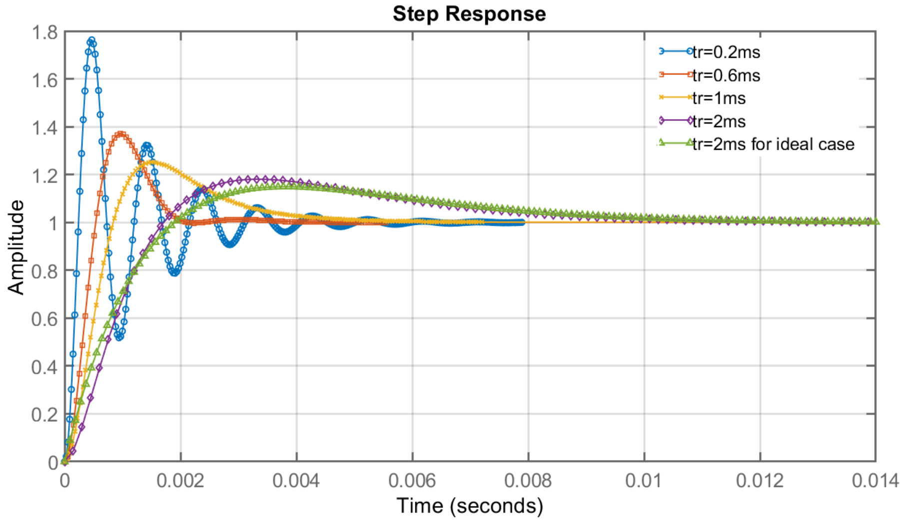

(b)

Figure 5.6 (a) Bode diagram at different t_r; (b) Step responses at different t_r.

Taking account of the small overshoot and sufficient stability margin, the damping ratio ξ=0.93 and rising time t_r=2ms are selected. Then, by using equation (5.41), the natural frequency of DC link voltage loop is obtained as ω_{DC}=537.63 rad/s. Finally, by (5.35) the proportional and integral gains are obtained as K_{P_DC}=5 and K_{I_DC}=1445.3.

5.1.5 Output Voltage Controller

The output voltage controller is activated only when the connected network has lost the connection to the mains. The loss of mains could happen due to the excision of fault section, natural disasters or human intervention and so forth. The purpose of this controller is to control the B2B-VSC to provide a reliable AC voltage supply to the islanded network thus mitigating the harm due to the loss of mains. As shown in Figure 5.1, the inductor current is the sum of the output current and capacitor current. Therefore, the small signal equation between the inductor current, output current and output voltage is given as:

$$\vec{i}_{Labc} = \vec{i}_{oabc} + \vec{i}_{cabc} = \vec{i}_{oabc} + C_f \cdot \frac{d\vec{v}_{oabc}}{dt} \tag{5.42}$$

where i_{Labc}, i_{oabc} and i_{cabc} represent the three-phase inductor currents, output currents and capacitor currents, respectively; v_{oabc} is the three-phase phase voltages and C_f is the capacitance of the filter capacitor. Referring to (5.16), the equation for voltage loop plant in SRF can be similarly derived from (5.42):

$$\begin{bmatrix} i_{Ld} \\ i_{Lq} \end{bmatrix} = \begin{bmatrix} i_{od} \\ i_{oq} \end{bmatrix} + C \cdot \frac{d}{dt} \begin{bmatrix} v_{od} \\ v_{oq} \end{bmatrix} + C \cdot \begin{bmatrix} 0 & \omega \\ -\omega & 0 \end{bmatrix} \begin{bmatrix} v_{od} \\ v_{oq} \end{bmatrix}. \tag{5.43}$$

Applying Laplace Transform to (5.43) and then writing it in complex form:

$$I_{Ldq}(s) - I_{odq}(s) = \left(C_f s - j\omega C_f\right) \cdot V_{odq}(s) \tag{5.44}$$

where the coupling component $-j\omega C$ is observed and the plant transfer function of output voltage loop is given as:

$$H_V(s) = \frac{1}{C_f s}. \tag{5.45}$$

The block diagram of the whole control loop of the output voltage control loop is shown in Figure 5.7. The saturation blocks are installed to restrict current reference in case of overcurrent. The feedforward component i_{odq} and decoupling component $j\omega C$ are applied for better performance. Similar to the process when designing controller gains for DC link voltage loop, we first ignore the inner loop to simplify the model to design controller gains and then analyse the influence of the inner loop under the determined gains.

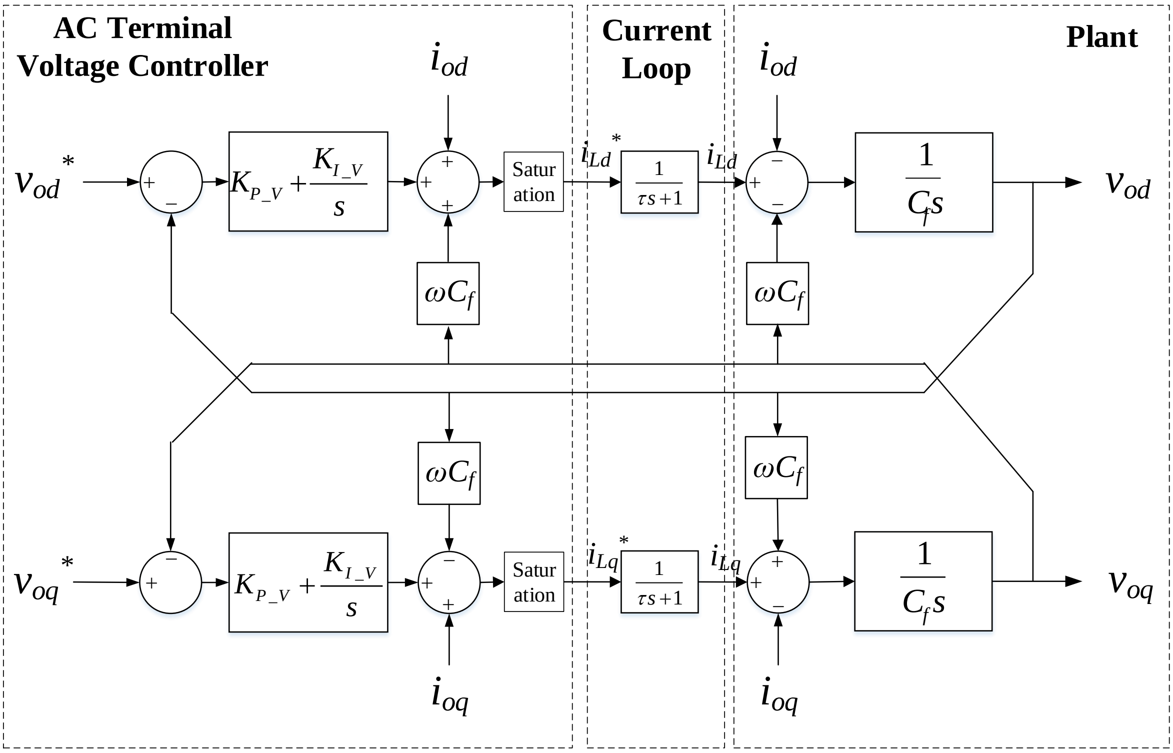

Figure 5.7 Block diagram of output voltage control loop

If the inner current control loop is ignored, the disturbance from output current i_{odq} and coupling would be perfectly cancelled. Defining a PI controller:

$$G_V(s) = K_{P\_V} + \frac{K_{I\_V}}{s}. \tag{5.46}$$

Then, the closed-loop transfer function of the output voltage loop can be readily obtained as

$$G'_{VL}(s) = \frac{G_V(s)H_V(s)}{1+G_V(s)H_V(s)} = \frac{\frac{K_{P\_V}}{C_f}s + \frac{K_{I\_V}}{C_f}}{s^2 + \frac{K_{P\_V}}{C_f}s + \frac{K_{I\_V}}{C_f}} \,. \tag{5.47}$$

The transfer function takes the form of a second-order system which can be written as:

$$G'_{VL}(s) = \frac{2\xi_V\omega_V s + \omega_V^2}{s^2 + 2\xi_V\omega_V s + \omega_V^2} \,. \tag{5.48}$$

where

$$K_{P\_V} = 2\xi_V\omega_V C_f \text{ and } K_{I\_V} = \omega_V^2 C_f \,. \tag{5.49}$$

The transfer function possesses the same form as $G'_{DCVL}(s)$ by (5.34). Therefore, the damping ratio ξ_V=0.93 is preferred for relatively small overshoot. And then, for a determined output voltage loop rising time t_{r_V}, the natural frequency ω_V can be found by using equation (5.41). Different from the DC link voltage loop, the output voltage loop would be a multiple-input and multiple-output (MIMO) system if the inner loop is considered. The disturbance and coupling components cannot be perfectly cancelled due to the existence of the current control loop. Thus, the outputs v_{od} and v_{oq} are subjected to four inputs, voltage reference v_{od}^*, v_{oq}^* and output currents i_{od}, i_{oq}. For the ease of analysis, the state-space method is selected. And to acquire the state-space matrices, a state-space representation of the full output voltage control loop that shown in Figure 5.7 can be plotted as illustrated in Figure 5.8.

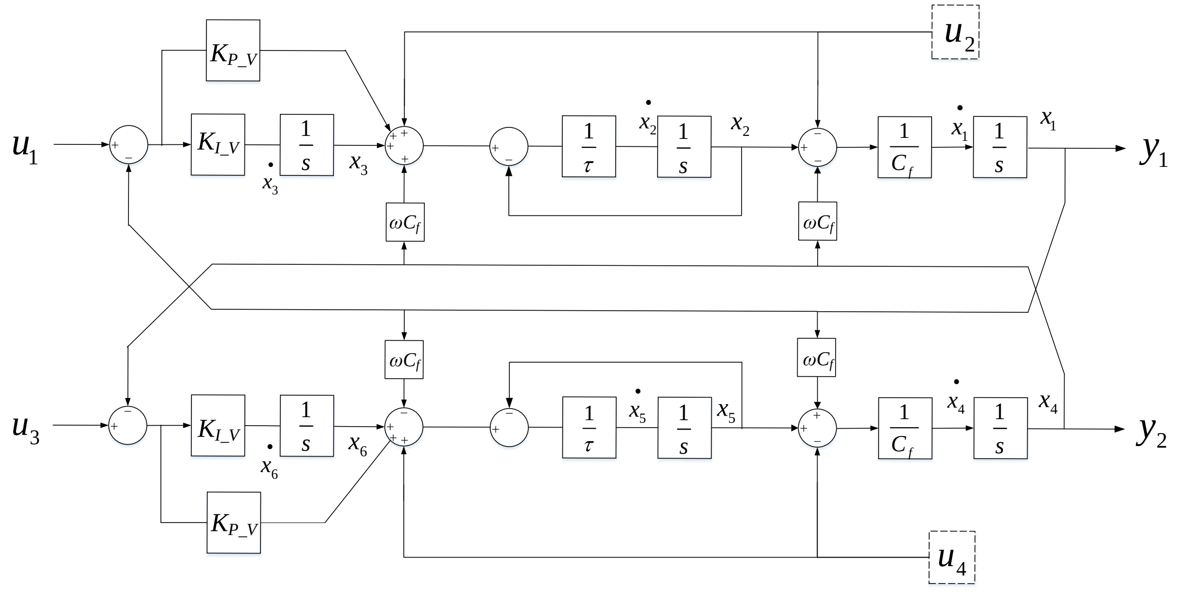

Figure 5.8 State-space representation of output voltage control loop

The inputs *u*1, *u2*, *u3*, *u4* and the outputs *y1* and *y2* are defined as:

$$\begin{cases} u_1 = v_{od}^* \\ u_2 = i_{od} \\ u_3 = v_{oq}^* \\ u_4 = i_{oq} \end{cases} \text{ and } \begin{cases} y_1 = v_{od} \\ y_2 = v_{oq} \end{cases}. \tag{5.50}$$

Then the state-space matrices can be readily derived from Figure 5.8 which owns the form as:

$$\begin{aligned} x' &= Ax + Bu \\ y &= Cx + Du \end{aligned} \tag{4.12}$$

where the matrices A, B, C, and D are listed in Appendix I.

The damping ratio is selected at 0.93 as previously mentioned. The pole-zero maps of the whole system at different rising times are first plotted in Figure 5.9. A pair of poles are located at the right half plane when t_{r_V}=0.2ms, i.e. the same as the inner loop's time constant, which means the system is unstable. Afterwards, once the rising time has been increased over 0.4ms (2 times slower than the inner loop), all poles are located in the left half plane which indicates the system is stable.

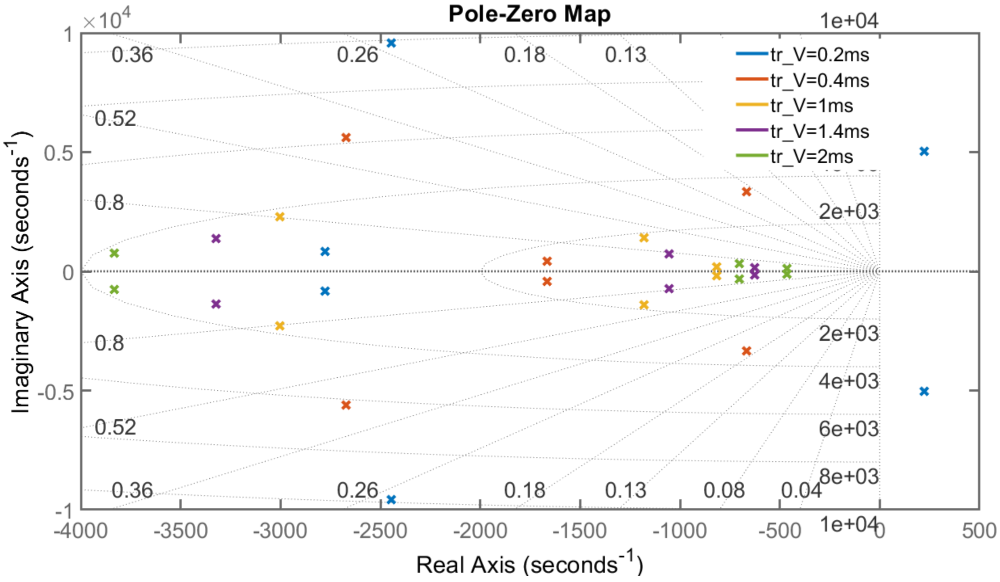

Figure 5.9 Pole-zero map of the whole system at different rising time

In the following, the magnitude diagrams of all four inputs to output *y1* are plotted in Figure 5.10 to observe the influences of each input to the output. The system is symmetric so that the results can be also applied to *y2*. The results show that for all rising time values, the inputs *u2*, *u3*, *u4* have very low gains to output *y1* at zero hertz that can be neglected. Therefore, it is reasonable to consider that the output *y1* is only responsive to input *u1*. The step response of *u1* to *y1* is plotted in Figure 5.11. Considering a small overshoot, the rising time of 2ms is selected.

Then, by (5.41) the natural frequency of output voltage loop is found as ω_V=537.6. Finally, the proportional and integral gains can be calculated by (5.49): K_{P_V}=2 and K_{I_V}=578.1.

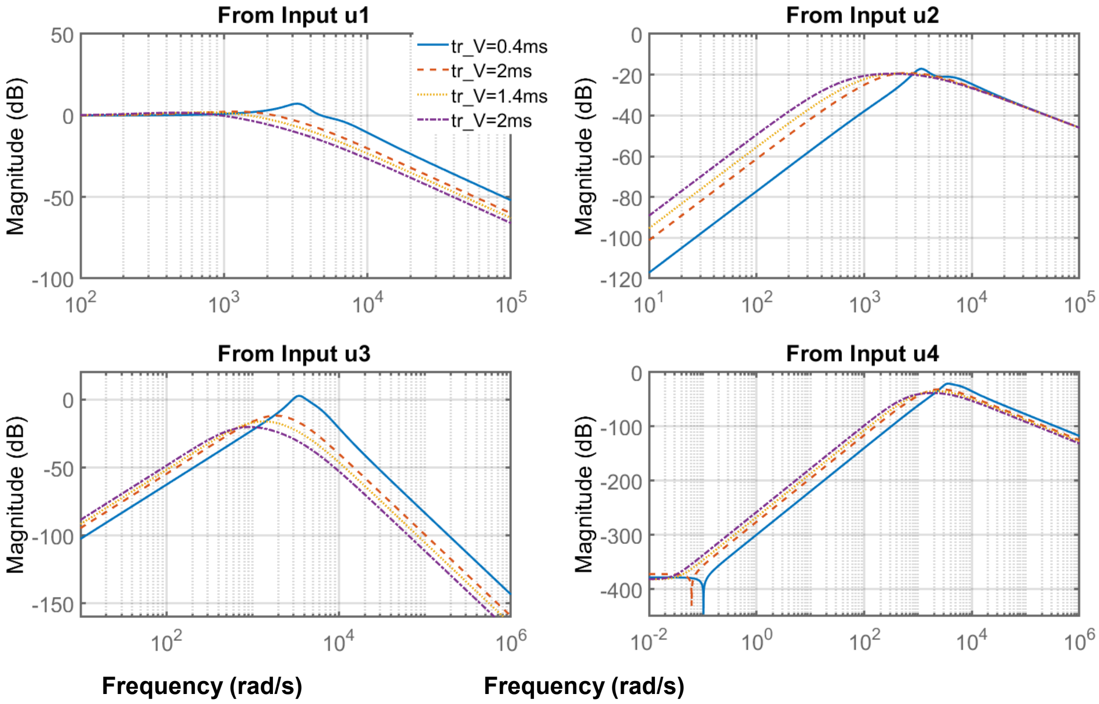

Figure 5.10 Magnitude diagram from inputs *u1*, *u2*, *u3* and *u4* to output *y1*.

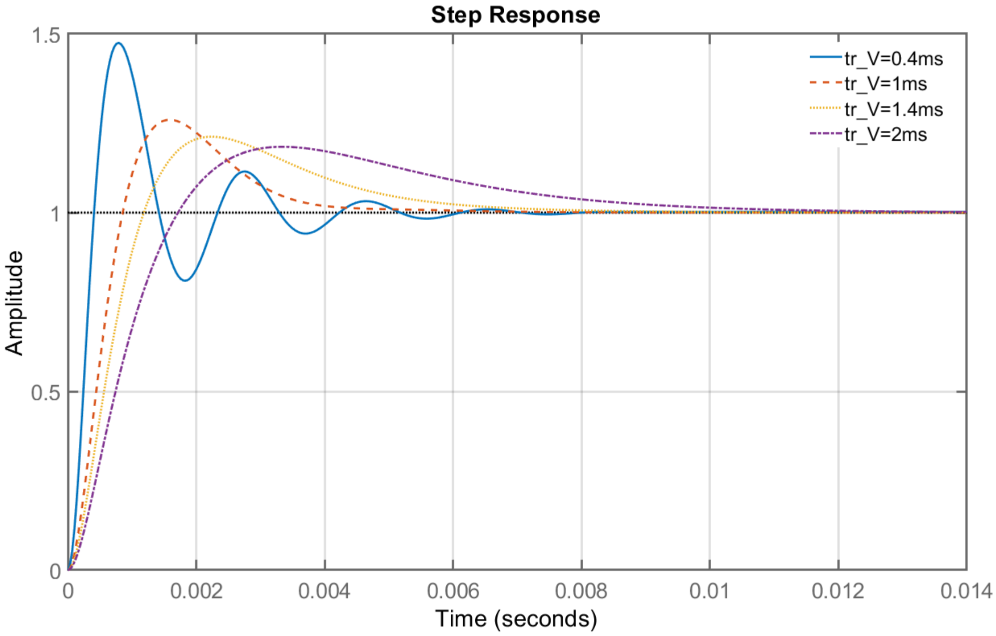

Figure 5.11 Step response of *u1* to *y1* at different rising times

5.2 Simulation Results

As the application of SOPs that has been discussed in Chapter 4, a B2B-VSC-based SOP is installed to connect *Feeder 1* and *Feeder 2* at the endpoints via two 0.69/11kV coupling transformers. The single-line diagram of the whole system is shown in Figure 5.12 and associated parameters are listed in Table 5-3.

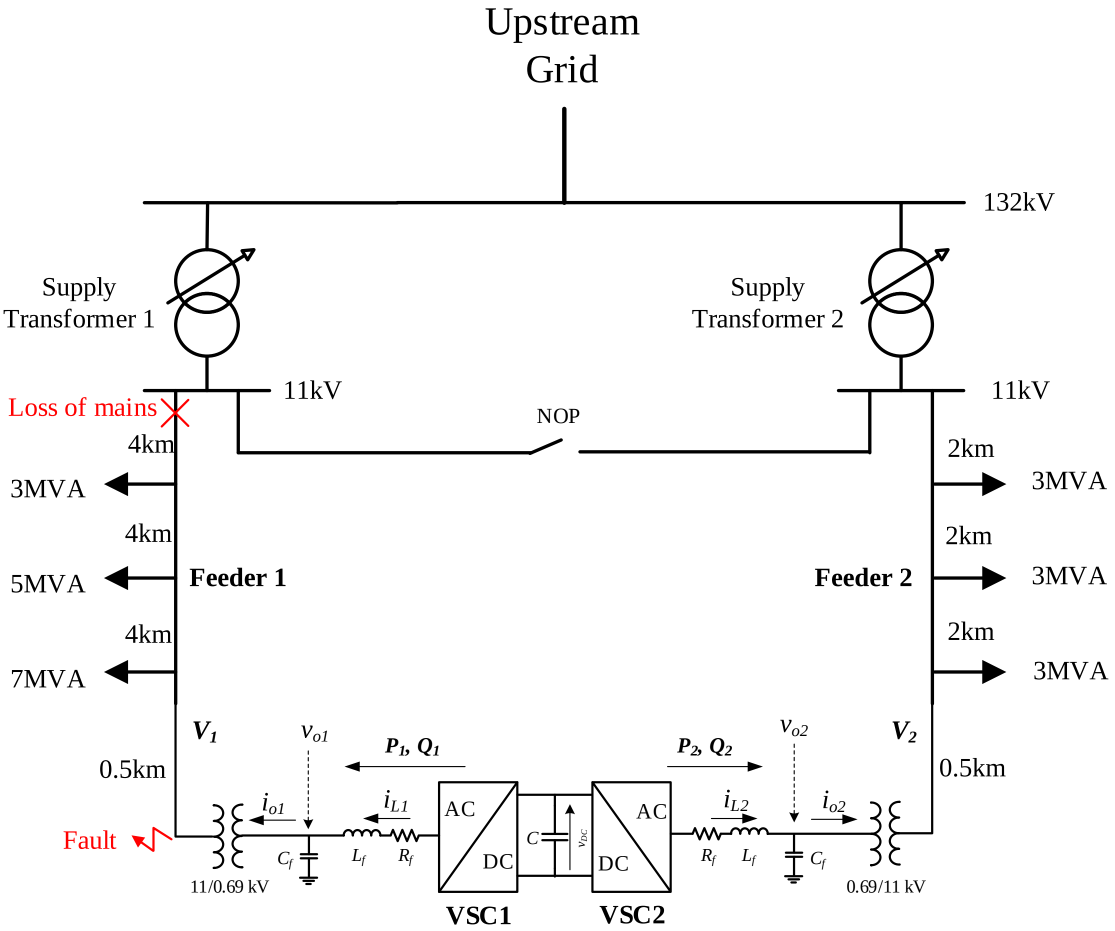

Figure 5.12 Single-line diagram of studied network

Table 5-3 System parameters

Parameters	Description	Values
L_{line}	Network line/cable inductance	0.134mH/km
R_{line}	Network line/cable resistance	0.06Ω/km
PF	Load power factor	0.98
L_f	Filter inductance	0.05mH
R_f	Resistance of filter inductor	0.31mΩ
C_f	Filter capacitance	2mF
C	DC link capacitance	10mF
V_{DC}	Nominal DC link voltage	1300V
f_s	PWM sampling frequency/switching frequency	4950Hz
K_{P_PLL}	Phase-locked loop controller proportional gain	1.42
K_{I_PLL}	Phase-locked loop controller integral gain	328.36
K_{P_C}	Current controller proportional gain	0.25
K_{I_C}	Current controller integral gain	1.57
K_{P_DC}	DC link voltage controller proportional gain	5
K_{I_DC}	DC link voltage controller integral gain	1445.3
K_{P_V}	Output voltage controller proportional gain	2
K_{I_V}	Output voltage controller integral gain	578.1

As introduced in the beginning of this chapter. The B2B-VSC must satisfy the following three functionalities: independent active and reactive power control, fault current restriction and stand-alone load supply in island mode. Therefore, simulations for the three cases will be carried out to verify the controller design and the idea of implementing a B2B-VSC as the SOP.

5.2.1 Power Control and Voltage Compensation

As discussed in Chapter 4, the voltage at the endpoint of *Feeder 1* (*V1)* can be effectively compensated by balancing the load at the two feeders. The active power reference for the SOP should be selected to ensure that the active power supplied by the two supply transformers to be close in all load conditions. In practice, load changes gradually and thus power dispatch is carried out every half or one hour. Similarly, the power reference of the SOP can be updated at the same period. Dynamic adjustments can also be implemented but will not be discussed in this thesis. A scenario sequence is made as listed in Table 5-4 to test the performance of the B2B-VSC. The measured *V1* and *V2* in per unit are also listed.

Table 5-4 Events in voltage compensation simulation

	0.2s~0.4s	0.4s~0.6s	0.6s~0.8s	0.8s~1.0s	1.0s~1.2s
Load at Feeder 1 (MVA)	10	10	15	15	15
Load at Feeder 2 (MVA)	1	1	1	1	1
$P1^*$ (MW)	0	5	5	7.5	7.5
$Q1^*$ (MVar)	0	0	0	0	2
Measured *V1* (p.u.)	0.9340	0.9652	0.9396	0.9545	0.9693
Measured *V2* (p.u.)	0.9985	0.9816	0.9822	0.9730	0.9725

Feeder 1 is the heavily-loaded feeder while *Feeder 2* is lightly-loaded and considered always having 1MVA load connected in the simulation period. In the initial stage, the 10MVA load is supplied by *Feeder 1* and the voltage at the endpoint (V_1) is 0.934p.u. which is below the lower limit, 0.94p.u., as shown in Figure 5.14. Then, at t=0.4s, the B2B-VSC is controlled to transfer the active power of 5MW from *Feeder 2* to *Feeder 1* as shown in Figure 5.13. As for the symmetric design of the controller, the direction from the B2B-VSC to the network is defined as positive for both VSC_1 and VSC_2. Therefore, the negative power shown in Figure 5.13 (b) means that the power is flowing from the network to the B2B-VSC. According the law of reservation of energy, P_1 should always be approximately equal to $-P_2$ (not exactly the same due to the power loss). Because of the active power compensation, V_1 rises to 0.9652p.u. which has come back to the permitted range.

Meanwhile, due to increased power experienced by *Feeder 2*, the voltage at the endpoint of *Feeder 2* (V_2) drops to 0.9816p.u. from 0.9985p.u. but is still within the limits as shown in Figure 5.14. At t=0.6s, a step change of the load at *Feeder 1* from 10MVA to 15MVA occurs which results in the voltage V_1 dropping to 0.9396 which is again below the lower limit. In response to the voltage drop due to increase of active power demand, from t=0.8s, the active power transferred by the B2B-VSC is controlled to be increased to 7.5MW as shown in Figure 5.13. V_1 accordingly rises to 0.9545p.u. and V_2 drops to 0.973p.u. as shown in Figure 5.14. Finally, at t=0.8s, reactive power of 2MVar is compensated by the B2B-VSC in order to further improve the voltage profile. Consequently, the voltage V_1 is further increased from 0.9545p.u. to 0.9693p.u. thanks to the additional reactive power compensation.

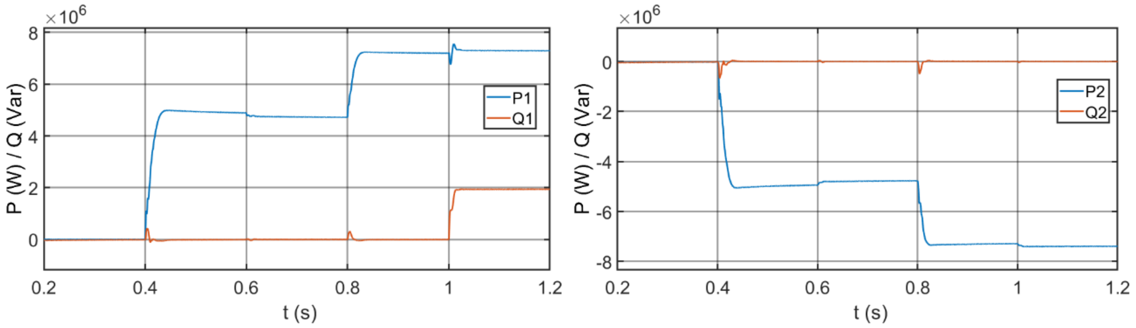

(a) (b)

Figure 5.13 (a) Output power of VSC1; (b) Output power of VSC2.

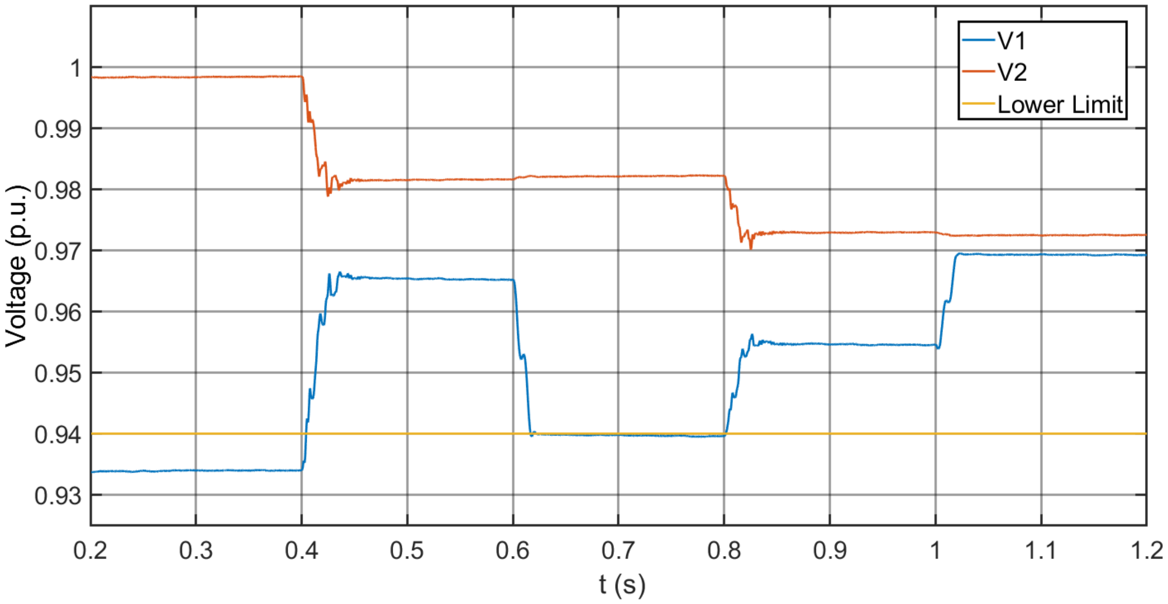

Figure 5.14 Phase voltage at endpoints of Feeder 1 and Feeder 2 in per unit.

The DC link voltage response during this period is shown in Figure 5.15. Two voltage drops at t=0.4s and t=0.8s are observed which are due to sudden increase of active power demand. The voltage always recovers to the nominal value which is 1300V in a sufficient speed and no overshoot occurs.

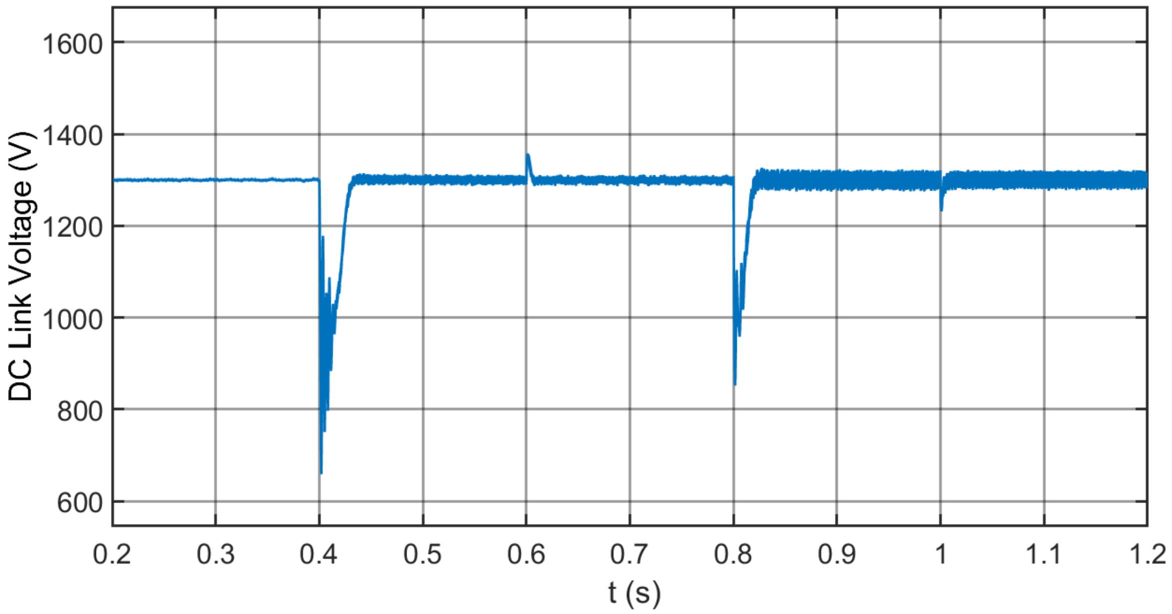

Figure 5.15 DC link voltage

The output three-phase voltages and currents of VSC_1, i.e. v_{o1} and i_{o1}, between the times of 0.76s and 0.9s are shown in Figure 5.16. At t=0.8s, the active power is increased from 5MW to 7.5MW which leads to the increase of the current. There is almost no influence on the voltage. The transient in the current is smooth (no overshoot) and distortions disappear after 2 cycles. The total harmonic distortion (THD) of the voltages and currents are 2.28% and 0.60%, respectively.

The simulation results have validated the controller designs of the PLL loop, current control loop and DC link voltage loop. The responses to the defined step changes are fast and without overshoot. The functionality of voltage compensation by the B2B-VSC has also been verified. The voltage can be regulated within the permitted range in the worst condition and independent reactive power compensation is an optional functionality for further improvement on the voltage profile.

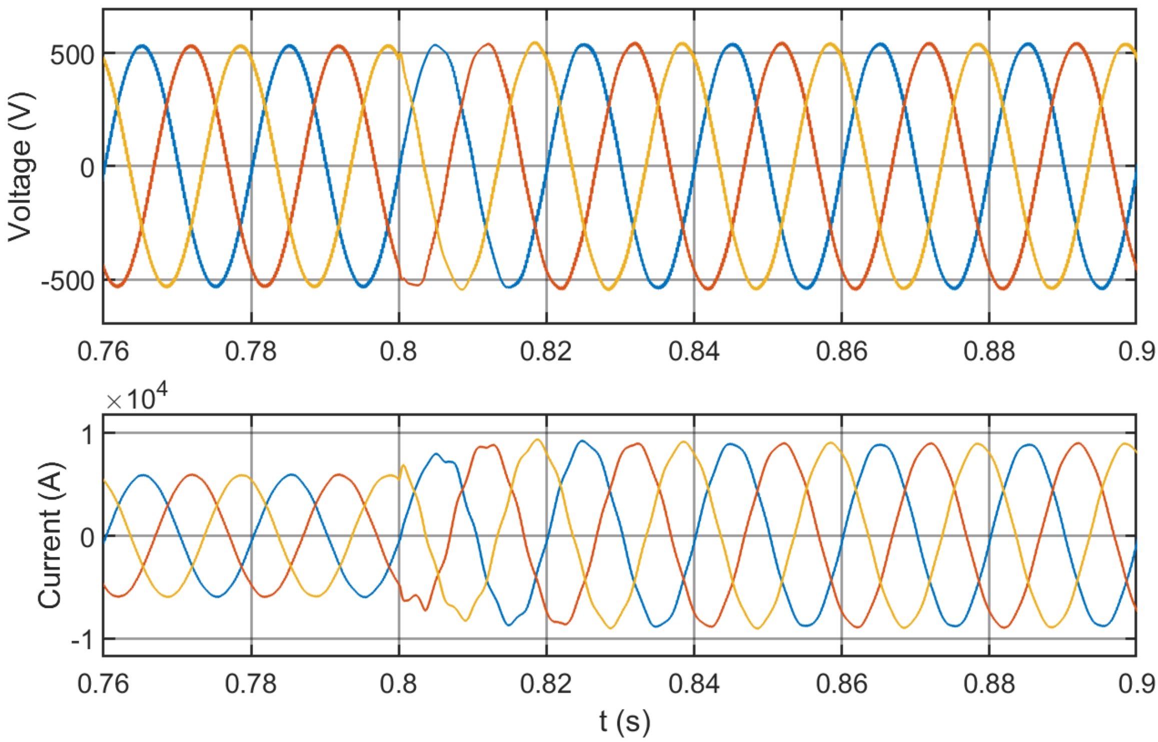

Figure 5.16 Output voltage and current of VSC1

5.2.2 Fault Current Restriction

One of the most important advantages of B2B-VSCs compared to other types of SOP is the capability of restricting fault current. Once a fault occurs in the network, current tends to increase dramatically. However, the current control loop in the B2B-VSC can lock the current to the reference value no matter how the outside circuit would be.

A three-phase-to-ground fault at the endpoint of *Feeder 1* is simulated to occur at *t*=0.2s. The B2B-VSC is assumed to be transferring 5MW active power from Feeder 2 to *Feeder 1* before the fault. The output three-phase voltage and inductor current of both converters of the B2B-VSC around the fault moment are shown in Figure 5.17. When the fault happens at *t*=0.2s, the output phase voltage of VSC_1, v_{o1} drops to zero immediately as a matter of course, but the current is limited at the previous reference value thanks to the current control loop as shown in Figure 5.17 (a). On the other hand, the voltage and current of VSC_2 during fault are shown in Figure 5.17 (b). Because there is no demand on active power on VSC_1 once the fault has occurred, the DC link does not drain active power from VSC_2 afterwards. Consequently, the inductor current of VSC_2 drops to a value close to zero which only supplies a small power that dissipated in the device. The voltages of VSC_2 is almost undisturbed during the whole period. Therefore, the fault is demonstrated to be automatically isolated from the rest of the network by the B2B-VSC.

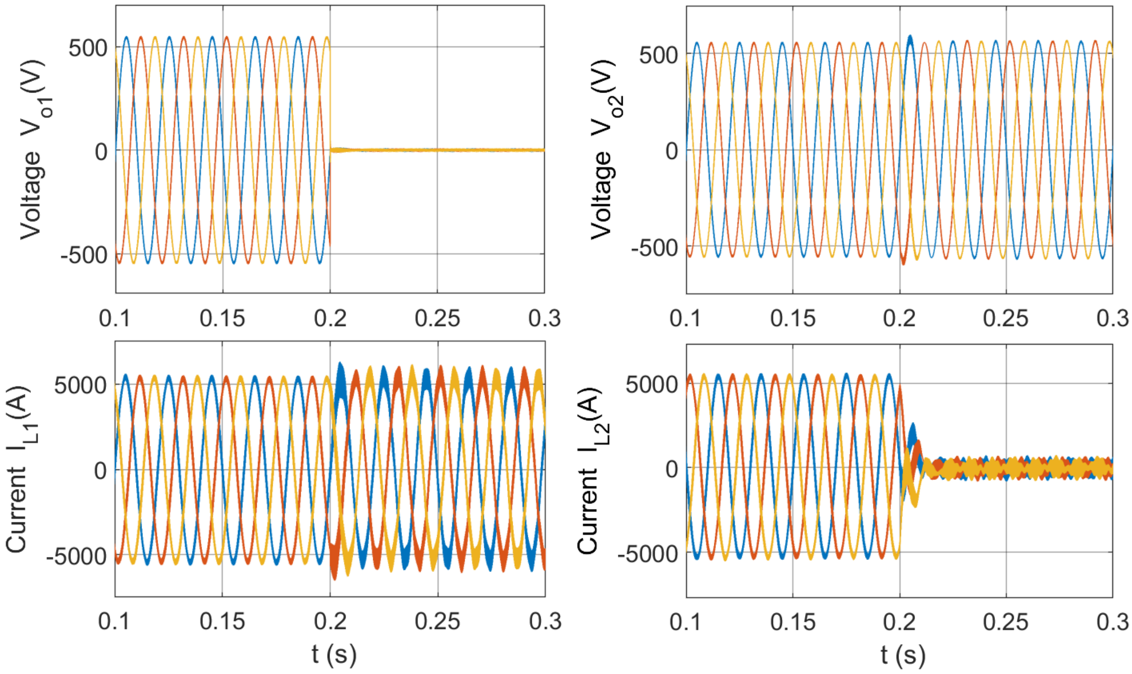

(a) (b)

Figure 5.17 (a) Three-phase output voltages and inductor currents of VSC1 during fault; (b) Three-phase output voltages and inductor currents of VSC2 during fault.

The current at the fault point is shown in Figure 5.18 compared to the condition that the B2B-VSC is a normally-closed point. If the connection of the two feeder endpoints is only power line/cable, the fault current will be more than doubled than that with B2B-VSC connection. This increased fault current could break the duty of circuit breakers and cause serious consequences.

The B2B-VSC's capability of restricting fault current has been verified in this section. The fault point can be automatically blocked, and the fault level increase is limited which is important to the network safety.

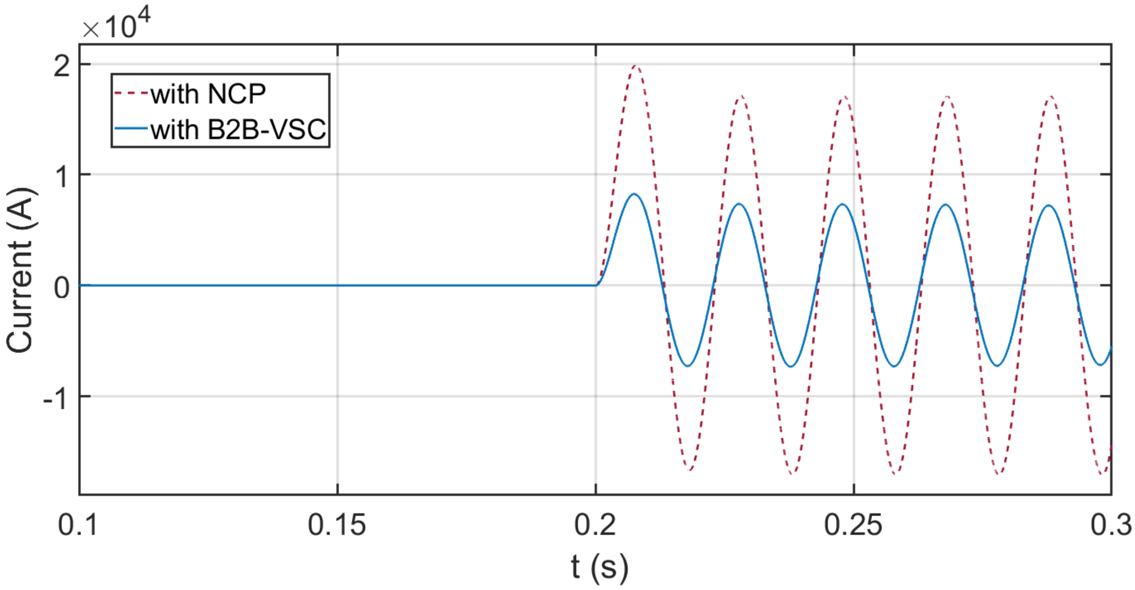

Figure 5.18 Phase-a current at the fault point with B2B-VSC and NCP

5.2.3 Loss of Mains

A loss of mains event is simulated by opening the circuit breaker at *Supply Transformer 1*. The worst case is considered: loading level at *Feeder 1* is at the maximum while the loss of mains occurs. As the power rating of B2B-VSC is designed as 8MVA with 100% current margin. To support 8MVA load with 0.98 power factor, the corresponding i_d and i_q will be 9283.6A and 1885.1A at 690V voltage level. However, due to the variation of power factor and power loss in the device and line/cable, more current should be required. Therefore, saturation values of 10000A for i_d and 3000A for i_q are selected which leads to a maximum allowed current of 10440A. The events during the simulation is listed in Table 5-5.

The three-phase output voltages and currents of VSC_1 during the loss of mains transient are shown in Figure 5.19. At t=0.2s, the loss of mains occurs which results in an immediate voltage drop and frequency drifting away from the nominal value. If a time of 100ms is required for the detection of loss of mains, then the B2B-VSC will switch to stand-alone voltage supply mode at t=0.3s, i.e. the output voltage controller kicks in to provide current reference for the current controller and the PLL controller now provides a constant 50×2π (rad/s) angular velocity instead of referring to grid frequency.

However, the power demand by the load at this moment is way large than the rating of the B2B-VSC. To supply 15MVA load, the current amplitude will be about 18000A at 690 voltage level which is significantly higher than the saturation value, 10440A. As a result, the output current amplitude is limited under 10440A thanks to the inner current control loop, and the voltage is then determined by Ohm's Law. As the voltage is much lower than the nominal value, relays in the network should start to trigger in a sequence determined by the time delay settings. In this simulation, at t=0.4, 5MVA load is cut out and at t=0.5s, another 3MVA is cut out. Now there is 7MVA load remaining which is within the rating of the B2B-VSC. Therefore, the output voltage controller is able to control the voltage at the reference value. In real condition, the relay should work in a smoother way, i.e. load is cut out by small steps and may take longer time until the voltage recovers.

Finally, after a short period of small oscillation, the voltage is controlled to be stabilized at the nominal value. The amplitude in per unit of the voltages at each feeder endpoints, V_1 and V_2 during this period are show in Figure 5.20. As can be seen, the voltage at the endpoint of *Feeder 2* is almost unaffected.

Table 5-5 Events in loss of mains simulation

	0.1s~0.2s	0.2s~0.3s	0.3s~0.4s	0.4s~0.5s	0.5s~0.8s
Connection to *Supply Transformer 1*	Y	N	N	N	N
Load at Feeder 1 (MVA)	15	15	10	7	6.3
Load at Feeder 2 (MVA)	1	1	1	1	1
$P1^*$ (MW)	5	5	NA	NA	NA
$Q1^*$ (MVar)	2	2	NA	NA	NA
Measured $V1$ (p.u.)	0.9541	0.5550	0.5271	0.7355	0.9960
Measured $V2$ (p.u.)	0.9815	0.9925	0.9826	0.9763	0.9742

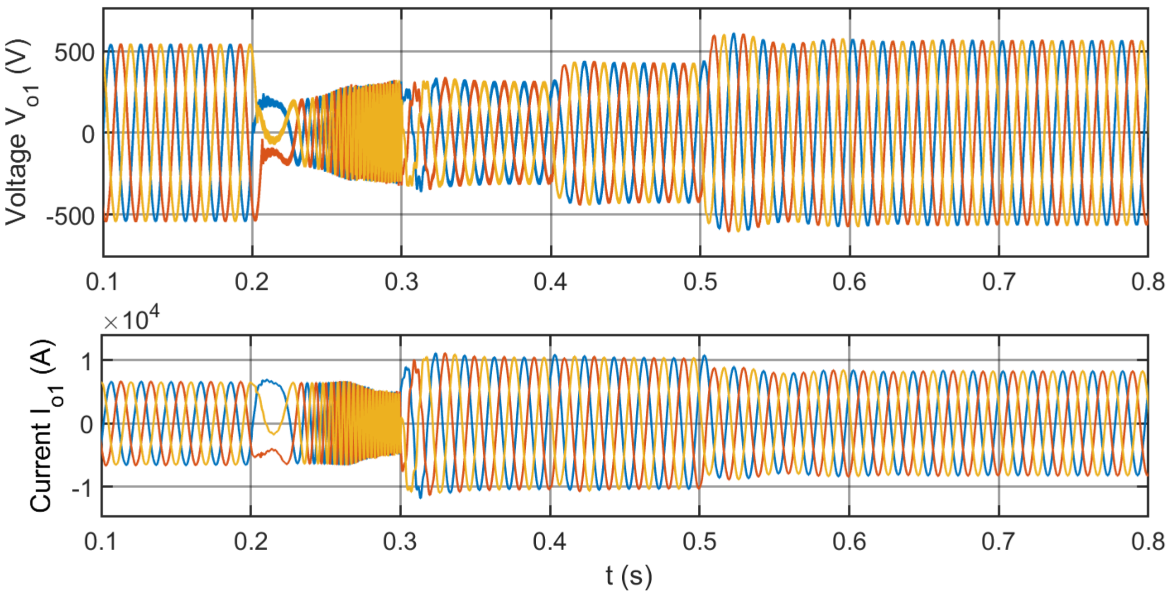

Figure 5.19 Three-phase voltages and currents during loss of mains.

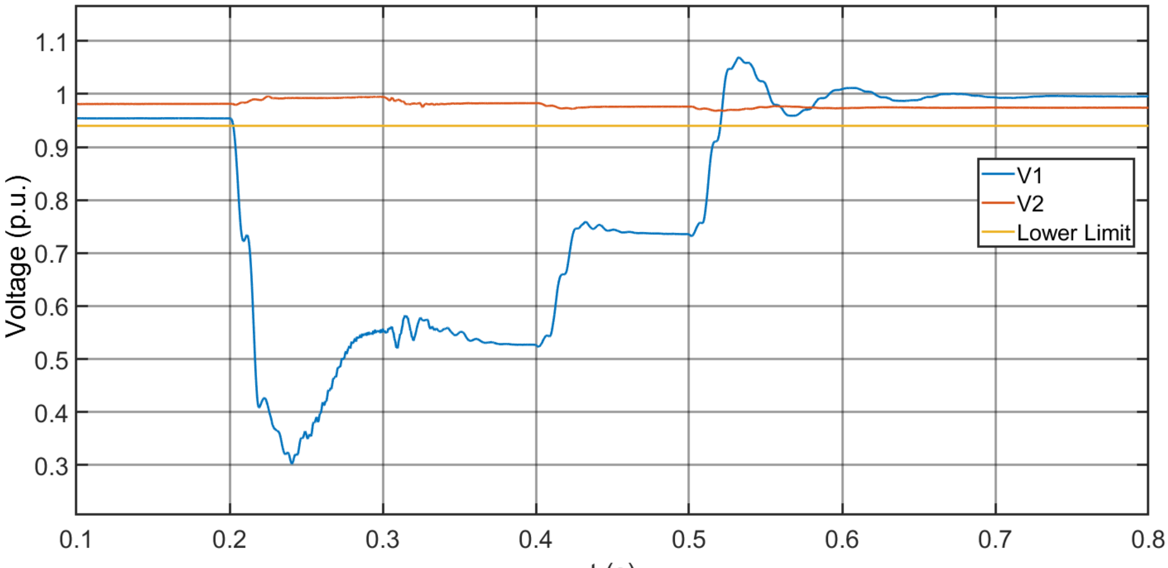

Figure 5.20 Amplitude in per unit of endpoints voltages *V1* and *V2*.

It is worth mentioning that a trick has been applied to achieve the smooth transient: regular reset of the integrator in output voltage controller when the controller's output is beyond the current saturation. If the reset was not applied, a much longer transient would be required for the voltage to be finally stabilized as shown in Figure 5.21. From the time that the output voltage loop is switched in, it takes about 1.8 seconds for the voltage to be stabilized and the transient is rough. Note that it takes only 0.4 seconds to stabilize for a smooth transient if the reset was applied.

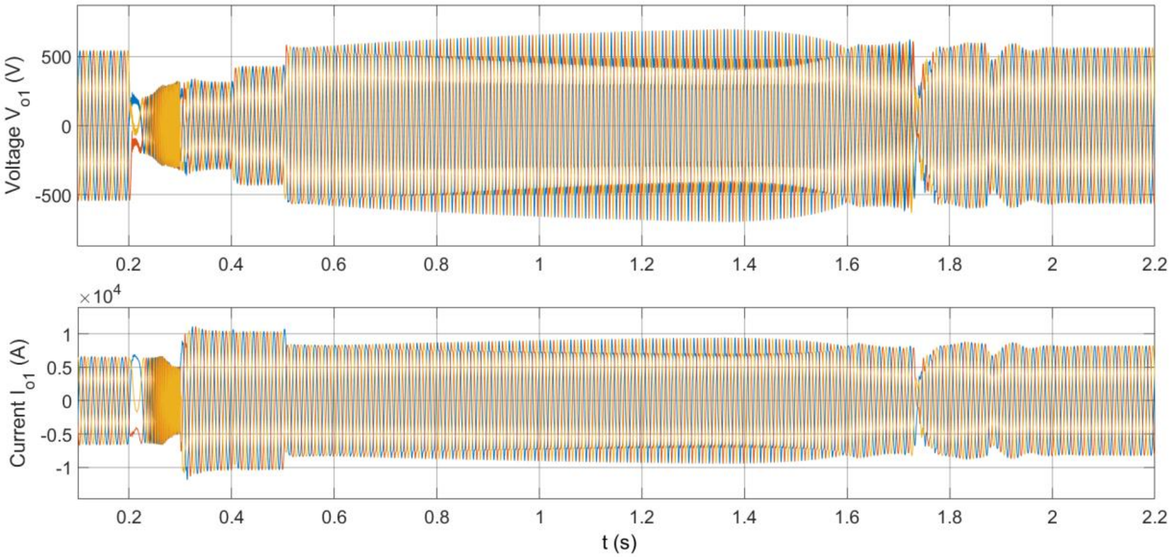

Figure 5.21 Three-phase voltages and currents during loss of mains without reset in the output voltage controller.

The reason will be explained in the following. In the beginning stage when the output voltage controller kicks in, the load demand is larger than the B2B-VSC's rating, and the output voltage is limited due to that the output current is clamped by the inner current control loop. The error between the output voltage reference and the feedback measured output voltage is significant and further enlarged by the controller integrator. As a result, the output voltage controller's output, i.e. the inductor current reference, will keep increasing to a very high value until the output voltage amplitude recovers after excessive load demand is cut off. Once the excessive load demand has been cut off, the output voltage rises to a value slightly larger than the reference. Then, a negative error is generated and gradually eliminate the integrated positive error in the beginning stage. Finally, it takes a long and rough transient for the integrated error to be eventually eliminated and for the voltage to stabilize.

At last of this section, the voltage and current responses to a load change in the island mode are shown in Figure 5.22. At *t*=1s, 10% of the remaining load, i.e. 0.7MVA, is cut off.

The current drops by about 10% and the voltage remains unchanged. The transient is very smooth which verifies the sufficient performance of the output voltage controller.

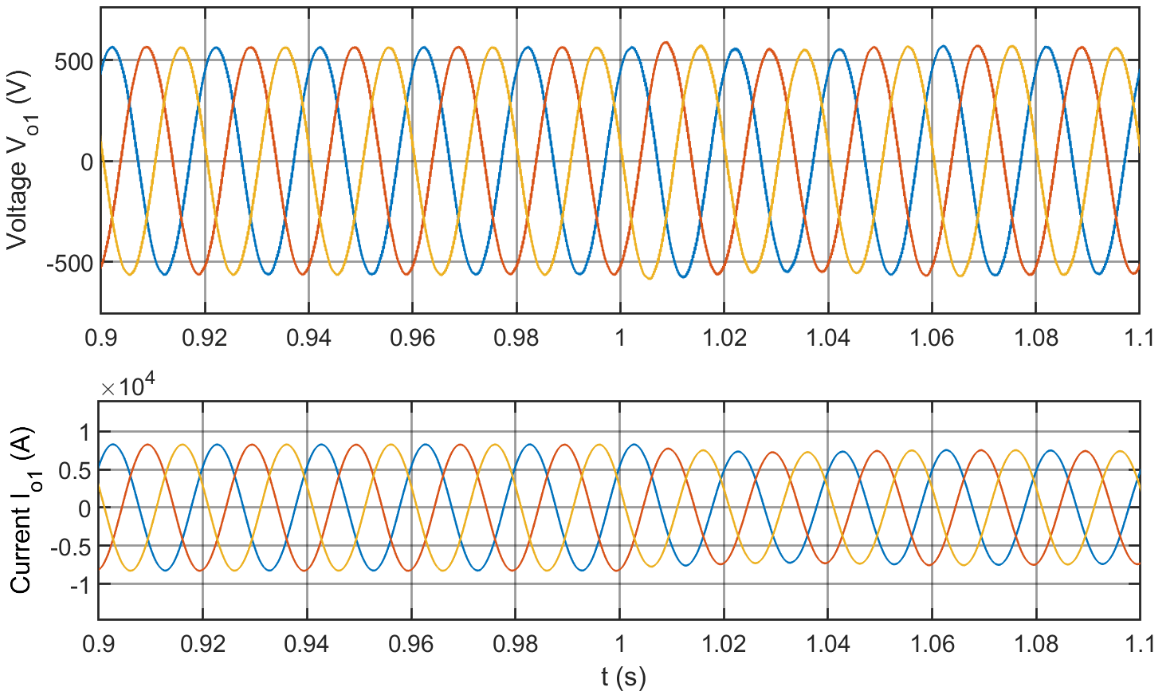

Figure 5.22 Voltage and current responses during a load change.

5.3 Experiment Results

Due to the restriction of experimental conditions, a scale-down experiment has been carried out. The voltage is scaled down to 50V (amplitude of phase voltage). A grid emulator is used to provide 50V three-phase voltage (amplitude of phase voltage) and act as the mains. A resistive load bank is used as the load. Assuming the DC link is always well maintained by one of the VSC, a DC power supply is used in the experiment. Therefore, only the PLL controller, output voltage controller and current controller are implemented in the experiment. The controller is implemented using dSpace platform which can compile the code generated in Matlab/Simulink. The measured results can be also conveniently saved in the computer via dSpace PC tool. The experiment circuit and facilities are shown in Figure

5.23 (a) and (b), respectively. The sampling rates is 20 kHz. Parameters in the experiment are shown in Table 5-6. Simulation using the same parameters is also carried out for comparison.

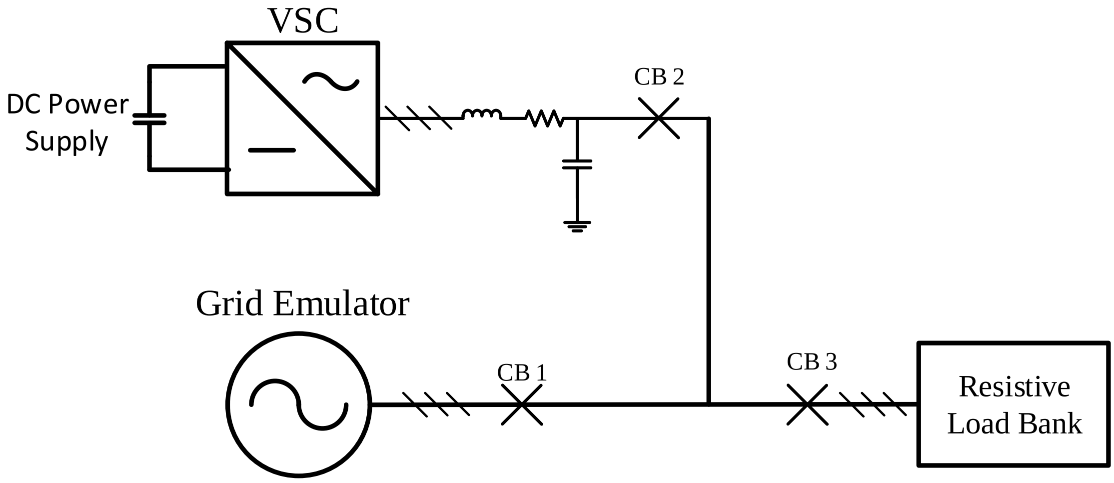

(a)

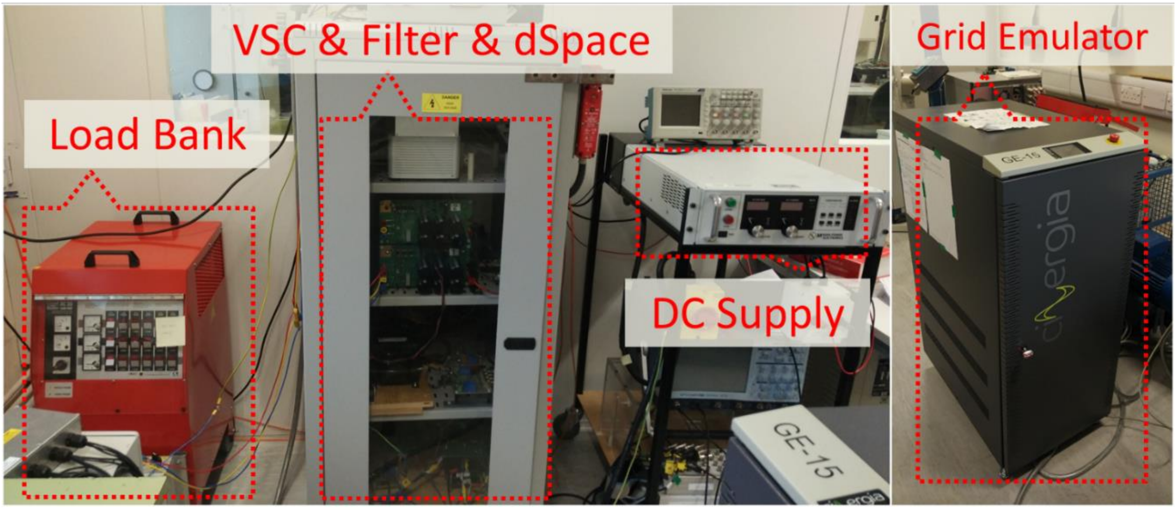

Figure 5.23 Experiment Setup: (a) Experiment circuit; (b) Experiment facilities.

Table 5-6 Parameters in experiment

Parameters	Description	Values
PF	Load power factor	1
L_f	Filter inductance	10mH
R_f	Resistance of filter inductor	0.08Ω
C_f	Filter capacitance	15μF
V_{DC}	Nominal DC link voltage	111V
f_s	PWM sampling frequency/switching frequency	4950Hz
K_{P_C}	Current controller proportional gain	5
K_{I_C}	Current controller integral gain	40
K_{P_V}	Output voltage controller proportional gain	0.1
K_{I_V}	Output voltage controller integral gain	0.082

Figure 5.24 shows the three-phase voltage and current at the load during the transition of the loss of mains including load fluctuation afterwards. Before the loss of mains occurs, the AC source and the VSC supply the equal power to the load. When the connection to the mains is lost, i.e. circuit breaker *CB1* is open, the voltage and frequency are both decreasing. After 60ms, the voltage controller initiates to drive the voltage amplitude as well as the frequency back to rated values immediately. Load fluctuation is applied afterwards to test the performance of the output voltage controller. The result shows that, in island mode, the voltage is very stable and current changes corresponding to the load change according to Ohm's law.

To have a closer look at the loss of mains transient, detailed view in SRF during the loss of mains transient is shown in Figure 5.25. The voltage at q axis, v_q is locked to zero by the PLL. The load is purely resistive so that no reactive power should be generated, i.e. i_q is zero. The voltage and current in d axis, v_{od} and i_{oq} respond as described in the last paragraph. In general, the simulation and experiment results are matched well, and the transition is also smooth.

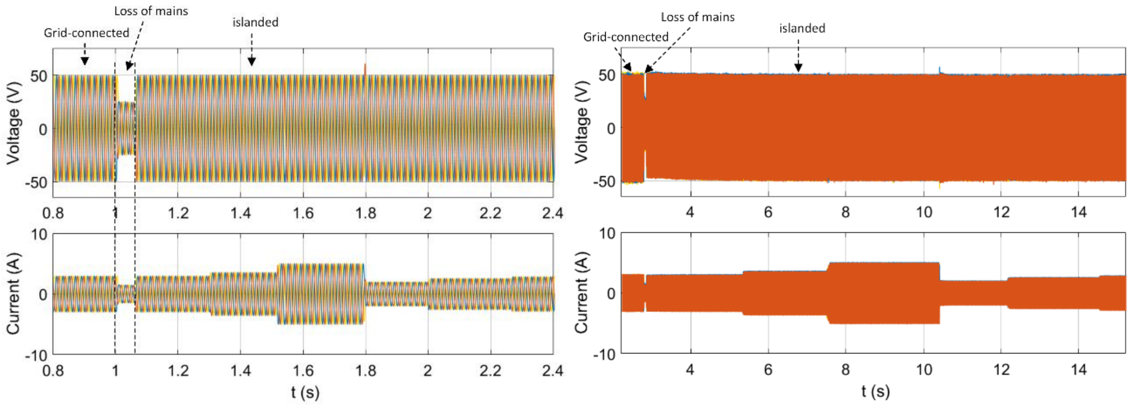

(a) (b)

Figure 5.24 Three-phase voltages and currents at the load (a) Simulation result; (b) Experiment result.

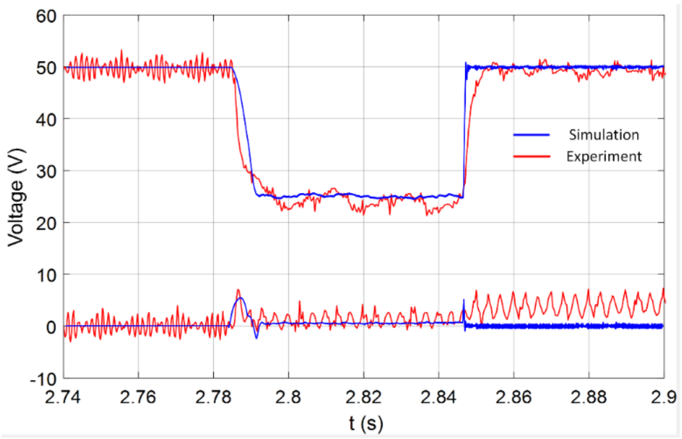

(a) Voltage

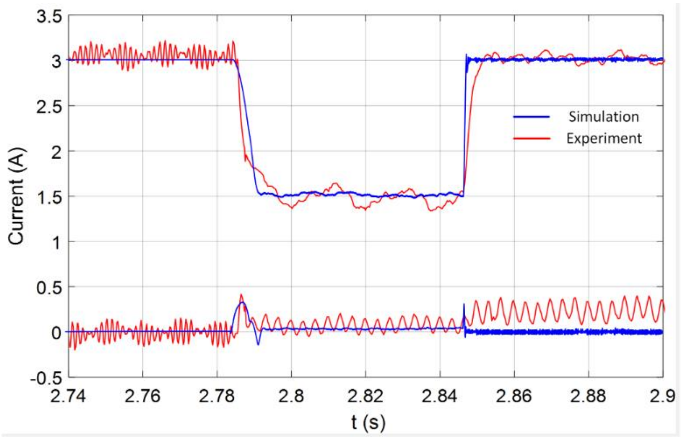

(b) Current

Figure 5.25 Voltage and current in SRF during the loss of mains for the comparison between experiment and simulation results.

A zoom-in view of the output three-phase voltage and current in island mode is shown in Figure 5.26. The THDs in the voltages and currents are 3.01% and 2.70%, respectively.

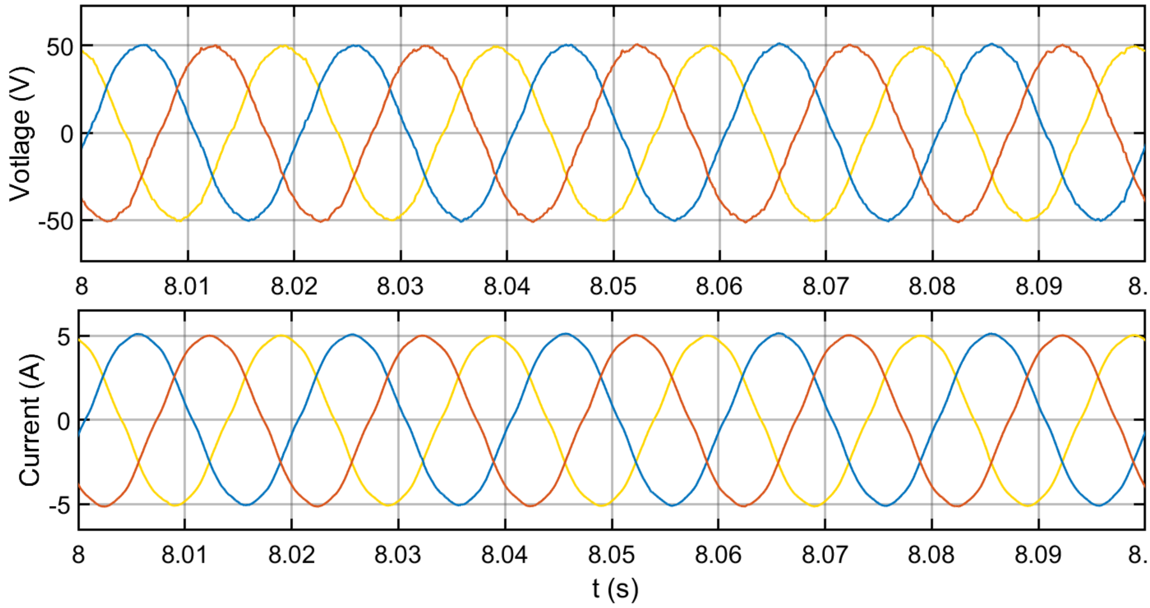

Figure 5.26 Output voltage and current of the VSC.

5.4 Summary

In this chapter, the details on controller designs for a B2B-VSC type SOP have been discussed. The whole control system is symmetric and each VSC has a PLL controller, a current controller, a DC link controller and an output voltage controller. The PLL controller and current controller are always applied in all condition; the DC link voltage controller and output voltage controller are connected depending on situations to provide reference for current controller. The modelling and gain selections for all sub controllers have been included. Then, all controller designs have been validated by simulation and experiment except that the DC link voltage controller has not been implemented in experiment.

The functionality of independent active and reactive power control is first tested by simulation. Effective voltage regulation in a defined heavily-loaded distribution network has been successfully applied thanks to the controlled active and reactive power compensation.

Then, the functionality of fault current restriction has been verified by simulation. The controller can automatically restrict the fault current thus the fault level in the network is almost unchanged. The other side of the B2B-VSC to the fault point remains undisturbed which shows that the fault is automatically isolated by the B2B-VSC. The situation in loss of mains is more complicated than the previous two scenarios. The worst loss of mains case has been simulated, i.e. the mains is lost at the maximum loading level. An important technique of resetting output voltage controller's integrator is proposed to achieve smooth islanding transition. Then, load changes in island mode is applied and the results verifies that the B2B-VSC can provide reliable voltage supply to the load alone.

The scale-down experiment has been carried out to verify the designs of PLL controller, current controller and output voltage controller. Simulation using the experiment's parameter setup is also carried out and showed very similar response to the experiment result. This validates the controller modelling and the analyses on parameters selection.

However, there are drawbacks needs to be mentioned. In the loss of mains event, firstly, the output voltage loop needs to be switched in and a signal switching in PLL controller is also required. And if the loss of mains occurred at the side which the connected VSC is in charge of supporting DC link voltage, more switching actions are required, i.e. at the side where the loss of mains occurs, the DC link voltage controller needs to be switched out and the output voltage controller needs to be switched in; at the other side, the DC link voltage controller needs to be switched in. These requirements on signal switches increase the computational burden and reduce the reliability of the whole system as mis-operation of the selection switch could happen. Another drawback is that during the loss of mains as Figure 5.19 shows, the voltage and current frequency drop to zero hertz within one cycle (20ms) and continue decreasing as a negative value until the controller reacts. This is because the grid voltage which the PLL relies on is lost due to the loss of mains. The massive change on frequency in such a short time could lead all the frequency sensitive relays in the network to trigger instantly.

In the next chapter, a controller that requires less detections and switching actions will be developed. Furthermore, the frequency decrease during the loss of mains can be mitigated to reduce the loss from unnecessary load-shedding.

6.Controller Design of B2B-Synchronverter

When a voltage source converter (VSC) is controlled to mimic a synchronous machine, this converter and associated controller together are called a synchronverter which was first proposed in [94]. Compared to a synchronous machine, the synchronverter has the same dynamic equations; but it exchanges power with the DC link instead of exchanging power with the prime mover. An advantage of synchronverter is that the parameters such as inertia and friction coefficient, which are determined and limited by physical condition in a real synchronous machine, can be selected freely according to requirements. Another advantage is that the synchronverter can be shut down instantly, which is impossible for a synchronous machine, by blocking all the switching units. The integration of renewable energies via inverters as distributed generations (DGs) is an inevitable trend in the development of modern electric power system. For current situation, the management of all these DGs does not have a united pattern, and the power injected into the grid by DGs is solely according to the generation plan of each DG operator individually. The random power fluctuation caused by the irresponsible generation from DG is compensated by the conventional central generation units. However, when the renewable energy becomes the dominant power source in a network, such irresponsible generation pattern will not be tolerated. Therefore, the original motivation of synchronverter is to propose a method which uses the well-established theory of synchronous generators to fulfil energy management in a distribution network or a microgrid in which inverter-based power sources are the majority.

Since the concept of synchronverter was proposed, it has gained increasing attentions from academics. A self-synchronized synchronverter has been proposed which can synchronize with the grid without the need of a dedicated synchronization unit which improves the feasibility [95]. A research has implemented synchronverters to HVDC transmission making one of the synchronverter as a synchronous generator while the other one as a synchronous machine and achieved better dynamic performance and stability margin [96]. A synchronverter-dominant microgrid has been presented by simulation and results showed that this microgrid can be properly designed to meet the radiality requirement of the power system [97]. An idea of integrating more renewable energy and providing remote islands with proper power supply based on improved synchronverters has been proposed, and the improvement has been verified by comparing with the original design [98]. A restraining method to protect the synchronverter from inrush fault current has been proposed which is to switch the synchronverter to hysteresis mode and make it stay connected to the grid when the fault is detected [99]. Control strategies to make a rectifier as a synchronverter have been developed for different applications and verified by simulation results [100]. Three modifications have been made to the original synchronverter design to have virtual inductors, virtual capacitors and anti-windup thus achieving better stability [101]. An improved synchronverter has been developed by including the synchronous machines' transient parameters which makes the synchronverter behave similarly to a real synchronous machine in all circumstances [102].

In this thesis, the focus will be using the synchronverter idea on the application of an SOP. In the SOP case, a synchronverter could be especially useful for sudden islanding as a synchronous machine is inherently capable of providing three-phase voltage supply alone. In Chapter 5, a PI-based controller for B2B-VSC has been developed and validated by simulation and experiment. However, it relies on fast and accurate situation detections and signal switches to make the controller work properly. Delay or miss-operation of detections could result in fault of the B2B-VSC. In this chapter, a controller less relying on detections for the B2B-VSC based on the synchronverter idea will be developed. Modifications to the original design will be proposed to adapt the controller to the application.

The original synchronverter controller will be firstly introduced and followed by the modifications. The performance of B2B-Synchronverter in the aspects of voltage regulation, independent load supply and fault current restriction will then be evaluated by simulations. At last, the experiment result will be shown to validate most part of the controller design.

6.1 Synchronverter Controller

Synchronverter is a VSC that is controlled to behave similarly to a synchronous machine to regulate its output voltage (emf), frequency and power angle. Therefore, firstly a simplified model of a synchronous machine is illustrated as shown in Figure 6.1. The following model of a synchronous machine is under the assumption that the machine is working in the steady state and the three phases are perfectly balanced.

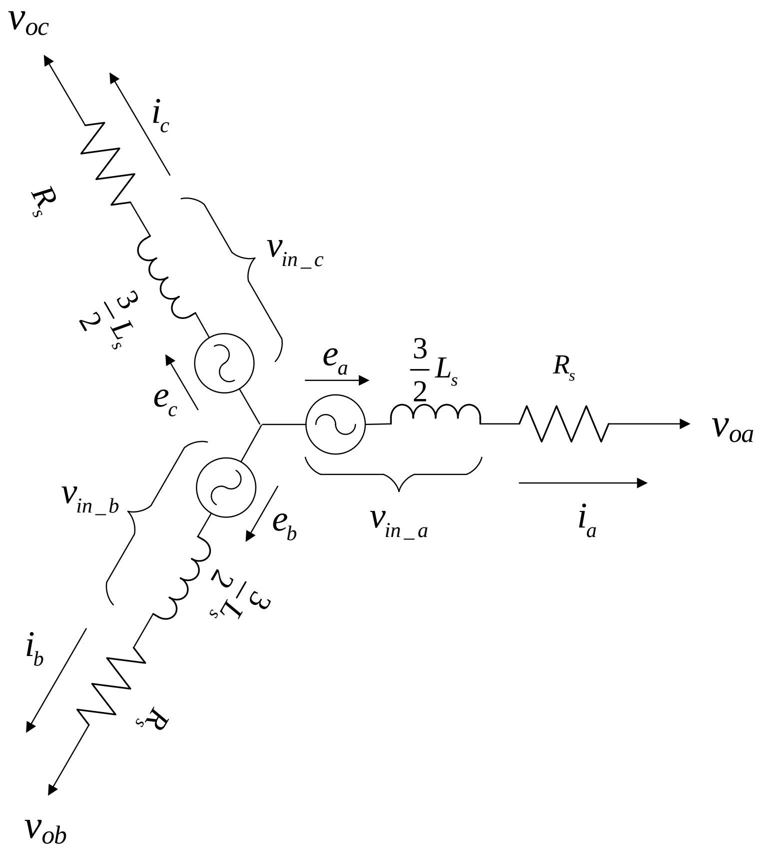

Figure 6.1 Simplified synchronous generator model

Then, the output voltage of the synchronous generator is given as:

$$v_{oabc} = v_{in\_abc} - i_{abc} \cdot R_s \tag{6.1}$$

where $v_{oabc} = [v_{oa}, v_{ob}, v_{oc}]^T$ represents the output three-phase phase-to-neutral voltages at the output, $i_{abc} = [i_a, i_b, i_c]^T$ represents the three-phase currents in corresponding phases, R_s is the stator resistor and $v_{in\_abc} = [v_{in\_a}, v_{in\_b}, v_{in\_c}]^T$ represents the induced voltages for phases a, b and c, $e_{abc} = [e_a, e_b, e_c]^T$ are the voltage induced by the rotor current.

The voltage v_{in_abc} are determined by the flux linkages $\lambda_{abc} = [\lambda_a, \lambda_b, \lambda_c]^T$ which are calculated as

$$\begin{bmatrix} \lambda_a \\ \lambda_b \\ \lambda_c \end{bmatrix} = \begin{bmatrix} L_s & -M & -M & M_{ar} \\ -M & L_s & -M & M_{br} \\ -M & -M & L_s & M_{cr} \end{bmatrix} \begin{bmatrix} i_a \\ i_b \\ i_c \\ i_r \end{bmatrix} \tag{6.2}$$

where L_s is the self-inductance of the stator windings (ignoring the leakage); M is the mutual inductance between two stator phase windings across the air-gap and a round rotor which is typically equal to $1/2L_s$; M_{ar}, M_{br} and M_{cr} are the mutual inductances between each stator phase and the rotor excitation winding; i_r is the rotor excitation current or field current which is assumed to be constant in the steady state. The stator-rotor mutual inductance changes with the rotor angle θ as

$$\begin{aligned} M_{ar} &= M \cdot \cos(\theta) \\ M_{br} &= M \cdot \cos(\theta - \frac{2\pi}{3}) \; . \\ M_{cr} &= M \cdot \cos(\theta + \frac{2\pi}{3}) \end{aligned} \tag{6.3}$$

Now, by applying $M = 1/2L_s$ and substituting (6.3) into (6.2), the stator flux linkages can be rewritten as

$$\begin{bmatrix} \lambda_a \\ \lambda_b \\ \lambda_c \end{bmatrix} = \begin{bmatrix} \frac{3}{2}L_s & 0 & 0 & M \cdot \cos(\theta) \\ 0 & \frac{3}{2}L_s & 0 & M \cdot \cos(\theta - \frac{2\pi}{3}) \\ 0 & 0 & \frac{3}{2}L_s & M \cdot \cos(\theta + \frac{2\pi}{3}) \end{bmatrix} \cdot \begin{bmatrix} i_a \\ i_b \\ i_c \\ i_r \end{bmatrix} \tag{6.4}$$

where the stator phases are decoupled. Note this is under the assumption that the fundamental components of stator currents are perfectly balanced in steady state operation.

Then the induced stator voltages can be obtained from the differentiation of the stator flux linkages. In the steady state, it is assumed that the rotor current i_r is a constant hence $\frac{\mathrm{d}i_r}{\mathrm{dt}} = 0$. Therefore,

$$v_{in\_abc} = \frac{d\lambda_{abc}}{dt} = -\frac{3}{2}L_s \cdot \frac{di_{abc}}{dt} + \begin{bmatrix} \sin(\theta) & \sin(\theta - \frac{2\pi}{3}) & \sin(\theta + \frac{2\pi}{3}) \end{bmatrix}^T \cdot \omega \cdot M \cdot i_r \quad (6.5)$$

where the latter term takes the form of a balanced three-phase voltage if considering the product of ω, M and i_r as the voltage amplitude. Then, define the latter term in (6.5) as a voltage:

$$e_{abc} = \begin{bmatrix} \sin(\theta) & \sin(\theta - \frac{2\pi}{3}) & \sin(\theta + \frac{2\pi}{3}) \end{bmatrix}^T \cdot \omega \cdot M \cdot i_r \quad (6.6)$$

Now substitute (6.5) and (6.6) into (6.1) to rewrite the output voltages as:

$$v_{oabc} = e_{abc} - \frac{3}{2}L_s \cdot \frac{di_{abc}}{dt} - R_s \cdot i_{abc} \quad (6.7)$$

which takes the same form as equation (5.14). Therefore, if considering $\frac{3}{2}L_s$ and R_s to be the filter inductance and resistance, e_{abc} and v_{oabc} to be the voltage before the filter and the output voltage after the filter, i_{abc} to be the inductor current, equation (6.7) can be seen as representing a VSC output circuit as shown in Figure 6.2. However, in the expression of e_{abc}, the rotor inductance M and rotor current i_r are not existed in the VSC. As a result, the term Mi_r is required to be generated virtually in the controller.

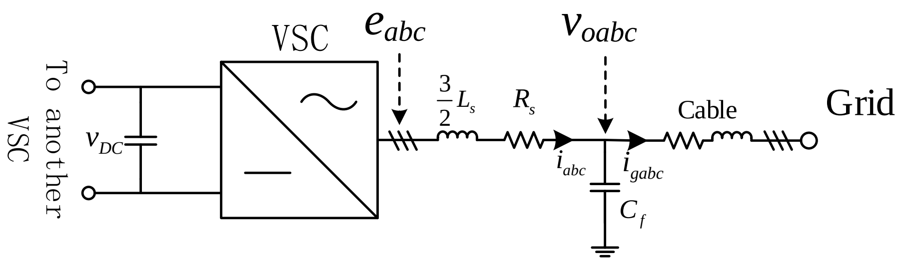

Figure 6.2 A VSC with an LC filter

By making a quick analysis on equation (6.6) it can be found that ω determines the angular velocity of e_{abc}, while ω and Mi_r together determine the amplitude of e_{abc}. Therefore, ω and Mi_r should be the two state variables of the controller. To find an obvious solution for the non-linear equation like (6.6) could be very difficult. Fortunately, the dynamic equations of synchronous machines could be useful to this case. The dynamic equations are shown as following:

$$\frac{d\omega}{dt}=\frac{1}{J}\left(T_m-T_e+D_{p\_t}\left(\omega^*-\omega\right)\right), \tag{6.8}$$

and

$$\frac{dMi_r}{dt}=\frac{1}{K}\left(Q^*-Q+D_q\left(v_m^*-v_m\right)\right) \tag{6.9}$$

where J is the inertia of the rotor (a virtual value in synchronverter), T_m and T_e are the mechanical torque and electromagnetic torque, ω^* is the reference angular velocity and D_{P_t} is the angular velocity damping factor; K is a gain, Q^* and Q are the reference and measured reactive power, v_m^* and v_m are the reference and measured voltage amplitudes, D_q is a droop constant. In a VSC, neither the mechanical torque, T_m nor the electromagnetic torque, T_e exists. But, by the definition of torque, the mechanical power exchanged with the prime mover, P_m and the electromagnetic power absorbed by the rotor, P_e can be found as:

$$P_m = \frac{T_m}{\omega} \text{ and } P_e = \frac{T_e}{\omega}. \tag{6.10}$$

Now, substituting (6.10) into (6.8) and defining $D_P = \omega \cdot D_{P\_t}$, equation (6.8) can be rewritten as:

$$\frac{d\omega}{dt} = \frac{1}{J\omega}\left(P_m - P_e + D_p\left(\omega^* - \omega\right)\right) \tag{6.11}$$

In a synchronverter, P_m is actually the electric power exchanged with the DC link and P_e denotes the output electric power to the AC terminal which can be obtained as:

$$P_e = \left\langle i_{abc} \cdot e_{abc} \right\rangle = \omega \cdot M i_r \cdot \begin{bmatrix} i_a & i_b & i_c \end{bmatrix} \cdot \begin{bmatrix} \sin(\theta) \\ \sin\left(\theta - \frac{2\pi}{3}\right) \\ \sin\left(\theta + \frac{2\pi}{3}\right) \end{bmatrix}. \tag{6.12}$$

Consider an amplitude-invariant *dq0* transformation for balanced three-phase current as:

$$\begin{bmatrix} i_d \\ i_q \end{bmatrix} = \frac{2}{3} \begin{bmatrix} \cos(\theta) & \cos\left(\theta - \frac{2\pi}{3}\right) & \cos\left(\theta + \frac{2\pi}{3}\right) \\ \sin(\theta) & \sin\left(\theta - \frac{2\pi}{3}\right) & \sin\left(\theta + \frac{2\pi}{3}\right) \end{bmatrix} \begin{bmatrix} i_a \\ i_b \\ i_c \end{bmatrix}. \tag{6.13}$$

By combining equations (6.13) and (6.12), P_e can be obtained by a simplified equation as:

$$P_e = \frac{3}{2} \omega \cdot M i_r \cdot i_q. \qquad (6.14).$$

In the practice, the ω in equations (6.11) and (6.14) except for the controller object is replaced by the nominal angular velocity ω_n which is a reasonable simplification. Equation (6.9) and (6.11) together constitute the reactive power–voltage loop (Q-V loop) and the active power-frequency loop (P-ω loop) of the controller as shown in Figure 6.3.

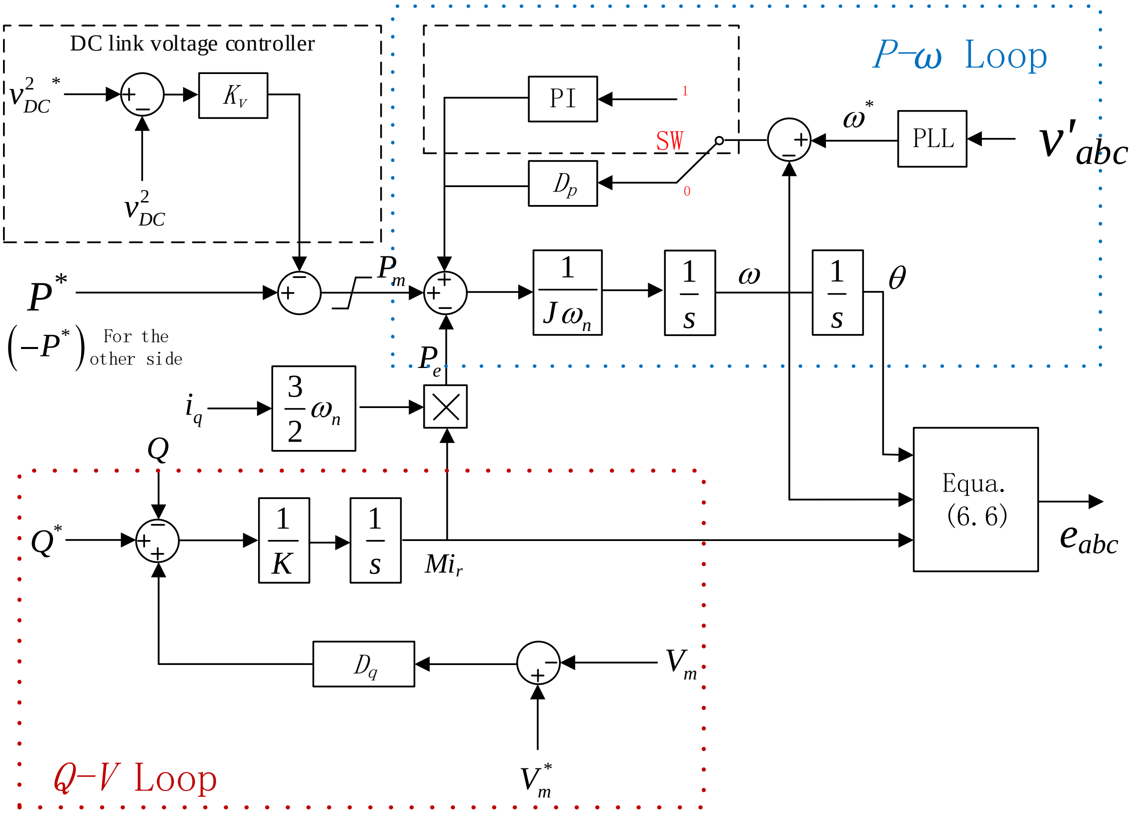

Figure 6.3 Controller for one side of the B2B-synchronverter

As in steady state the generated power P_e should be equal to P_m, P_m therefore can be seen as the active power reference in the original design. The idea about parameters selection is introduced in the following. The droop constant of P-ω loop, D_p reflects the ratio of the active power change to the frequency change and is defined as:

$$D_p = -\frac{\Delta P}{\Delta \omega} \tag{6.15}$$.

It reflects that the synchronverter can help regulate the grid voltage by tuning its output active power. And if the mains is lost, the controller will increase the output power to compensate the frequency drop which is different from the controller in Chapter 5.

Similarly, the droop constant of *Q*-*V* loop, D_q reflects the ratio of the reactive power change to the voltage amplitude change and is defined as

$$D_q = -\frac{\Delta Q}{\Delta V_m} \ . \tag{6.16}$$

The inertia J is a virtual parameter in synchonrverter and is determined as

$$J = D_p \cdot \tau_1 \tag{6.17}$$

where τ_1 is the time constant of *P*-*ω* loop. The τ_1 can be set much smaller in the synchronverter than in a real synchronous machine because it is not subjected to physical conditions. The parameter K in *Q*-*V* loop can be estimated as

$$K \approx \omega_n \cdot D_q \cdot \tau_2 \tag{6.18}$$

where the nominal angular velocity ω_n is used instead of the real time angular velocity ω for simplification and τ_2 is the time constant of *Q*-*V* loop. The *Q*-*V* loop's output Mi_r will be fed into *P*-*ω* loop, so we consider *Q*-*V* loop as the outer loop and *P*-*ω* loop as the inner loop. Therefore, τ_2 is recommended being at least 3~5 times larger than τ_1 to ensure the stability of the whole system.

6.2 B2B-synchronverter controller

Modifications must be made accordingly when applying synchronverter idea to the B2B-VSC type SOP. The three differences between a B2B-synchronver and a synchronverter listed below.

1. A synchronverter is connected to a DC voltage source, but B2B-synchronverter has two VSCs connected by a DC link in between which needs to be supported by the B2B-synchronverter itself.
2. A synchronverter generates power which is related to the grid frequency according to the *P*-*ω* droop control, but B2B-synchronverter is desired to transfer a certain amount of power to balance the load in the meshed network. If the meshed networks are connected to the same substation which means they have the same grid frequency at any given moment. Then, the variation of grid frequency will result in the change of the power being transferred by B2B-synchronter which is not desired.
3. As just mentioned, a synchronverter generates power related to the grid frequency. But if a B2B-synchronverter is the largest power source in an islanded network, the B2B-synchronverter should be responsible for regulating the network frequency in island mode within its power rating.

To address the challenges introduced by the above differences, three modifications will be applied accordingly. First, a modification to the P_m is made to guarantee the DC link voltage is maintained steady. Ideally, the power flows into and out from the B2B-synchronverter should be the same considering the law of conservation of energy. However, due to the power loss in reality, the power flowing into the B2B-synchronverter must be large than the power flowing out. Therefore, an additional DC link voltage controller must be added to amend the reference power. As previously analysed in Section 5.1.4, the plant transfer function of the DC link is given as

$$H_{DC}(s) = \frac{U(s)}{P_{DC}(s)} = \frac{2}{Cs} \tag{6.19}$$

where $U(s)$ is the square of DC link voltage in s domain and $P_{DC}(s)$ is the power flowing into or out from the DC link in s domain. A sole proportional controller is selected instead of a PI controller because the PI controller will be in conflict with the modified *P*-*ω* loop which will be introduced later. Again, as the analysis in Chapter 5 shows, the inner loop can be neglected when the outer loop is sufficiently slower than the inner loop. So, assuming the DC link voltage controller is slow enough, the closed-loop transfer function will be

$$G_{DC}(s)=\frac{K_{DC}\cdot H(s)}{1+K_{DC}\cdot H(s)}=\frac{1}{\frac{2}{K_{DC}C}s+1} \tag{6.20}$$

where the time constant is

$$\tau_{DC}=\frac{2}{K_{DC}C}. \tag{6.21}$$

It is beneficial to have a symmetric control system for the B2B-synchronverter because it can avoid the switch of modes when the power flow is reversed, or a fault occurs. Therefore, the responsibility of controlling the DC link voltage should be evenly distributed to the two synchronverters. The P_m, reference active power in original synchronverter design, will be obtained by the new reference plus a correction term from the DC link voltage controller as:

$$\begin{aligned} P_{m1}&=P^{*}-\frac{K_{DC}}{2}\left({v_{DC}^{*}}^{2}-{v_{DC}}^{2}\right)\\ P_{m2}&=-P^{*}-\frac{K_{DC}}{2}\left({v_{DC}^{*}}^{2}-{v_{DC}}^{2}\right)\end{aligned}. \tag{6.22}$$

where the subscript *1* and *2* denote the variables for the sides of *Feeder 1* and *Feeder 2*, respectively. Because of the symmetric design, the direction of power flowing from the B2B-synchronverter to the network is always considered to be positive. Therefore, the reference active power for the two synchronverters should be the same value with opposite symbols, i.e. the P^{*} and $-P^{*}$ in (6.22). Considering the case that the DC link voltage is lower than the reference value which happens when the output power is larger than the input power. In equation (6.22), it can be found that the reference to the *P-ω* loop at *Feeder 1* side, P_{m1} will be smaller than the reference P^* which results in the output power to *Feeder 1* is reduced; while the absolute value of the reference to the *P*-*ω* loop at *Feeder 2* side, P_{m2} will be larger than the absolute value of reference P^* which results in the power flowing in the B2B-synchronverter is increased. Similarly, if the DC link voltage is higher than the reference, the P_{m1} will become larger which results in the power to *Feeder 2* increased, and the absolute value of P_{m2} will become smaller which results in the power drawing from *Feeder 2* decreased. By this manner, the DC link voltage can be maintained steady and the responsibility is evenly shared by the two synchronverter.

Secondly, the reference of the angular velocity ω^* in *P*-*ω* loop is replaced by the measured angular velocity at the other side. The dynamic equations for the whole B2B-synchronverter are given as:

$$\begin{aligned} \frac{d\omega_1}{dt} &= \frac{1}{J\omega_n}\left(P_{m1} - P_{e1} + D_p\left(\omega_{2g} - \omega_1\right)\right) \\ \frac{d\omega_2}{dt} &= \frac{1}{J\omega_n}\left(P_{m2} - P_{e2} + D_p\left(\omega_{1g} - \omega_2\right)\right) \end{aligned} \tag{6.23}$$

where ω_{2g} and ω_{1g} are the angular velocities of the *Feeder 2* and *Feeder 1*. The networks meshed by a SOP are usually adjacent and connected to the same substation which means that the grid frequency of the two networks are the same. Therefore, using the measured angular velocity at the other side as the reference is actually making the frequency of the synchronverter always track the grid frequency. In steady state, equation (6.23) will be

$$\begin{aligned} 0 &= P_{m1} - P_{e1} \\ 0 &= P_{m2} - P_{e2} \end{aligned} \tag{6.24}$$

which demonstrates that the controlled active power is independent of the frequency. The reason of using the grid frequency at the other side as the reference is to avoid the demand on fault detection or mode switch when a loss of mains occurs. For example, if *Feeder 1* lost the connection to the supply transformer, the frequency at *Feeder 1* will drop but the reference angular velocity is not affected as it is from *Feeder 2*. Therefore, no detection or switch of the reference value is needed. It is important to mention that the angular velocities ω_{2g} and ω_{1g} should be obtained by a phase-locked loop (with at least 3~5 times large time constant than the P-ω loop) from measuring the grid voltage. It is easy to cause the system being unstable if using the internal generated angular velocity as the references.

The last modification is an optional update to the P-ω loop which is to improve the B2B-synchronverter's capability of supplying load in island mode. From the functionality point of view, a B2B-synchronverter is mainly to balance the load in the meshed network. Therefore, its capacity should not exceed the half of the load capacity at the heavily-loaded feeder because larger capacity brings higher capital cost and power losses. For most of the time, the B2B-synchronverter works at an operating point which is lower than its capacity and the heavily-loaded feeder has the load which is twice of the B2B-synchronverter's operating point.

When a loss of mains occurs at the heavily-loaded feeder, the voltage and frequency will drop rapidly, and all the load demand will be transferred to the B2B-synchronverter. Subsequently, the B2B-synchronverter will increase its output power trying to meet the load demand because of the P-ω loop. However, due to the massive gap between the load demand and the B2B-synchronverter's capacity, the voltage and frequency cannot be recovered thus relays in the network should start to cut out loads in sequence. The eventually stabilized condition will likely be that the remaining load is close to the B2B-synchronverter's operating point and the frequency is just above the lower limit. Although the B2B-synchronverter can already supply the load with proper voltage and frequency, a slight load increase could result in the frequency dropping under the lower limit again. To improve its performance, a PI controller can be implemented to replace the D_p gain in P-ω loop. The integrator will generate an increment to the P_m so the error between ω and ω^* will be eliminated. This will require a detection logic following by a signal switch, i.e. the selection switch S shown in Figure 6.3 should be at *position 0* in grid-connected mode and optionally be at *position 1* in island mode. Once the PI controller is activated, the frequency in the islanded network will be driven to the reference value with zero steady-state error. Theoretically, load changes will not affect the frequency anymore and the B2B-synchronverter will be able to support the load close to its capacity no matter what the operating point was before the event.

As previously mentioned, the capability of restricting overcurrent is critical to the survival of power-electronic devices during a fault. Because of the absence of the current control loop in the B2B-synchronverter, the controller itself has no capability of restricting overcurrent. In this thesis, a straightforward and simple protection is considered as following: a comparison between the inductor current and a pre-set threshold is made, and result is multiplied with the gate signal. The comparison will output 1 if the current is lower than the threshold, and output 0 if the current is equal or greater than the threshold. Then, in normal operation when the inductor current is lower than the threshold, the gate signal will be unaffected; if the inductor current equals or exceeds the threshold, the gate signal will be zero thus the switching unit is blocked. This method will be named as *direct protection* in the following parts of this thesis. If a fault occurs, the inductor current will soar up and be limited at the threshold value because of the *direct protection*; then all the gate signals should be set to zero once the fault detection is completed; as a result, the synchronverter at the fault side will be fully blocked thus the current will become zero. The synchronverter at the other side should continue working to compensate reactive power similarly to the fault case studied in Chapter 5.

6.3 Simulation Results

To validate the controller design, simulations have been carried out using Matlab/Simulink. The network as shown in Figure 6.4 is built. Each of the two supply transformers in the substation supplies load along a feeder. The total length of *Feeder 1* is 12km and three load groups are evenly connected to the feeder having the capacity of 3MVA, 5MVA and 7MVA, respectively. The total length of *Feeder 2* is 6km and three load groups are evenly distributed along the feeder having the same capacity of 3MVA. The B2B-synchronverter is implemented at the middle point of a 1km line/cable connecting the endpoints of Feeder 1 and 2. The load power factor is assumed to be 0.98 in all conditions. Distributed generations (DGs) of close to 75% penetration level (11MW) is considered to be concentrated at the endpoint of *Feeder 1* and represented by one single unit.

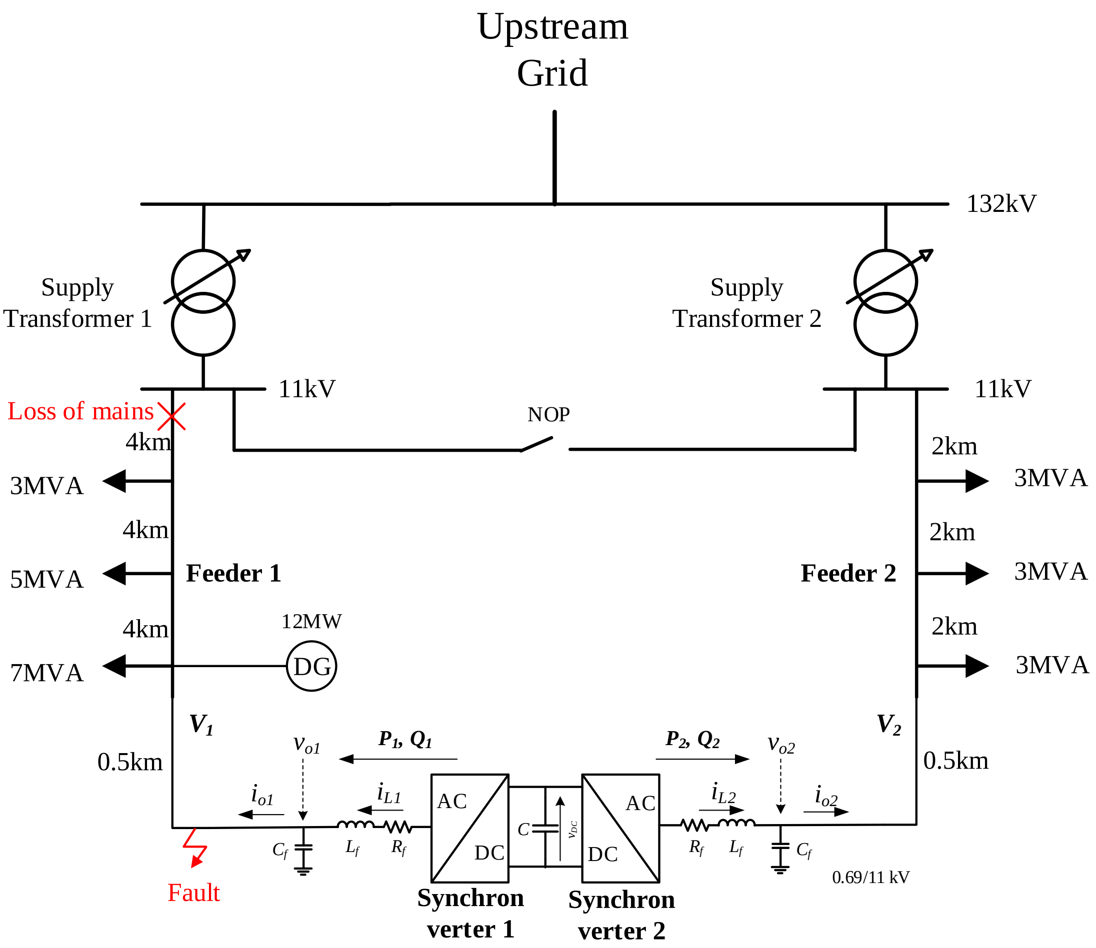

Figure 6.4 Single-line diagram of the network setup.

A default condition of the network is firstly defined for easier description on the following simulations. The default condition is defined as following:

- all the three load groups at Feeder 1 are at 80% of the capacity making the total load demand 12MVA;
- all the three load groups at Feeder 2 are at 40% of the capacity making the total load demand 3.6MVA;
- the B2B-synchronverter transfers the active power of about 4MW from Feeder 2 to Feeder 1 to balance the load in the looped network.

Table 6-1 Simulation Parameters

Name	Symbol	Value
Amplitude of nominal grid phase voltage	v_m^*	8981.5V
Nominal grid angular velocity	ω_n, ω^*	50×2π Hz
DC bus voltage	v_{DC}^*	22kV
Filter inductance, resistance, capacitance	L_f, R_f, C_f	10mH, 0.01Ω, 15.8μF
Cable impedance		0.29mH/km, 0.05Ω/km
PWM carrier frequency		2550 Hz
P-ω droop gain	D_p	4.2e5
Q-v droop gain	D_q	1.1e4
The virtual inertia	J	0.405
Reactive power integration gain	K	1.75e5
DC voltage control loop gain	K_{DC}	0.1
P-ω loop PI gain	K_p, K_i	4.2e5, 1.27e7

6.3.1 Power Control and Voltage Compensation

The functionalities of active power control and voltage regulation in grid-connected mode are tested in load variations including two extreme cases: maximum load with minimum DG and minimum load with maximum DG. The load variations and DG connections are all considered at *Feeder 1*, while *Feeder 2* remains in the default condition. The voltages and frequencies at each feeder's endpoint, V_1 and V_2 shown in Figure 6.4, are measured to observe how the compensation works. The active and reactive power at both terminals of the B2B-synchronverter are also measured and shown. The voltage of the DC link is measured to validate the first modification which controls the DC link voltage. A simulation including all the scenarios were carried out and the sequence of the scenarios is listed in Table 6-2:

- between *t=0.4~0.6s*, the networks are in default condition;
- at *t=0.6s*, the load at Feeder 1 jumps to the maximum, i.e. 15MVA;
- at *t=1s*, the DGs start to inject 12MW active power to *Feeder 1*;
- at *t=1.4s*, almost all the load at Feeder 1 is disconnected and only 0.1MVA load is reserved which is to simulate an extremely lightly-loaded condition;
- power is rescheduled to be transferred from *Feeder 1* to *Feeder 2*.

Note that the output voltage of the *Supply Transformer 1* in the substation is set at 1.02

p.u. which is done by tuning the tap changer. This is a more practical assumption for a network with high load capacity.

Table 6-2 Operation scenarios in simulation

Time (s)	Scenario
0.4~0.6	Default condition
0.6~1	Maximum load of 15MVA with no DG (extreme case 1)
1~1.4	Maximum load of 15MVA with maximum DG of 11MW
1.4~1.8	Maximum DG of 11MVA with 0.1MVA load (extreme case 2)
1.8~2.4	7.5MW power is transferred from Feeder 1 to Feeder 2

The simulation results are shown in Figure 6.5 including the active and reactive power, voltages on both sides of the B2B-synchornverter as well as the DC link voltage. The subscripts *L* and *R* in the figure indicate *Left* and *Right* which correspond to quantities at *Feeder 1* and *Feeder 2* respectively.

In the beginning stage during *t*=0.4~0.6s, the networks are in default condition, i.e. 12MVA load connected at Feeder 1 and 3.6MVA load connected at *Feeder 2*. Therefore, about 4MW active power should be expected to be transferred from *Feeder 2* to *Feeder 1* to balance the load. As shown in Figure 6.5 (a) and (b), the active power of about 4MW flows from *Feeder 2* to *Feeder 1* through the B2B-synchronverter during this period. Reactive power compensation is also carried out thanks to the *Q-V* loop. The voltages at the endpoint of *Feeder 1* (V_1) is improved with the compensation by B2B-synchronverter as shown in Figure 6.5 (c).

Then, during *t*=0.6~1.8s, two extreme cases are simulated. Between *t*=0.6~1.0s, the load at *Feeder 1* is at the maximum while DGs having zero output (extreme case 1) which would cause V_1 dropping below the lower limit (0.94p.u.) if without any compensation; and when the active and reactive power compensation is carried out by the B2B-synchronverter, the voltage drops slightly but stays within the permitted range as shown in Figure 6.5 (c). At *t*=1.0s, the DG starts to work at the maximum power rating outputting 11MW active power to *Feeder 1*. In this condition, the 15MW load is supplied by the DGs (11MW) and the B2B-synchronverter (4MW) thus almost no power is drawn from or reversely fed into *Supply*

Transformer 1. As a result, the voltage is close to the nominal value. Then, between *t*=1.4~1.8s, the load at *Feeder 1* becomes almost zero while the DG is at the maximum (extreme case 2). During this period, all the active power of 15MW (11MW from the DG and 4 MW from the B2B-synchronverter) is fed back into *Supply Transformer 1* which results in a significant voltage rise on the endpoint of *Feeder 1*. V_1 would violate the upper limit (1.04p.u.) if without any compensation; when with the B2B-synchronverter, V_1 is stabilized at about 1.04p.u. thanks to the reactive power compensation (4MVar absorbed by the B2B-synchronverter).

At t=1.8s, the active power of 7.5MW is rescheduled to be transferred from *Feeder 1* to *Feeder 2* to rebalance the load in the network. The transient of the step change on the active power takes about 0.04 second without overshoot which is considered a sound response. After the power flow is reversed, the voltage rise on V_1 is mitigated as less power is flowing reversely at *Feeder 1*.

During the whole period, the voltage at the endpoint of *Feeder 2*, V_2 in general is maintained well. It rises from about 0.99p.u. to 1.01p.u. after the active power flow is rescheduled at *t*=1.8s because there is about 3.9MW power flowing reversely to *Supply Transformer 2*. The DC link voltage is also well maintained throughout the whole period as shown in Figure 6.5 (e). Transients appear due to load changes, but neither the dips nor the overshoots exceed 2% of the nominal value which is acceptable.

The three-phase voltages and currents at the output of the synchronverter at *Feeder 1* (v_{o1} and i_{o1}) during the period around *t*=1.8s are shown in Figure 6.6. the transition of the reverse of power flow is relatively smooth and the THDs in the voltage and current in steady state are 4.26% and 1.53%, respectively.

In summary, the measured active power passing the B2B-synchronverter tracks the reference value very well and the reactive power compensation is carried out automatically because of the *Q*-*V* droop. The overall voltage profile at *Feeder 1* is greatly improved in various conditions (always within permitted range even in extreme cases) thanks to the B2B-synchronverter's independent active and reactive power compensation. It is also worth mentioning that the extreme step changes of the operation scenarios in the simulation, i.e. a sudden load loss of 15MVA and a sudden DG access of 12MW, can rarely occur in reality. Therefore, the transient dips and overshoots in the voltage and power in practice should be much smaller.

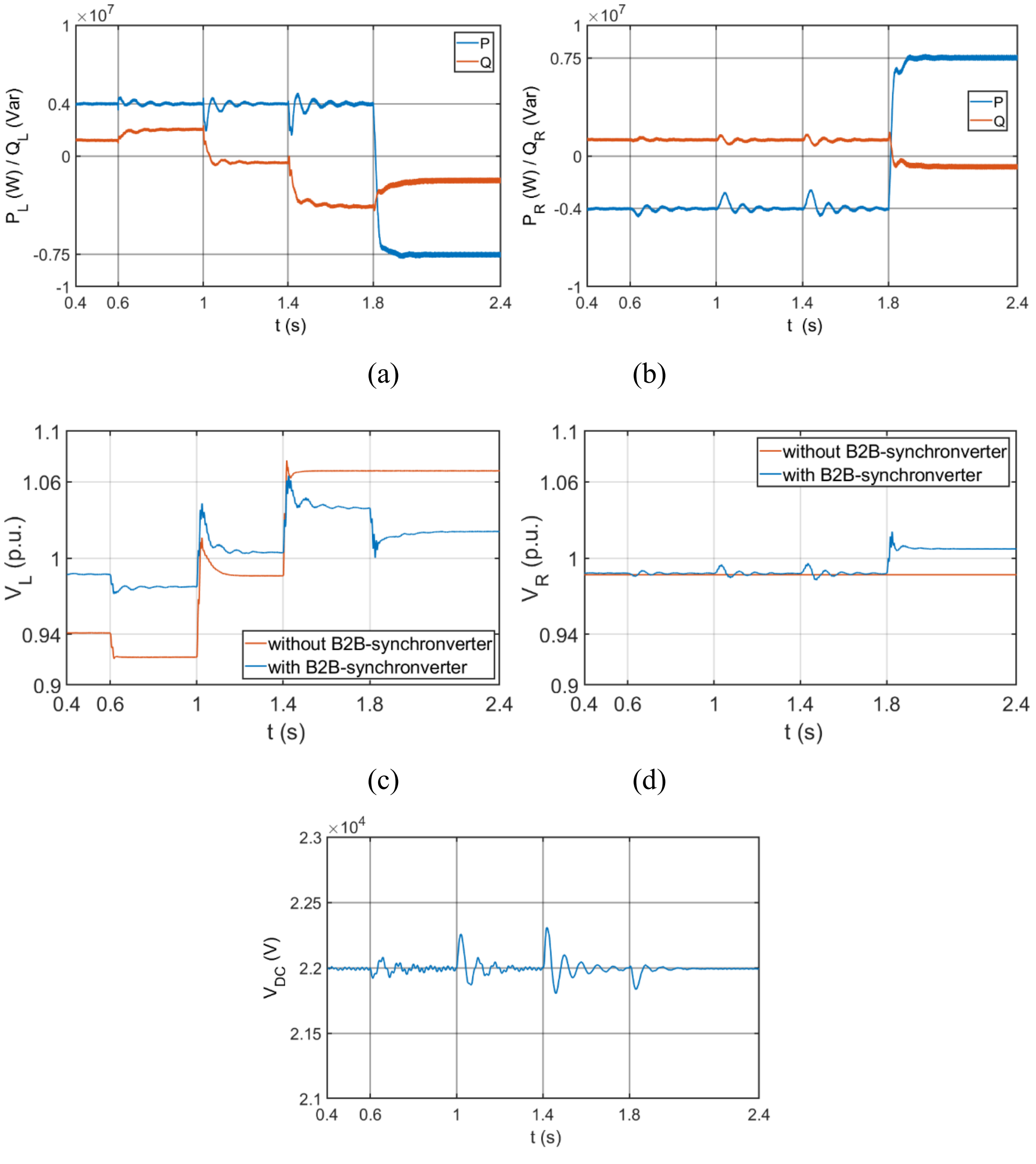

(a) (b)

(c) (d)

(e)

Figure 6.5 Simulation results for power control and voltage compensation: (a) Output power of the synchronverter at *Feeder 1*; (b) Output power of the synchronverter at *Feeder 2*; (c) Voltage amplitude at endpoint of *Feeder 1* in per unit; (d) Voltage amplitude at endpoint of *Feeder 2* in per unit; (e) DC link voltage in volt.

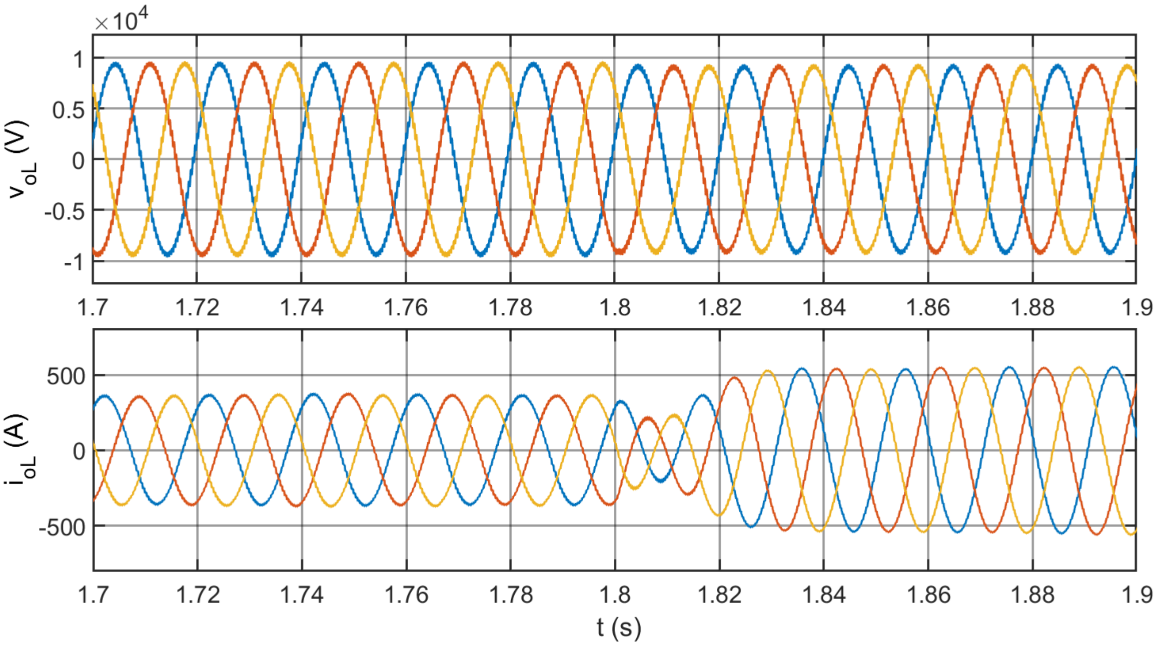

Figure 6.6 Three-phase output voltage and current of the synchronverter at *Feeder 1*.

6.3.2 Load Supply in Islanded Condition

The load supply by the B2B-synchronverter including the transition during the loss of mains is investigated by simulation in this section. The *Supply Transformer 1* is cut out at a moment to simulate the loss of mains.

The default condition is again applied in the initial stage except that the load at *Feeder 1* is at the maximum which is 15MVA. When the connection between *Feeder 1* and the substation is lost, a huge power shortage between the 4MW power supplied by the B2B-synchronverter and the nearly 15MW power demanded by the load at *Feeder 1* will be found. Therefore, the voltage and frequency are expected to decrease rapidly. Then, the B2B-synchronverter should respond and increase its output active power trying to help stabilize the frequency because of the *P*-*ω* loop. However, due to that the power demand is way larger than the operating point and even beyond the power rating of the B2B-synchronverer, it is impossible to recover the frequency until part of the load is cut out. The load shedding is usually carried out by relays which are operated according to one or several network parameters such as the voltage value, frequency value and their changing rates and so forth [103]. In this chapter, sole frequency relays with different time delays are considered for simplification.

The simulation results of the voltages, frequencies and power are shown in Figure 6.7. The voltage amplitude and frequency at *Feeder 1* decrease rapidly after the loss of mains event occurs at t=0.5s as shown in Figure 6.7 (a) and (c), respectively. It is important to point out that the frequency drops to the lowest point 43.25Hz after 150ms of the loss of mains. This is a rapid decrease compared to normal operation, but it is much slower than the case in Chapter 5 – the frequency drops to zero within 20ms after the loss of mains. It is a benefit of the B2B-synchronverter because the slower decreasing rate gives time to the frequency sensitive relays in the network to operate in order. Note that Figure 6.7 (c) is the internal frequency of synchronverter connected to *Feeder 1* which is more sensitive to the changes of network parameters due to the smaller time constant compared to the phase-locked loop used to obtain grid frequency. In terms of the output power by *synchronverter 1*, the active power increases rapidly tending to make up the power shortage as shown in Figure 6.7 (e).

The first load shedding of 3.5MVA happens at around t=0.655s, and the frequency starts to rise back as well as the voltage amplitude; meanwhile, the output active power begins to decrease accordingly. The second load shedding of 2.5MVA happens at around t=0.734s, and the frequency continues rising with a faster speed and stabilize at about 48.25Hz; the voltage continues rising and stabilize at around 0.98p.u. after an overshoot of 0.1p.u.; the output power continues decreasing and stabilize at approximately 8.5MW which is still larger than the power rating of the B2B-synchronverter. The third load shedding of 1.2MVA happens at around t=1.134s, and the frequency rises again and stabilizes at about 48.7Hz; the output active power drops to approximately 7.5MW which is within the power rating now; the voltage amplitude still remains at about 0.98p.u..

Finally, at about t=1.5s, the PI controller in the P-ω loop is activated to replace the D_p gain and drives the frequency to the nominal value 50Hz; the voltage amplitude eventually stabilizes at 0.988p.u.. From about t=2s, the voltage amplitude, frequency and output power at *Feeder 1* are all in steady state which means the remaining load is now supplied properly by the B2B-synchronverer. The voltage amplitude and frequency at *Feeder 2* are affected by the loss of mains at *Feeder 1* to a limited extend: oscillations are observed but neither the voltage nor the frequency drops beyond the lower limit (0.94p.u. for voltage and 49.5Hz for frequency). The output active power of the synchronverter connected to *Feeder 2* changes accordingly to satisfy the power demand at *Feeder 1*.

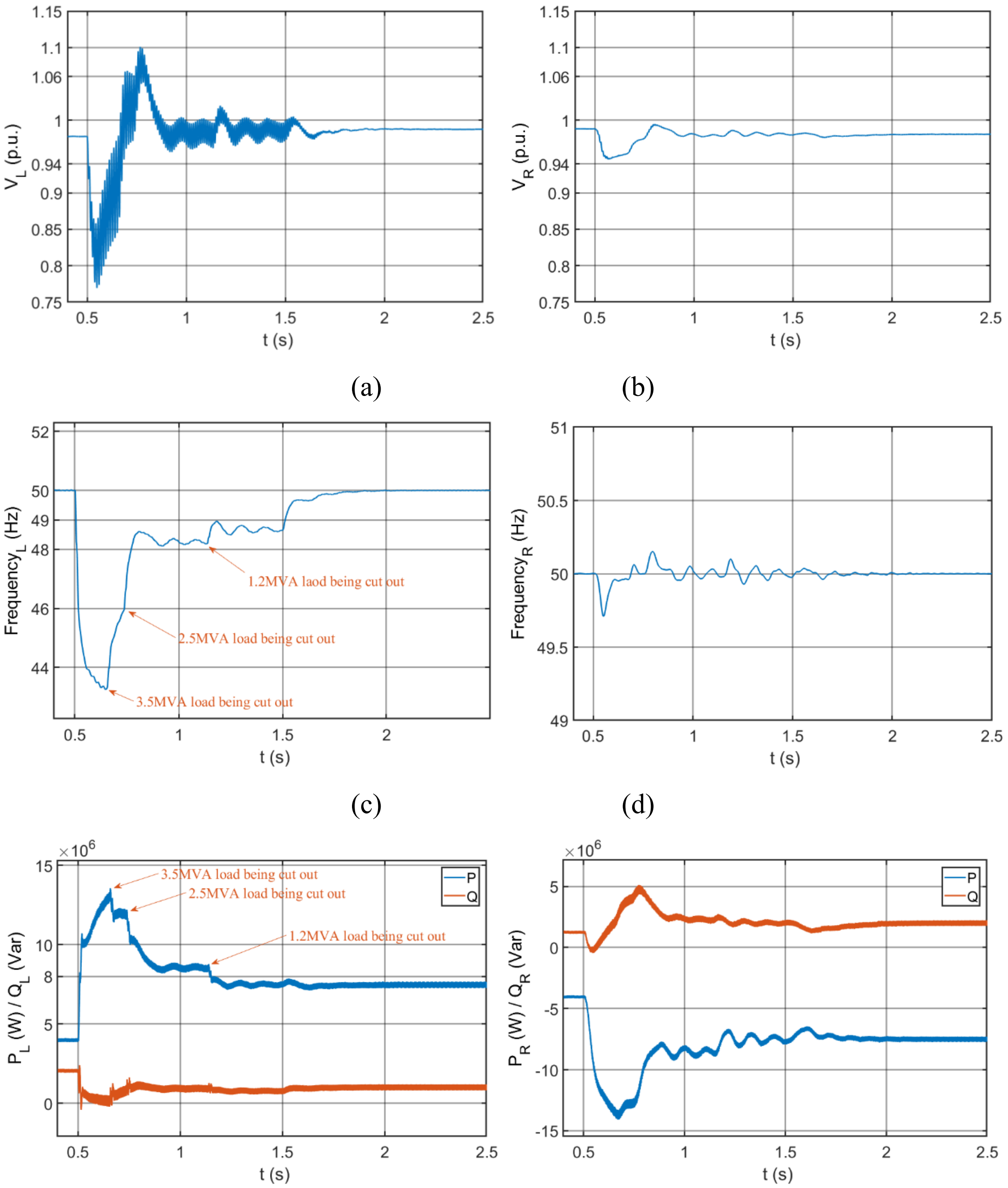

(a) (b)

(c) (d)

(e) (f)

Figure 6.7 Simulation results for loss of mains: (a) Voltage amplitude at endpoint of *Feeder 1*; (b) Voltage amplitude at endpoint of *Feeder 2*; (c) Internal frequency of *synchronverter 1*; (d) Grid frequency at *Feeder 2*; (e) Output power of the synchronverter at *Feeder 1*; (f) Output power of the synchronverter at *Feeder 2*.

It should be emphasized that the logic to switch in the PI controller, in this thesis, is determined by the time length of the frequency below the lower limit (one second in this simulation) meanwhile the output power must be within the power rating. It is possible that more load would be cut out than the results shown before the PI controller is activated. This could cause unnecessary load shedding and the PI controller may even not be activated. Therefore, the logic of the activation of the PI controller must be selected carefully by comparing with the time delay settings of the relays in the network.

The DC link voltage during the event is shown in Figure 6.8. It drops by approximately 2.3% when the loss of mains occurs due to the instant increase of power drawn by *synchronverter 1* and starts to rise back at about t=0.55s before the first load shedding happens. After approximately 0.4 seconds, the DC link voltage comes back at the nominal value which is 2.2kV. Then, when the PI controller in the P-ω loop is activated, the DC link voltage drops slightly and stabilizes at 2.11kV which is about 96% of the nominal value. The 4% steady-state error is introduced by the increment from the integrator in the PI controller in the P-ω loop. It is natural to consider adding an integrator to eliminate the steady-state error, but it will be conflict with the PI controller in the P-ω loop. As the frequency has a much stricter standard (±1%), the DC link voltage controller is therefore implemented with a sole proportional gain rather than a PI gain.

The three-phase voltage and current during the islanding transition are shown in Figure 6.9. The overall transitions are smooth, but it should be noted that the current amplitude exceeds the rated value (594A corresponding to 8MVA) reaching 1077A at the maximum which is 181% of the rated current during the transition. Though power-electronic modules are usually capable of supporting twice the rated current for a certain time period. However, it depends on the thermal limit in practice thus requiring to be considered with extra care. The THDs of the voltage and current in islanded condition are 3.26% and 2.56%, respectively.

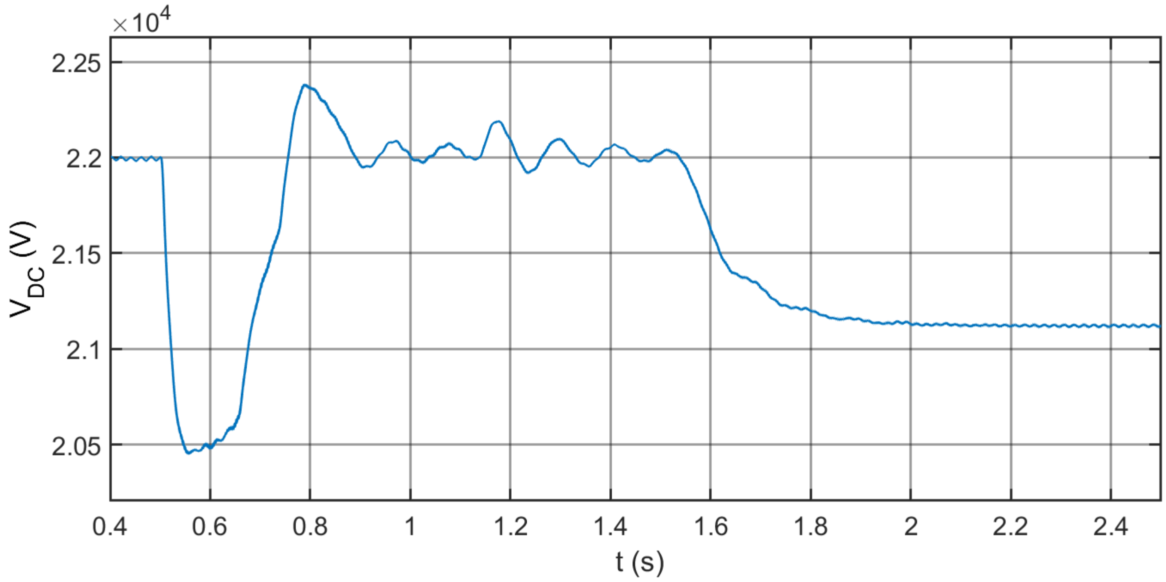

Figure 6.8 DC link voltage during the loss of mains.

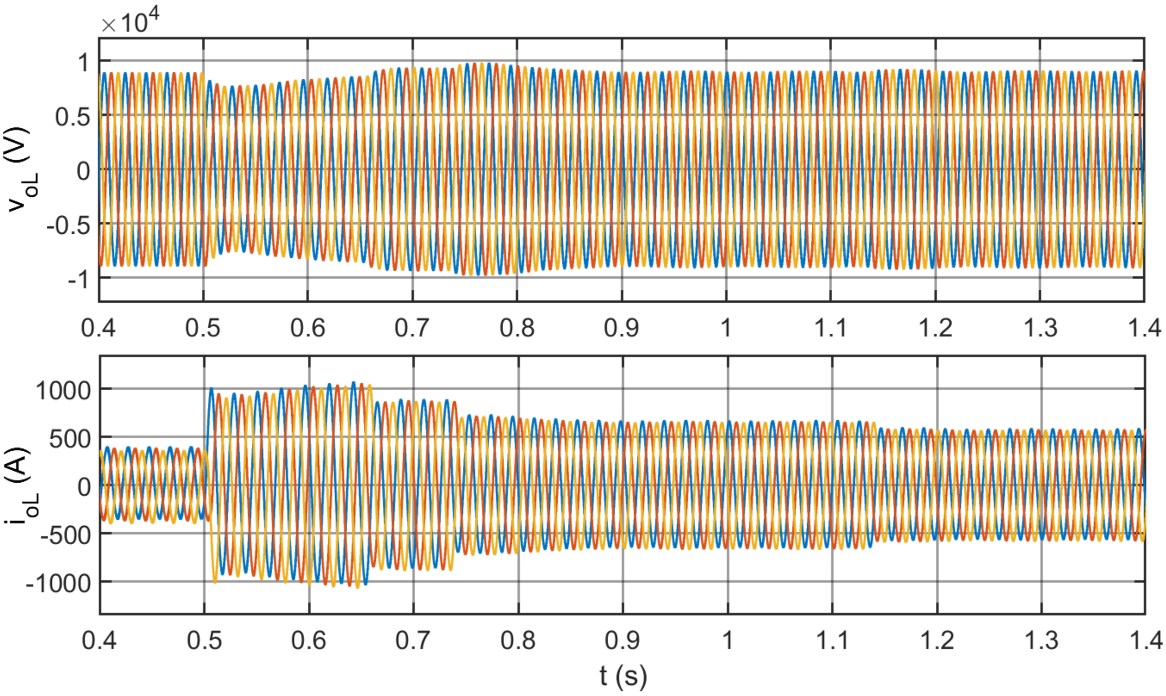

Figure 6.9 Three-phase output voltage and current of *synchronverter 1*.

6.3.3 Fault Current Limit

When applying an SOP, the increase of fault level is the most concerned issue. A power-electronic switch like IGBT can be turned off almost instantly when a negative voltage is applied between the gate and emitter. This provides the capability of restricting overcurrent to a synchronverter which is impossible for a real synchronous machine. The previously discussed *direct protection* scheme with a threshold of 1200A is used. Whenever the current flowing through the device exceeds 1200A, the gate signal will become zero to make the gate driver supply a negative voltage between the device's gate and emitter to turn off the device. A three-phase-to-ground short circuit at *Feeder 1* close to the B2B-synchronverter is simulated at *t*=0.4s. The results are shown in Figure 6.10.

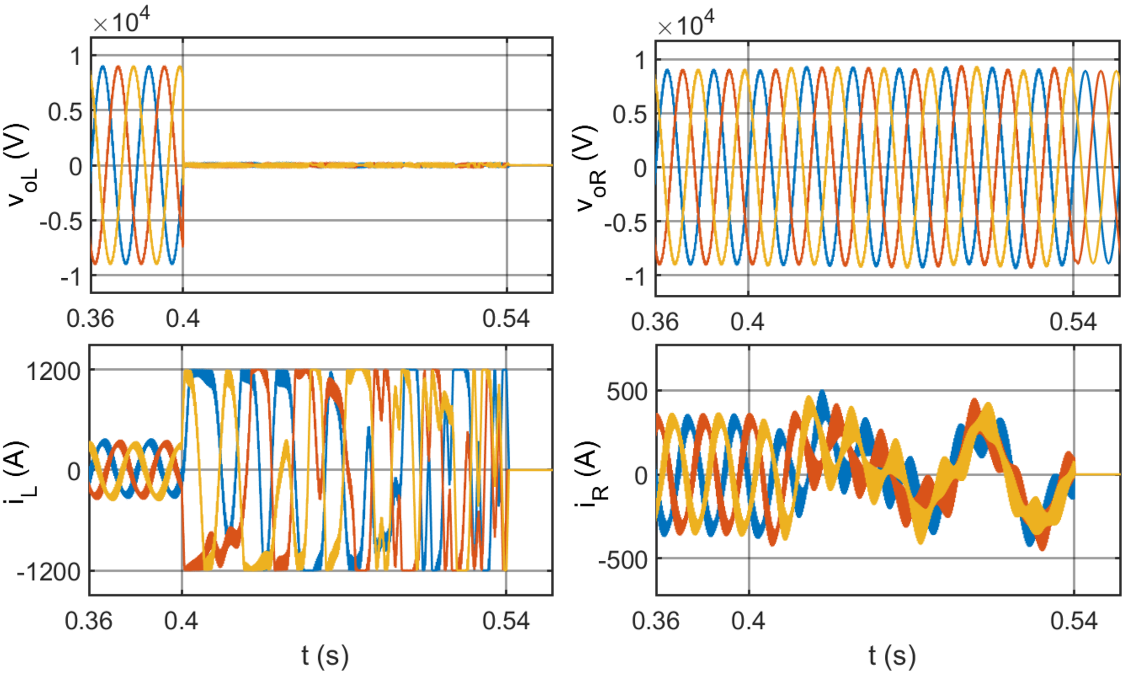

(a) (b)

Figure 6.10 Output voltages and inductor currents during a three-phase-to-ground fault at Feeder: (a) Voltage and current of *synchronverter 1*; (b) Voltage and current of *synchronverter 2*.

The network is in the default condition before the fault occurs. The output voltages and currents flowing through the filter inductors at both sides are shown in. When the three-phase-to-ground fault occurs, the voltage at *Feeder 1* becomes almost zero instantly while the inductor current soars up rapidly but the amplitudes are limited at 1200A as shown in Figure 6.10 (a). It is assumed that after 7 cycles (140ms) the fault detection is completed, and all the gate signals are set at zero so that the B2B-synchronverter is fully blocked which results in no current passing through after *t*=0.54s. In terms of the voltage and current at

Feeder 2 side, the voltage remains unaffected and the current amplitude is decreasing as no active power is required by the DC link. However, the current is distorted and *synchronverter 2* should be turned off as well with the completion of fault detection.

A comparison between the fault current with B2B-synchronverter and the fault current with direct power line/cable connection is shown in Figure 6.11. It is clearly that the fault current is limited at 1200A which indicates that the fault level increase is also limited.

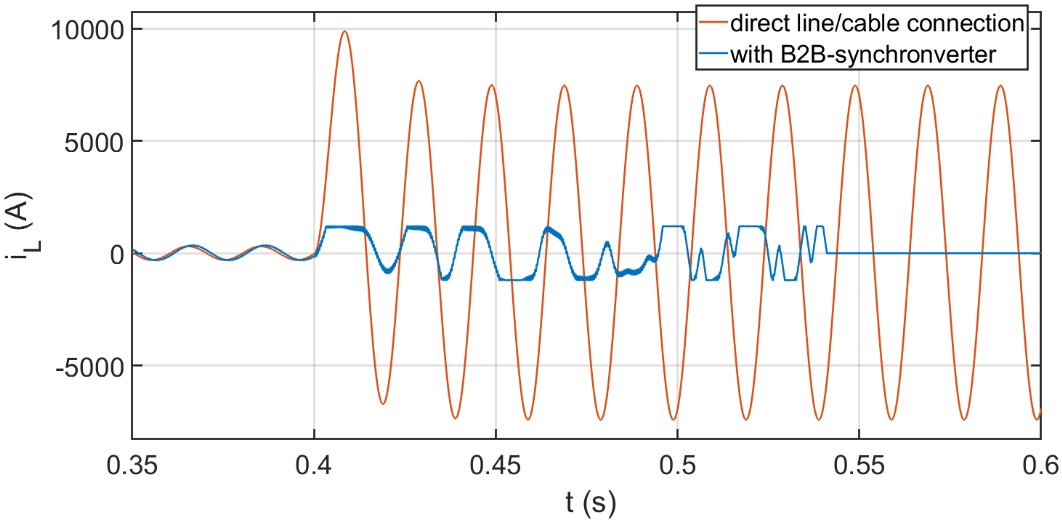

Figure 6.11 Comparison between fault current (phase a) with B2B-synchronverter and with direct line/cable connection.

6.4 Experiment Results

As it is not practical to carry out experiment at 11kV in our laboratory, the experiment is scaled down to low voltage level to verify the controller design. Also, simplification is made compared to the simulation. First, instead of using whole back-to-back structure, only one VSC is used and the DC link is replaced by a DC power supply. Secondly, the grid is provided by grid emulator which is connected close to a resistive load bank and the VSC, thus there is no cable impedance between the source and load causing voltage drop. Thirdly, load shedding is not carried out in the experiment. The power control in grid-connected mode and load supply by synchronverter in island mode are tested by experiment. The pictures of the experiment facilities are shown in Appendix II. The parameters in the experiment are given in Table 6-3.

Table 6-3 Experiment Parameters

Name	Symbol	Value
Nominal phase voltage amplitude	v_m	50V
Nominal grid angular velocity	ω_n	49.88×2π rad/s
DC bus voltage	v_{DC}^*	110V
Filter inductance, resistance, capacitance	L_f, R_f, C_f	10mH, 0.08Ω, 15μF
PWM carrier frequency		5000 Hz
Rated power, reactive power	P^*, Q^*	225W, 0Var
Nominal load		330W
P-*ω* droop gain	D_p	23.87
Q-*v* droop gain	D_q	200
The virtual inertia	J	9.2e-5
Reactive power integral gain	K	3.8e3
P-*ω* loop PI gain	K_p, K_i	1500, 3000

The initial condition is set as following: the 330W resistive load is supplied at 50V (amplitude of phase voltage) by the grid emulator and the synchronverter is outputting about 235W power. As shown in Figure 6.12 (a) and (b), the voltage amplitude is at about 50V in the initial stage (50.3V to be precise which is due to the error in the grid emulator), and the frequency is 48.87Hz which was the grid frequency when the experiment being carried out.

At about *t*=2.9s, the grid emulator is disconnected to simulate the loss of mains. The voltage drops rapidly because the operating point of the synchronverter is much lower than the load demand, and the frequency begins to decrease while the output active power of synchronverter increases because of the *P*-*ω* droop control. As shown, the voltage is driven back to the nominal value within 300ms, but the frequency remains at approximately 49.24Hz which is beneath the lower limit.

Then, after about 2.5s since the frequency drops below 49.5Hz which is pre-defined as the criteria for the activation of PI controller in the *P*-*ω* loop, the PI controller is activated to replace the D_p gain and drives the frequency back to the nominal value immediately. Then, the synchronverter begins to provide proper voltage and frequency to supply the load in island mode. Afterwards, load fluctuations are applied to test how well the load is supplied. The voltage in general is maintained at the nominal value very well despite some transient dips and overshoots when the load changes. The frequency is very stable during the load fluctuation, as shown in Figure 6.12 (c), the variations are almost unnoticeable. Finally, the output power tracks the load demand very well.

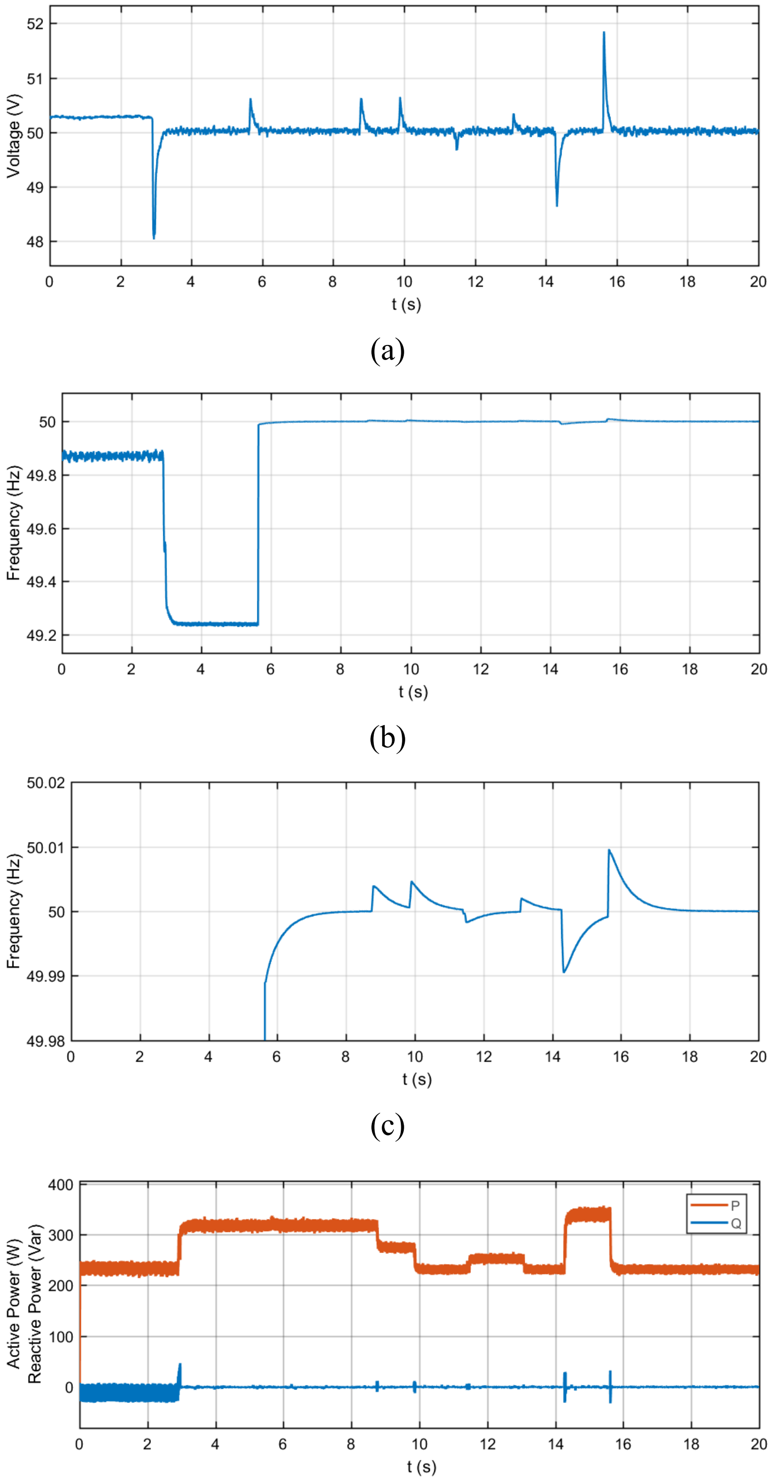

(a)

(b)

(c)

(d)

Figure 6.12 Experiment results during an islanding case: (a) Load voltage amplitude; (b) Frequency response; (c) Partially enlarged plot of the frequency; (d) Output power .

The three-phase voltage and current during the largest load increase at around *t*=14.27s are shown in Figure 6.13. The transition of the current increase due to the load increase is smooth and the THDs of the voltage and current in steady-state are 3.36% and 3.52%, respectively.

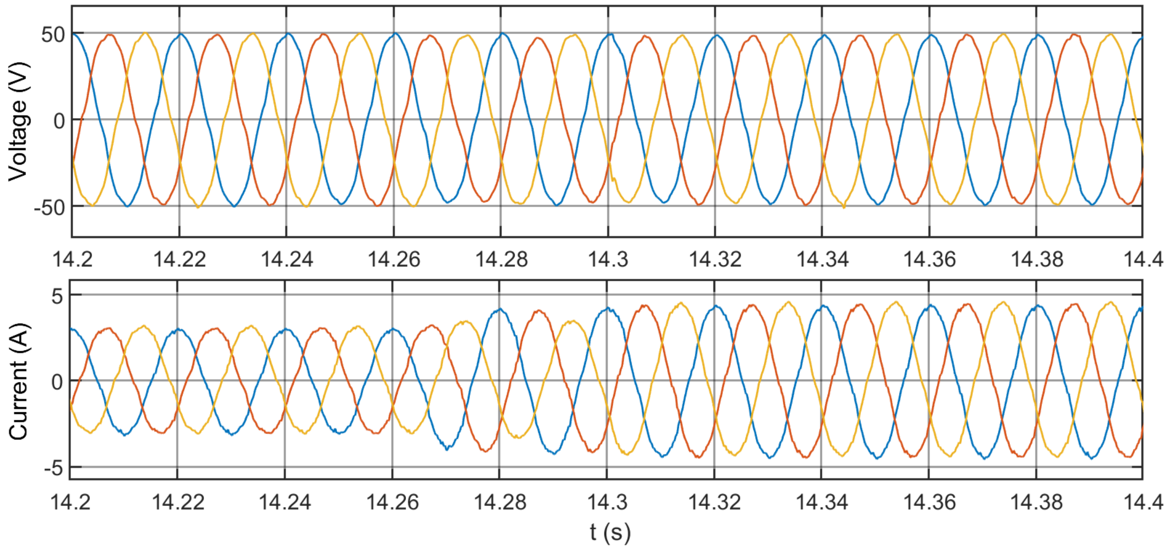

Figure 6.13 Three-phase voltage and current at the load.

6.5 Summary

In this chapter, the controller of a B2B-synchronverter type SOP has been proposed based on the concept of synchronverter and then validated by simulation and experiment.

In the simulation, the active power control and effect of voltage compensation in grid-connected mode are tested first. The results demonstrate that the P-ω loop can control the active power tracking the reference value very well, and the added DC link voltage controller controls the DC link to be steady at the reference value. The Q-V loop controls the amount and direction of the reactive power accordingly to assist the regulation of voltage. A severe loss of mains event was then simulated to test the B2B-synchronverter's capability of supplying load alone in island mode. The simulation results demonstrate that B2B-synchronverter is able to continue supplying the load within its power rating in island mode. The islanding transition including voltage/frequency drop and load shedding have been discussed in detail. The three-phase-to-ground fault is simulated at last to test the capability of restricting overcurrent. Through the *direct protection*, the current flowing through the B2B-synchronverter can be limited at a defined value. Meanwhile, the load at the other side of the B2B-synchronverter remains unaffected. In experiment, the active power control in grid-connected mode and the load supply in island mode were tested at a scale-down voltage level.

The proposed controller of a B2B-synchronverter is fully symmetric both in design and operation, and no detection or signal switch is required for islanding. Though the activation of the PI controller in the P-ω loop requires a simple logic, it is only an optional improvement to be made which is not compulsory. Being free of detection and detecting logic will increase the reliability as there is no risk in mis-detections. However, a drawback of this controller should be considered carefully which is the lack of current control loop to restrict overcurrent. Though the fault current can be limited by the *direct protection* scheme, the restricted current cannot be kept in sinusoidal form which affects its fault ride-through capability. Besides, the reactive power compensation cannot be continued after the fault as the PI-based controller does.

7. Supplying a Network Dominated by Dynamic Load via a VSC

In the previous two sections, the loss of mains has been studied and discussed. However, the load was considered as purely passive. The passive load can be considered as constant impedance which will not disturb the system. This is a reasonable assumption for general distribution networks because the power factor for most distribution networks is above 0.97. However, in some conditions, especially for factory local networks, the dynamic load such as induction machines could be the dominant type of load. The dynamic load will respond to power supply changes thus making conditions more complicated. Therefore, the loss of mains when using an SOP in a network with pure dynamic load needs to be studied.

7.1 An Induction Motor during a Fault at the Stator Side

For an induction motor, when the loss of mains happens, the induction motor will lose the power supply and the rotor flux linkage will therefore decay, and the induced electromagnetic torque will be lost accordingly; then as a result, the rotor speed starts to decrease. Once the connection to the mains is restored or another power supply is connected, a large reactive power will be required for re-magnetization so that the electromagnetic torque can be recovered; then, if the induced electromagnetic torque is larger than the load torque, the rotor can be accelerated again.

Before studying the supply of an induction motor by a VSC after a loss of mains. The following case is studied: a three-phase-to-ground fault occurs at a branch between the induction motor and the mains as shown in Figure 7.1, and is cleared after 200ms by opening circuit breaker *CB2* which would be a practical assumption.

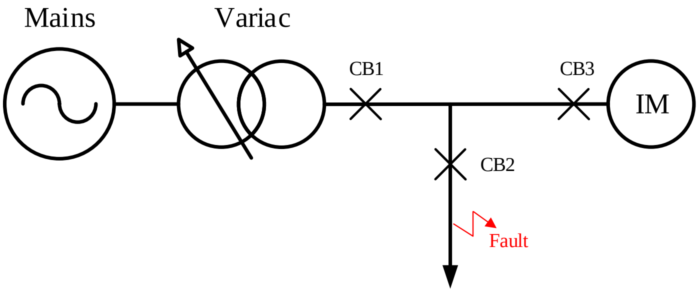

Figure 7.1 Single-line diagram of an induction motor supplied by the mains via a variac.

When the fault happens, the stator side of the induction motor is short-circuited, and the per-phase equivalent circuit is shown in Figure 7.2. L_s and L_M are the stator induction and magnetizing inductance, L_r and R_r are the referred rotor inductance and resistance which can be obtained by measurement. The decaying time of the rotor flux linkage is approximately equal to the rotor time constant which can be estimated by [104]:

$$\tau_r = \left(1 - \frac{{L_M}^2}{(L_s + L_M)(L_r + L_M)}\right)\frac{L_r}{R_r} \tag{7.1}$$

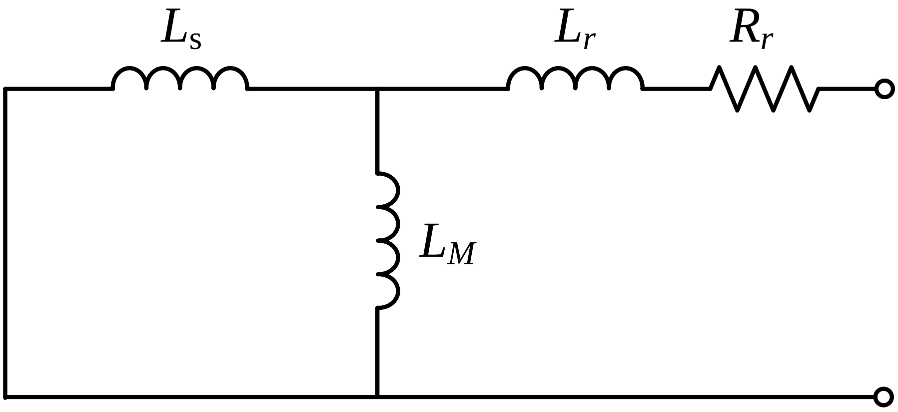

Figure 7.2 Per-phase equivalent circuit when the stator side is short-circuited.

For induction motors, the rotor time constant is normally less than 100ms which means the rotor flux linkage will be likely to vanish before the fault to be cleared. A “400V 50Hz

2.2kW 1430RPM” three-phase induction motor with the parameters listed in Table 7-1 is considered and used in experiment for this chapter. The parameters are measured from the no-load test and the locked rotor test. By substituting the parameters into equation (7.1), the rotor time constant is obtained as τ_r=14.2ms.

Table 7-1 Parameters of the induction motor and VSC’s filter

Parameters	Description	Values at 50Hz (Ω)
R_s	Stator resistance	2.47
X_s	Stator reactance	5.5
R_r	Referred rotor resistance	2.26
X_r	Referred rotor reactance	5.5
X_M	Magnetizing reactance	28.27

Therefore, it is expected that the flux will vanish, and the rotor speed will drop to certain value before the fault is cleared. Assuming the connection between the induction motor and the mains was not cut out, then the power supply would recover once the fault has been cleared. Then a large reactive power and relatively high current will be required for re-magnetization and acceleration of the rotor. A simulation is carried out to investigate this process. The voltage level is scaled down to 95V (rms of line voltage) corresponding to the experiment which is going to be discussed in the next section. The load to the induction motor is assumed to be a constant load torque of 1.4N·m.

As shown in Figure 7.3 (a), the voltage and current at the induction motor drop to zero instantly when the fault occurs at t=2s. As a matter of course, the active and reactive power flowing into the induction motor drop to zero as shown in Figure 7.3 (b). The rotor flux also decreases rapidly, and it takes about 14.835ms for the flux to be reduced to near zero as shown Figure 7.3 (c). The rotor speed decreases at a constant rate as shown in Figure 7.3 (d). After 200ms when the fault is cleared, the voltage at the stator is recovered to the value before the fault. An increased current and reactive power, compared to that before the fault, is required to re-generate the flux and accelerate the rotor. Then with the gradual recovery of the rotor flux and speed, the current and reactive power gradually decrease to the nominal value from the overshoots. At about t=5s, the induction motor is fully recovered the statues before the fault. Compared to passive load, induction motors require larger reactive power and current than the nominal value to recover.

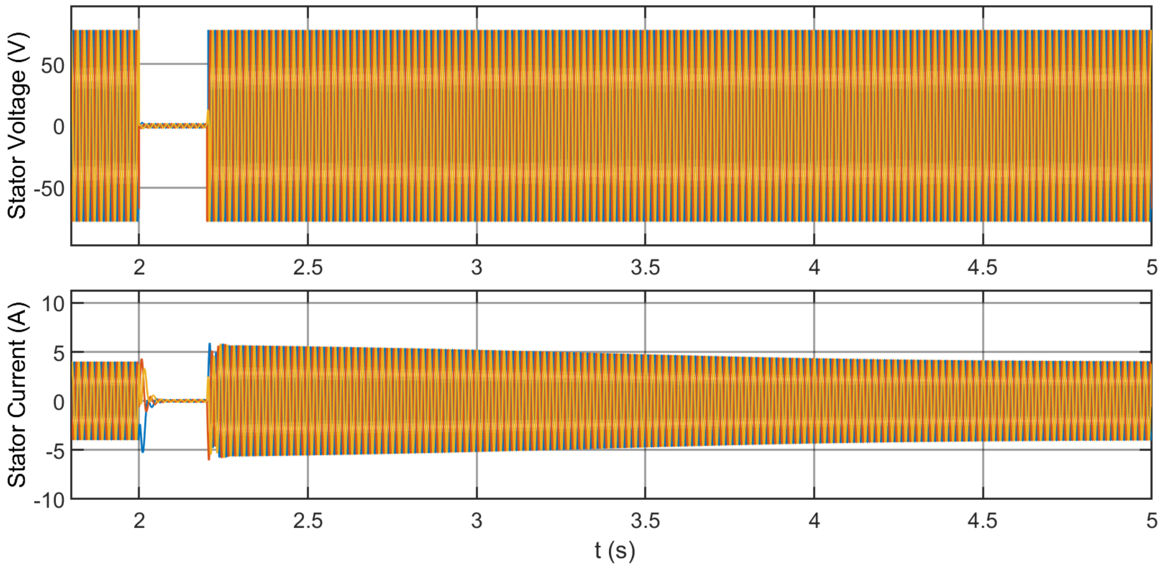

(a)

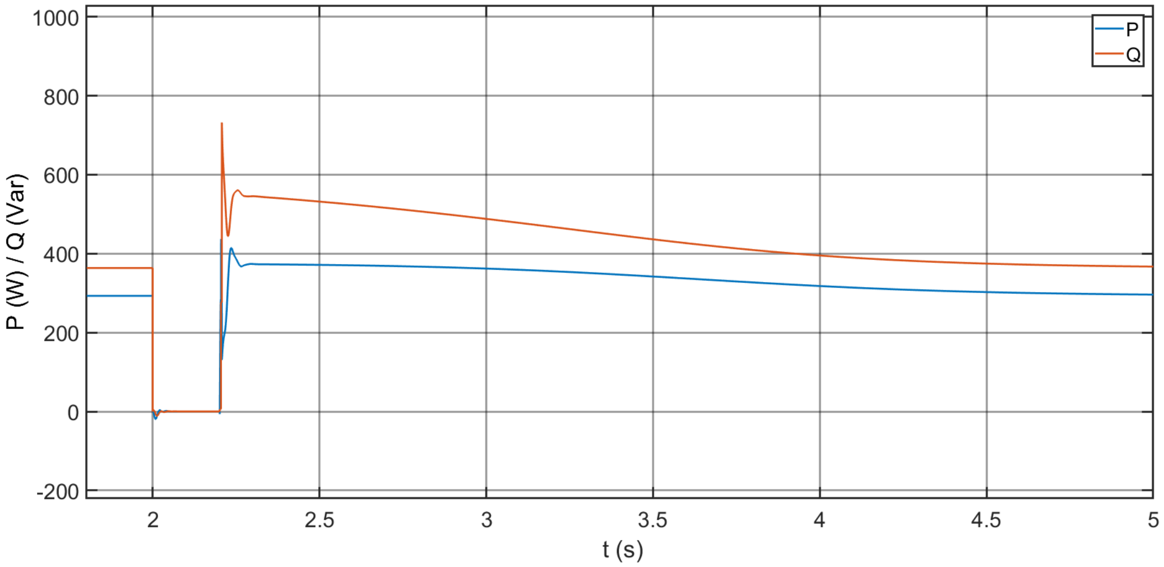

(b)

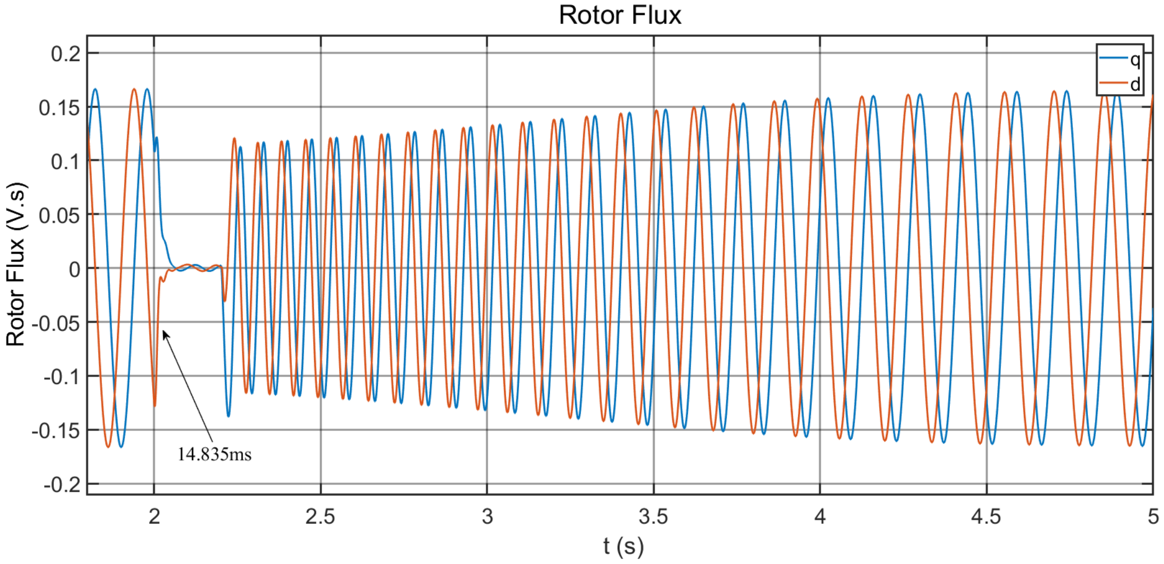

(c)

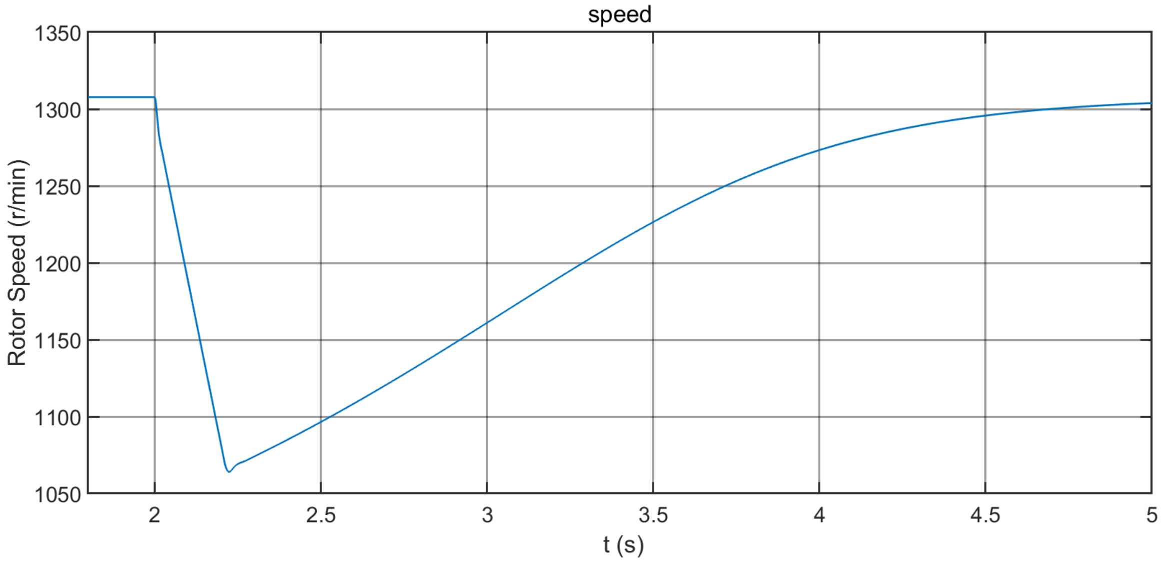

(d)

Figure 7.3 Simulation of effects of a fault to an induction motor: (a) Three-phase voltage and current at stator; (b) Active and reactive power flowing in the motor; (c) Rotor flux; (d) Rotor speed.

7.2 Stability Margin of an Induction Machine

How an induction motor recovers from a transient fault has been investigated in the last section. However, the situation could be different if the power supply becomes a VSC after the fault is cleared. Considering a situation as following: a fault happens at a branch between the induction motor and the mains as shown in Figure 7.4; after 200ms, the circuit breakers *CB1* and *CB2* are both open, thus the VSC will continue supplying the induction motor. However, due the existence of the VSC's filter, the stability margin of the induction motor could be affected considerably.

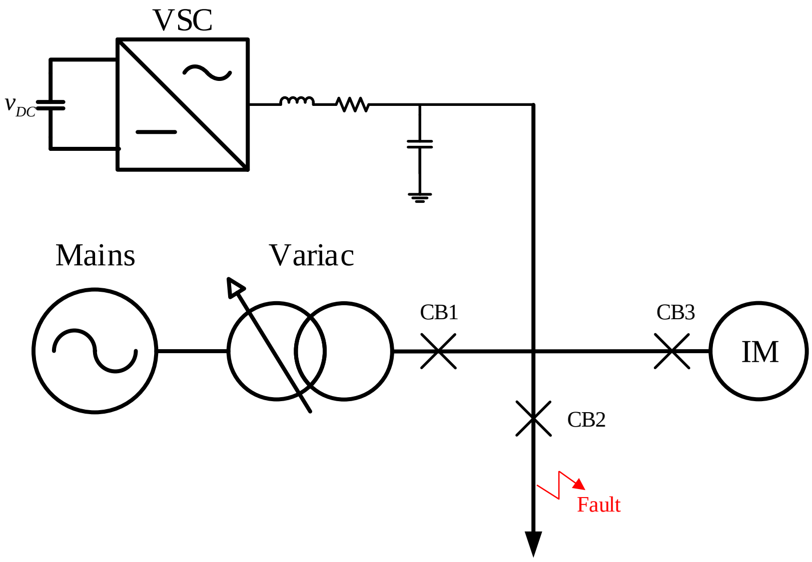

Figure 7.4 Single-line diagram of an induction motor supplied by the mains via a variac.

The stability margin of an induction motor here refers to the pull-out torque or breakdown torque which is the maximum torque can be induced in the rotor. In the first, a per-phase equivalent circuit of an induction motor is shown in Figure 7.5.

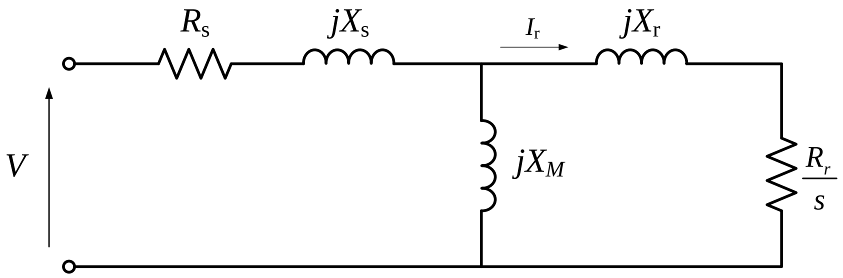

Figure 7.5 Per-phase equivalent circuit of an induction motor

The R_s and X_s are the stator resistance and reactance; X_M is the magnetizing reactance; R_2 and X_2 are the referred resistance and reactance of the rotor which can be obtained by measurement. Finally, s is the slip which is defined by

$$s = \frac{n_{sync} - n_m}{n_{sync}} \tag{7.2}$$

where n_{sync}, n_m are the magnetic field speed and the mechanical shaft speed, respectively.

Then, the induced toque in an induction motor can be expressed as [105]:

$$T = \frac{3P_{ag}}{\omega_{sync}} \tag{7.3}$$

where ω_{sync} is the synchronous angular velocity and P_{ag} is the air-gap power of one phase. The ω_{sync} is a constant and the air-gap power is the power across the gap between the stator and rotor which is equal to the power absorbed by the term R_r/s. Therefore, the air-gap power can be calculated using:

$$P_{ag} = I_r^2 \cdot \frac{R_r}{s} \ . \tag{7.4}$$

Thevenin equivalent could be one of easiest method to solve the circuit in Figure 7.5. First, an open-circuit is built for determining the Thevenin voltage as shown in Figure 7.6 (a); then, short-circuit on the voltage source is applied to find out the Thevenin impedance as shown in Figure 7.6 (b).

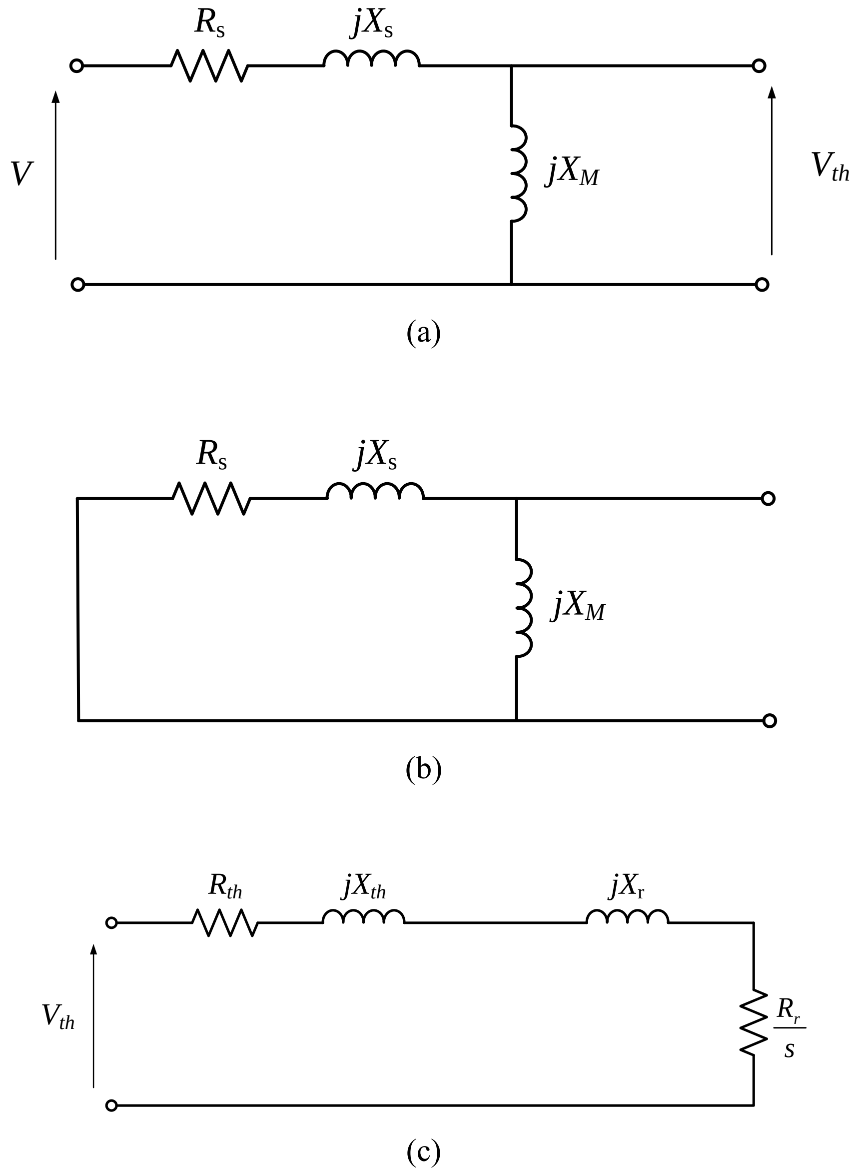

(a)

(b)

(c)

Figure 7.6 Thevenin equivalent of induction motor circuit (a) Thevenin voltage of the input circuit; (b) Thevenin impedance of the input circuit; (c) Whole Thevenin equivalent circuit.

The Thevenin voltage is given by the voltage divider rule as

$$V_{th} = \frac{jX_M}{R_s + jX_s + jX_M} V \,, \tag{7.5}$$

and the Thevenin impedance is given as

$$Z_{th} = \frac{jX_M \left(R_1 + jX_s\right)}{R_s + jX_s + jX_M} \ . \tag{7.6}$$

Since both the Thevenin voltage and impedance have been obtained, the Thevenin equivalent circuit for the induction motor is given in Figure 7.6 (c) and the rotor current will be

$$I_r = \frac{V_{th}}{Z_{th} + jX_r + \dfrac{R_r}{s}} \ . \tag{7.7}$$

Then, the magnitude of rotor current I_r can be calculated as

$$\left|I_r\right| = \frac{\left|V_{th}\right|}{\sqrt{\left(R_{th} + \dfrac{R_r}{s}\right)^2 + \left(X_{th} + X_r\right)^2}} \tag{7.8}$$

where $|V_{th}|$ is the magnitude of Thevenin voltage, R_{th} and X_{th} are the real and imaginary parts of the Thevenin impedance, respectively. The air-gap power can be therefore obtained by substituting (7.8) into (7.4):

$$P_{ag} = \left|I_r\right|^2 \cdot \frac{R_r}{s} = \frac{\left|V_{th}\right|^2 \cdot \dfrac{R_r}{s}}{\left(R_{th} + \dfrac{R_r}{s}\right)^2 + \left(X_{th} + X_r\right)^2} \ . \tag{7.9}$$

Finally, by substituting (7.9) into (7.3), the equation of the induced torque in the rotor is given as:

$$T=\frac{3\cdot\left|V_{th}\right|^{2}\cdot\frac{R_{r}}{s}}{\omega_{sync}\cdot\left[\left(R_{th}+\frac{R_{r}}{s}\right)^{2}+\left(X_{th}+X_{r}\right)^{2}\right]}\quad. \tag{7.10}$$

This equation can describe the torque-speed characteristic of an induction motor for given parameters. The maximum value of the above equation is the pull-out torque, referred as stability margin in this chapter, which represents the maximum electromagnetic torque that can be induced in the rotor at a certain voltage at the stator side. If the load torque is larger than the pull-out torque, i.e. the mechanical torque on the shaft is always larger than the induced torque in the rotor, the rotor speed is physically impossible to be maintained and will eventually drop to zero.

However, when the motor is connected to a source, the impedance between the source and the stator impedance should also be considered to achieve the result as accurate as possible. When an induction motor is directly connected to the grid, the grid impedance is in series and can be directly added to the stator impedance. When an induction motor is connected to a VSC which has an LC filter as shown in Figure 7.7 (a), the situation will be slightly more complicated. Thevenin equivalent is again preferred for solving the circuit. The solution for the torque-speed curve for an induction motor supplied by a VSC with LC filter is shown in Figure 7.7. R_f, X_{Lf} and X_{Cf} are the filter inductor resistance, filter reactance by the inductor and filter reactance by the capacitor, respectively. Firstly, the Thevenin equivalent for the filter circuit (the brown dashed frame in Figure 7.7 (a)) is applied:

$$V_{fth}=\frac{-jX_{Cf}}{R_{f}+jX_{Lf}-jX_{Cf}}V \quad \text{and} \quad \begin{cases} Z_{fth}=\dfrac{-jX_{Cf}\left(R_{f}+jX_{Lf}\right)}{R_{f}+jX_{Lf}-jX_{Cf}} \\ R_{fth}=real(Z_{fth}),X_{fth}=imag(Z_{fth}) \end{cases}\quad. \tag{7.11}$$

Then, the Thevenin equivalent circuit for the filter is as shown by the brown dashed frame in Figure 7.7 (b). Next, The Thevenin equivalent for the stator side circuit (blue dashed frame in Figure 7.7 (b)) is applied:

$$V_{th} = \frac{jX_M}{R_{fth} + R_s + jX_{fth} + jX_s + jX_M} V_{fth} \quad \text{and} \quad \begin{cases} Z_{th} = \dfrac{jX_M\left(R_{fth} + R_s + jX_{fth} + jX_s\right)}{R_{fth} + R_s + jX_{fth} + jX_s + jX_M} \\ R_{th} = real(Z_{th}), X_{th} = imag(Z_{th}) \end{cases} . \quad (7.12)$$

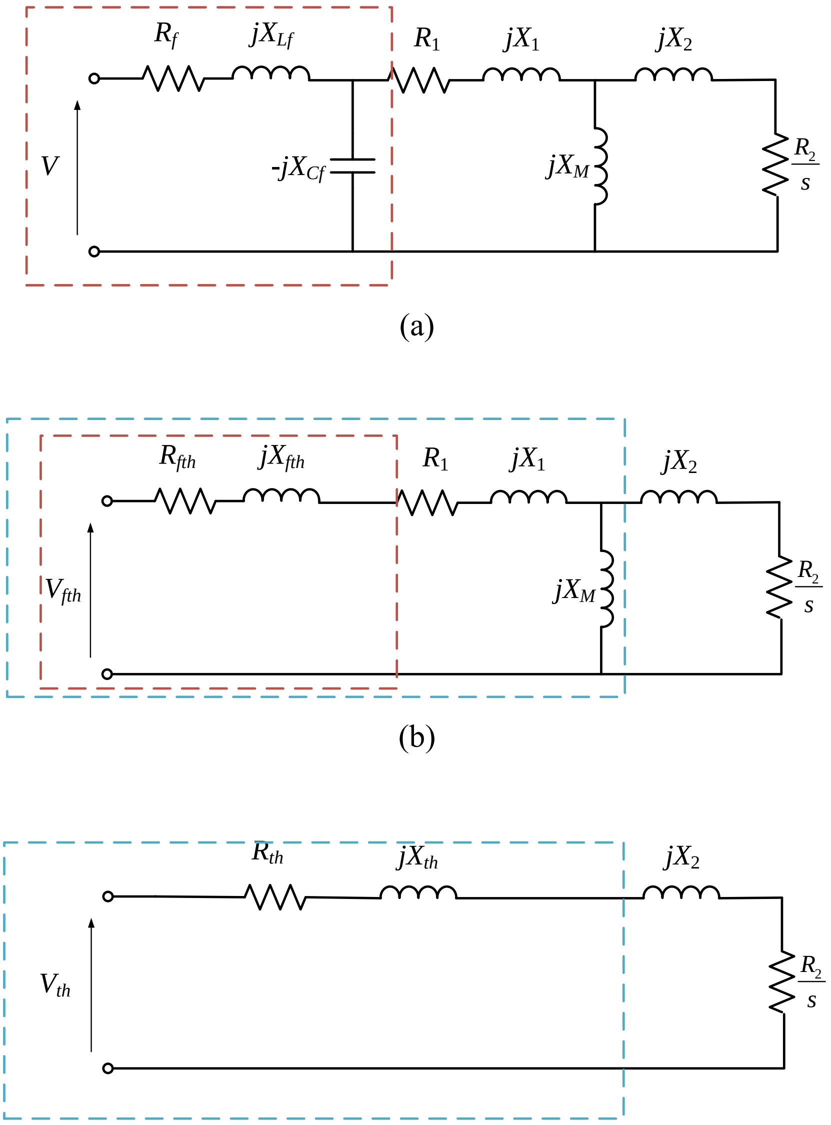

(a)

(b)

(c)

Figure 7.7 Thevenin equivalent solution for an induction motor supplied by an VSC with LC filter: (a) original circuit; (b) Thevenin circuit for filter has been applied; (c) final Thevenin equivalent circuit for the whole circuit.

By substituting (7.11) and (7.12) into (7.10), the toque-speed characteristic of an induction motor supplied by a VSC with LC filter can be obtained. Then, a comparison between the torque-speed curves of an induction motor that supplied by the grid and by a VSC with LC filter is made. For grid-connected mode, the voltage V is considered to be directly at the stator. For island mode, the VSC is considered to be operated in open-loop control mode, i.e. a given voltage reference is sampled by the PWM generator which then feeds gate signals to the converter. Therefore, the voltage V can be seen as being placed before the filter as shown in Figure 7.7 (a). The calculated torque-speed curves in these two modes are shown by the solid and dashed lines in Figure 7.8. The used parameters of the induction motor and filter are listed in Table 7-1. The induction motor is a squirrel cage induction machine with the following rated values: 400V 50Hz 2.2kW 1430RPM. The voltage on the stator V is scaled down to 50V (rms phase-to-neutral). Experiments are carried out to measure the torque-speed characteristic for validation of the calculation. Results show relatively good matches to the calculated results. The experiment setup will be introduced later.

It is obvious to that the stability margin of the induction motor is significantly reduced when in island mode than in grid-connected mode due to the reactance in the VSC's filter. Considering the case as following: a constant load corresponding to a mechanical torque of 1.2N·m was being applied to the motor shaft before a loss of mains event, and the motor is being continually supplied by a VSC after the event. Because the 1.2N·m load is above the maximum torque that can be induced in the rotor in island mode, the rotor speed will keep decreasing until the rotor stalls or even starts to rotate reversely.

The most straightforward way to address this problem could be to enhance the IM's stability margin by simply increasing the direct output voltage of the VSC (v_i in Figure 7.9 (a)). Although this is feasible when the IM is the only load, it is not practical for the circumstance considered in this chapter - a whole local network is supplied by the VSC. As shown in Figure 7.9, in island mode the voltage established after the filter, v_o is determined by the voltage, v_i and inductor current, i_L. And because i_L is determined by the total load in the network, which is changing all the time, the established voltage v_o cannot be maintained at the rated value dynamically. This is to say, even the output voltage of VSC has been increased, in heavy load condition, the established voltage v_o could be not enough to support the IM to induce sufficient torque in the rotor to keep speed. Therefore, the closed-loop control is required and it is necessary to investigate methods to mitigate the negative effect to the stability margin from the filter impedance.

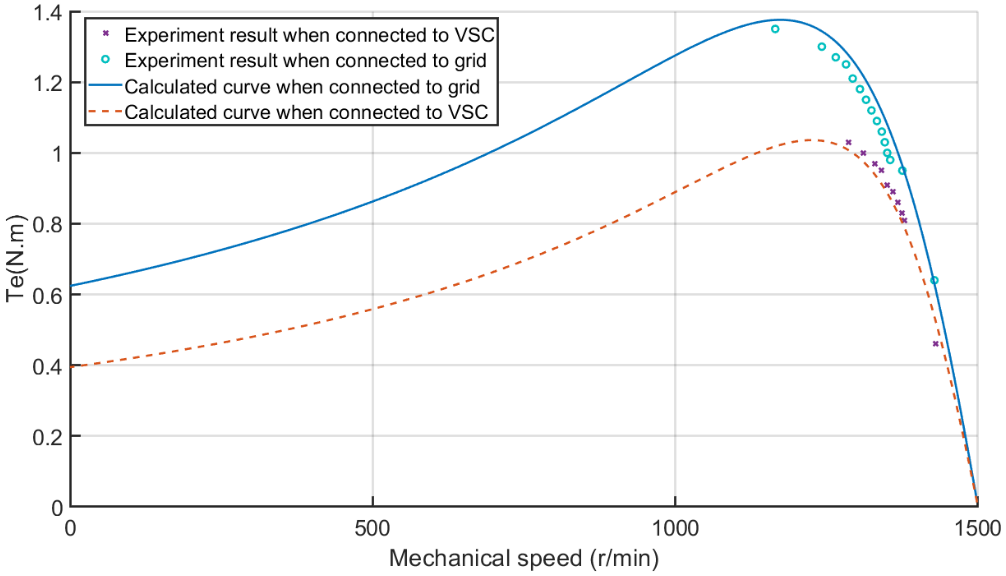

Figure 7.8 Toque-speed characteristics

7.3 Controlling the Output Impedance of a VSC

The output circuit of a VSC with LC filter is shown in Figure 7.9 (a) and its block diagram is shown in Figure 7.9 (b). The L_f, R_f and C_f are the filter's inductance, inductor's internal resistance and the filter capacitance; v_i is the voltage close to the converter before the filter; v_o is the output voltage; i_L and i_o are the currents flowing through the filter inductor and the output current, respectively.

The per-phase frequency domain expression of the VSC's output can be readily derived from Figure 7.9 (b) as:

$$V_o(s)=\frac{1}{L_fC_fs^2+R_fC_fs+1}V_i(s)-\frac{L_fs+R_f}{L_fC_fs^2+R_fC_fs+1}I_o(s) \tag{7.13}$$

where the latter term reflects the output impedance. Therefore, defining the output

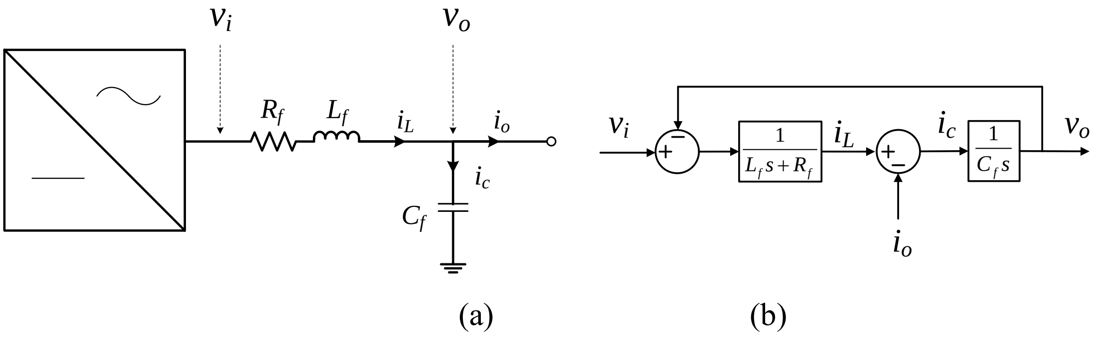

Figure 7.9 (a) Single-line diagram of a VSC with LC filter; (b) Corresponding block diagram.

impedance transfer function as:

$$Z_o(s) = \frac{V_o(s)}{I_o(s)} = -\frac{L_f s + R_f}{L_f C_f s^2 + R_f C_f s + 1} \quad . \tag{7.14}$$

Considering the same filter that used in the experiment in Chapter 5, parameters are given in Table 5-6: L_f=10mH, R_f=0.08Ω, C_f=15μF. The bode diagram of the output impedance is shown in Figure 7.10. The magnitude is 10.0305db at 50Hz which leads the ratio of the output voltage to current to be 10^(10.0305/20)=3.1734Ω, and the corresponding phase is close to -90° which indicates the impedance is dominantly inductive.

In Chapter 5, an output voltage controller is introduced (section 5.1.5) which is to provide reliable voltage supply to loads in island condition. As the coupling effect after decoupling is negligible (demonstrated by the magnitude diagram of $u3$ to $y1$ in Figure 5.10), the full control loop will be as shown in Figure 7.11. Note the control loops for d and q axes are fully symmetric when neglecting the coupling. The gain G is added for manipulating the output impedance which will be introduced later.

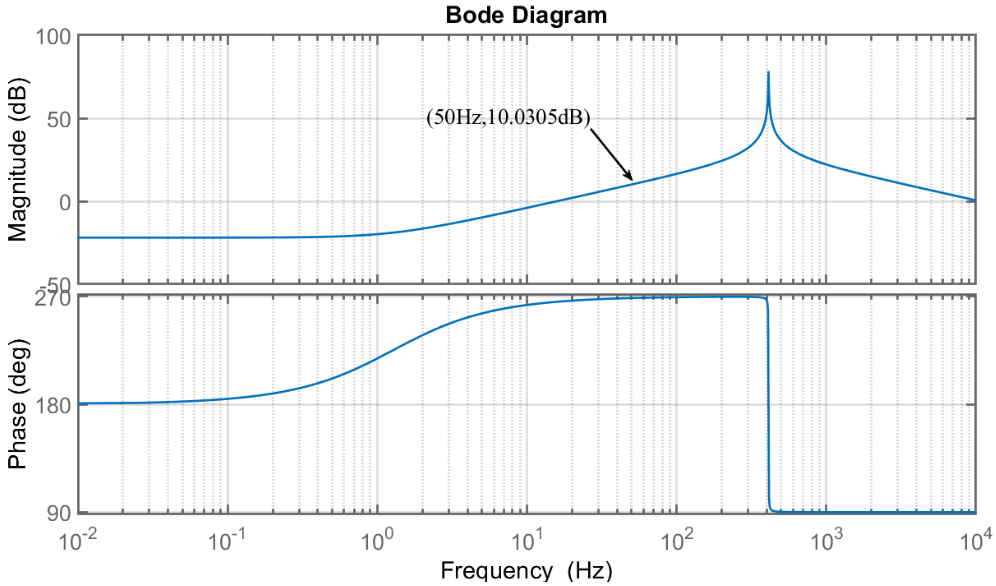

Figure 7.10 Bode diagram of output impedance Z_o.

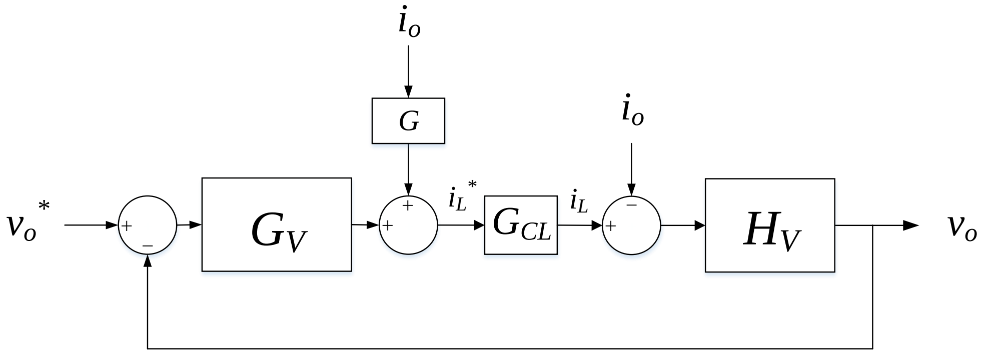

Figure 7.11 Output voltage control loop by neglecting coupling and decoupling

The transfer function G_V, H_V and G_{CL} have been given by equations (5.46), (5.45) and (5.25) in Chapter 5, respectively. Then, the transfer function of reference v_o^* and output current i_o to the output voltage v_o can be derived as:

$$V_o(s)=\frac{G_V(s)G_{CL}(s)H_V(s)}{G_V(s)G_{CL}(s)H_V(s)+1}V_o^*(s)-\frac{H_V(s)\left(1-G_{CL}(s)G(s)\right)}{G_V(s)G_{CL}(s)H_V(s)+1}I_o(s) \quad (7.15)$$

where the former term has been analysed in Chapter 5, and the latter term is the output impedance transfer function when the VSC is controlled by the output voltage controller. Now, defining the new output impedance:

$$Z_1(s) = \frac{V_o(s)}{I_o(s)} = -\frac{H_V(s)\left(1 - G_{CL}(s)G(s)\right)}{G_V(s)G_{CL}(s)H_V(s) + 1} \quad . \tag{7.16}$$

When parameters are selected as listed in Table 7-2, the bode diagram of $Z_1(s)$ when $G(s)=0$ and $G(s)=1$ are as shown in Figure 7.12. Note the bode diagram is in SRF, so the 0Hz corresponds to the 50Hz in stationary frame. When $G(s)=0$, i.e. no feedforward of output current i_o is applied, a gain of about 16.1dB corresponding to 6.38Ω is observed at 0Hz. When G(s)=1, i.e. direct feedforward of i_o is applied, the gain at 0Hz is about -44.8dB corresponding to 5.8mΩ which is reasonable to be neglected. Therefore, when the output voltage controller is used to control the VSC to provide voltage supply, the output impedance at 50Hz is reduced to a very low value which can be neglected.

Table 7-2 Parameters for analysing output impedance

Parameters	Description	Values
L_f	Filter inductance	10mH
R_f	Resistance of filter inductor	0.08Ω
C_f	Filter capacitance	15μF
τ	Current control loop time constant	1ms
t_{rV}	Output voltage loop rising time	10ms
K_{P_V}	Output voltage controller proportional gain	0.003
K_{I_V}	Output voltage controller integral gain	0.1734

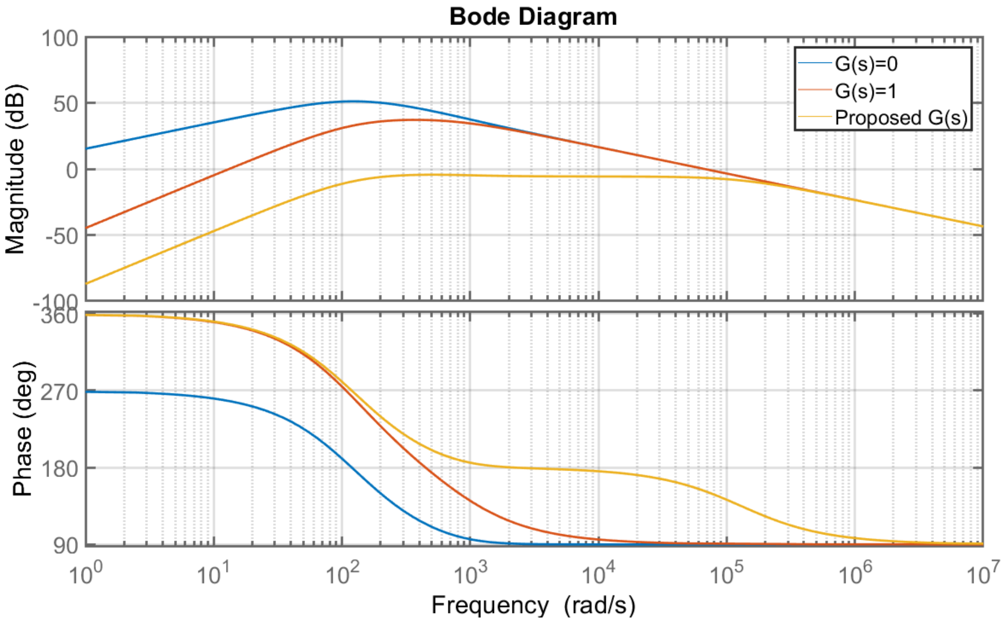

Figure 7.12 Bode diagrams of $Z_1(s)$ when $G(s)=0$, $G(s)=1$ and for proposed $G(s)$.

However, there is a wide frequency range where the gain is very large. This means high frequency components appears in the current could result in big distortions in the voltage. A modification to the feedforward to address this problem is proposed in the following. It is tempting to make $G(s)=1/G_{CL}(s)$ so that the impedance will be zero as the numerator becomes zero. However, a differential term will introduce large gains at high frequencies thus causing unwanted disturbance. To overcome this problem, a low pass filter could be implemented to limit the gains at high frequencies [106]. The feedforward gain can be made as:

$$G(s)=\frac{1}{G_{CL}(s)}\cdot G_{LF}(s)=(\tau s+1)\cdot\frac{1}{\frac{1}{\omega_{LF}}s+1}\quad . \tag{7.17}$$

where ω_{LF} is the cut-off frequency of the low pass filter. The bode diagrams of $G(s)$ and $1/G_{CL}(s)$ are plotted in Figure 7.13 when τ=1ms and ω_{LF}=129100 rad/s. As seen, the gains of $\tau s+1$ is linearly increasing at high frequencies, and the gains of $G(s)$ at high frequencies are limited to below 40dB thanks to the low pass filter $G_{LF}(s)$.

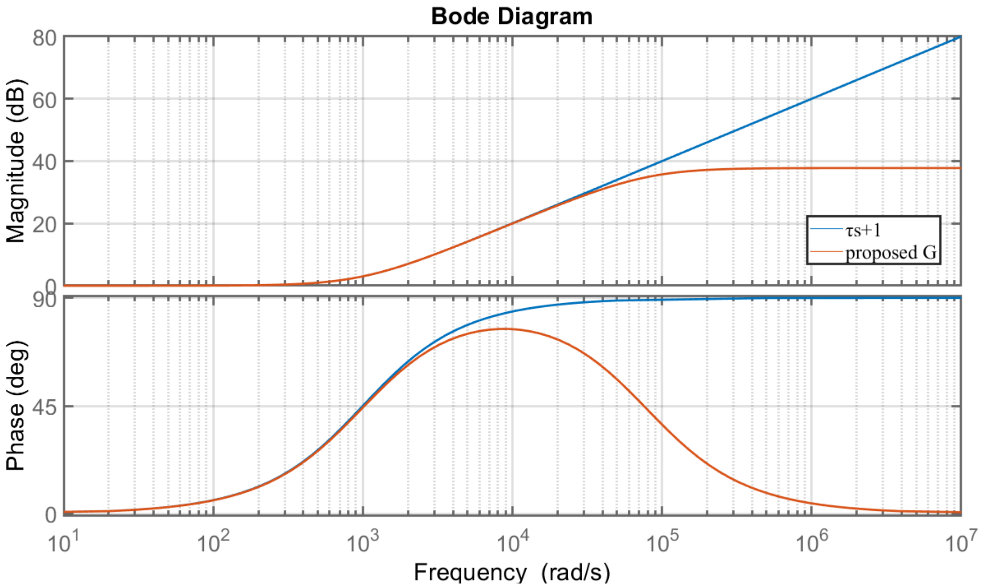

Figure 7.13 Bode diagram of proposed G and $\tau s+1$

Now, applying the proposed feedforward gain $G(s)$ to the output voltage controller, i.e. substituting (7.17) into (7.16), the bode diagram has been shown by the yellow line in Figure 7.12. There is no positive gain existing at all frequencies which means that the resonance at high frequency is supressed.

7.4 Simulation Results

The simulation and experiment are both carried out using the same network setup shown in Figure 7.4 to validate the analysis and the controller design in the previous sections. The parameters of the induction motor used have been listed in Table 7-1, and the parameters of the VSC's filter and controller gains have been given in Table 7-2. The root-mean-square line voltage is scaled down at 95V. The torque-speed characteristic of the induction motor at this voltage is shown in Figure 7.14. The stability margin of the induction motor is about 1.66N·m without filter impedance and about 1.25N·m with the filter impedance.

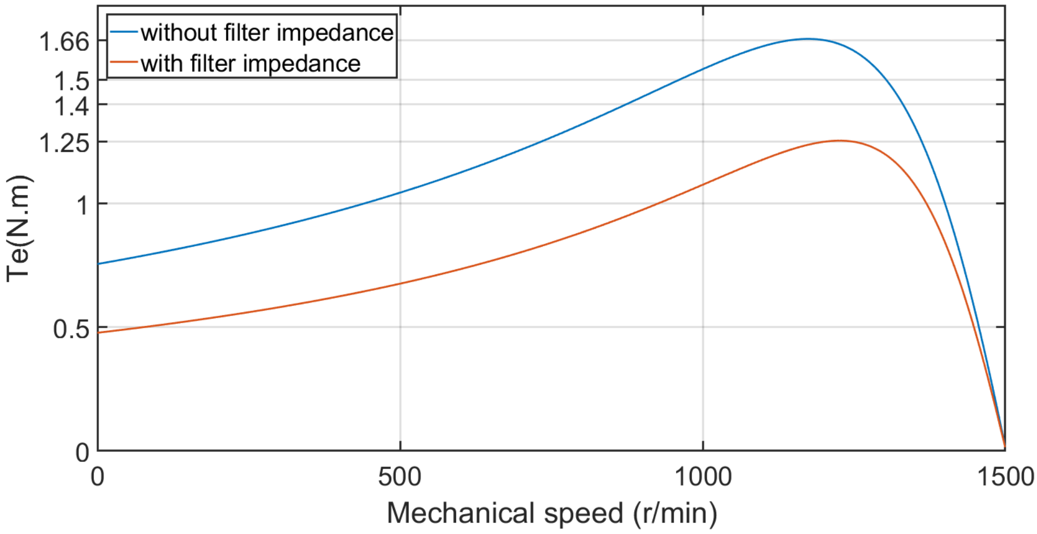

Figure 7.14 Torque-speed characteristic at 95V line voltage when connected to grid and open-loop controlled VSC.

The load torque in the simulation is set at 1.6N·m constantly. In the initial stage in the simulation, the VSC powered by a DC voltage source, the variac and the induction motor are connected in shunt. The VSC is generating 235W active power to the network. The induction motor is drawing the active and reactive power of approximately 293W and 364Var, respectively, to drag the load. At t=2s, a three-phase-to-ground fault is simulated to occur. Then, after 200ms which is at the moment t=2.2s, the circuit breaker *CB1* and *CB2* are open simultaneously. Meanwhile the proposed voltage controller of the VSC is activated to operate as the outer loop to provide current reference to the inner current control loop. Then, the VSC will provide required active and reactive power to the induction motor for re-magnetization and re-acceleration. The results are shown in Figure 7.15.

When the fault occurs at t=2s, the voltage drops to zero, but the output current of the VSC remains at the same amplitude thanks to the current control loop. Meanwhile, the rotor speed of the induction motor start to drop because the power supply is lost. When the fault is cleared and the connection to the mains is cut out at t=2.2s, the voltage controller in the VSC kicks in and drives the voltage back to the nominal value within 50ms. Similar to the simulation and experiment carried out in Chapter 5, this is done by connect the select switch *S* to *position 1* in Figure 5.1.

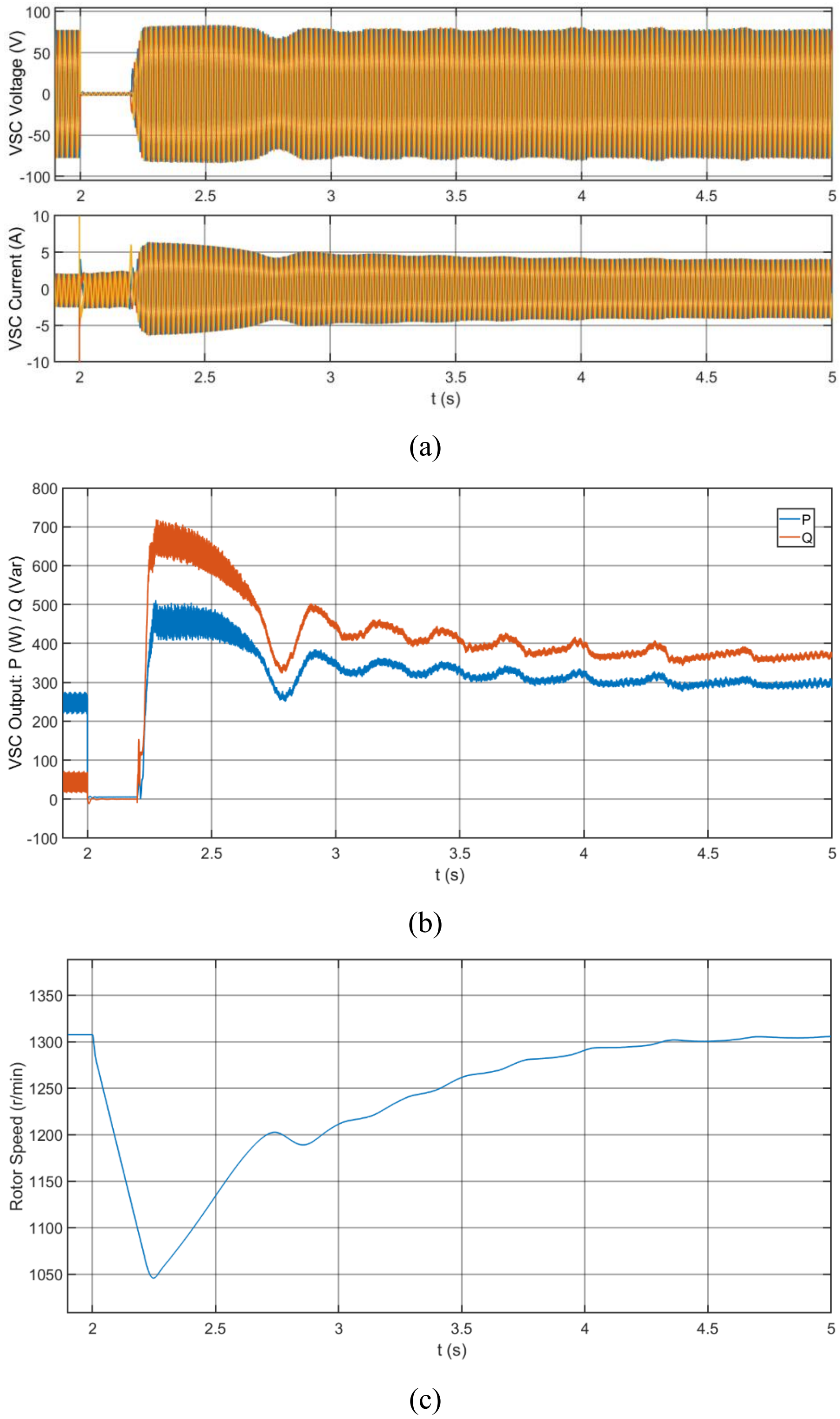

Figure 7.15 Simulation results of power supply to an induction motor by a VSC in island mode including the islanding transition: (a) Output three-phase voltage and current of the VSC; (b) Output active and reactive power of the VSC; (c) Rotor speed of the induction motor.

The output current of the VSC responds to the requirement of the induction motor, increasing rapidly (with an overshoot) to supply a large reactive power for re-magnetization to induce electromagnetic torque to re-accelerate the rotor. The overshoot of the current gradually disappears with the recovery of the rotor speed as well as the active and reactive power required by the motor. The results show a similar process to the case studied in section 7.1 (results shown in Figure 7.3): the induction motor is reconnected to the mains after the fault. Therefore, the simulation verifies that the VSC supplies the induction motor properly like the mains.

To validate the analysis on the stability margin reduction due to the filter impedance of the VSC. A simulation is carried out again, but the VSC is open-loop controlled this time. The results are shown in Figure 7.16.

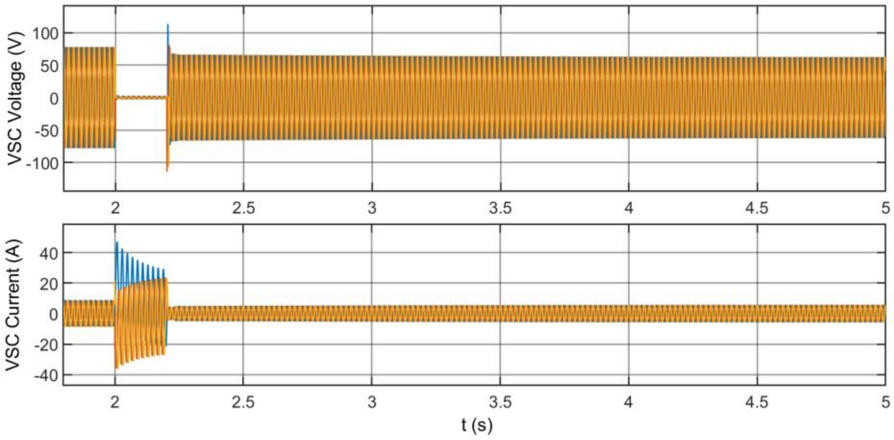

(a)

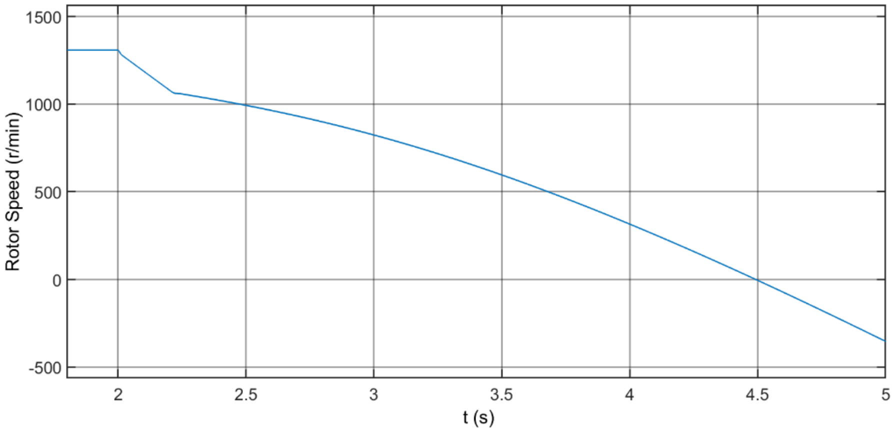

(b)

Figure 7.16 Simulation results when the VSC is open-loop controlled: (a) Output voltage and current of the VSC; (b) Rotor speed of the induction motor.

When the fault happens, the rotor speed drops as the as the previous simulation. The output current of the VSC increases by nearly 5 times (making current) due to the lack of current control loop. Although overcurrent is critical to power-electronic devices, it is the not the key issue in this chapter. Therefore, the overcurrent during the fault is not going to be discussed here. After *CB1* and *CB2* are open, the induction motor is connected to the VSC. However, due to the filter impedance, the maximum electromagnetic torque can be induced in the rotor is smaller than the load torque as demonstrated in Figure 7.14 which means that the VSC will not be able to drive the rotor speed back. As shown in Figure 7.16, the rotor speed drops to zero at about t=4.5s and starts to rotate reversely.

7.5 Experiment Results

As aforementioned, the network setup is as the same as in the simulation, and related parameters have been listed in Table 7-1 and Table 7-2. To generate a constant load to the induction motor, another induction machine is coupled with the induction motor as a generator and the torque is controlled by a commercial drive (ABB-ACS580). To measure the rotor speed and torque, a torque transducer is installed as the coupling of the shafts of the two induction machines. The regenerative energy in the induction generator is dissipated in the brake resistor. The experiment setup and equipment are shown in Figure 7.17 (a) and (b). Due to the safety concern, instead of the loss of mains after a three-phase-to-ground fault, the loss of mains is directly applied by opening *CB1* in the experiment.

The experiment results for the VSC using proposed controller are shown in Figure 7.18. In the initial stage, the induction motor is supplied by the mains via the variac, and the VSC is in current control mode outputting 3A (amplitude) current. The AC drive controls the induction generator to generate 1.6N·m torque which is measured by the torque transducer on the rotor shafts. The rotor speed is at about 1303 (r/min) which is very close to simulation result, 1308 (r/min).

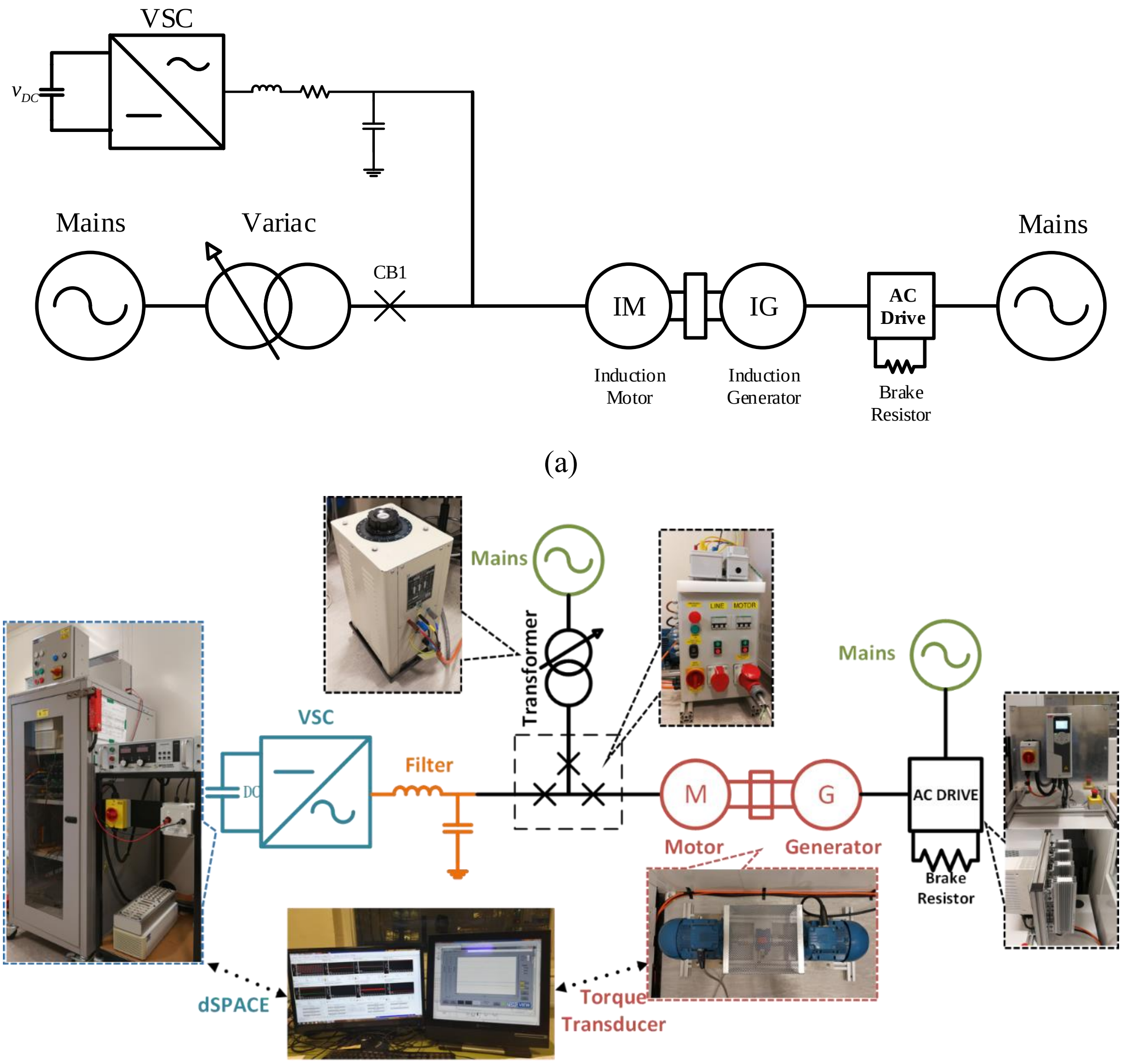

(a)

(b)

Figure 7.17 Experiment Setup: (a) single-line diagram of the experiment setup; (b) photos of equipment.

Around the moment *t*=12.05, the *CB1* is open thus the connection to the mains is lost. The voltage controller in the VSC is activated once the PLL detects the frequency drops below 48Hz, which takes less than one cycle. Then, the VSC starts to work as a voltage source, and its output current responds to the load need. As previously discussed, a large reactive power is required to re-induce the rotor flux which is shown in the experiment result in Figure 7.18 (b). The current overshoot appears accordingly as shown in Figure 7.18 (a).

The transition is over after *t*=12.5s, and the rotor speed stablizes at about 1301 (r/min) which is considered to be unchanged. Thus, the VSC is verified to be capable of supplying the indution motor properly in islande mode. The THDs in the votlage and current are 4.86% and 3.85%, respectively.

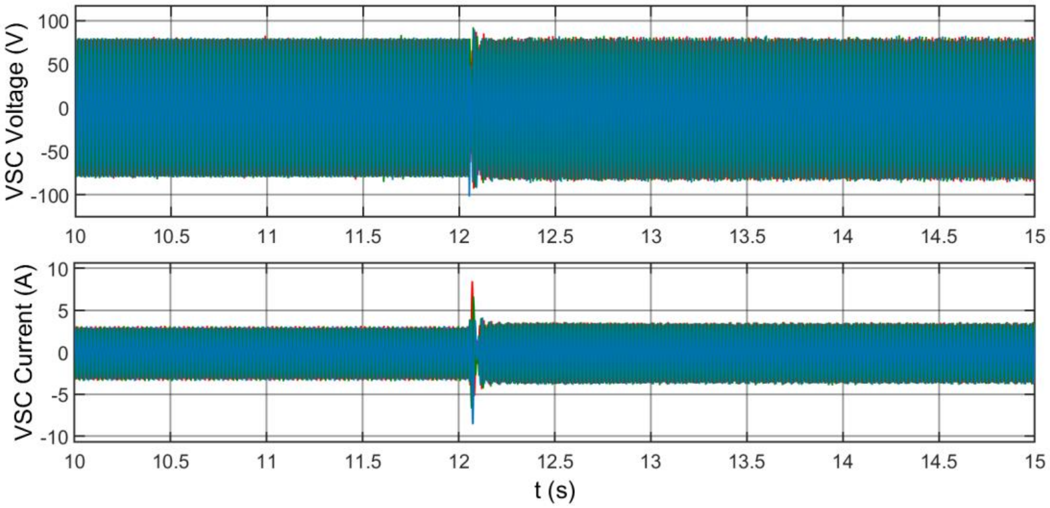

(a)

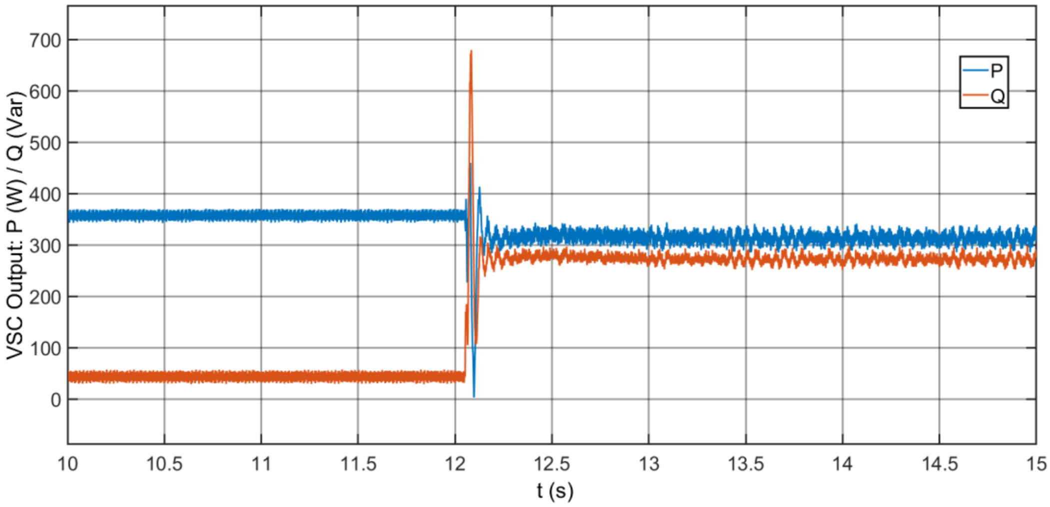

(b)

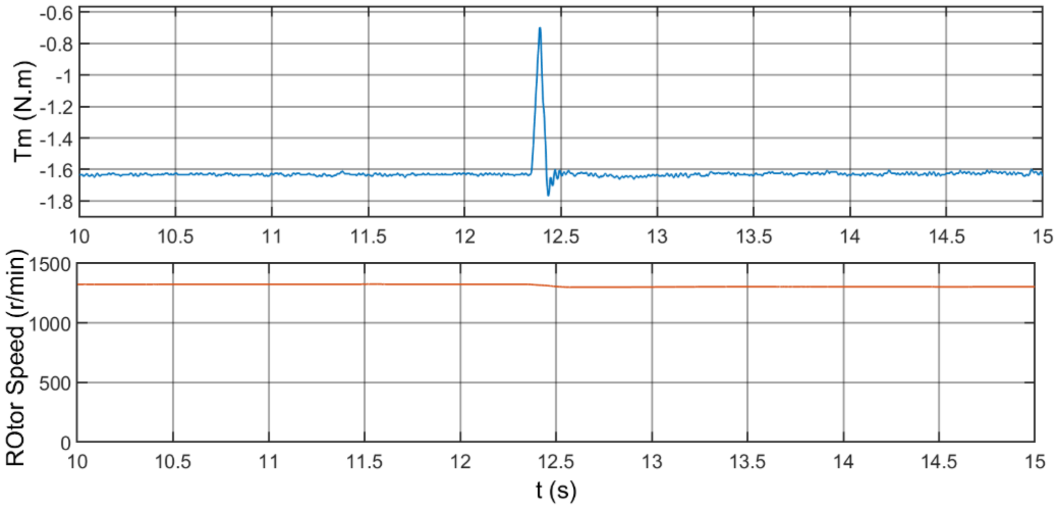

(c)

Figure 7.18 Experiment result during the loss of mains when the VSC is in the proposed closed-loop control: (a) Output three-phase voltage and current of the VSC; (b) Output active and reactive power of the VSC; (c) Torque on the rotor shaft and rotor speed.

Another experiment for the VSC in open-loop control is carried out to verify the analysis on the induction motor's stability margin. The results are shown in Figure 7.19. The circuit breaker *CB1* is open at about *t*=17.46s. As shown in Figure 7.19 (b) the large reactive power overshoot appears which indicates the reactive power required for re-magnetization in the rotor. However, the induced electromagnetic torque is smaller than the load torque due to the existence of the filter impedance, and as a result the rotor speed keeps decreasing and cannot be recovered as shown in Figure 7.19 (c).

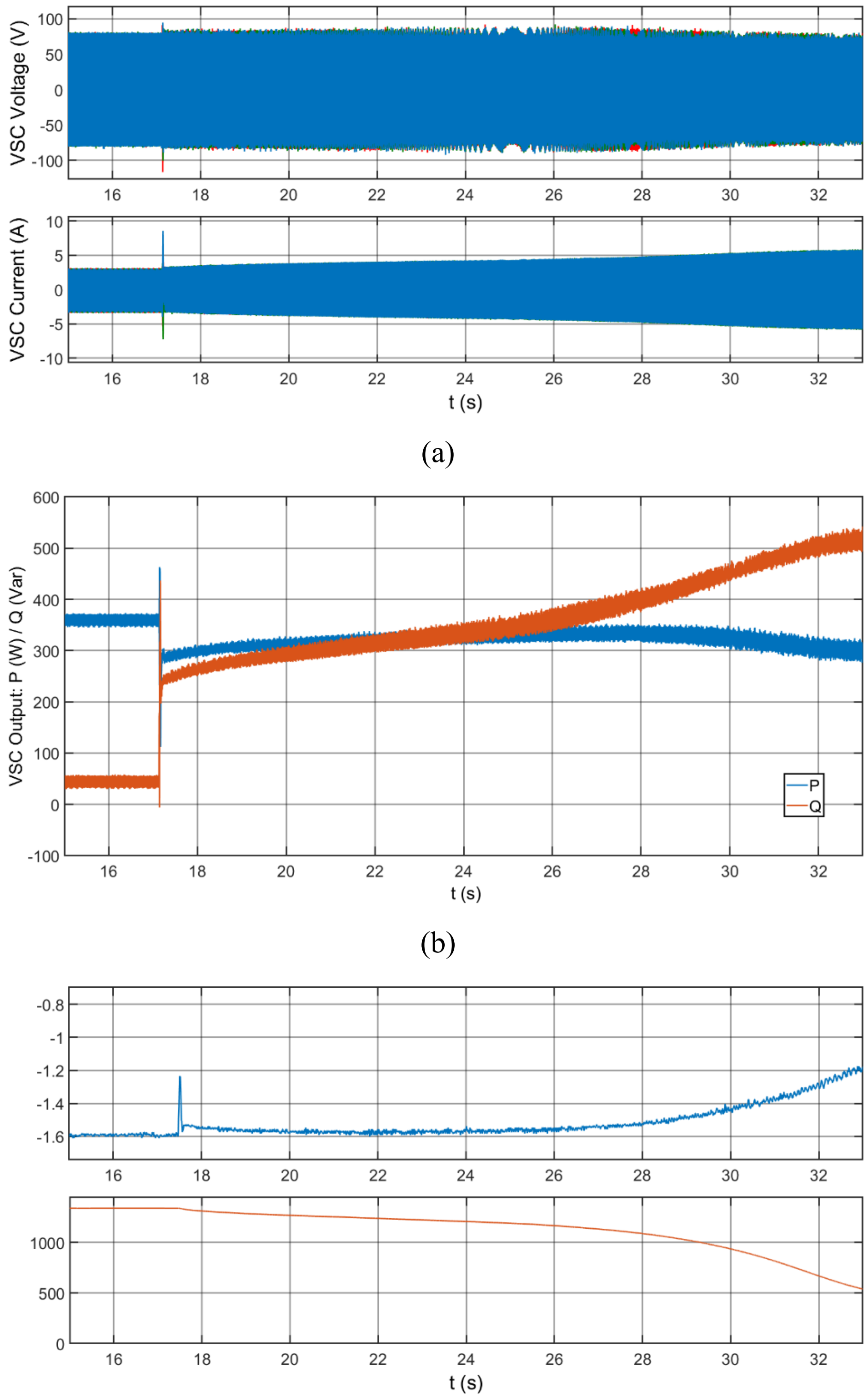

(a)

(b)

(c)

Figure 7.19 Experiment result during the loss of mains when the VSC is in open-loop control: (a) Output three-phase voltage and current of the VSC; (b) Output active and reactive power of the VSC; (c) Torque on the rotor shaft and rotor speed.

7.6 Summary

In the first section, the influence of network fault to an induction motor is first investigated. The sequences including the decay of rotor flux linkage, loss of electromagnetic torque, speed drop, re-magnetization and speed recovery have been shown in the first section.

Then in the second section, the stability margin reduction of an induction motor due to the filter impedance when connected to a VSC is investigated. The calculation method has been given and validated by experiment tests. For given parameters in this chapter, result showed that the stability margin would be significantly reduced when the VSC is in open-loop control.

In the third section, closed-loop output voltage control that developed in Chapter 5 is adopted, and the output impedance of the VSC was analysed using transfer function and associated bode diagrams. Results showed that the output impedance at the fundamental frequency was greatly reduced because of the output current feedforward in the controller, but resonance at high frequency was found due to the effect of inner current control loop. Then improved feedforward term was proposed which can supress the high frequency resonance.

Then simulation and experiment under same network setup and parameters were carried out to validate the analyses and controller design by comparing the proposed controller to the open-loop controller in a direct loss of mains case. Constant load torque was applied by another induction machine with a commercial drive. Both simulation and experiment results validated that the proposed controller successfully reduced the output impedance of the VSC, and as a result the stability margin of the induction motor was not affected.

8.Conclusions and Future Work

8.1 Conclusions

The focus of this thesis lies in the controller design of a B2B-VSC-based SOP for increasing the flexibility of power distribution networks.

In Chapter 2, issues on the voltage profile and fault level increase due to high DG penetration level are analysed via simulations on a network with reasonable setup. Results show that the voltage violation could happen when the DG penetration level reaches around 35% in the earliest and 80% in the latest. In terms of the fault current increase, the fault level is increased to 93% of the duty of the circuit breakers when the DG penetration level is at 100%. Therefore, voltage violation is likely to be the first constraint to be met when increasing DG penetration level in distribution networks.

In Chapter 3, for solving the voltage violation issue could be posed by high DG penetration level. Existing compensators that have been widely used in transmission networks to increase transmittable active power and improve voltage profile are reviewed. Compensators based on power-electronic converters due to the fast response and continues compensation value are more suitable for applications in distribution networks having the high uncertainties in load and DGs.

In Chapter 4, the potential utilisation of compensators based on power-electronic converters in distribution networks is discussed. Due the low *X/R* ratio of power lines/cables and the high load power factors in distribution networks, sole reactive power compensation will be less effective than that in transmission networks. Therefore, active power compensation is required to effectively regulate voltage profiles in a distribution network with high DG penetration level. However, installing small-scale energy storage systems in SSSCs and STATCOMs are less cost-effective. Utilising SOPs, power-electronic devices that replace normally-open points, is a promising strategy to address voltage issues in distribution networks with high DG penetration level. An SSSC-based SOP as the representative of partially-rated device and a B2B-VSC-based SOP as the fully-rated device are compared on the aspects of voltage regulation and power loss by simulations. The SSSC-based SOP has sufficient performance on improving voltage profile and 20 to 40 times lower power loss than a B2B-VSC. But, it requires additional protection schemes such as the crowbar protection. In terms of the B2B-VSC-based SOP, it has better performance on regulating voltage profile because of its independent reactive power compensation at both terminals. In addition, fault current can be limited, and no additional protection scheme is required. But, the B2B-VSC-based SOP as a fully-rated device will have higher power loss and capital cost, and its reliability must be sufficiently high because the fault of the device itself could significantly affect the network. In this thesis, the B2B-VSC is selected as the SOP considering its versatility and most importantly the capability of restricting fault current.

In Chapter 5, a controller of B2B-VSC based on the PI control theory is developed in SRF. Four controllers, the PLL controller, current controller, DC link voltage controller and output voltage controller are included. The PLL controller and current controller are reserved in all circumstances, and the rest two controllers are activated and connected to the current control loop depending on scenarios. This controller is designed to fulfil three functionalities: active power control and reactive power compensation, fault current restriction and load supply in island mode. The step by step development of the controller is introduced including all details on parameter selections. The method to precisely choose the damping ratio of the nonstandard second-order system appeared in the controller is also derived in detail. A technique of regularly resetting the integrator in the output voltage controller is proposed to achieve fast and smooth transition from grid-connected mode to island mode. Simulation results show that in grid-connected mode, the active power and reactive power is well controlled at the reference value and the voltage therefore is regulated well to be within the permitted range all the time even in the extreme case. In the simulation of three-phase-to-ground fault, the B2B-VSC successfully restricts the current at the reference value and the network on the other side remains unaffected. In the loss of mains event, the current flowing through the B2B-VSC is always restricted within the safe range because of the current control loop, and the B2B-VSC can supply the load properly once excessive load has been cut out. The proposed technique has been verified by comparing the transitions with and without the technique. A much longer and rough transition is shown if the reset of the integrator is not applied. At last, the experiment has been carried out at a scale-down voltage level and validated the designs of the PLL controller, current controller and output voltage controller. Simulation using the same parameters as in the experiment have also been made and showed well-matched results which further validates the accuracy of the system modelling.

In Chapter 6, another controller based on the concept of synchronverters is developed. The controller makes the B2B-VSC behave like two synchronous machines generating active power according to the frequency and reactive power according to the voltage. Three modifications are made to adapt the synchronverter idea to the application of an SOP. Firstly, the reference angular velocity of one of the synchronverters is obtained from the grid at the other side by a slow PLL instead of using the grid frequency at its own side or the internal angular velocity or the nominal angular velocity. This modification is to make the B2B-syncrhonverter generate active power independent of the grid frequency and do not require the detection when the loss of mains occurs. Secondly, DC link voltage controller is added to both of the synchronverters and share the equal burden of regulating the DC link voltage. Thirdly, a PI controller in the *P*-*ω* loop is proposed as an optional improvement to utilise the B2B-synchornverter up to its power rating in certain conditions or make the B2B-synchornverter in charge of providing frequency reference in island mode. The simulation for grid-connected condition was carried out first. The results show that the output active power of the B2B-syncrhonverter is controlled to track the reference well and the reactive power is generated according to the *Q*-*V* droop. The voltage regulation is well demonstrated in load variations and extreme cases. Then the loss of mains is simulated, and load shedding is considered in the islanding process because the load should be about twice of the operation point of the B2B-synchronverter at any given moment and the load demand could be larger than the power rating of the B2B-synchronverter. The following sequence of the islanding transition was shown in the simulation: voltage and frequency drop rapidly when the mains is lost; B2B-synchronverter increases active power output due to the *P*-*ω* droop; power supplied by the B2B-syncrhonverter does not meet the load demand, so the load frequency keeps decreasing; then load shedding takes place in sequence thus the load voltage and frequency starts to rise back; when the output power of the B2B-sychronverter is within its power rating the PI controller in the *P*-*ω* loop is activated which drives the frequency to the nominal value. The transition shows a possible scenario when the loss of mains happens while the load demand is larger than the power rating of the B2B-synchronverter. It should be noted that overcurrent during the transition appears which must be considered with care. In the last, three-phase-to-ground fault was simulated and the result shows that the by using *direct protection* scheme the fault current is successfully blocked but it relies on the overcurrent detection.

In Chapter 7, the feasibility of using VSCs to supply induction motors in island condition is investigated. The influence of fault and the loss of mains to an induction motor is studied. The main issue of supplying an induction motor by a VSC is the influence of the VSC's filter impedance on the stability margin of the induction motor. Analysis, simulation and experiment have been carried out to verify the torque-speed calculation and reduction of stability margin due the filter impedance. Then, the reduction of the output impedance of the VSC by the output voltage controller is demonstrated using transfer functions and associated bode diagrams. An improvement on the feedforward to achieve lower impedance gain at high frequency is proposed. Simulation and experiment results show that the proposed output voltage controller can properly supply the induction motor in island mode.

The versatility of the B2B-VSC has been demonstrated in the last three chapters. It can regulate the voltage in distribution networks via active and reactive power controls and thus improve the flexibility of the network. It can also improve the reliability of the network by the capability of supplying load in islanded condition.

8.2 Future work

In Chapter 5 and Chapter 6, two controllers for the B2B-VSC-based SOP have been developed. They both provide sound performance on active control, reactive power compensation and voltage regulation. But in other conditions they have their own merits and drawbacks. Regarding the controller design, conventional PI theory is easier to apply because all the system can be easily linearized, and parameters selection can be clearly defined. On the other hand, the controller of synchronverter is non-linear and it is hard to explicitly define the effect of each parameter to the system response. However, it might be easier for DNOs to manage distribution networks with synchronverter-based DGs as the theory of synchronous generator has been well-established and widely used for nearly 100 years. From the reliability and computational burden point of view, B2B-syncrhonverter is better because no condition detection is required and thus there is no risks in delayed detections or misdetections. However, in terms of dealing with overcurrent or fault current, PI control based B2B-VSC is superior because of the current control loop. The current is limited at reference value without distortions even in the islanding transaction, and fault is automatically isolated thus reactive power compensation to the other network is unaffected. But for B2B-synchronverter, though fault current can be restricted by the *direct protection* scheme, the current is distorted during a fault and the reactive power compensation at the other side cannot be continued. Besides, the current increases beyond the rating if the load demand is larger than power rating of the B2B-synchronverter when the loss of mains occurs. Therefore, to develop a controller combining the advantages of these two controllers could be a direction of the future work.

In fact, there is a key problem preventing DNOs from using VSCs to supply a conventional network. The action of circuit breakers throughout a distribution networks rely on the large fault current to trigger the relays. However, a surge current like the make current during a fault instant can easily generate huge heat that exceeding the thermal limit of a power-electronic device and consequently damage the device. Therefore, various protection schemes are always implemented incorporate with the devices to ensure that surge current is not experienced by the device. If a power-electronic converter is the only power source of the load such as the islanded condition illustrated in Chapter 5 and 6, no large fault current should appear in the network because protections are implemented to prevent large current flowing through the converter. In this condition, the relays cannot be triggered and thus the fault section cannot be cut out. To use VSCs to supply a conventional network in island mode, this problem must be addressed. An idea of installing phase changing material between the chip and the DBC board to absorb the transient heat to improve the power-electronic converters' capability of withstanding surge current has been proposed [107, 108]. However, more solid experiment results are required to validate this idea. This could be an important research direction and of great importance on using VSCs as sole power supplies in islanded condition.

Bibliography

[1] Ofgem, "Distributed Energy - A Call for Evidence for the Review of Barriers and Incentives to Distributed Electricity Generation, Including Combined Heat and Power," 2006, Available: https://www.ofgem.gov.uk/ofgem-publications/43685/15939-19306pdf.

[2] S. W. Blume, *Electric Power System Basics for the Nonelectrical Professional*, 2nd ed. ed. 2007.

[3] T. S. Foundation. (2010). *EXHAUSTION OF FOSSIL FUELS*. Available: http://www.terra-symbiosis.org/EN_epuisement-fossiles.pdf

[4] T. Senjyu, Y. Miyazato, A. Yona, N. Urasaki, and T. Funabashi, "Optimal Distribution Voltage Control and Coordination With Distributed Generation," *Power Delivery, IEEE Transactions on,* vol. 23, no. 2, pp. 1236-1242, 2008.

[5] A. Yadav and L. Srivastava, "Optimal placement of distributed generation: An overview and key issues," in *Power Signals Control and Computations (EPSCICON), 2014 International Conference on*, 2014, pp. 1-6.

[6] M. F. AlHajri and M. E. El-Hawary, "Improving the voltage profiles of Distribution Networks using multiple Distribution Generation Sources," in *2007 Large Engineering Systems Conference on Power Engineering*, 2007, pp. 295-299.

[7] e.on. (2017). *On Site Generation : Learn more about our onsite renewable energy generation technologies*. Available: https://www.eonenergy.com/for-your-business/large-energy-users/manage-energy/on-site-generation

[8] ofgem. (2017). *Distributed Generation*. Available: https://www.ofgem.gov.uk/electricity/distribution-networks/connections-and-competition/distributed-generation

[9] Ofgem. (2018). *Distributed generation*. Available: https://www.ofgem.gov.uk/electricity/distribution-networks/connections-and-competition/distributed-generation

[10] T. Ackermann, G. Andersson, and L. Soder, "Distributed generation: a definition," *Electric Power Systems Research,* vol. 57, pp. 195-204, 2001.

[11] G. Pepermans, J. Driesen, and D. Haeseldonckx, "Distributed generation: definition, benefits and issues," KU Leuven, Department of Economics - Research Group Energy, Transport and Environment2003, Available: https://EconPapers.repec.org/RePEc:ete:etewps:ete0308.

[12] N. M. Ijumba, A. A. Jimoh, and M. Nkabinde, "Influence of distribution generation on distribution network performance," in *Africon, 1999 IEEE*, 1999, vol. 2, pp. 961-964 vol.2.

[13] R. Dettmer, "Home station [domestic CHP capacity]," *IEE Review,* vol. 44, no. 1, pp. 11-13, 1998.

[14] R. J. R. Budden, "CHP and the Energy Act," *IEE Review,* vol. 34, no. 9, pp. 341-343, 1988.

[15] D. Green, "Coming out of the cold (cogeneration)," *IEE Review,* vol. 38, no. 3, pp. 117-120, 1992.

[16] (2018). *Digest of UK Energy Statistics (DUKES): combined heat and power*.

Available: https://assets.publishing.service.gov.uk/government/uploads/system/uploads/attachment_data/file/729356/Ch7.pdf

[17] Ofgem, "Distributed Energy A Call for Evidence for the Review of Barriers and Incentives to Distributed Electricity Generation, Including Combined Heat and Power," ed, 2006.

[18] Wikipedia. (2018). *Renewable energy*. Available: https://en.wikipedia.org/wiki/Renewable_energy#Growth_of_renewables

[19] UK. (2018). *Digest of UK Energy Statistics (DUKES): electricity*. Available: https://www.gov.uk/government/statistics/electricity-chapter-5-digest-of-united-kingdom-energy-statistics-dukes

[20] UK. (2018). *DIgest of UK Energy Statistics (DUKES): renewable sources of energy*. Available: https://www.gov.uk/government/statistics/renewable-sources-of-energy-chapter-6-digest-of-united-kingdom-energy-statistics-dukes

[21] J. Xiaoling, Z. Yibin, and W. Xue, "Strategy and coordinated development of strong and smart grid," in *IEEE PES Innovative Smart Grid Technologies*, 2012, pp. 1-4.

[22] R. Zhang, Y. Du, and Y. Liu, "New challenges to power system planning and operation of smart grid development in China," in *2010 International Conference on Power System Technology*, 2010, pp. 1-8.

[23] G. Tuna, E. Kaya, K. Gülez, G. Kiokes, and V. Ç. Güngör, "Performance evaluations of next generation networks for smart grid applications," in *2015 3rd International Istanbul Smart Grid Congress and Fair (ICSG)*, 2015, pp. 1-5.

[24] H. Farhangi, "The path of the smart grid," *IEEE Power and Energy Magazine,* vol. 8, no. 1, pp. 18-28, 2010.

[25] X. Fang, S. Misra, G. Xue, and D. Yang, "Smart Grid — The New and Improved Power Grid: A Survey," *IEEE Communications Surveys & Tutorials,* vol. 14, no. 4, pp. 944-980, 2012.

[26] A. Ipakchi and F. Albuyeh, "Grid of the future," *IEEE Power and Energy Magazine,* vol. 7, no. 2, pp. 52-62, 2009.

[27] H. Louie, M. Burns, and C. Lima, "An introduction and user's guide to the IEEE Smart Grid Web Portal," in *2010 IEEE PES Innovative Smart Grid Technologies Conference Europe (ISGT Europe)*, 2010, pp. 1-5.

[28] V. C. Gungor *et al.*, "Smart Grid Technologies: Communication Technologies and Standards," *IEEE Transactions on Industrial Informatics,* vol. 7, no. 4, pp. 529-539, 2011.

[29] S. M. Amin and B. F. Wollenberg, "Toward a smart grid: power delivery for the 21st century," *IEEE Power and Energy Magazine,* vol. 3, no. 5, pp. 34-41, 2005.

[30] K. Zheng, J.-h. Zhang, and W.-x. Liu, "Distribution network reliability considering complementary distribution generation with wind and photovoltaic powers," in *Critical Infrastructure (CRIS), 2010 5th International Conference on*, 2010, pp. 1-5.

[31] P. K. Olulope, K. A. Folly, and G. K. Venayagamoorthy, "Modeling and simulation of hybrid distributed generation and its impact on transient stability of power system," in *Industrial Technology (ICIT), 2013 IEEE International Conference on*, 2013, pp. 1757-1762.

[32] P. Barker and R. W. de Mello, "Determining the Impact of Distributed Generation on Power Systems: Part 1 - Radial Distribution Systems," Power Technologies, Inc.2000,

Available: https://s3.amazonaws.com/academia.edu.documents/37008557/impact_of_dg_in_dist._generation.pdf?AWSAccessKeyId=AKIAIWOWYYGZ2Y53UL3A&Expires=1538586426&Signature=Y4KZC%2BEtXfg9M75Qj0kkQctHtBw%3D&response-content-disposition=inline%3B%20filename%3DImpact_of_dg_in_dist._generation.pdf.

[33] C. C. d. Prado, D. P. Bernardon, C. L. Pires, C. C. Martins, and F. C. Lucchese, "Analysis of distributed generation impact on the voltage stability margin," in *2016 51st International Universities Power Engineering Conference (UPEC)*, 2016, pp. 1-6.

[34] S. Daud, A. F. A. Kadir, and C. K. Gan, "The impacts of distributed Photovoltaic generation on power distribution networks losses," in *2015 IEEE Student Conference on Research and Development (SCOReD)*, 2015, pp. 11-15.

[35] A. Keane, L. F. Ochoa, E. Vittal, C. J. Dent, and G. P. Harrison, "Enhanced Utilization of Voltage Control Resources With Distributed Generation," *IEEE Transactions on Power Systems,* vol. 26, no. 1, pp. 252-260, 2011.

[36] S. Barik and D. Das, "Determining the sizes of renewable DGs considering seasonal variation of generation and load and their impact on system load growth," *IET Renewable Power Generation,* vol. 12, no. 10, pp. 1101-1110, 2018.

[37] H. Golpîra, H. Seifi, A. R. Messina, and M. Haghifam, "Maximum Penetration Level of Micro-Grids in Large-Scale Power Systems: Frequency Stability Viewpoint," *IEEE Transactions on Power Systems,* vol. 31, no. 6, pp. 5163-5171, 2016.

[38] M. Milligan, "Market implications of high levels of wind and solar generation," in *2012 IEEE Power and Energy Society General Meeting*, 2012, pp. 1-1.

[39] W. P. DISTRIBUTION, "INDUSTRIAL AND COMMERCIAL DESIGN FRAMEWORK DLH SPECIFIC APPENDIX," 2005, Available: file:///D:/1PhD/Progress%20Documents/4th%20year/Thesis/reference/G81_4.pdf.

[40] N. Grid, "Review of Grid Code Connection Conditions for Frequency and Voltage Operating Ranges," 2009, vol. 09 Available: https://www.nationalgrid.com/sites/default/files/documents/15420-Frequency%20and%20Voltage%20Operating%20Range.pdf.

[41] H. a. Qin, "Network fault analysis with increased distributed generation penetration and evaluation of solutions to issues caused by distributed generation," Thesis (Ph.D.), University of Warwick, 2017.

[42] *Reactive power control in AC power systems*. New York, NY: Springer Berlin Heidelberg, 2017, p. pages cm.

[43] B. M. Weedy, *Electric power systems*, 5th ed. Chichester, West Sussex, UK: John Wiley & Sons, Ltd., 2012, pp. xvi, 496 p.

[44] S. Galvani, M. T. Hagh, and M. B. B. Sharifian, "Unified power flow controller impact on power system predictability," *IET Generation, Transmission & Distribution,* vol. 8, no. 5, pp. 819-827, 2014.

[45] A. J. Raju and J. P. Therattil, "Stability enhancement of a multi-area power system with unified power flow controller," in *2014 IEEE 8th International Power Engineering and Optimization Conference (PEOCO2014)*, 2014, pp. 24-29.

[46] Q. Wang and S. S. Choi, "The Design of Battery Energy Storage System in a Unified Power-Flow Control Scheme," *IEEE Transactions on Power Delivery,* vol. 23, no. 2,

pp. 1015-1024, 2008.

[47] "Proposed terms and definitions for flexible AC transmission system (FACTS)," *IEEE Transactions on Power Delivery,* vol. 12, no. 4, pp. 1848-1853, 1997.

[48] S. Bhowmick, *Flexible AC Transmission Systems (FACTS) : Newton power-flow modeling of voltage-sourced converter based controllers*. Boca Raton: CRC Press, Taylor & Francis Group, 2016, pp. xxviii, 291 pages.

[49] N. G. Hingorani and L. Gyugyi, *Understanding FACTS : concepts and technology of flexible AC transmission systems*. New York: Institute of Electrical and Electronics Engineers, 1999.

[50] N. Flourentzou, V. G. Agelidis, and G. D. Demetriades, "VSC-Based HVDC Power Transmission Systems: An Overview," *IEEE Transactions on Power Electronics,* vol. 24, no. 3, pp. 592-602, 2009.

[51] J. M. Carrasco *et al.*, "Power-Electronic Systems for the Grid Integration of Renewable Energy Sources: A Survey," *IEEE Transactions on Industrial Electronics,* vol. 53, no. 4, pp. 1002-1016, 2006, doi: 10.1109/TIE.2006.878356.

[52] S. Parhizi, H. Lotfi, A. Khodaei, and S. Bahramirad, "State of the Art in Research on Microgrids: A Review," *IEEE Access,* vol. 3, pp. 890-925, 2015, doi: 10.1109/ACCESS.2015.2443119.

[53] S. B. Kjaer, J. K. Pedersen, and F. Blaabjerg, "A review of single-phase grid-connected inverters for photovoltaic modules," *IEEE Transactions on Industry Applications,* vol. 41, no. 5, pp. 1292-1306, 2005, doi: 10.1109/TIA.2005.853371.

[54] T. Esram and P. L. Chapman, "Comparison of Photovoltaic Array Maximum Power Point Tracking Techniques," *IEEE Transactions on Energy Conversion,* vol. 22, no. 2, pp. 439-449, 2007, doi: 10.1109/TEC.2006.874230.

[55] M. G. Villalva, J. R. Gazoli, and E. R. Filho, "Comprehensive Approach to Modeling and Simulation of Photovoltaic Arrays," *IEEE Transactions on Power Electronics,* vol. 24, no. 5, pp. 1198-1208, 2009, doi: 10.1109/TPEL.2009.2013862.

[56] C. Newton, P. Lang, and S. Terry, "Field trial results of power electronics in low-voltage distribution networks," *CIRED - Open Access Proceedings Journal,* vol. 2017, no. 1, pp. 184-188, 2017, doi: 10.1049/oap-cired.2017.0110.

[57] W. Jianhua, S. Wanxing, S. Changkai, D. Qing, Q. Lijun, and L. Zhen, "Fully Flexible Power Distribution System for the next generation distribution grid," in *IECON 2016 - 42nd Annual Conference of the IEEE Industrial Electronics Society*, 23-26 Oct. 2016 2016, pp. 3854-3859, doi: 10.1109/IECON.2016.7793655.

[58] Q. Duan, C. Ma, G. Sha, C. Zhao, and Z. Li, "Research on flexible power distribution unit and its key technologies for energy internet," in *2018 13th IEEE Conference on Industrial Electronics and Applications (ICIEA)*, 31 May-2 June 2018 2018, pp. 2660-2665, doi: 10.1109/ICIEA.2018.8398160.

[59] A. H. Zaidi, K. Sunderland, and M. Conlon, "Role of reactive power (STATCOM) in the planning of distribution network with higher EV charging level," *IET Generation, Transmission & Distribution,* vol. 13, no. 7, pp. 951-959, 2019, doi: 10.1049/iet-gtd.2018.6046.

[60] B. McMillan, P. Guido, O. Leitermann, V. Martinelli, A. Gonzaga, and R. McFetridge, "Application of Power Electronics LV Power Regulators in a Utility Distribution System," in *2015 IEEE Rural Electric Power Conference*, 19-21 April 2015 2015, pp. 43-47, doi: 10.1109/REPC.2015.15.

[61] Q. Duan *et al.*, "Flexible power distribution unit — A novel power electronic transformer development and demonstration for distribution system," in *IECON 2015 - 41st Annual Conference of the IEEE Industrial Electronics Society*, 9-12 Nov. 2015 2015, pp. 000534-000537, doi: 10.1109/IECON.2015.7392155.

[62] Y. Tong, H. Zhang, L. Jing, and X. Wu, "Flexible substation and its control for AC and DC hybrid power distribution," in *2018 13th IEEE Conference on Industrial Electronics and Applications (ICIEA)*, 31 May-2 June 2018 2018, pp. 423-427, doi: 10.1109/ICIEA.2018.8397754.

[63] H. Zhang, L. Jing, X. Wu, J. Jiang, H. R. Wickramasinghe, and G. Konstantinou, "Power flow control scheme for multiport power electronics transformers," *High Voltage,* vol. 3, no. 4, pp. 255-262, 2018, doi: 10.1049/hve.2018.5034.

[64] J. M. Bloemink and T. C. Green, "Benefits of Distribution-Level Power Electronics for Supporting Distributed Generation Growth," *Power Delivery, IEEE Transactions on,* vol. 28, no. 2, pp. 911-919, 2013.

[65] N. G. Hingorani, "FACTS technology and opportunities," in *IEE Colloquium on Flexible AC Transmission Systems (FACTS) - The Key to Increased Utilisation of Power Systems*, 1994, pp. 4/1-410.

[66] E. V. Larsen, J. J. Sanchez-Gasca, and J. H. Chow, "Concepts for design of FACTS controllers to damp power swings," *IEEE Transactions on Power Systems,* vol. 10, no. 2, pp. 948-956, 1995.

[67] C. Schauder *et al.*, "Development of a /spl plusmn/100 MVAr static condenser for voltage control of transmission systems," *IEEE Transactions on Power Delivery,* vol. 10, no. 3, pp. 1486-1496, 1995.

[68] N. G. Hingorani, "Flexible AC transmission," *IEEE Spectrum,* vol. 30, no. 4, pp. 40-45, 1993.

[69] R. Grunbaum, M. d. Grijp, and V. Moshi, "Enabling long distance AC power transmission by means of FACTS," in *AFRICON 2009*, 2009, pp. 1-6.

[70] M. J. Afzal°, S. Ahmad, M. A. Arshad, and S. A. A. Kazmi, "Voltage improvement of loop configured distribution networks with DGs & FACTS devices," in *2018 1st International Conference on Power, Energy and Smart Grid (ICPESG)*, 2018, pp. 1-5.

[71] R. Gitibin and F. Hoseinzadeh, "Comparison of D-SVC and D-STATCOM for performance enhancement of the distribution networks connected WECS including voltage dependent load models," in *2015 20th Conference on Electrical Power Distribution Networks Conference (EPDC)*, 2015, pp. 90-100.

[72] M. Masuda, E. Bormio, J. A. Jardini, F. A. T. Silva, S. Copeliovitch, and J. Camargo, "Development and implementation of FACTS (flexible AC transmission systems) devices in distribution networks," in *2004 IEEE/PES Transmision and Distribution Conference and Exposition: Latin America (IEEE Cat. No. 04EX956)*, 2004, pp. 839-844.

[73] M. M. E. Metwally, A. A. E. Emary, F. M. E. Bendary, and M. I. Mosaad, "Using FACTS controllers to balance distribution systems based ANN," in *2006 Eleventh International Middle East Power Systems Conference*, 2006, vol. 1, pp. 81-86.

[74] F. Z. Peng, "Flexible AC Transmission Systems (FACTS) and Resilient AC Distribution Systems (RACDS) in Smart Grid," *Proceedings of the IEEE,* vol. 105, no. 11, pp. 2099-2115, 2017.

[75] I. J. Diaz De Leon, B. Lieblick, and E. Wilie, "How facts on the distribution system are being used to improve power quality," *CIRED - Open Access Proceedings Journal,* vol. 2017, no. 1, pp. 691-694, 2017.

[76] A. Kechroud, J. M. A. Myrzik, and W. Kling, "Taking the experience from Flexible AC Transmission Systems to flexible AC distribution systems," in *2007 42nd International Universities Power Engineering Conference*, 2007, pp. 687-692.

[77] J. M. Bloemink and T. C. Green, "Increasing distributed generation penetration using soft normally-open points," in *Power and Energy Society General Meeting, 2010 IEEE*, 2010, pp. 1-8.

[78] W. Cao, J. Wu, and N. Jenkins, "Feeder load balancing in MV distribution networks using soft normally-open points," in *IEEE PES Innovative Smart Grid Technologies, Europe*, 2014, pp. 1-6.

[79] L. J. Thomas, A. Burchill, D. J. Rogers, M. Guest, and N. Jenkins, "Assessing distribution network hosting capacity with the addition of soft open points," in *5th IET International Conference on Renewable Power Generation (RPG) 2016*, 2016, pp. 1-6.

[80] N. Bottrell, P. Lang, and T. Green, "Algorithm for soft open points to solve thermal and voltage constraints in low-voltage distribution networks," *CIRED - Open Access Proceedings Journal,* vol. 2017, no. 1, pp. 1567-1570, 2017.

[81] P. Li *et al.*, "Coordinated Control Method of Voltage and Reactive Power for Active Distribution Networks Based on Soft Open Point," *IEEE Transactions on Sustainable Energy,* vol. 8, no. 4, pp. 1430-1442, 2017.

[82] A. Aithal, C. Long, W. Cao, J. Wu, and C. E. Ugalde-Loo, "Impact of soft open point on feeder automation," in *2016 IEEE International Energy Conference (ENERGYCON)*, 2016, pp. 1-6.

[83] P. Li, H. Ji, C. Wang, G. Song, J. Zhao, and Y. Song, "Robust operation strategy of soft open point for active distribution network with uncertainties," in *2017 IEEE Power & Energy Society General Meeting*, 2017, pp. 1-5.

[84] P. Li, G. Song, H. Ji, J. Zhao, C. Wang, and J. Wu, "A supply restoration method of distribution system based on Soft Open Point," in *2016 IEEE Innovative Smart Grid Technologies - Asia (ISGT-Asia)*, 2016, pp. 535-539.

[85] H. Qin, R. Wu, A. M. Abd-el-Motaleb, L. Ran, X. Deng, and P. Sensarma, "Utilisation of back-to-back VSC in a distribution network with DG," in *2016 IEEE International Conference on the Science of Electrical Engineering (ICSEE)*, 2016, pp. 1-5.

[86] E. Bashar, R. Wu, W. Shao, L. Ran, and H. Qin, "An Appraisal of Possible Protecton Schemes of Static Series Compensators in Medium Voltage Power Networks," in *REMOO-2018*, Venice, Italy, 2018, vol. 10, pp. 405-420.

[87] Z. Yan, Y. Xue, and X. Zhang, "PI parameters determination in dq decoupling control of VSC terminals," in *13th IET International Conference on AC and DC Power Transmission (ACDC 2017)*, 2017, pp. 1-5.

[88] S. Kumaravel, R. S. Narayan, T. O. Donnell, and C. O. Loughlin, "Genetic algorithm based PI tuning of VSC-HVDC system and implementation using OPAL-RT," in *TENCON 2017 - 2017 IEEE Region 10 Conference*, 2017, pp. 2193-2197.

[89] Y. Teng, C. Xiong, C. Li, Q. Hui, and Y. Zhu, "Grid-connected PV power plant LCL filter based on PI and PR control strategy," in *2015 IEEE Advanced Information*

Technology, Electronic and Automation Control Conference (IAEAC), 2015, pp. 1191-1196.

[90] A. Manoloiu, H. A. Pereira, R. Teodorescu, M. Bongiorno, M. Eremia, and S. R. Silva, "Comparison of PI and PR current controllers applied on two-level VSC-HVDC transmission system," in *2015 IEEE Eindhoven PowerTech*, 2015, pp. 1-5.

[91] B. Bon-Ho and S. Seung-Ki, "A compensation method for time delay of full-digital synchronous frame current regulator of PWM AC drives," *IEEE Transactions on Industry Applications,* vol. 39, no. 3, pp. 802-810, 2003.

[92] A. V. González, "Transient Response Analysis and Design of Current-Controlled Grid-Tied Converters," Ph.D., Department of Electronics Technology, University of Vigo, Vigo, Spain, 2015.

[93] L. Harnefors and H. P. Nee, "Model-based current control of AC machines using the internal model control method," *Industry Applications, IEEE Transactions on,* vol. 34, no. 1, pp. 133-141, 1998.

[94] Q. C. Zhong and G. Weiss, "Synchronverters: Inverters That Mimic Synchronous Generators," *IEEE Transactions on Industrial Electronics,* vol. 58, no. 4, pp. 1259-1267, 2011.

[95] Q. Zhong, P. Nguyen, Z. Ma, and W. Sheng, "Self-Synchronized Synchronverters: Inverters Without a Dedicated Synchronization Unit," *IEEE Transactions on Power Electronics,* vol. 29, no. 2, pp. 617-630, 2014.

[96] R. Aouini, B. Marinescu, K. B. Kilani, and M. Elleuch, "Synchronverter-Based Emulation and Control of HVDC Transmission," *IEEE Transactions on Power Systems,* vol. 31, no. 1, pp. 278-286, 2016.

[97] Z. Shuai, Y. Hu, Y. Peng, C. Tu, and Z. J. Shen, "Dynamic Stability Analysis of Synchronverter-Dominated Microgrid Based on Bifurcation Theory," *IEEE Transactions on Industrial Electronics,* vol. 64, no. 9, pp. 7467-7477, 2017.

[98] S. Dong, Y. Chi, and Y. Li, "Active Voltage Feedback Control for Hybrid Multiterminal HVDC System Adopting Improved Synchronverters," *IEEE Transactions on Power Delivery,* vol. 31, no. 2, pp. 445-455, 2016.

[99] Z. Shuai, W. Huang, C. Shen, J. Ge, and Z. J. Shen, "Characteristics and Restraining Method of Fast Transient Inrush Fault Currents in Synchronverters," *IEEE Transactions on Industrial Electronics,* vol. 64, no. 9, pp. 7487-7497, 2017.

[100] Z. Ma, Q. Zhong, and J. D. Yan, "Synchronverter-based control strategies for three-phase PWM rectifiers," in *2012 7th IEEE Conference on Industrial Electronics and Applications (ICIEA)*, 2012, pp. 225-230.

[101] V. Natarajan and G. Weiss, "Synchronverters with better stability due to virtual inductors, virtual capacitors and anti-windup," *IEEE Transactions on Industrial Electronics,* vol. PP, no. 99, pp. 1-1, 2017.

[102] C. Zhang *et al.*, "An improved synchronverter model and its dynamic behaviour comparison with synchronous generator," in *2nd IET Renewable Power Generation Conference (RPG 2013)*, 2013, pp. 1-4.

[103] S. H. a. Horowitz, A. G. a. Phadke, and J. K. a. Niemira, *Power system relaying*, 4th edition ed.

[104] D. W. Novotny and T. A. Lipo, *Vector Control and Dynamics of AC Drives* (Monographs in electrical and electronic engineering). Clarendon Press, 1996.

[105] S. J. Chapman, *Electric machinery fundamentals*, 5th ed. ed. New York: McGraw-

Hill, 2012.

[106] S. Tolani and P. Sensarma, "Output impedance mitigation at filter resonance for single and three-phase UPS systems with reduced sensor count," in *IECON 2015 - 41st Annual Conference of the IEEE Industrial Electronics Society*, 2015, pp. 003206-003211.

[107] W. Shao *et al.*, "Power Modules for Pulsed Load Applications Using Phase Change Material," in *Proc. IEEE 3D Power Electronics Integration and Manufacturing International Symposium (3D-PEIM)*, Maryland, USA, 2018, pp. 1-6.

[108] W. Shao *et al.*, "Power Module with Large Short Term Current Capability by Using Phase Change Material," in *Proc. IEEE Workshop on Wide Bandgap Power Devices and Applications in Asia (WiPDA Asia)*, Xi'An, China, 2018, pp. 1-6.

Appendix I

State-space matrices for output voltage control loop:

$$A=\begin{bmatrix} 0 & \frac{1}{C} & 0 & -\omega & 0 & 0 \\ -\frac{K_p}{\tau_I} & -\frac{1}{\tau_I} & \frac{1}{\tau_I} & \frac{\omega C}{\tau_I} & 0 & 0 \\ -K_i & 0 & 0 & 0 & 0 & 0 \\ \omega & 0 & 0 & 0 & \frac{1}{C} & 0 \\ -\frac{\omega C}{\tau_I} & 0 & 0 & -\frac{K_p}{\tau_I} & -\frac{1}{\tau_I} & \frac{1}{\tau_I} \\ 0 & 0 & 0 & -K_i & 0 & 0 \end{bmatrix} \qquad B=\begin{bmatrix} 0 & -\frac{1}{C} & 0 & 0 \\ \frac{K_p}{\tau_I} & \frac{1}{\tau_I} & 0 & 0 \\ K_i & 0 & 0 & 0 \\ 0 & 0 & 0 & -\frac{1}{C} \\ 0 & 0 & \frac{K_p}{\tau_I} & \frac{1}{\tau_I} \\ 0 & 0 & K_i & 0 \end{bmatrix}$$

$$C=\begin{bmatrix} 1 & 0 & 0 & 0 & 0 & 0 \\ 0 & 0 & 0 & 1 & 0 & 0 \end{bmatrix} \qquad D=\begin{bmatrix} 0 & 0 & 0 & 0 \\ 0 & 0 & 0 & 0 \end{bmatrix}$$

Appendix II

Characteristics of 'ABB HiPak IGBT Module 5SNE 0800M170100' used in Chapter 4.

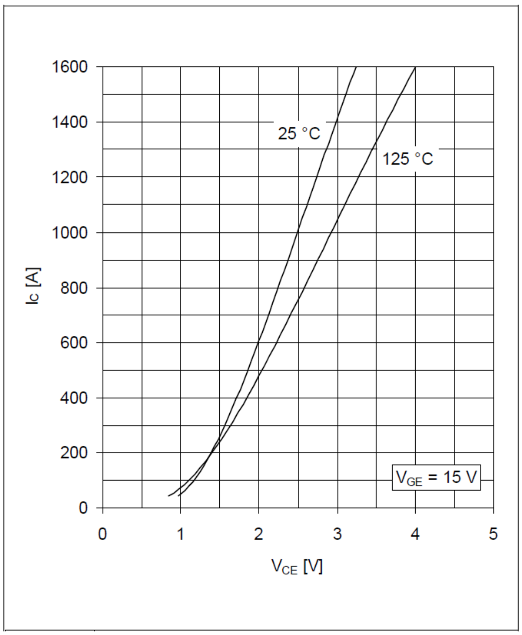

Fig. 1 Typical on-state characteristics, chip level

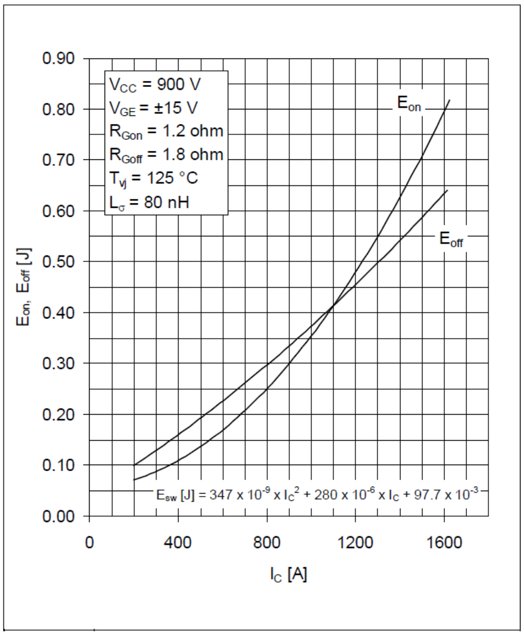

Fig. 5 Typical switching energies per pulse vs collector current

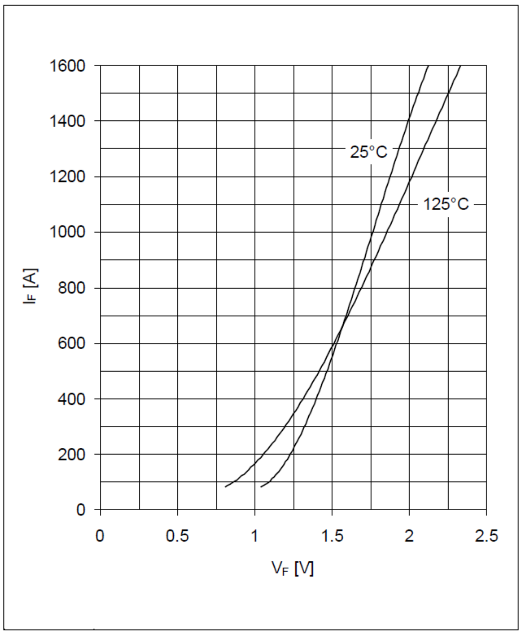

Fig. 14 Typical diode forward characteristics, chip level

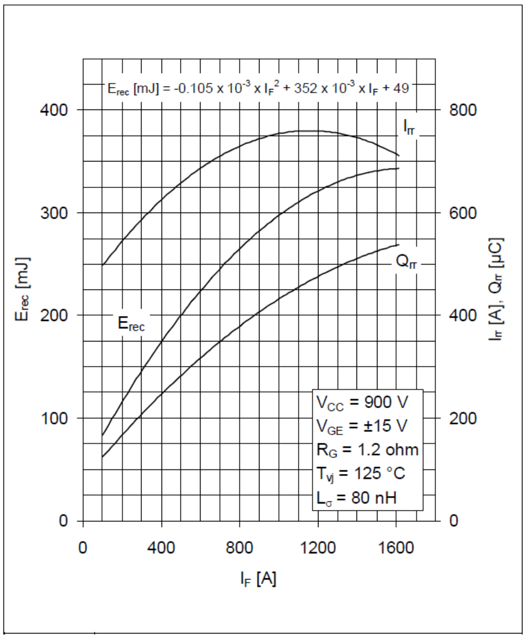

Fig. 12 Typical reverse recovery characteristics vs forward current

Appendix III

J1 R. Wu, L. Ran, G. Weiss, and J. Yu, "Control of a synchronverter-based soft open point in a distribution network," The Journal of Engineering, vol. 2019, no. 16, pp. 720-727, 2019.

C1 H. Qin, R. Wu, A. M. Abd-el-Motaleb, L. Ran, X. Deng, and P. Sensarma, "Utilisation of back-to-back VSC in a distribution network with DG," in *2016 IEEE International Conference on the Science of Electrical Engineering (ICSEE)*, 2016, pp. 1-5.

C2 E. Bashar, R. Wu, W. Shao, L. Ran, and H. Qin, "An Appraisal of Possible Protecton Schemes of Static Series Compensators in Medium Voltage Power Networks," in *REMOO-2018*, Venice, Italy, 2018, vol. 10, pp. 405-420. (has been accepted and in production)

C3 W. Shao *et al.*, "Power Modules for Pulsed Load Applications Using Phase Change Material," in *Proc. IEEE 3D Power Electronics Integration and Manufacturing International Symposium (3D-PEIM)*, Maryland, USA, 2018, pp. 1-6. (has been accepted and in production)

C4 W. Shao *et al.*, "Power Module with Large Short Term Current Capability by Using Phase Change Material," in *Proc. IEEE Workshop on Wide Bandgap Power Devices and Applications in Asia (WiPDA Asia)*, Xi'An, China, 2018, pp. 1-6. (has been accepted and in production)